Monitoring the deformation behavior of an immersed tunnel with Distributed Optical Fiber Sensor (DOFS)

Zhang, X.

Important note
To cite this publication, please use the final published version (if applicable).
Please check the document version above.

MONITORING THE DEFORMATION BEHAVIOR OF AN IMMERSED TUNNEL WITH DISTRIBUTED OPTICAL FIBER SENSOR (DOFS)

MONITORING THE DEFORMATION BEHAVIOR OF AN IMMERSED TUNNEL WITH DISTRIBUTED OPTICAL FIBER SENSOR (DOFS)

Dissertation

for the purpose of obtaining the degree of doctor
at Delft University of Technology
by the authority of the Rector Magnificus prof. dr. ir. T.H.J.J. van der Hagen
chair of the Board for Doctorates
to be defended publicly on Thursday 9 February at 10:00 o'clock

by

Xuehui ZHANG

Master of Engineering in Architectural and Civil Engineering,
Tongji University, Shanghai, China,
born in Jiangxi, China

This dissertation has been approved by the promotors

Composition of the doctoral committee:

Rector Magnificus,   chairperson
Prof. dr. K. G. Gavin,   Delft University of Technology, promotor
Dr. ir. W. Broere,   Delft University of Technology, copromotor

Independent members:
Prof. dr. ir. T. J. Heimovaara,   Delft University of Technology
Prof. dr. ir. M. A. N. Hendriks,   Delft University of Technology
Prof. dr. H. Yu,   Tongji University, China
Dr. ir. G.G. Drijkoningen,   Delft University of Technology
Dr. ir. R. Spruit,   Gemeentewerken Rotterdam, The Netherlands

An electronic version of this dissertation is available at
http://repository.tudelft.nl/.

To my beloved family and friends

CONTENTS

LIST OF FIGURES

SUMMARY

Deformation monitoring is essential for reliably assessing the structural safety of existing immersed tunnels. The vertical settlement measured by manual leveling with yearly intervals has been the dominant method employed in immersed tunnel monitoring until now. However, the daily and seasonal deformation behavior, both along vertical and longitudinal direction, are another important aspect in tunnel structure monitoring. There are signs that an immersed tunnel may exhibit cyclic daily deformation under tide variation and seasonal deformation under temperature fluctuation, which potentially impacts the tunnel structural integrity. Investigations of such deformation behavior of immersed tunnels will firstly require field monitoring. The conventional monitoring practice of settlements measured at yearly intervals with an accuracy of one millimeter or less is incapable of capturing the potential daily and seasonal behavior of an immersed tunnel. The distributed optical fiber sensor (DOFS) possesses advantages of long-distance sensing and flexibility in configuration, which have high potential to improve field monitoring capabilities.

This thesis presented an investigation into the daily and seasonal behavior of immersed tunnels based on field monitoring over a one-year period in the Heinenoordtunnel, a rectangular cross-section immersed tunnel in the Netherlands, using DOFS. The first step of this research project was to develop a DOFS monitoring system capable of measuring joint deformations along three directions (longitudinal joint opening, vertical uneven settlement and transverse drift) at frequencies in the order of once per hour. As a starting point, the optical fiber (as the sensing part) properties and its potential effects on system accuracy are investigated. The critical metrics for optimal fiber selection include the physical structure of optical fiber, the maximum working strain (MWS), the limit strain, the relaxation behavior, amongst others, and these properties can be calibrated by a combined tension test, or a manual tension test as demonstrated in this thesis. Finally, the characteristic loop proposed can describe the relaxation behavior of the sensing fiber and quantify an upper bound estimate of the measurement error.

After a proper selection of the optical fiber, a special sensor block was designed which consists of two (optical fiber) extensometers fixed by a three-point anchorage. This sensor block was experimentally validated as capable of measuring joint deformation along three directions, with acceptable submillimeter measurement accuracy. Finally, the developed DOFS monitoring system was successfully applied to instrument both dilation and immersion joints on the west sidewall of the Heinenoordtunnel, for a field monitoring period of one year. The installed system proves capable of measuring joint opening and uneven settlements (between the two joint sides) with an accuracy of 0.1mm and data-collection frequencies in the order of once per half-hour.

The second part of this research investigates the daily and seasonal behavior of the Heinenoordtunnel based on the field monitoring results. With regards to daily behavior, monitoring shows that the whole immersed tunnel (five elements with a total length

of 575m) behaves more or less like a rigid body and moves upwards (at low tide) and downwards (at high tide) periodically with a movement amplitude of about 0.3mm, when subjected to tidal variations with an amplitude of around 1.2m and a half-day period at the Heinenoordtunnel site. This cyclic movement can be modelled by a coupled flow and consolidation model of the underlying soil layers under tidal variations. The numerical simulation reveals that the tidal wave retards in the bottom sand layer below the clay layer. The soil domain response shows a lag of about 60 mins to the tidal variation, which falls in the time lag range of between 39 and 99 minutes as estimated by field conditions.

When looking at the seasonal behavior of the tunnel, monitoring results confirm a seasonal periodic joint opening at the tunnel joints, and this joint opening exhibits a negative correlation with temperature, indicating that the joint gap tends to close during the summer and open during the winter. If longitudinal thermal segment expansion is fully compensated by joint opening, a total seasonal expansion of about 41.5mm is measured along the (575m long) immersed tube section. The amplitudes of seasonal joint opening at immersion joints (within a range of 1.77 to 6.15mm) are larger than those of most dilation joints (within a range of 0.6mm to 2.0mm). However, at a few dilation joints, the amplitude (within a range of 2.2mm to 4.9mm) of the joint opening is comparable to that of immersion joints, indicating that for segmented immersed tunnel monitoring, dilation joints should be given the same extent of consideration as immersion joints. There exists a lag (mostly around 1 to 2 days) between joint opening deformation and temperature change, suggesting that joint opening variation is delayed compared to the temperature change. Over the one-year monitoring period, the uneven settlement has a smaller magnitude (mostly with an amplitude of below 1mm) than joint opening. The measured joint uneven settlement also shows seasonal variation, but its correlation to temperature is weak.

Finally, a beam-spring model is adopted to investigate the effects of seasonal joint opening on tunnel structural safety. Simulation results illustrate that the seasonal segment expansion enhances the integrity of the tunnel element longitudinally, and it tends to reduce the shear deformation at all dilation joints while increasing it at immersion joints. This agrees with the deformation tendency revealed by the measurement results. Moreover, seasonal segment expansion alters tunnel segment shear and rotation deformation, and the degree of change is more pronounced in the first and last elements. For tunnel maintenance, simulation and measurements both indicate that excess joint opening may have occurred at local joints within the first and last tunnel elements, and these joints deserve more attentions in regular maintenance checks.

In summary, the research findings validate the hypotheses of cyclic daily deformation under tidal variation and seasonal deformation under temperature fluctuation, which further support a more comprehensive safety assessment for immersed tunnels in the service stage. Also, the applicability of DOFS to upgrade the current monitoring practice in immersed tunnels is confirmed, which provides a good reference for future behavior monitoring in this area.

SAMENVATTING

Het monitoren van de vervorming is van essentieel belang voor het betrouwbaar beoordelen van de constructieve veiligheid van bestaande afgezonken tunnels. De zetting, gemeten door handmatige waterpassing met een interval van een jaar, is de meest toegepaste methode bij de monitoring van afgezonken tunnels. Het dagelijkse en seizoensgebonden vervormingsgedrag, zowel in verticale als in longitudinale richting, is echter een belangrijk aspect bij het bewaken van de tunnel. Er zijn aanwijzingen dat afgezonken tunnels cyclische dagelijkse vervorming onder invloed van getijdevariaties en seizoensgebonden vervorming onder invloed van temperatuurschommelingen kunnen vertonen, wat mogelijk van invloed is op de integriteit van de constructie. Voor onderzoek naar dergelijke vervormingen van afgezonken tunnels is eerst veldonderzoek vereist. De conventionele monitoringpraktijken (zetting gemeten met een jaarlijks interval met een nauwkeurigheid van één millimeter) waren niet in staat om het potentiële dagelijkse en seizoensgebonden gedrag van afgezonken tunnels vast te leggen. Een meting met gedistribueerde optische vezel sensor (DOFS) heeft de voordelen van lange-afstands detectie en flexibiliteit in de configuratie, die een groot potentieel in zich dragen om een dergelijke veldstudie uit te voeren.

In dit proefschrift is een onderzoek gedaan naar het dagelijkse en seizoensgebonden gedrag van afgezonken tunnels op basis van een monitoringcampagne van een jaar in de Heinenoordtunnel (een rechthoekige afgezonken tunnel in Nederland) met behulp van DOFS. De eerste stap van dit onderzoek is de ontwikkeling van een DOFS-monitoringsysteem dat in staat is de vervorming van voegen in drie richtingen te meten (voegopening in de lengterichting, verticale ongelijke zetting en dwarsdrift) met een frequentie in de orde van een uur. Als uitgangspunt worden de eigenschappen van de optische vezel (als het detectiedeel) en de mogelijke effecten daarvan op de nauwkeurigheid van het systeem onderzocht. De kritische maatstaven voor een optimale vezelkeuze omvatten de fysische structuur van de optische vezel, de maximale werkspanning (MWS), de grensspanning, het relaxatiegedrag, als belangrijkste parameters, en deze eigenschappen kunnen worden gekalibreerd door een gecombineerde trekproef, of een handmatige trekproef zoals aangetoond in dit proefschrift. Tenslotte kan de voorgestelde karakteristieke lus het relaxatiegedrag van de meetvezel beschrijven en de bovengrensschatting van de meetfout kwantificeren.

Na een selectie van de juiste optische vezel werd een speciaal sensorblok ontworpen dat bestaat uit twee (optische vezel) extensometers die door middel van driepuntsverankering worden opgesteld. Het aldus ontworpen sensorblok werd experimenteel gevalideerd als zijnde in staat om de vervorming van de voeg in drie richtingen te meten, met een aanvaardbare submillimeter meetnauwkeurigheid. Tenslotte werd het ontwikkelde DOFS-monitoringssysteem met succes toegepast op zowel dilatatie- als zinkvoegen in de westelijke zijwand van de Heinenoordtunnel, voor een monitoringcampagne van één jaar. Het geïnstalleerde systeem blijkt in staat te zijn de opening van de voegen en ongelijke

zettingen (van de twee voegzijden) te meten, met een nauwkeurigheid van 0,1 mm en frequenties in de orde van eens per half uur.

De tweede stap van dit onderzoek is het onderzoeken van het dagelijkse en seizoensgebonden gedrag van de Heinenoordtunnel op basis van veldmetingen. Voor het dagelijks gedrag toont de monitoring aan dat de hele afgezonken tunnel (vijf elementen met een totale lengte van 575m) zich min of meer gedraagt als een star lichaam en periodiek opwaarts (bij eb) en neerwaarts (bij vloed) beweegt met een amplitude van ongeveer 0.3mm, onderhevig aan getijdevariaties met een amplitude van ongeveer 1.2m met een periode van een halve dag op de locatie van de Heinenoordtunnel. Deze cyclische beweging kan worden gemodelleerd met een gekoppeld stromings- en consolidatiemodel van de onderliggende bodemlagen onder invloed van getijdevariaties. Deze numerieke simulatie toont aan dat de getijgolf vertraagd is in de onderste zandlaag onder de klei; de respons van de bodem vertoont een vertraging van ongeveer 60 minuten op de getijdegolf, wat valt binnen het tijdsverschil tussen 39 en 99 minuten zoals geschat op basis van de veldomstandigheden.

Wat het seizoensgebonden gedrag van de tunnel betreft, bevestigen de monitoringresultaten een seizoensgebonden periodieke voegopening bij de tunnelvoegen, en deze voegopening vertoont een negatieve correlatie met de temperatuur, wat erop wijst dat de voegopening de neiging heeft zich te sluiten tijdens de zomer en zich te openen tijdens de winter. Indien de longitudinale thermische segmentuitzetting volledig gecompenseerd wordt door de voegopening, wordt een totale seizoensgebonden uitzetting van ongeveer 41,5 mm gemeten langs het (575 m lange) gesloten buisgedeelte. De amplitudes van de seizoensgebonden voegopening bij zinkvoegen (met een bereik van 1,77 tot 6,15 mm) zijn groter dan die van de meeste dilatatievoegen (met een bereik van 0,6 tot 2,0 mm). Bij enkele dilatatievoegen is de amplitude (met een bereik van 2,2 tot 4,9 mm) van de voegopening echter vergelijkbaar met die van zinkvoegen, hetgeen erop wijst dat voor de bewaking van afgezonkengesegmenteerde tunnels evenveel aandacht moet worden besteed aan dilatatievoegen als aan zinkvoegen. Er bestaat een tijdsverschil (meestal ongeveer 1 à 2 dagen) tussen de vervorming van de voegopening en de variatie van de temperatuur, wat erop wijst dat de verandering van de voegopening wordt vertraagd ten opzichte van de temperatuursverandering. Over de monitoringsperiode van één jaar heeft de ongelijke zetting een kleinere omvang (meestal met een amplitude van minder dan 1 mm) dan de voegopening. De gemeten ongelijke zetting van de voegen vertoont ook seizoensgebonden variatie, maar de correlatie met de temperatuur is zwak.

Tenslotte wordt een balk-veren model gebruikt om de effecten van seizoensgebonden voegopening op de betrouwbaarheid van de tunnelconstructie te onderzoeken. De resultaten tonen aan dat de seizoensgebonden segmentuitzetting de integriteit van het tunnelelement in de lengterichting verbetert, en de neiging heeft om de afschuiving bij alle dilatatievoegen te verminderen, terwijl deze bij de dilatatievoegen toeneemt. Dit komt overeen met de vervormingstendens die uit de meetresultaten naar voren komt. Bovendien wijzigt de seizoensgebonden segmentuitzetting de afschuiving en rotatievervorming van de tunnelsegmenten, en de mate van verandering is meer uitgesproken in het eerste en laatste element. Wat het onderhoud van de tunnel betreft, blijkt uit zowel de simulatie als de metingen dat de zich overmatige opening van de voegen kan hebben voorgedaan bij enkele voegen in het eerste en laatste tunnelelement, en dat deze voegen

meer aandacht verdienen bij de regelmatige onderhoudscontroles.

Samenvattend valideren de onderzoeksresultaten de cyclische dagelijkse vervorming onder getijdevariatie en de seizoensgebonden vervorming onder temperatuurfluctuatie, die een meer uitgebreide veiligheidsbewaking voor afgezonken tunnels in de gebruiksfase verder ondersteunen. Ook wordt de toepasbaarheid van DOFS om de huidige monitoringspraktijk voor afgezonken tunnels te verbeteren bevestigd, wat een goede referentie vormt voor toekomstige monitoring op dit gebied.

1

INTRODUCTION

1

1.1. BACKGROUND

Immersed tunnelling is a method of constructing a tunnel across waterways that offers significant benefits compared to other tunneling techniques. This tunneling method relies on water to transport and place the tunnel, and since the tunnel can be set at a very shallow depth on the riverbed, an immersed tunnel has advantages over a general circular bored tunnel or mined tunnel, such as less cover, shorter ramps, easier fit for the required space profile, to name a few (Gursoy, 1995; Glerum, 1988; Lunniss & Baber, 2013). Immersed tunneling has a relatively long history since the first immersed tunnel, a 2.7 m diameter sewage tunnel built with brick and concrete, was finished in 1893 in the USA. Since then, the first large cross-section immersed tunnel for traffic use was the Detroit River Tunnel, a railway tunnel opened in 1910. Currently, there are more than 150 immersed tunnels in service worldwide (Lunniss & Baber, 2013).

Although the immersed tunnel construction method has evolved over its more-than-a-century history, its fundamental construction principles and inherent characteristics have stayed unchanged (Lunniss & Baber, 2013). The overall construction procedure for an immersed tunnel consists of:

1. Tunnel element fabrication. Usually the long tunnel is divided into several shorter elements (about 100-200m long) and fabricated in a dry dock, and each element can be either monolithic or segmented. For a segmented element, dilation joints are formed in the element fabrication;

2. Underwater trenching. A trench along the designated tunnel alignment is excavated below the riverbed, and the trench bottom is paved with a gravel or sand layer. This trenching process can be conducted simultaneously with element fabrication;

3. Element transport. The two ends of each element are sealed temporarily with bulkheads, and then the element is floated and towed to the immersion location;

4. Element immersion. The towed element is immersed and connected to the finished element or the cast-on-site approach structure, with the connection joint referred to as an immersion joint;

5. Foundation construction. The gap between tunnel bottom and trench bottom is filled with sand by a specific sand-flow method or grouting. In some recent tunnel projects a screed gravel bed is placed before tunnel immersion and serves as the foundation layer;

6. Trench backfilling. The two sides and top of the tunnel are further backfilled with gravel or soil.

The above steps only describe the most general outline of an immersed tunnel construction, minor changes do exist across tunnels in aspects of element fabrication (Hu et al., 2018; Lin et al., 2018; Luttikholt et al., 2022), foundation construction (Gursoy, 1995; Lunniss & Baber, 2013; Olsen et al., 2022), as well as others (Ingerslev, 2012).

1.1.1. Structural aspects of immersed tunnels

An immersed tunnel can be constructed from both monolithic and segmented elements (Vos, 1988; Lunniss & Baber, 2013). Most immersed tunnels are designed as segmented elements as shown in Fig.1.1a, where the element (generally between 100 and 200m long) is subdivided into several segments (each of about 20m in length), with a special dilation joint between segments. In the case of a monolithic immersed tunnel, the elements are usually constructed as one integral section; although construction joints exist, there is no such dilation joint between individual cast segments, see Fig.1.1b.

Based on construction material type, the element (or segment) can be generally divided into three types (Vos, 1988): (1) (double or single) circular steel shell (most used in USA); (2) rectangular reinforcement concrete box (most used in Europe and China); (3) steel-concrete sandwich box (most used in Japan).

(a) Segmented immersed tunnel

(b) Monolithic immersed tunnel
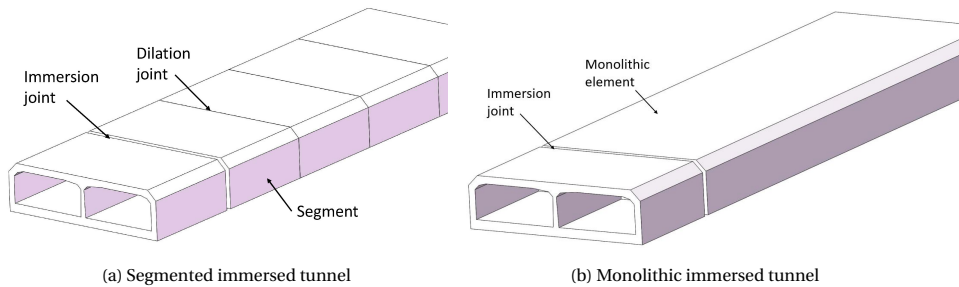
Figure 1.1: Schematic of an immersed tunnel

For the first half-century of immersed tunnelling, the monolithic element was the dominant type used, mostly made of brick and steel, steel shell with filling concrete. After the 1960s concrete segmented elements start to gain popularity, especially in Europe. For example, in the Netherlands almost all immersed tunnels constructed after 1960 use segmented elements with dilation joints. The First Heinenoordtunnel, which opened in 1969, is an example. Segmented immersed tunnels seem to have gained higher popularity in recent decades, as it is the dominant type used in most newly-built immersed tunnel projects (Lunniss & Baber, 2013; Luttikholt *et al.*, 2022). This thesis focuses on monitoring the deformation behaviour of a segmented immersed tunnel. Three key components within a segmented immersed tunnel structure will be discussed in succession: the tunnel segment, the dilation joint and the immersion joint.

Tunnel Segment

The long tunnel element is usually fabricated segment by segment, especially in the case of concrete tunnels where the quantity of one pouring is usually limited, and construction joints are mostly unavoidable. By dividing the long element into several short segments in concreting process, the possibility of thermal shrinking cracking in concrete curing can be reduced, which further helps to control concrete quality and assures a high watertightness in the long term (Vos, 1988).

1

DILATION JOINT

Dilation joints reduce the risk of thermal shrinkage cracking in element casting. For water-tightness assurance, a special metal-rubber strip was developed and embedded between adjoining segments, as shown in Fig.1.2a, for the first time in the 1st Heinenoordtunnel. The currently often used W9Ui type rubber gasket has been developed based on this initial profile (Glerum *et al.*, 1976).

(a) Dilation joint   (b) Immersion joint
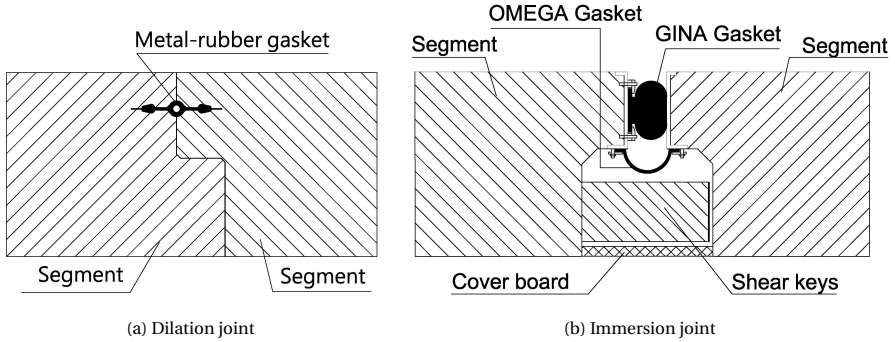
Figure 1.2: Schematic of tunnel joints

At the end of each segment a "concrete collar" is designed, which provides shear resistance between segments. Fig.1.2a shows a standard design of dilation joint with this concept. In addition, extra shear keys may be constructed in the dilation joint to increase its shear resistance, and further information can be found in Lunniss & Baber (2013).

IMMERSION JOINT

Immersion joints (or element joints) are the joints formed when a new element is connected to the earlier element or the approach structure underwater. There have been many ways to construct an immersion joint over time, such as by rubber gasket and grouting, on-site concreting from inside the tunnel, and use of GINA and Omega gaskets, as well as many other methods, see Lunniss & Baber (2013); Sinha (2017). Besides, there are also special immersed joints designed for seismic mitigation (Kiyomiya, 1995).

However, immersion joints with GINA and Omega gaskets have become the preferred scheme for immersed tunnels. As shown in Fig.1.2b, the end of the element is designed with an outer flange on which a GINA gasket is attached prior to immersion. This GINA gasket will be compressed and works as a primary seal during the element immersion process. On the inside of the element a larger gap (compared to the dilation joint) allows for the installation of an OMEGA gasket, which is intended as the permanent joint seal. Although GINA is designed as a temporary seal during construction only, it actually functions as the primary seal in most tunnels during its lifespan and the OMEGA effectively functions as a backup. In addition, horizontal and vertical shear keys are installed in the joint gap to provide shear resistance in the event of uneven settlements after immersion; moreover, exterior cover boards are affixed for (fire) protection, as seen in Fig.1.2b.

In most tunnels, the final immersion joint, also known as the closing joint, is designed differently and concreted from inside the tunnel(as in Heinenoordtunnel), which results in a distinct profile that acts more like a rigid joint.

1.1.2. DEFORMATION OF IMMERSED TUNNEL SEGMENTS

Different deformation modes exist on a segment, namely longitudinal segment expansion or shrinkage, vertical segment settlement and transverse shear displacement.

Longitudinal segment expansion or shrinkage is due mainly to (daily or seasonal) temperature change. Such thermal expansion and shrinkage will have adverse effects on the structure, such as a widening of existing concrete cracks, which may lead to leakages (ATKINS *et al.*, 2019). As such segment expansion or contraction will mainly be compensated by the cyclic opening and closure at the joint (see Fig.1.3a), monitoring joint opening can help infer the segment expansion behavior. Note theoretically segment expansion causes a volume change and deformation along three directions, but since the longitudinal dimension of immersed tunnel is well larger than transverse and vertical directions, the longitudinal expansion exhibits the most significant effects on tunnel structure and will be studied in this thesis.

(a) Longitudinal segment expansion

(b) Differential settlement of adjacent segments

(c) Differential settlement within a segment

(d) Transverse movement of adjacent segments
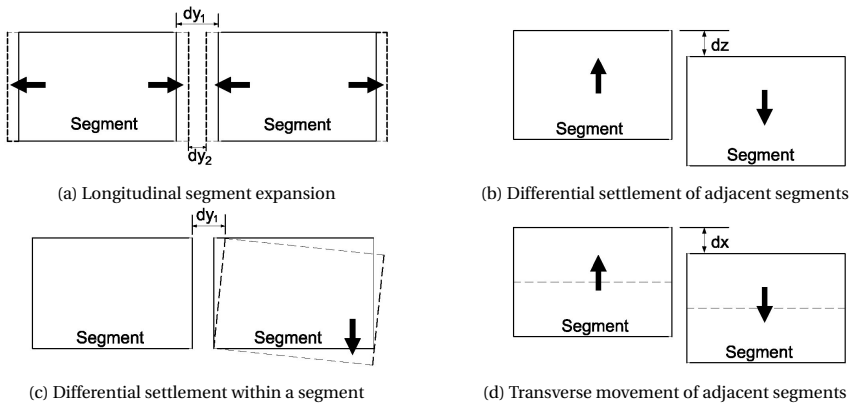
Figure 1.3: Tunnel segment deformation modes

Both global and local uneven settlement are the most commonly observed deformation mode in immersed tunnels, and it has been recorded to varying extent. If two adjacent segments settle differentially (see Fig.1.3b), vertical concentrated shear deformation occurs at the joint. This uneven settlement (of the two sides) can cause a failure of the shear connection, like local concrete cracking at the dilation joint, which is typically localized at the roof and floor concrete collars (Leeuw, 2008) and shear key cracking at immersion joint. Therefore, monitoring uneven settlement at the joints can serve as an early indicator of ongoing structural issues.

Apart from uneven settlement concentrated on the joint, differential settlement between two ends of a segment will also cause segment tilting (see Fig.1.3c), leading to an unequal joint opening at the upper and lower cross-sections. For instance, in the Kiltunnel this joint opening caused by segment tilting is supposed to result in a leakage (Leeuw, 2008); in the Shanghai Outer-ring Expressway Tunnel, large segment tilting caused an excessive joint closure at the roof of one immersion joint, which further resulted in damage of the GINA and OMEGA gaskets (Bai & Lu, 2016).

Transverse drift displacement of segments over the foundation plane (see Fig.1.3d)

is rarely observed, as the loading conditions at two sides of the tunnel cross-section are generally highly symmetrical and therefore, significant transverse drift is less likely to occur. However, this drift deformation is possible in extreme scenarios like under seismic loading.

It is worth noting that, in contrast to vertical settlements, longitudinal and transverse segment deformation modes are difficult to measure, since monitoring the full-length of an immersed tunnel that extends several hundred or thousand meters longitudinally is impractical or not economical. However, since segment deformation will directly result in joint deformation in most cases, monitoring and analyzing joint deformation provides a straightforward way to investigate the behavior of an immersed tunnel.

1.1.3. JOINT DEFORMATION OF EXISTING IMMERSED TUNNELS

Based on the aforementioned deformation modes of tunnel segments, there exist three main corresponding joint deformation modes (see Fig.1.4), which are summarized as follows:

- Joint opening, or negative opening indicating joint closure, as shown in Fig.1.4c. The joint opening is related to the horizontal segment thermal expansion or segment tilting due to the differential settlement between two ends;

- Joint uneven settlement, as seen in Fig.1.4d, mainly the result from unequal settlement of two adjacent segments. Uneven settlement can forecast the functional status of shear keys, as a too large uneven settlement may indicate the failure of shear connection or crack at the joint;

- Joint transverse (shear) displacement, as illustrated in Fig.1.4b. It represents the concentrated shear deformation at a joint caused by transverse segment movement on the foundation plane. Note that this is rarely reported in existing immersed tunnels under normal loading conditions.

The joint deformation, if it exceeds a certain threshold, will deteriorate tunnel structural integrity and watertightness of the tunnel. When considering maintenance of existing immersed tunnels, excessive joint deformation may result in various deterioration problems, including: joint leakage, as seen in Fig.1.5a and Fig.1.5d; concrete cracking, for instance due to concentrated compression force or shear forces at joint, shown in Fig.1.5b and Fig.1.5d; adverse twisting of OMEGA gasket due to uneven settlement, as in Fig.1.5c.

Based on observations at some existing immersed tunnels, the deterioration problems at joints are partially summarized in Tab.1.1. It should be noted that problems such as leakages and cracking are more common in reality than reported here, as the information in Tab.1.1 only covers publicly available literature. Therefore, the deformation behavior of immersed tunnels could be monitored and investigated more carefully to provide early indications of structural degradation issues and optimize structural safety.

1.1.4. LIMITATIONS TO IMMERSED TUNNEL MONITORING

At present, the monitoring of structural behaviour of most immersed tunnels is still limited to vertical settlement monitoring and regular visual inspections locally (especially at the

(a) Segment and joint

(b) Joint transverse deformation

(c) Joint opening

(d) Joint uneven settlement
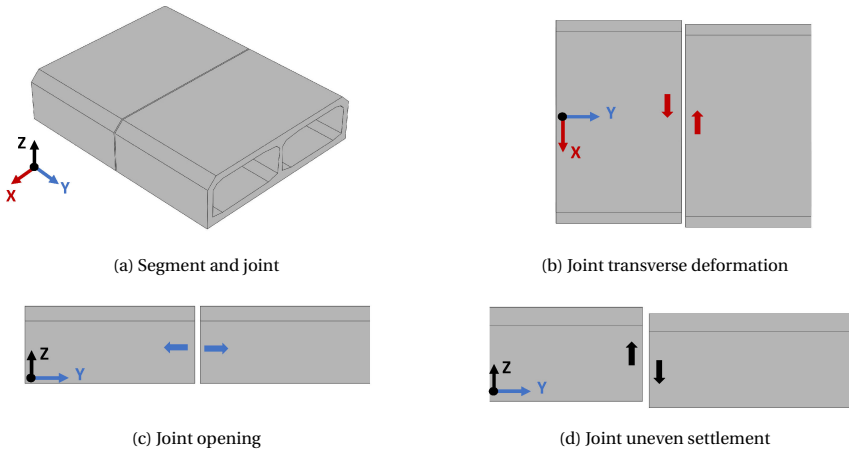
Figure 1.4: Tunnel joint deformation modes

joint). In vertical settlement measuring, several measure points along the longitudinal axis are selected, often at the two ends and the center of an element, and manual levelling is conducted, using a total-station plus an invar rule, to measure the vertical height change relative to the nearby reference point outside the tunnel of individual measurement points, as demonstrated in Fig.1.6. In normal monitoring practice, this manual levelling is mostly conducted at yearly or even longer intervals and usually requires a tunnel closure.

Only recently has the necessity to monitor more deformation parameters been recognized, and tunnel managers have started to pay more attention to monitoring immersion joints, see Xu *et al.* (2019). Nevertheless, monitoring of dilation joints remains quite rare and is not highly-researched in the study of segmented immersed tunnel behavior.

Despite the necessity to monitor joint deformations, the conventional monitoring practices have defects as listed below:

- The conventional monitoring practice, in most cases, only measures tunnel vertical settlement, and in rare cases, immersion joint openings. The transverse deformation is normally not considered in the literature. For a comprehensive behavior monitoring of segmented immersed tunnels, it is vital to extend the joint monitoring into a full three-directional one.

- Longitudinal joint deformation measuring, if conducted, is still limited to immersion joints in the majority of instances, and detailed information on dilation joints is lacking. This is partially due to the fact that the number of dilation joints is typically much larger than the number of immersion joints, and there is a lack of suitable sensing techniques that are economical and accurate enough. Notably, excessive deformation of dilation joints occurs just as commonly as at immersion joints, and there are validated structural deterioration problems at dilation joints (see Tab.1.1). A qualified monitoring study should reasonably incorporate both immersion and dilation joints.

1

(a) Joint leakage(Leeuw, 2008)

(b) Concrete cracking at dilation joint(Leeuw, 2008)

(c) Twisted OMEGA profile(NEBEST, 2018)
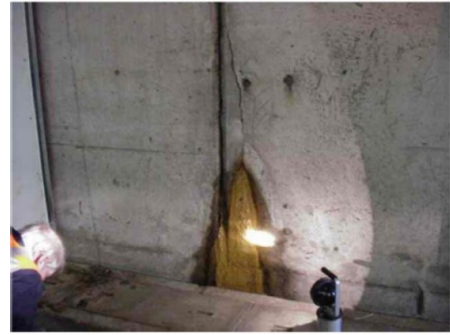
(d) Concrete cracking and leakage (Gavin *et al.*, 2019)

Figure 1.5: Typical joint deterioration problems

- The present monitoring practice on a yearly basis (or in better cases, half-year) fails to capture the daily or seasonal deformation behavior of immersed tunnels. There are signs that seasonal joint deformation potentially negatively impact structural safety (Rahadian *et al.*, 2018; van Amsterdam, 2019). Additionally, daily tidal fluctuation above the tunnel (with a period of about 12 hours) may impact the immersed tunnels (Grantz, 2001), but there is rare field monitoring to confirm this behavior. Investigation into such daily and seasonal deformation behavior will firstly necessitate a high-frequency monitoring (with daily or even sub-hour intervals), which is hardly possible with the current monitoring practices considering their limitations.

1.1.5. DISTRIBUTED OPTICAL FIBER SENSOR (DOFS)

Distributed optical fiber sensor (DOFS) is a relatively new sensor type which offers the unique advantage of distributed sensing along a single long optical fiber. The working

Table 1.1: Joint deterioration problems of some existing immersed tunnel

Tunnel Name	Open Year	Main Joint Problem	Source
1st Coen Tunnel, Netherlands	1966	(1)Leakage at dilation and immersion joint (2)Concrete cracking at dilation and immersion joint	Leeuw (2008)
Heinenoordtunnel, Netherlands	1969	(1)Leakage at dilation joint (2)Concrete cracking at dilation joint (3)Twisting of OMEGA gasket at immersion joint	Leeuw (2008)
Rotterdam Metro tunnel, Netherlands	1969	(1)Damage of GINA gasket at immersion joint (2)Concrete cracking at immersion joint	Molendijk *et al.* (2020)
Vlake tunnel, Netherlands	1975	(1)Leakage at dilation joint	Leeuw (2008)
Drechttunnel, Netherlands	1977	(1)Leakage at dilation joint (2)Concrete cracking at dilation joint	Leeuw (2008)
Kiltunnel, Netherlands	1977	(1)Leakage at dilation and immersion joint (2)Concrete cracking at dilation joint	Leeuw (2008) Gavin *et al.* (2019)
Noord Tunnel, Netherlands	1992	(1)Leakage at dilation joint	Leeuw (2008)
2nd Benelux Tunnel, Netherlands	2002	(1)Leakage at immersion joint (2)Twisting of OMEGA gasket at immersion joint	Leeuw (2008)
Shanghai Outer-ring Expressway Tunnel, China	2003	(1)Damage of GINA and OMEGA gasket at immersion joint (2)Concrete cracking	Bai & Lu (2016)

principles of DOFS are generally based on the optical phenomena of light scattering, optical loss, and polarization (López-Higuera *et al.*, 2011; Udd & Spillman Jr, 2011). Among them DOFS based on Brillouin scattering is the most widely used commercial technique for strain and temperature sensing in structure health monitoring.

When light propagates along the optical fiber, Brillouin scattering occurs where a part of the propagating light will be backscattered. The frequency of Brillouin backscattered light will shift (compared with that of the forward propagating light), and this Brillouin frequency shift (BFS) is proportional to the fiber strain and temperature (López-Higuera *et al.*, 2011; Motil *et al.*, 2016; Ohno *et al.*, 2001). Accordingly, if the BFS corresponding to each light backscattering point along the fiber axis can be measured, the spatial-resolved strain or temperature information distributed along the fiber axis longitudinally can be obtained, as shown in Fig.1.7.

A complete DOFS system generally consists of a long optical fiber (known as the

Figure 1.6: Tunnel settlement measured by manual leveling
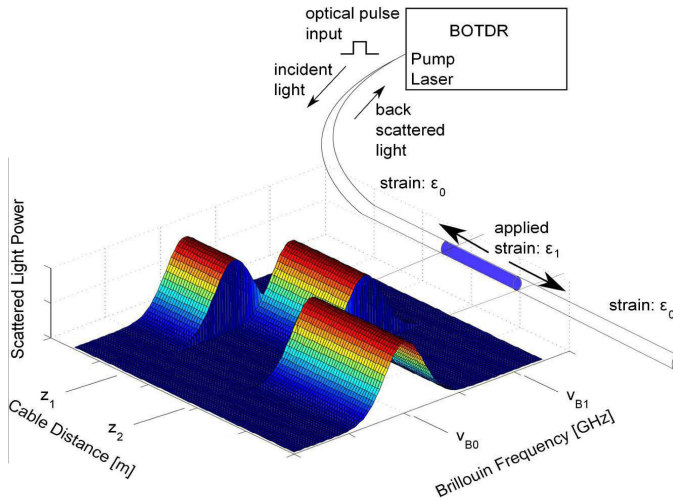
Figure 1.7: Schematic of working principle on DOFS (Pelecanos *et al.*, 2018)

sensing fiber) plus an interrogator, where the optical fiber is extended to the targeted structure with one or both fiber ends plugged into the interrogator for measurement (see Fig.1.8). DOFS has highlighted advantages over traditional electric sensors: immunity to electromagnetic interference, distributed sensing and long-distance sensing (of above a hundred kilometres).

In this thesis, DOFS is selected to set up a qualified system for monitoring the behaviour of a segmented immersed tunnel, based on the following reasons:

- As the sensing length of a DOFS system can be more than a hundred kilometres, a
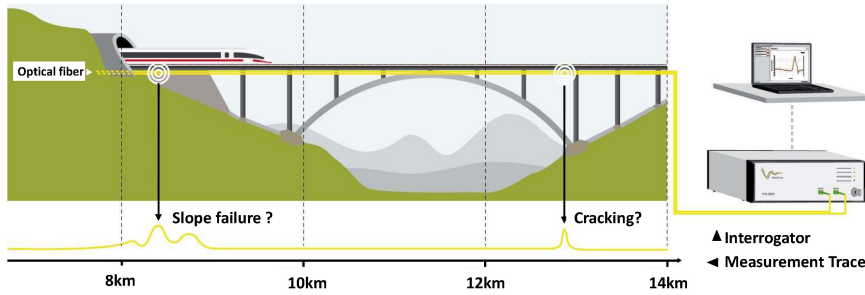
Figure 1.8: A typical DOFS monitoring system for infrastructure (based on fibrisTerre (2021))

remote-controlled sensing system can be set up with minimal interference on the normal operation of the monitored structure;

- The optical fiber can be flexibly installed to sense deformation in multiple directions, for instance, the three-direction deformations of both immersion and dilation joints within an immersed tunnel;

- High-frequency monitoring is possible. Once installed, the DOFS monitoring system can perform measurements at sub-hour intervals. Therefore, it is possible to monitor the immersed tunnel behavior under daily tidal impacts and seasonal temperature fluctuation;

- It is relatively cost-effective. DOFS is favourable in terms of cost per sensing point when compared to conventional electric connected point sensors. Consequently, instrumenting both dilation and immersion joints over a long tunnel can be performed more economically than otherwise.

1.2. MOTIVATION AND RESEARCH OBJECTIVES

This thesis is motivated by the following questions:

- How does a typical segmented immersed tunnel behave under external impacts (temperature and tide) over daily and seasonal periods?

- Can this behavior be properly monitored with distributed optical fiber sensor (DOFS)?

- How to model the observed behavior with a focus on geotechnical aspects?

- What is the impact of observed behavior on structural safety? or, what are the implications of the observed behavior for tunnel safety maintenance?

This thesis reports a monitoring study of daily and seasonal behavior of segmented immersed tunnels.

The first point considered is: can DOFS be used to design a reliable monitoring system for use in an immersed tunnel, taking into account the tunnel operation constraints and the required accuracy?

1

Therefore, this research starts with designing a novel DOFS-based monitoring system for field monitoring (in the Heinenoordtunnel), which is capable of measuring three-directional joint deformations at high frequency (with sub-hour intervals). Subsequently, the daily behavior of an immersed tunnel under tidal impacts are investigated specifically, followed by an numerical simulation on the tunnel-soil domain. Furthermore, the seasonal segment deformation behavior, i.e. under temperature fluctuations, will be examined in detail, and the effects of seasonal segment expansion on tunnel structure are modeled and discussed, to further provide suggestions on tunnel maintenance.

1.3. THESIS OUTLINES
The thesis contains 7 main chapters, and the outline for the remaining part is:

- Chapter 2: Reviews the literature on immersed tunnel deformation, distributed optical fiber sensors (DOFS) and their application in civil engineering monitoring. A summary of research gaps related to the above three aspects is also presented based on the literature study.

- Chapter 3: Focuses on the properties of optical fibers and their influence on the performance of a DOFS monitoring system in field conditions. The metrics of proper sensing fiber selection are firstly detailed, followed by proposed calibration experiments. Based on an experimental study, the fiber calibration procedure is described, with a focus on fiber relaxation behavior; a relaxation model is proposed to quantify the potential measurement error of the DOFS system.

- Chapter 4: Designs a DOFS monitoring system for field application. The sensor layout design which can measure three-directional joint deformation (longitudinal joint opening, vertical uneven settlement and transverse drift), is demonstrated and verified by a laboratory experiment. Finally, the designed DOFS system was successfully applied to instrument both the dilation and immersion joints in the Heinenoordtunnel, an immersed tunnel in the Netherlands, and it was demonstrated to work effectively for high-frequency data-taking.

- Chapter 5: Studies the daily behavior of immersed tunnels based on the monitoring results. The tidal impact on the tunnel is specifically analyzed, followed by a numerical study.

- Chapter 6: Assesses the seasonal behavior of immersed tunnels over one year period, as well as evaluates the effects of seasonal deformation on the structural behavior of an immersed tunnel.

- Chapter 7: Concludes with a summary of the thesis results and recommendations for further research on the subject.

REFERENCES
ATKINS, COWI, TEC, ChristiansenEssenbak, DeltaMarineConsultants, nmGeo & RAMBOLL (2019). Limfjord tunnel assessment and retrofitting-technical summary report, v 1.0. *Technical report*.

Bai, Y. & Lu, H. (2016). Damage analysis and repair technology of omega gasket in immersed tube tunnel. *Journal of Railway Engineering Society* **33**, No. 9, 87–92.

fibrisTerre (2021). Product brochure ftb5025-fiber-optic sensing system for distributed strain and temperature monitoring. https://www.fibristerre.de/products/, accessed: July-2022.

Gavin, K., Broere, W., Kovačević, M. & de Haas, K. (2019). Investigation of the remaining life of an immersed tube tunnel in the netherlands. In *Tunnels and Underground Cities: Engineering and Innovation meet Archaeology, Architecture and Art*, CRC Press, pp. 4831–4838.

Glerum, A. (1988). Immersed tunnels: Why, when and where. *Tunnelling and underground space technology* **3**, No. 4, 347–351.

Glerum, A., Righter, B. P., Eysink, W. D. & Heins, W. F. (1976). Rijkswaterstaat communications-motorway tunnels built by the immersed tube method. *Technical report*, RIJKSWATERSTAAT.

Grantz, W. C. (2001). Immersed tunnel settlements. part 1: nature of settlements. *Tunnelling and Underground Space Technology* **16**, No. 3, 195–201.

Gursoy, A. (1995). Immersed steel tube tunnels: An american experience. *Tunnelling and Underground Space Technology* **10**, No. 4, 439–453.

Hu, Z., Xie, Y., Xu, G., Bin, S., Liu, H. & Lai, J. (2018). Advantages and potential challenges of applying semi-rigid elements in an immersed tunnel: A case study of the hong kong-zhuhai-macao bridge. *Tunnelling and Underground Space Technology* **79**, 143–149.

Ingerslev, L. C. (2012). Innovations in resilient infrastructure design: immersed and floating tunnels. *Proceedings of the Institution of Civil Engineers-Civil Engineering* **165**, No. 6, 52–58.

Kiyomiya, O. (1995). Earthquake-resistant design features of immersed tunnels in japan. *Tunnelling and Underground Space Technology* **10**, No. 4, 463–475.

Leeuw, L. (2008). Lekkage in tunnels-dilatatievoegen en beton. *Technical report*, RWS Bouwdienst.

Lin, M., Lin, W., Wang, Q. & Wang, X. (2018). The deployable element, a new closure joint construction method for immersed tunnel. *Tunnelling and Underground Space Technology* **80**, 290–300.

López-Higuera, J. M., Cobo, L. R., Incera, A. Q. & Cobo, A. (2011). Fiber optic sensors in structural health monitoring. *Journal of lightwave technology* **29**, No. 4, 587–608.

Lunniss, R. & Baber, J. (2013). *Immersed tunnels*. New York, USA: CRC Press.

Luttikholt, A., Doorduyn, A., de Wit, H. & Li, Y. (2022). Consideration of concrete and steel sandwich tunnel elements. *Tunnelling and Underground Space Technology* **121**, 104309.

1

Molendijk, A., Dalmeijer, R., Taffijn, E., Hol, M. & van Nes, P. (2020). Technical report article: Zinkvoegen hersteld. https://www.cementonline.nl/zinkvoegen-klaar-voor-de-toekomst-ii, accessed: July-2022.

Motil, A., Bergman, A. & Tur, M. (2016). State of the art of brillouin fiber-optic distributed sensing. *Optics & Laser Technology* **78**, 81–103.

NEBEST (2018). Rapportage aanvullend onderzoek zinkvoegen heinenoordtunnel. *Technical report.*

Ohno, H., Naruse, H., Kihara, M. & Shimada, A. (2001). Industrial applications of the botdr optical fiber strain sensor. *Optical fiber technology* **7**, No. 1, 45–64.

Olsen, T., Kasper, T. & de Wit, J. (2022). Immersed tunnels in soft soil conditions experience from the last 20 years. *Tunnelling and Underground Space Technology* **121**, 104315.

Pelecanos, L., Soga, K., Elshafie, M., de Battista, N., Kechavarzi, C., Ye Gue, C., Ouyang, Y. & Seo, H.-J. (2018). Distributed fiber optic sensing of axially loaded bored piles. American Society of Civil Engineers.

Rahadian, R., van der Woude, S., Wilschut, D., Blom, C. & Broere, W. (2018). A new test setup for studying sand behaviour inside an immersed tunnel joint gap. In *Physical Modelling in Geotechnics*, CRC Press, pp. 443–448.

Sinha, T. (2017). *Alternative of an immersion joint*. Master's thesis, Delft University of Technology, the Netherlands.

Udd, E. & Spillman Jr, W. B. (2011). *Fiber optic sensors: an introduction for engineers and scientists*. John Wiley & Sons.

van Amsterdam, B. (2019). *Probabilistic analysis of immersed tunnel settlement using cpt and masw*. Master's thesis, Delft University of Technology, the Netherlands.

Vos, C. J. (1988). Developments and quality safeguards in immersed tunnel technique. *Tunnelling and underground space technology* **3**, No. 4, 363–367.

Xu, X., Tong, L., Liu, S. & Li, H. (2019). Evaluation model for immersed tunnel health state: A case study of honggu tunnel, jiangxi province, china. *Tunnelling and Underground Space Technology* **90**, 239–248.

2

LITERATURE REVIEW

This chapter reviews the prior research on topics relevant to this thesis: immersed tunnel (deformation) behaviour and monitoring; distributed optical fiber sensor(DOFS) and its application in civil engineering. At the end of each topic review, a summary of the research gap in previous studies is briefed.

2.1. IMMERSED TUNNEL BEHAVIOR AND MONITORING

A typical segmented immersed tunnel with dilation and immersion joints behaves longitudinally like a jointed beam on an elastic foundation. Theoretically, flexural stress can occur in the segment body, but few problems have been reported in individual segments which can be attributed to large longitudinal and transverse flexural deformation. For a concrete immersed tunnel, the large cross sections of walls and roofs with generally greater than 1m thickness assure a high stiffness within the segment body, and any flexural stresses and deformations are typically very small as not to be observed. On the other hand, deformations at dilation and immersion joints are much more significant and can be observed more easily (van Montfort, 2018; Leeuw, 2008).

In a segmented immersed tunnel, the individual segments divided by joints has higher flexibility to displace (than in a continuous non-segmented tunnel), and theoretically deformations along three directions can occur, as described in Chapter 1. In literature, there exist a few studies on immersed tunnel behavior, although in most cases the structural analysis is based on estimation and assumptions rather than on field observation data.

2.1.1. SEGMENT DEFORMATION BEHAVIOR

LONGITUDINAL SEGMENT EXPANSION OR SHRINKAGE

When considering movement and deformation in longitudinal tunnel direction, segment expansion or shrinkage is the primary observed deformation mechanism. Segment expansion, after the initial concrete curing, is mostly due to temperature change and will mostly result in opening and closure of the joint. However, for tunnels with monolithic elements, i.e. no dilation joints, such thermal expansion and shrinkage has a higher tendency to cause cracking. For instance, in Limfjord tunnel (ATKINS *et al.*, 2019), an immersed tunnel in Demark, concrete shrinkage widens the cracking gap and causes a more severe leakage.

In the Shanghai Outer-ring Expressway Tunnel, an unexpectedly large joint closure was observed at one immersion joint, which caused compression damage to the GINA gasket (Bai & Lu, 2016). It was inferred that the seasonal segment expansion may exacerbate the joint closure, but there is no monitoring to confirm this supposition.

The possibility of seasonal expansion has also been evaluated theoretically by van Amsterdam (2019), and its potential effects on the long-term tunnel safety are assessed based on an assumed immersion joint deformation. Such longitudinal tunnel expansion was also estimated and its consequences on joint watertightness were discussed by van Montfort (2018). The impact on dilation joints is not considered in these studies.

VERTICAL SEGMENT SETTLEMENT

Vertical settlement is the most commonly observed behavior of immersed tunnel. It should be noted that uniform settlement of the whole tunnel longitudinally usually causes no harm to structural safety, but uneven settlements will have detrimental effects on the structural integrity.

Many immersed tunnels have suffered excessive uneven settlement longitudinally, at least much larger than the values anticipated in the initial project design. For example, Grantz (2001a,b)summarized potential causes of excessive settlements, including geological conditions, foundation treatment methods, amongst others. Excessive differential

settlements will result in subsequent problems such as joint leakage, concrete cracking and damage to rubber gaskets. These problems have been partially observed in the Kiltunnel and the Heinenoordtunnel in the Netherlands (van Montfort, 2018; Leeuw, 2008), Shanghai Outer-ring Expressway Tunnel(Bai & Lu, 2016) and the Yongjiang tunnel, China (Li *et al.*, 2011).

If the two adjacent segments settle differentially, vertical concentrated shear deformation occurs at the joint, and this uneven settlement (of two sides) generally causes failure of shear connection, such as the local concrete cracking at dilation joints (especially at the roof and floor concrete collar) and immersion joints (at shear keys or the concrete frame at roof and floor). For example, according to van Montfort (2018), the uneven settlement at the immersion joint and the resultant cracking may be the most likely cause of a severe leakage in the Kiltunnel, the Netherlands.

Besides concentrated joint uneven settlement, differential settlement at the two ends of a segment will cause segment tilting, leading to the unequal joint opening at the upper and lower areas of the tunnel cross-section. For instance, unexpected differential settlement has been observed at many immersed tunnels, such as in the Kiltunnel (van Montfort, 2018), Heinenoordtunnel (Commission-T330, 2014), and others. In the Shanghai Outer-ring Expressway Tunnel, a substantial segment tilting causes an excessive joint closure at the roof of one immersion joint, resulting in damage to the GINA and OMEGA gasket (Bai & Lu, 2016).

Transverse segment movement on foundation plane

The transverse drift of segment on the foundation plane is rarely observed and its effects remain unclear. Generally, since the loading conditions at two sides of the tunnel cross-section are highly symmetrical, such transverse shear displacement is less likely to happen. However, in extreme scenarios such as seismic loading, this transverse drift is possible.

There is monitoring data available showing unexpected joint gap offsets were on the sidewalls at the upstream and downstream sides (Li *et al.*, 2011), which potentially indicates segment transverse drift is also possible, see Fig. 2.1. However, it should be noted that this segment body drift is not caused by a concentrated shear displacement at the joint, but by a rotation along the foundation plane.
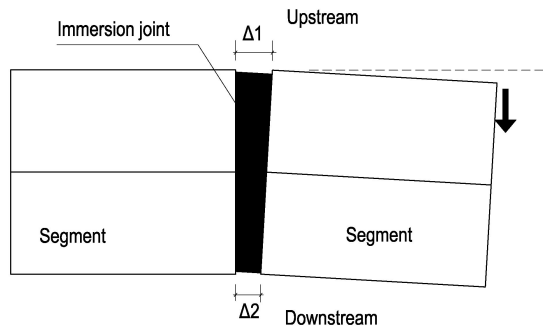
Figure 2.1: Transverse drift of segment body (top view)

The joint deformation, if it exceeds a certain limit, will deteriorate the structure safety

and watertightness. In many existing immersed tunnels, issues such as joint leakage, local concrete cracking (due to concentrated compression force or shear forces)and significant uneven settlements have been observed. A partial overview of such cases is presented in Tab.2.1.

2.1.2. Behavior of immersed tunnel under tide impacts

For some immersed tunnels constructed under a river or harbor, daily tidal variation may result in loads impacting the tunnel structure. For example, Wei *et al.* (2018) measured the concrete surface strain variation at several locations of a small immersed tunnel (for pedestrian use only), and it shows the concrete strain fluctuates slightly (with an amplitude of about seven micro-strain) under a 2.5m tide difference. The vertical deformation behavior of the immersed tunnel under tide was not measured.

The tide was observed to impose effects on the longitudinal behavior of underwater tunnels. For instance, Schotte *et al.* (2016) found the Liefkenshoek rail tunnel (a bored tunnel under River Scheldt in Belgium) exhibits a cyclic settlement under tide impacts, with an amplitude of around 10mm. Grantz (2001a,b) also mentioned the tidal effect on immersed tunnel's vertical response, but there is no specific monitoring study to confirm such behavior.

2.1.3. Monitoring technique in immersed tunnel

With more attention focused on immersed tunnel behavior monitoring, researchers started to work to obtain more deformation information, by utilizing multiple types of sensors and expanding the amount of measuring points. All this facilitates a more reasonable tunnel status evaluation.

The monitoring practices of some available literature are detailed in below Tab.2.2.

Table 2.1: Observed problems at immersed tunnel joints

Tunnel Name	Construction Year	Dilation Joint		Immersion joint		Source
		Deformation type	Problems	Deformation type	Problems	
Heinenoordtunnel, Netherlands	1969	Joint opening	Leakage, cracking	Joint opening and uneven settlement	Twisting of OMEGA gasket	Leeuw (2008)
Kiltunnel, Netherlands	1977	Joint opening and uneven settlement	Leakage, cracking	Joint opening and uneven settlement	Leakage	Leeuw (2008) Gavin et al. (2019)
Shanghai Outer-ring Expressway Tunnel China	2003	Unavaliable	Unavaliable	Joint opening	Damage of GINA and OMEGA gasket	Bai & Lu (2016)
Rotterdam Metro tunnel Netherlands	1969	Unavaliable	Unavaliable	Joint opening and uneven settlement	Cracking, Damage of GINA gasket	Molendijk et al. (2020)
Drechttunnel Netherlands	1977	Joint opening	Leakage, cracking	Unavaliable	Unavailable	Leeuw (2008)
Yongjiang Tunnel, China	1995	Unavaliable	Unavaliable	Joint opening	Cracking, decompression of GINA gasket	Li et al. (2011)
Vlake tunnel	1975	Joint opening	Leakage	Unavaliable	Unavailable	Leeuw (2008)
1st Coen Tunnel	1966	Joint opening, Uneven settlement	Leakage, cracking	Unavaliable	Leakage and Concrete cracking	Leeuw (2008)
Noord Tunnel	1992	Unavaliable	Leakage	Unavaliable	Unavailable	Leeuw (2008)
Second Benelux Tunnel	2002	Unavaliable	Unavaliabl	Joint opening and uneven settlement	Leakage, Twisting of OMEGA gasket	Leeuw (2008)

Table 2.2: Monitoring techniques employed in immersed tunnels

Tunnel	Measurands	Monitoring technique	Source
Shanghai Outer-ring Expressway Tunnel, China	Immersion joint opening; Settlement at immersion joint;	Manual measuring plus displacement transducer; Total station (settlement);	Bai & Lu (2016)
Honggu tunnel, China	Immersion joint: opening, uneven settlement; Shear key stress; Uneven settlement;	Total station (settlement); Strain gauge; Displacement transducer (joint opening);	Xu et al. (2019)
Heinenoordtunnel	Uneven settlement longitudinally; General condition check (leakage, cracking);	Total station (settlement); Visual check;	Leeuw (2008)
Kiltunnel	Uneven settlement longitudinally; General condition check (leakage, cracking);	Total station (settlement); Visual check;	Leeuw (2008); Gavin et al. (2019)
Ningbo Shenjiamen Tunnel, China	Tunnel strain (construction period)	FBG sensor(concrete strain)	Wei et al. (2018)
Yongjiang Tunnel, China	Uneven settlement longitudinally; Immersion joint opening; Concrete strain(locally); Rebar corrosion status;	Hydrostatic level (uneven settlement at joint); Displacement transducer (joint opening); Strain gauge; Corrosion sensor(locally);	Liu et al. (2008)

2

2.1.4. Summary of immersed tunnel behavior monitoring

Based on the above literature review on immersed tunnel behavior studies, it can be found that: (1) vertical settlements at discrete points longitudinally along the tunnel are most commonly measured for immersed tunnel monitoring; (2) more emphasis is now being put on immersion joint, as the joint opening is measured more frequently than it was before; (3) several researchers have realized the existence of seasonal deformation either by observed joint problems (a variable leakage rate with season), or by limited field monitoring. In some studies, potential effects of joint opening on the structure integrity and watertightness were evaluated, and such theoretic calculation are mostly based on a rough estimation of joint deformation; (4) more types of sensors or techniques are used in tunnel behavior monitoring (see Tab.2.2), although some are applied as remedial measures after unexpectedly excessive deformation was observed (Bai & Lu, 2016).

However, the previous studies still have research gaps that need to be bridged:

- Firstly, there is limited field monitoring data, such as seasonal or daily joint opening and uneven settlement, to strongly support a more comprehensive tunnel behavior analysis, and only a rough estimate is available in literature;

- Secondly, the dilation joints of segmented tunnel are overlooked. Dilation joints are observed to have shown problems such as leakage and cracking as commonly as immersion joints (see Tab.2.2), and for a comprehensive behavior study, both immersion joint and dilation joints should be monitored;

- Thirdly, most current monitoring practices fail to conduct high-frequency measurements and are therefore unable to capture daily behavior such as tide-induced settlement.

The abovementioned research gaps in previous studies also contribute to the motivations in this thesis.

2.2. Application of DOFS in Geotechnical and Structure Monitoring

2.2.1. Distributed optic fiber sensor (DOFS)

Distributed optical fiber sensor (DOFS) is a type of sensor that features distributed sensing and has become more and more widely used in structure health monitoring. For DOFS working on Brillouin scattering, the frequency of Brillouin backscattered light will shift (compared with the original forward light), and this Brillouin frequency shift(BFS) shows a linear dependency to the fiber strain and temperature (López-Higuera *et al.*, 2011; Horiguchi *et al.*, 1995), as demonstrated in Eq.2.1

$$f(T, \varepsilon) = C_\varepsilon(\varepsilon - \varepsilon_0) + C_T(T - T_0) + f_0(T_0, \varepsilon_0) \tag{2.1}$$

where $f(T, \varepsilon)$ is the Brillouin frequency shift(BFS) at temperature T and strain ε; C_ε is the strain sensitivity MHz/%; C_T is the temperature sensitivity, as MHz/°C; $f_0(T_0, \varepsilon_0)$ indicates the baseline BFS at the temperature T_0 and strain ε_0.

2

Generally, a complete distributed optical fiber sensors (DOFS) system comprises a sensing optical fiber plus a signal interrogator. The optical fiber can be extended remotely and attached to the monitored structure. It works both as a sensing part and signal transmission channel, while the fiber end (one end or both ends) is plugged into the interrogator for signal stimulation and processing. According to different signal-processing principles, commercially available (Brillouin scattering) interrogators for structural monitoring can be classified as based on: (1) Brillouin Optical Time Domain Reflectometry (BOTDR); (2) Brillouin Optical Time Domain Analyzer (BOTDA); (3) Brillouin Optical Frequency Domain Analyzer (BOFDA) and (4) Brillouin Optical Frequency Domain Reflectometry (BOFDR),see López-Higuera *et al.* (2011) and Motil *et al.* (2016) for more details.

DOFS has many advantages over conventional electronic sensors, such as:(1) distributed sensing; (2) immunity to electromagnetic interferences; (3) long sensing distances of above a hundred kilometers. Therefore, DOFS has been more and more used in civil engineering, including in monitoring buildings and bridge structures (Ohno *et al.*, 2001; Leung *et al.*, 2015), pile foundations (Schwamb *et al.*, 2014), tunnels and landslides(Soga, 2014; Iten *et al.*, 2009; Wang *et al.*, 2018), among others (Pei *et al.*, 2014).

As a general classification, in structure and geotechnical monitoring DOFS has been mainly used for:(1) distributed strain sensing and (2) point displacement measuring.

2.2.2. DOFS FOR DISTRIBUTED STRAIN SENSING

In distributed strain sensing, the sensing fiber is continuously bonded to the host structure, either on the surface or embedded internally; the structure strain can be transferred to the sensing fiber through interface bonding and hence measured. In geotechnical and structure engineering, DOFS has been explored for distributed strain sensing in pile foundation, concrete tunnel lining, and others.

Klar *et al.* (2006) applied DOFS with a BOTDR of 1m spatial resolution (spatial resolution refers to the length on which the measured strain or temperature of a sampling point is averaged) to measure strain in a pile foundation, and evaluated the advantage of the DOFS over conventional discrete strain gauges. The maximum measured pile strain is about 0.095%. The study concluded that the DOFS is a cost-effective pile monitoring method compared with discrete strain measurement methods such as vibrating wire strain gauges and fiber Bragg gratings (FBGs).

Mohamad *et al.* (2011) used an optical fiber sensor (BOTDR system with a spatial resolution of 1m) to monitor both axial strain and lateral movements of a secant pile wall during the construction of an adjacent basement in London. The fiber was imposed a prestrain of about 0.2% and the measured strain is about 0.04% in the test. Results showed that measurements obtained by the DOFS were in good agreement with those by the conventional inclinometer.

Schwamb *et al.* (2014) utilized optical fiber sensors to measure bending and circumferential hoop strains of a shaft wall in London. Optical fiber cables were embedded into concrete panels with a primary prestrain of about 0.25%. Both BOTDR (spatial resolution of 1m) and BOTDA (spatial resolution of 0.5m) interrogators were used to take the strain reading, and the behavior of the shaft wall in the excavation process was studied.

Pelecanos *et al.* (2018) presented measurement results of three concrete bored piles in axially loaded tests using both conventional vibrating wire strain gauges and DOFS

(BOTDR with spatial resolution 0.5-1.0m). The fibers are imposed a primary tension of 0.1% to 0.2%, while the measured strain change is about 0.07%. Results showed DOFS could provide a continuous strain profile within piles, and this offers advantages in studying the skin friction development in piles compared with discrete strain gauges.

Besides distributed strain in piles, DOFS has also been used to measure concrete tunnel lining strain. By bonding the sensing fiber to the tunnel lining with glue (e.g., epoxy resins), the strain information along the bonding length can be thus obtained. Shi et al. (2005) used optic fibers to monitor the deformation of an urban road tunnel, where the sensing fiber is bonded continuously on the vault as well as to fixture points at the wall, see Fig.2.2a, and a BOTDR with a spatial resolution of 1m is used to collect the data. The study shows the surface strain at the tunnel vault is small while at the expansion joint displacement is more significant. In another study by Gue et al. (2015), DOFS is glued continuously along the circumference of an existing tunnel at the segment flanges, see Fig.2.2b, to measure the continuously distributed strain within a transverse cross-section. A BOTDR (spatial resolution of 1m) is used to collect data, and measurement results show a maximum recorded cumulative strain in both tension and compression in the order of $550\mu\varepsilon$(0.055%). These studies show that DOFS can work well to obtain the distributed strain information along tunnel lining when bonded properly.
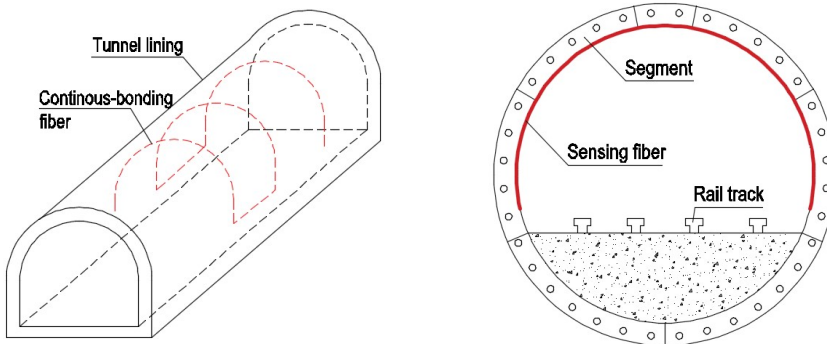
(a) Strain sensing at tunnel viaduct, from Liu et al. (2018)   (b) Segment strain measuring, from Gue et al. (2015)

Figure 2.2: Tunnel segment deformation modes

In another study by Seo et al. (2017), DOFS is buried into the concrete segment of a bored tunnel to measure circumferential strain (BOTDR of 1m spatial resolution), and the strain difference on intrudes and extrudes of the lining is used to estimate the moment on tunnel lining. The sensing fiber was prestrained and installed along the reinforcement cage before segment concreting, and the maximum measured strain is about 0.035%.

Besides quantitative studies on structure strain using embedded optical fiber, there are also qualitative studies on ground movement with optical fiber cables. For example, a fiber cable buried into the ground may possibly detect the soil movement caused by a landslide or close underground construction activities (such as tunneling and pit excavation). Such studies can be found in Klar & Linker (2010); Damiano et al. (2017); Iten et al. (2009). It should be noted that in these studies, the measured fiber strain generally

could not directly specify the actual ground deformation (both direction and magnitude), but DOFS is validated as effective in early warning of ground movement.

Another aspect of using DOFS for distributed strain sensing, is the systematic error by interrogator spatial resolution. For an interrogator with a large spatial resolution of 1.0m, it still possess limitations in measuring the point strain as precisely as conventional strain gauges (generally with centimeter-order gauge length). However, the superiority of distributed sensing can make up for this deficiency when the continuous strain distribution is more emphasized. Moreover, with more advanced signal processing techniques developed, the spatial resolution of commercial interrogators has been largely reduced from 1.0m to 0.2m in the recent decade, which indicates the great potential of DOFS to measure point strain as precisely as conventional strain gauges.

2.2.3. DOFS FOR POINT DISPLACEMENT MEASURING

When a short optical fiber length is anchored at two points (see fixation points P1 and P2 in Fig.2.3), the interval unbonded fiber (referred to as gauge length) can work as an extensometer, and the relative displacement of two anchorage points (along fiber axis direction) can be therefore measured. In structure health monitoring, such optical fiber extensometers have been used to monitor structure joint deformation (like the longitudinal joint opening of a bored tunnel), cracking width, and others.

It should be mentioned that when working as an extensometer, the superiority of distributed strain sensing capacity of DOFS seems not highly distinctive compared with conventional electrical extensometers. However, the most highlighted advantage of DOFS based extensometers is that numerous extensometers can be easily installed and assembled as a chain along a long single fiber cable longitudinally, due to the DOFS's long-distance sensing capacity, which can significantly simplify the complexity of the sensing network, as well as reduce the cost. This is especially advantageous when large numbers of measurement points are necessary for structure monitoring.
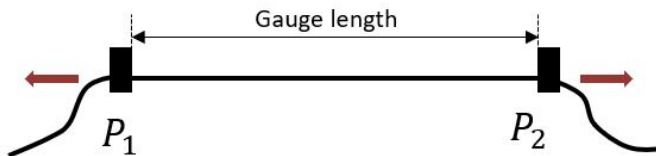
Figure 2.3: Schematic of optical fiber extensometers (P1 and P2 are fixture points)

DOFS extensometers have been applied to monitor joint opening of bored tunnels. When applying the DOFS for joint deformation (opening and closure) monitoring, the gauge length is usually pre-tensioned and fixed at two sides of the joint. In this way both joint opening and closure are measured. For example, in the study by Gue *et al.* (2015), the optical fiber is fixed at discrete points to measure the circumferential joint opening when nearby construction activities take place. In another study by Wang *et al.* (2018), the optical fiber is used to instrument the circumferential joint of a bored tunnel, see Fig.2.4). All these studies show DOFS can work well to detect joint openings in bored tunnels.

Moreover, multiple optical fiber extensometers can be also assembled together to
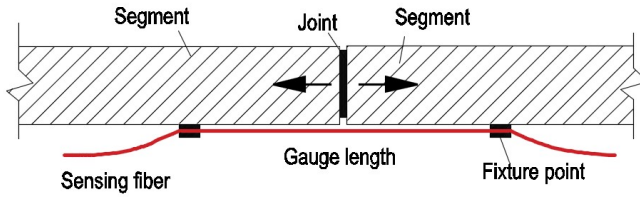
Figure 2.4: Fiber extensometer to measure joint opening of a bored tunnel

instrument a transverse cross-section of a bored tunnel, so as to help interpret the circumferential deformation behavior (such as cross-section distortion, and ovalization) of the tunnel. Such studies on tunnel circumferential deformation monitoring can be found in Mohamad *et al.* (2012); Acikgoz *et al.* (2017); Gue *et al.* (2015). It should be mentioned that in the above studies, multiple optical fiber extensometers are set within a tunnel cross-section which can only monitor the overall cross-section deformation behavior(as in Fig.2.5), and the precise displacement of each fixing point is unavailable since the number of extensometer is limited. This differs from the explicit accurate single-direction joint deformation measuring in Gue *et al.* (2015) and Wang *et al.* (2018).
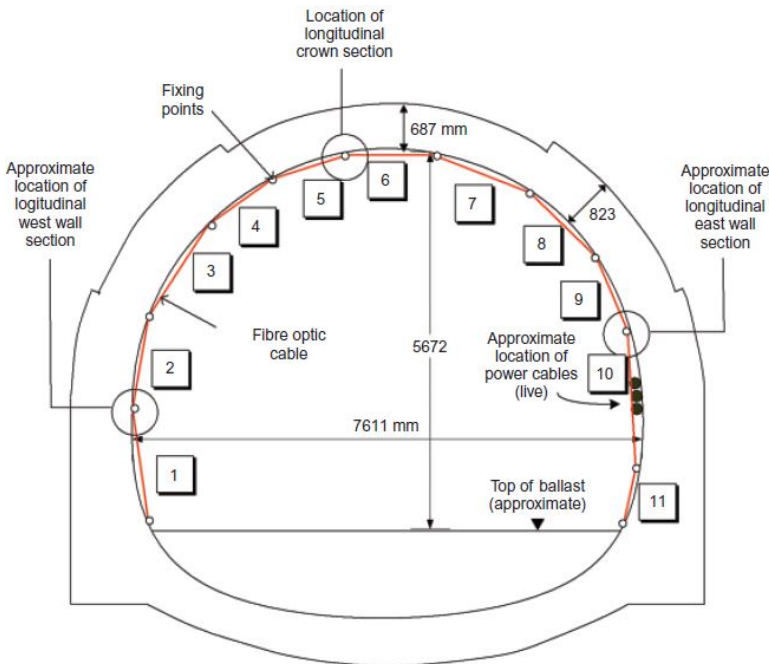
Figure 2.5: DOFS to measure tunnel cross-section behavior (Mohamad *et al.*, 2010)

Besides being used for structure joint deformation, optical fiber extensometers can also be buried into the ground or structure to measure internal cracking width or relative

deformation of two determined locations. For instance, in the study by Liu *et al.* (2018), an optical fiber extensometer was made and buried into a roadway subgrade to detect potential cracking. In another study by Lienhart *et al.* (2014), the optical fiber is embedded into the geogrids of reinforced earth structure by discrete point anchorage along the fiber axis, and thus multiple consecutive extensometers were set up to measure the horizontal deformation of reinforced earth structure.

When designing an optical fiber extensometer for joint opening (or closure) measuring, the following parameters should be considered: (1) the gauge length; (2) the necessity of fiber pre-straining and the level of it ; (3) the point fixing method (by glue or special clamps). In most studies, the gauge length is usually set longer than the spatial resolution of the interrogator used, so that the systematic error (resulting from spatial resolution) can be theoretically removed. The monitoring performance of optical fiber extensometers in previous studies is summarized in Tab.2.3.

2.2.4. Summary of DOFS application

The review of previous studies on distributed optic fiber(DOFS) application indicates: (1) the applicability of DOFS has been validated both in distributed strain sensing and point displacement measuring; (2) the majority of previous research concentrates more on the field application practices of DOFS on specific monitoring projects, and less on the optical fiber properties itself; (3) in point displacement measuring, DOFS are mainly used for accurate single-direction deformation sensing (like joint opening), and there is no study which applies DOFS for accurate point deformation measurement along two or three directions.

When utilizing DOFS for immersed tunnel joint monitoring, some critical issues in designing such a DOFS monitoring system need to be investigated:

- Optimal sensing fiber selection. As an essential part of the DOFS system, the optical fiber works as both the sensing part and the signal transmission channel, and its properties strongly affect the measurement accuracy. For example, the optical fiber used for point displacement measuring should have a higher strain limit (than for distributed strain sensing), but a too strong fiber may not be easy to handle, especially when manual pretension is required. Moreover, optical fiber typically has a multiple-layer structure in the radial direction with an external sheath made of polymer material, the possible relaxation and creep behavior of fiber at a high working strain level in monitoring should be investigated to assure reliable measurement in the long term;

- DOFS for accurate deformation sensing along two or three-directions. In this thesis, the DOFS is planned to instrument the joint and measure deformation in three-directions(opening, uneven settlement, and transverse drift). This is a more complex task compared with previous studies on single-directional deformation sensing, and a more complicated and reliable sensor layout design is firstly required.

The abovementioned research gaps in applying DOFS for immersed tunnel monitoring will be investigated in detail in this thesis.

Table 2.3: Summary of fiber installation parameters in previous studies

Source	Interrogator type	Spatial resolution	Installation method	Sensing fiber type	Pre-strain	Sensed strain range
Gue et al. (2015)	BOTDR	1.0m	Overall bonding; Point fixing, L=13m	Hitachi 0.9mm (0.6%); tight buffer fiber	0.1%-0.3%	0.055%
Mohamad et al. (2012)	BOTDR	1.0m	Point fixing, L=1.12m	Hitachi 0.9mm (0.6%) tight buffer fiber	0.15%	0.035%; -0.063%
Klar et al. (2006)	BOTDR	1.0m	Point fixing	0.9mm tight buffer fiber	0.2%	-0.03%; 0%
Mohamad et al. (2010)	BOTDR	1.0m	Point fixing, L=1.4m	Hitachi 0.9mm (0.6%) tight buffer fiber	0.2%-0.3%	0.2%; -0.05%
Moffat et al. (2015)	BOTDR	Unavaliable	Overall bonding	0.9mm tight buffer fiber	0.1%	0.062%
Schwamb et al. (2014)	BOTDR/A	1.0m	Point fixing, L=1.3m	Unavaliable	0.2%	0.04%; -0.03%
Wang et al. (2018)	BOFDA (fTB2502)	0.2m	Point fixing, L=1.2m	0.9mm tight buffer fiber	0.5%-1%	0.03%; -0.33%
Lienhart et al. (2014)	BOFDA (fTB121)	1.0m	Point fixing, L=1.2m	BRUGG Strain V4	0%	1.1%

REFERENCES

Acikgoz, S., Pelecanos, L., Giardina, G., Aitken, J. & Soga, K. (2017). Distributed sensing of a masonry vault during nearby piling. *Structural Control and Health Monitoring* **24**, No. 3, e1872.

ATKINS, COWI, TEC, ChristiansenEssenbak, DeltaMarineConsultants, nmGeo & RAMBOLL (2019). Limfjord tunnel assessment and retrofitting-technical summary report, v 1.0. *Technical report*.

Bai, Y. & Lu, H. (2016). Damage analysis and rpair technology of omega gasket in immersed tube tunnel. *Journal of Railway Engineering Society* **33**, No. 9, 87–92.

Commission-T330 (2014). Instandhouding zinkvoegen. *Technical report*, COB.

Damiano, E., Avolio, B., Minardo, A., Olivares, L., Picarelli, L. & Zeni, L. (2017). A laboratory study on the use of optical fibers for early detection of pre-failure slope movements in shallow granular soil deposits. *Geotechnical Testing Journal* **40**, No. 4, 529–541.

Gavin, K., Broere, W., Kovačević, M. & de Haas, K. (2019). Investigation of the remaining life of an immersed tube tunnel in the netherlands. In *Tunnels and Underground Cities: Engineering and Innovation meet Archaeology, Architecture and Art*, CRC Press, pp. 4831–4838.

Grantz, W. C. (2001a). Immersed tunnel settlements. part 1: nature of settlements. *Tunnelling and Underground Space Technology* **16**, No. 3, 195–201.

Grantz, W. C. (2001b). Immersed tunnel settlements: Part 2: case histories. *Tunnelling and Underground Space Technology* **16**, No. 3, 203–210.

Gue, C. Y., Wilcock, M., Alhaddad, M., Elshafie, M., Soga, K. & Mair, R. J. (2015). The monitoring of an existing cast iron tunnel with distributed fibre optic sensing (dfos). *Journal of Civil Structural Health Monitoring* **5**, No. 5, 573–586.

Horiguchi, T., Shimizu, K., Kurashima, T., Tateda, M. & Koyamada, Y. (1995). Development of a distributed sensing technique using brillouin scattering. *Journal of lightwave technology* **13**, No. 7, 1296–1302.

Iten, M., Schmid, A., Hauswirth, D. & Puzrin, A. M. (2009). Defining and monitoring of landslide boundaries using fiber optic systems. In *Int. Symp. on Prediction and Simulation Methods for Geohazard Mitigation, Kyoto, Japan*, pp. 451–456.

Klar, A., Bennett, P. J., Soga, K., Mair, R. J., Tester, P, Fernie, R., St John, H. D. & Torp-Peterson, G. (2006). Distributed strain measurement for pile foundations. *Proceedings of the Institution of Civil Engineers-Geotechnical Engineering* **159**, No. 3, 135–144.

Klar, A. & Linker, R. (2010). Feasibility study of automated detection of tunnel excavation by brillouin optical time domain reflectometry. *Tunnelling and Underground Space Technology* **25**, No. 5, 575–586.

Leeuw, L. (2008). Lekkage in tunnels-dilatatievoegen en beton. *Technical report*, RWS Bouwdienst.

Leung, C. K., Wan, K. T., Inaudi, D., Bao, X., Habel, W., Zhou, Z., Ou, J., Ghandehari, M., Wu, H. C. & Imai, M. (2015). Optical fiber sensors for civil engineering applications. *Materials and Structures* **48**, No. 4, 871–906.

Li, W., Wu, D., Guo, X. & Gao, X. (2011). Overhaul design and construction of ningbo yongjiang immersed tube tunnel. *MODERN TUNNELLING TECHNOLOGY* **48**, No. 1, 82–89.

Lienhart, W., Moser, F., Schuller, H. & Schachinger, T. (2014). Reinforced earth structures at semmering base tunnel—construction and monitoring using fiber optic strain measurements. In *10th International Conference on Geosynthetics (10ICG)*, ., pp. 8p–CD.

Liu, W., Zhou, H., Wang, B., Zhao, Y., Leng, Z., Chen, X., Li, L., Wang, S. & Chen, Z. (2018). A subgrade cracking monitoring sensor based on optical fiber sensing technique. *Structural Control and Health Monitoring* **25**, No. 9, e2213.

Liu, Z.-g., Huang, H.-w., Zhao, Y.-h. *et al.* (2008). Immersed tube tunnel real-time health monitoring system. *Chinese Journal of Underground Space and Engineering* **4**, No. 6, 1110–1115.

López-Higuera, J. M., Cobo, L. R., Incera, A. Q. & Cobo, A. (2011). Fiber optic sensors in structural health monitoring. *Journal of lightwave technology* **29**, No. 4, 587–608.

Moffat, R., Sotomayor, J. & Beltrán, J. F. (2015). Estimating tunnel wall displacements using a simple sensor based on a brillouin optical time domain reflectometer apparatus. *International Journal of Rock Mechanics and Mining Sciences* **75**, 233–243.

Mohamad, H., Bennett, P., Soga, K., Mair, R. & Bowers, K. (2010). Behaviour of an old masonry tunnel due to tunnelling-induced ground settlement. *Géotechnique* **60**, No. 12, 927–938.

Mohamad, H., Soga, K., Bennett, P. J., Mair, R. J. & Lim, C. S. (2012). Monitoring twin tunnel interaction using distributed optical fiber strain measurements. *Journal of geotechnical and geoenvironmental engineering* **138**, No. 8, 957–967.

Mohamad, H., Soga, K., Pellew, A. & Bennett, P. J. (2011). Performance monitoring of a secant-piled wall using distributed fiber optic strain sensing. *Journal of Geotechnical and Geoenvironmental Engineering* **137**, No. 12, 1236–1243.

Molendijk, A., Dalmeijer, R., Taffijn, E., Hol, M. & van Nes, P. (2020). Technical report article: Zinkvoegen hersteld. https://www.cementonline.nl/zinkvoegen-klaar-voor-de-toekomst-ii, accessed: July-2022.

Motil, A., Bergman, A. & Tur, M. (2016). State of the art of brillouin fiber-optic distributed sensing. *Optics & Laser Technology* **78**, 81–103.

Ohno, H., Naruse, H., Kihara, M. & Shimada, A. (2001). Industrial applications of the botdr optical fiber strain sensor. *Optical fiber technology* **7**, No. 1, 45–64.

Pei, H.-F., Teng, J., Yin, J.-H. & Chen, R. (2014). A review of previous studies on the applications of optical fiber sensors in geotechnical health monitoring. *Measurement* **58**, 207–214.

Pelecanos, L., Soga, K., Elshafie, M., de Battista, N., Kechavarzi, C., Ye Gue, C., Ouyang, Y. & Seo, H.-J. (2018). Distributed fiber optic sensing of axially loaded bored piles. American Society of Civil Engineers.

Schotte, K., Nuttens, T., De Wulf, A., Van Bogaert, P. & De Backer, H. (2016). Monitoring the structural response of the liefkenshoek rail tunnel to tidal level fluctuations. *Journal of Performance of Constructed Facilities* **30**, No. 5, 04016007.

Schwamb, T., Soga, K., Mair, R. J., Elshafie, M. Z., Sutherden, R., Boquet, C. & Greenwood, J. (2014). Fibre optic monitoring of a deep circular excavation. *Proceedings of the Institution of Civil Engineers-Geotechnical Engineering* **167**, No. 2, 144–154.

Seo, H., Wilcock, M., Soga, K., Mohammed, Elshafie & Mair, R. J. (2017). Distributed fibre optic monitoring of the time-dependent behaviour of tunnel segmental linings in london clay. In *The 2017 World Congress on Advanceds in Structure Engineering and Mechanics(ASEM17)*.

Shi, B., Xu, X., Wang, D., Wang, T., Zhang, D., Ding, Y., Xu, H. & Cui, H. (2005). Study on botdr-based distributed optical fiber strain measurement for tunnel health diagnosis. *Chinese Journal of Rock Mechanics and Engineering* **24**, No. 15, 2622–2628.

Soga, K. (2014). Understanding the real performance of geotechnical structures using an innovative fibre optic distributed strain measurement technology. *Riv. Ital. Geotech* **4**, 7–48.

van Amsterdam, B. (2019). *Probabilistic analysis of immersed tunnel settlement using cpt and masw*. Master's thesis, Delft University of Technology, the Netherlands.

van Montfort, R. (2018). *Insufficiency of immersion joints in existing immersed tunnels: Case study on functioning of gina-seal and omega-seal in the kil tunnel*. Master's thesis, Delft University of Technology, the Netherlands.

Wang, X., Shi, B., Wei, G., Chen, S.-E., Zhu, H. & Wang, T. (2018). Monitoring the behavior of segment joints in a shield tunnel using distributed fiber optic sensors. *Structural Control and Health Monitoring* **25**, No. 1, e2056.

Wei, G., Lu, S.-j., Wang, Z. & Huang, X. (2018). A theoretical model for the circumferential strain of immersed tunnel elements under tidal load. *Geotechnical and Geological Engineering* **36**, No. 3, 1633–1645.

Xu, X., Tong, L., Liu, S. & Li, H. (2019). Evaluation model for immersed tunnel health state: A case study of honggu tunnel, jiangxi province, china. *Tunnelling and Underground Space Technology* **90**, 239–248.

3

PROPERTY INVESTIGATION OF OPTICAL FIBER FOR DISPLACEMENT MEASURING APPLICATION

Distributed optical fiber sensors (DOFS) can be installed to function as extensometers for measuring point-displacements. This chapter discusses the metrics of optimal sensing fiber selection for extensometer use. Key metrics include the physical structure, mechanical parameters and light transmission coefficients. Calibration tests for verification of the optical fiber properties are designed and results of four fiber types are presented. Finally, creep and relaxation behavior of optical fibers is discussed based on manual tension test results, and a quantification model is proposed to assess the induced measurement error for sensing fiber. The maximum (absolute) measurement error for two common fiber types used in point displacement sensing is determined to be below 8%, and the study shows that pretensioning of the fiber helps to reduce such measurement errors.

3.1. INTRODUCTION

As an essential part of the DOFS system, the optical fiber properties strongly affect the measurement accuracy. However, previous studies mainly focus on field applications of DOFS on a project level, while limited attention is paid to the properties of the optical fiber itself.

There are many optical fiber products available designed primarily for use in the telecommunication industry, but not all of them are directly suitable for deformation measuring. The quality standards or metrics for telecommunication optical fiber products, such as the fracture stress, or the durability in corrosion (Glaesemann, 2017; Antunes *et al.*, 2012), are mostly focused on verifying the quality of bare optical fibers and do not fully cover the properties that are important for sensing purposes.

In this thesis the optical fiber is designed as extensometers to measure (immersed tunnel) joint deformation along three directions. The working strain level is anticipated to be above 1%, which is significantly higher than that in most previous studies (see Tab.2.3 in Chapter 2), such as maximum strain levels around 0.20% in Ohno *et al.* (2001), 0.25% in Schwamb *et al.* (2014) and 0.20% in Pelecanos *et al.* (2018). Under high working strain levels, many optical fibers have a tendency to creep or relax, which may cause significant measurement errors. The existence of creep at low-strain levels has been verified in several experimental studies (Ding *et al.*, 2004; Xu & Ansari, 2009; Song *et al.*, 2010), but creep or relaxation under high strains (around 1%, or even higher) and its effects on the DOFS system are not studied quantitatively, and there is no proposed model or methodology, theoretically or empirically, for evaluation of the measurement error induced by optical fiber relaxation.

This chapter focuses on the technical metrics and selection of sensing fibers for point displacement measuring application. The following key questions are investigated: (1) what metrics (of optical fiber) can be used to define a qualified sensing fiber (for extensometer use)? (2) how to calibrate the key metrics (or parameters) of potential sensing fibers? (3) how to verify the fiber relaxation and assess the corresponding measurement error?

In the rest of this chapter, the metrics of optimal sensing fiber are discussed and summarized firstly, and standard calibration methods for verifying important fiber parameters are proposed. Secondly, to illustrate the fiber calibration procedures, test results of four types of optical fiber are presented in detail. Finally, a quantitative model is put forward to describe the creep or relaxation properties of optical fiber (at given strain level) based on the calibration test results, and the maximum relative error (caused by fiber relaxation) of DOFS in measurement is assessed by the proposed model.

3.2. METRICS OF SENSING FIBER

In a DOFS system, property verification and calibration are necessary before deciding on a suitable sensing fiber type. A good understanding of fiber properties is the prerequisite for proper sensing fiber selection.

3.2.1. GENERAL STRUCTURE OF OPTICAL FIBERS

Single-mode fiber is preferred over multi-mode fibers in distributed sensing, as the latter has a higher signal attenuation and a lower sensing distance. In the optical fiber manufacturing industry, a general basic product is the 0.25mm-in-diameter bare fiber (D-0.25mm), e.g. Corning (2021). This bare fiber has an internal silica core with an outer diameter of 8-9µm, a cladding with an outer diameter of 125µm and external coating with an outer diameter of 250µm, see Fig.3.1a. Generally, the core plus cladding forms the route for light transmission and hence they are the actual "sensing part" of the fiber. The basic D-0.25mm bare fiber product from primary-level optical fiber manufacturers (like Corning, OCC, and others) are further processed (adding reinforcement parts and strong external protection jackets) by secondary-level manufacturers to make robust fiber cables for industry use. Another basic fiber product is the 0.9mm-in-diameter fiber (D-0.9mm) made from the D-0.25mm by adding an external polymer jacket, as shown by Fig.3.1b.

(a) D-0.25mm fiber   (b) D-0.90mm fiber
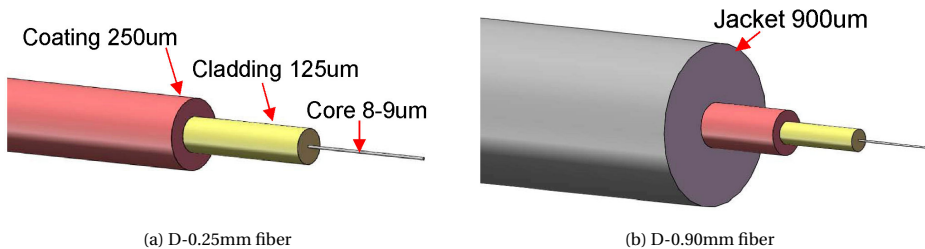
Figure 3.1: Schematic of basic optical fiber product

The D-0.9mm fiber can be processed to make tight-buffer or loose-buffer strong fiber cables for indoor and outdoor use, see Fig.3.2. It should be mentioned that the physical structure of the fiber generally decides the strain transfer between the internal fiber core and external jacket layer, as shown in Fig.3.3. The inter-layer shear transfer determines whether the external strain can be transmitted into fiber core and hence be sensed.

Generally, tight-buffered fiber assures strong inter-layer bonding, and very limited slippage (between the internal fiber core and external jacket) occurs when strained (under normal working strain level). A type of tight-buffered optical fiber (with an outer diameter of 2mm) is shown in Fig.3.2a and Fig.3.3. In contrast, loose-buffered optical fiber allows relative inter-layer slippage and hence very weak strain transfer, see Fig.3.2b and Fig.3.3. Therefore, strain sensing fiber should be tight-buffered, while loose-buffered fiber is more used for temperature measuring.

3.2.2. METRICS FOR SENSING FIBER SELECTION

The key metrics of potential sensing fibers are proposed and listed as below:

(1)The maximum working strain (MWS)

The maximum working strain (MWS) refers to the maximum strain sustained by an optical fiber where no (significant) relaxation occurs. For tight-buffered sensing fibers, MWS is strongly related to the material properties of the glass core, coating and jacket, and the interface bonding strength. Some researchers proposed to use the elastic limit strain

(a) Tight-buffered fiber   (b) Loose-buffered fiber
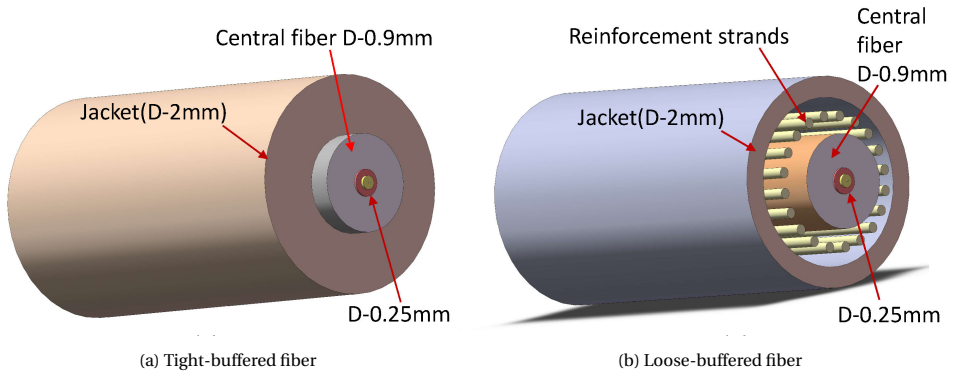
Figure 3.2: Physical structure of fiber
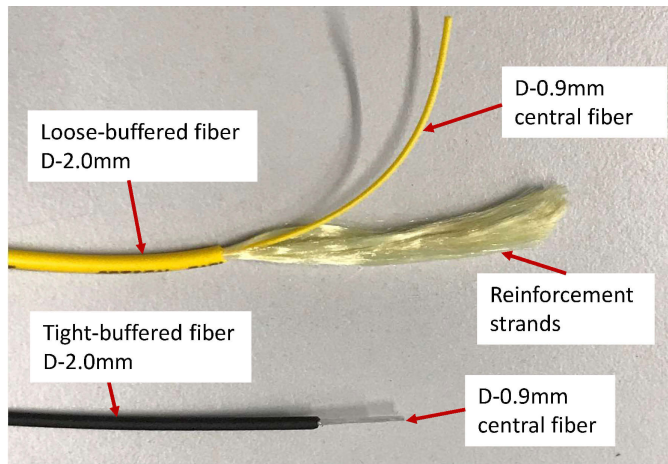
Figure 3.3: Tight-buffered and loose-buffered optical fiber

from the fiber stress-strain curve as a metric (Iten *et al.*, 2011), but the precise fiber stress is not straightforward to determine as the shrinkage of the optical fiber cross-section is usually quite significant when the fibers are tensioned.

A preferred method to define the MWS of optical fibers in deformation monitoring is to directly measure the Brillouin frequency shift (BFS) and the imposed strain (hereafter referred as strain unless otherwise specified). Within the MWS range, the Brillouin frequency shift (BFS) vs strain (f-ε) curve of the fiber maintains a high degree of linearity under loading-unloading (or tension/de-tension) cycles. When the optical fiber is tensioned beyond the MWS, the fiber usually creeps significantly, and serious inter-layer slippage may occur if the tension is sustained, which causes unacceptable errors for strain sensing applications. It should be noted that in some fiber types, creep may occur even under very low strain levels, and the MWS can be defined as the sensing range within which the measurement error (by creep or relaxation) remains limited (for example, below

10%). The MWS can for instance be measured by a cyclic tension test, as discussed below.

(2)The limit strain

The strength of the optical fiber is an important parameter for general fiber products. The limit strength (described either as a maximum fiber stress or strain) of optical fibers has been extensively studied by researchers (Glaesemann, 2017; Antunes *et al.*, 2012; Iten *et al.*, 2011). When used for sensing purposes, it is more practical to express this as the limit strain, which is the maximum strain an optical fiber can reach before breaking, leading to either partial (usually the jacket) or full rupture of the fiber cross-section.

Note that rupture of the jacket will expose the very fragile central fiber, which make the sensing fiber quite vulnerable. A full cross-section breakage, even at a single point along the fiber, usually results in a full failure of the whole distributed sensing network (although single-end measuring may be still possible, but at significantly reduced accuracy). Therefore, it is important for DOFS users to make sure the limit strain should not be reached under normal working conditions, so as to maintain a continuous robust signal transmission.

(3)Relaxation potential

Relaxation is the phenomenon that the stress level in an optical fiber, when subjected to a constant strain, tends to (partially) decrease over time. This can be described by a shift of elastic (recoverable) to plastic (non-recoverable) strain and as such relaxation is closely related to the creep that the optical fiber would undergo when subjected a continuous (even if not constant) tensile force. Therefore, a (standard) creep test can help to indicate the relaxation potential of the sensing fiber, but a calibrated tension test (imposing a given strain) is preferred when analyzing the potential measurement errors in deformation measuring.

A good sensing fiber shall not show significant relaxation behavior when tensioned below the maximum working strain (MWS). It must be mentioned that almost all tight-buffered optical fibers with polymer jackets shows signs of creep and relaxation, but what matters is to what extend this affects the measuring accuracy. Note that the Brillouin frequency shift (BFS) is linear to the actual optical fiber strain. If the BFS and the corresponding imposed strain of the optical fiber are measured simultaneously, relaxation will result in a hysteresis loop in the BFS-strain (f-ε) curve in a loading-unloading process, which may cause unacceptable errors when translating measured BFS to actual strain. Relaxation behavior of sensing fibers and their effects on DOFS measurement will be discussed in more detail in section 4.4.

(4)The strain sensitivity coefficient

The strain sensitivity coefficient (at a given light wavelength) relates the measured BFS to imposed strain (Horiguchi *et al.*, 1995; Motil *et al.*, 2016) and is an important parameter which needs to be well calibrated. In a tension test, the BFS-strain curve can be obtained, and generally the gradient of a linear fit line is determined as the strain sensitivity coefficient. In previous studies, the strain coefficient generally lies between 40-50 MHz/0.1% (Ohno *et al.*, 2001; Iten *et al.*, 2011; Wang *et al.*, 2018).

(5)The temperature sensitivity coefficient

The temperature sensitivity coefficient (at a given light wavelength) relates the BFS to temperature change(Horiguchi *et al.*, 1995; Motil *et al.*, 2016) and is measured usually by a warm-bath experiment, where a loose fiber is immersed into warm water or liquid. Based

on the fitted temperature-BFS curve the temperature sensitivity coefficient is obtained. However, according to some previous studies, determining the temperature sensitivity coefficient accurately may not be strictly necessary if the temperature effects can be appropriately compensated for, for example by setting up an additional loose fiber section (a zero-strain section) very close to the sensing fiber section (the strained section), and the measured BFS change of the zero-strain section will show the temperature influence which needs to be compensated for. Such methods can be seen in Gue *et al.* (2015); Lienhart *et al.* (2014).

(6)Axial stiffness of sensing fiber

The axial stiffness of sensing fiber EA (where E denotes the elastic modulus of the fiber and A the cross-sectional area) is an important metric which could generally be used to estimate the fiber's robustness to external impacts (Iten *et al.*, 2011). A high axial stiffness usually also indicates the fiber can withstand large axial tension forces and does not break easily. The axial stiffness is mostly determined by the reinforcement parts (sheaths or reinforcement strands) of the fiber cross-section. For optical fibers used in harsh field environments (say embedded into concrete or ground), the central fiber may be wrapped with longitudinal reinforcement metal strings or wires, and hence a high axial stiffness can be achieved. The axial stiffness of some potential optical fibers for strain sensing applications are shown in Tab.3.1.

Table 3.1: Axial stiffness of some potential optical fiber

Fiber Type	Outer Diameter	Axial Stiffness
SMF bare fiber by Coring Co.	0.25mm	About 1kN
TPEE tight buffered fiber by Nanzee Sensing Co.	0.9mm	About 1kN
Polyurethane tight buffered fiber by Nanzee Sensing Co.	2mm	About 3kN
Polyamide & metal protected fiber From Iten *et al.* (2011)	3.2mm	About 60kN

However, it should be mentioned that whereas a high axial stiffness can be beneficial to create a sturdy and protected fiber, it also makes the fiber tensioning and sensor installation quite difficult or even impossible, which is especially troublesome when manual pre-tensioning is needed during sensor installation. Therefore, selection of a DOFS fiber requires balancing between axial stiffness and ease of installation in different monitoring setups. The axial stiffness can be checked in a fiber tension test, such as in Iten *et al.* (2011). In general, keeping the ease of sensor installation in mind, it holds that:

(1) usually, bare fibers (D-0.25mm) and D-0.9mm tight-buffered fibers are very fragile (especially in bending) and are not highly recommended to be used directly in harsh environments unless reliable protection is provided.

(2) an axial stiffness of no more than 3 kN is preferred for manual pre-tensioning above 0.5% strain, for instance when the fiber is used as an extensometer in point displacement sensing.

(3) an axial stiffness of no more than 5 kN is preferred for manual pre-tensioning below 0.30%, for cases where the fiber is embedded into concrete walls or piles for distributed strain sensing.

(4) even higher stiffness (of above 5 kN) is acceptable when manual pre-tensioning is not needed during installation, for example when burying the fiber into the ground directly for landslide detection. However, measurement sensitivity should also be considered in these monitoring cases, as too stiff a fiber may de-bond easily from the surrounding soil. More information on fiber installation for such cases can be found in Iten *et al.* (2011).

3.3. CALIBRATION TESTS OF SENSING FIBER

3.3.1. COMBINED TENSION TEST

A combined tension test is the easiest way to verify both the mechanical properties and strain sensitivity of a sensing fiber. A typical calibration test can be set up on a tension machine, where a short fiber length is fixed at two points and tensioned step by step. The fiber ends are connected to the interrogator and the Brillouin frequency shift (BFS) corresponding to each loading step can be obtained, see Fig.3.4. From the imposed strain and tension force the BFS-strain (BFS-ε) curve and force-strain (F-ε) curve can be obtained, from which the strain sensitivity coefficient and axial stiffness can be derived by a linear fit, see Fig.3.4.
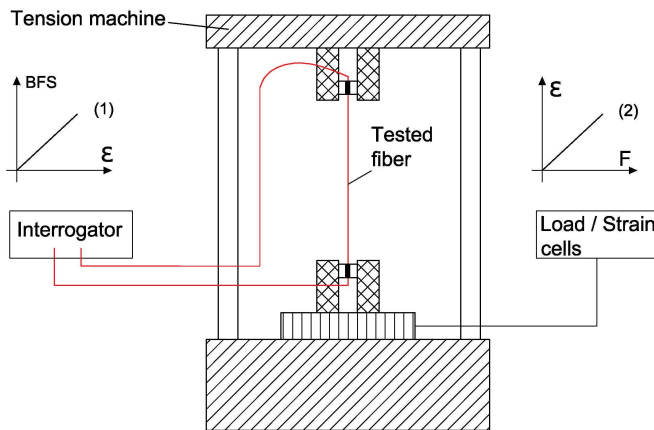
Figure 3.4: Schematic of fiber calibration test on a tension machine

When executing the combined tension test, small strain increments per loading step (for example 0.05%) should be imposed preferably, so as to detect the maximum working strain, and potentially the limit strain, as accurately as possible in a loading test cycle. Ideally, load-unload cycles are conducted at pre-determined strain levels, for example 0.25%, 0.5%, 0.75% and 1%, to verify the possible relaxation of the fiber as well, in addition to the normal test procedures for determining the mechanical properties and strain coefficient as described by Lienhart *et al.* (2014). The relaxation behavior will be further

studied in section 3.4. For a qualified sensing fiber, there should be limited relaxation (to be determined by the fiber property and monitoring requirements) before reaching a certain strain level, and this strain level can be established as the maximum working strain (MWS).

3.3.2. MANUAL TENSION TEST

For sensing fibers used in point displacement measuring applications, the axial stiffness is generally not too high and hence a manual tension test could also work. Calibration can be conducted with reduced difficulty on a simple tension platform, where a short fiber length is anchored at two ends using glue (or clamps), as in Fig.3.5. In the tension test, one anchorage is not permanently fixed and can be translated, while the other end is fixed on the sliding platform. Two dial-gauges are attached to measure the imposed displacement and avoid in-plane tilting of the movable anchorage. The fiber ends are then connected to the interrogator for BFS measurement. Using this type of set-up multiple sensing fibers can be tested simultaneously.
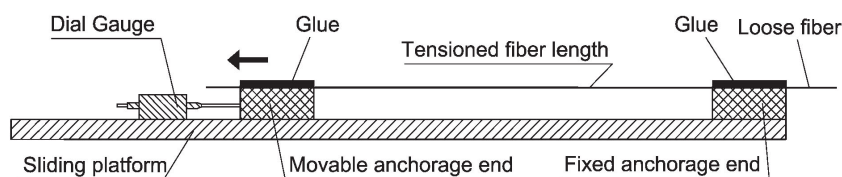
Figure 3.5: Manual tension test platform

3.3.3. TENSION TEST RESULTS ANALYSIS OF OPTICAL FIBER

To illustrate the impact of different fiber types on the fiber parameters, the results of a laboratory manual tension test of several potential sensing fibers is presented here. In this test, five fiber lengths of four different types are fixed at a horizontal platform, see Fig.3.6. Two dial-gauges are used to measure the displacement, and the imposed strain at each tension step is calculated. Each fiber length is set at 80cm, and point fixed by epoxy glue at the anchorage plates (with a bonding length of 4cm).

The tested sensing fiber types are:

(1) a polyurethane sheath tight-buffered fiber, typed NZS-DSS-C07 with a diameter of 2mm (D-2mm), manufactured by Nanzee Sensing Company from Suzhou, China;

(2) a thermoplastic polyester elastomer (TPEE) sheath fiber typed NZS-DSS-C09 (2019-batch) with a diameter of 0.9mm (white colored sheath, indicated as D-0.9mm-W in Fig.3.6), also manufactured by Nanzee Sensing Company;

(3) a tight-buffered fiber with a diameter of 0.9mm (yellow color, indicated as D-0.9mm-Y in Fig.3.6), which is obtained from the central fiber of a loose-buffered cable product typed AE001DSLA9YR (see Fig.3.3), manufactured by OCC Company, USA. From this fiber type with an outer diameter of 2mm and a D-0.9mm tight-buffer central fiber, the external loose jacket is peeled off and removed carefully and only the 0.9mm central fiber is used for testing;

(4) a bare fiber with diameter of 0.25mm (D-0.25mm), typed Corning SMF-28, manufactured by Corning Company, USA.
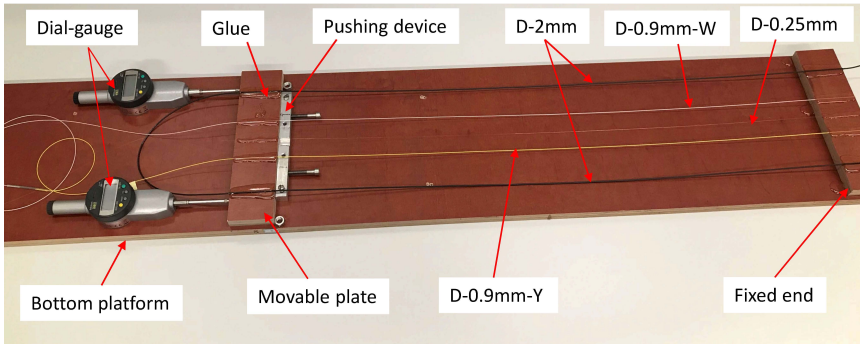
Figure 3.6: Fiber calibration by manual tension test

In the tension test, the four different fiber types are fusion-spliced (as they have the same fiber core dimension) to form a continuous fiber cable and both ends are connected into a Brillouin Optical Frequency Domain Analyzer (BOFDA) interrogator. This BOFDA, type fTB2505 and manufactured by fibrisTerre Systems GmbH, is used to measure the Brillouin frequency shift of the tensioned fibers at each loading step. It has a stated spatial resolution of 0.2m (up to 1km), a spatial accuracy of 0.05m, and strain accuracy of $2\mu\varepsilon$ (0.0002%), according to fibrisTerre (2021).

Another important aspect in the tension test is to determine the loading history. This experimental study targets to: (1) obtain the maximum working strain (the strain level below which no significant relaxation occurs); (2) analyze the strain behavior in a tensioned state (if significant relaxation is observed) and (3) detect possible residual strain when the optical fiber is fully de-tensioned. Previous studies have shown that the limit strain of a typical bare fiber (D-0.25mm) is around 1.2% (Iten *et al.*, 2011), and optical fiber generally exhibits only minimal creep behavior at strain levels below 0.20% (Ohno *et al.*, 2001; Schwamb *et al.*, 2014), which indicates the behavior of optical fiber with strain between 0.25% and 1.2% is of most interest here. In the tension test, loading-unloading cycles are conducted at strain levels of 0.25%, 0.5%, 0.75%, 1% and 1.2%, see the loading cycles in Fig.3.7. The five strain gradients are set in order to better verify the potential of relaxation and determine the MWS of each fiber type, with the impact of relaxation analyzed using the directly measured BFS. The temperature effects in the experiment period are compensated for by recording the BFS change of the loose section of each fiber type.

Fig.3.8 shows the BFS-strain curve of the D-0.25mm bare fiber under different loading cycles. From the results, it can be seen the bare fiber shows little relaxation (A BFS reduction of about 1 MHz) under a strain of 0.25%, but in the loading cycle of 0.50%, there is a permanent BFS reduction of about 4MHz, which is induced by a very small permanent slippage (less than 0.01%). In the third loading cycle, the BFS-strain curve remains a highly linear with no sign of relaxation below 0.65% strain. However, coating breakage occurs at 0.7% strain and significant slippage was found between the coating
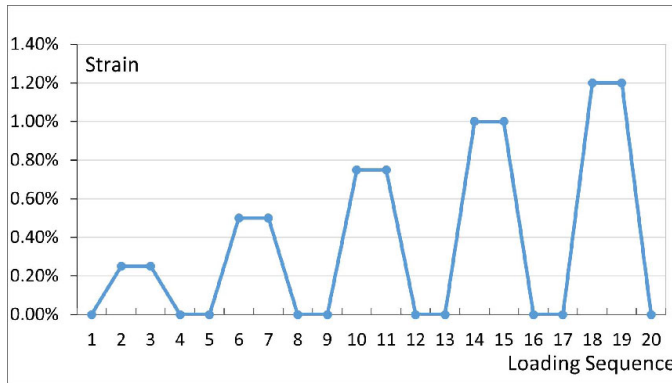
Figure 3.7: Loading cycles for fiber calibration

and cladding layer, see Fig.3.9a. In the subsequent loading cycles (cycle-1.0% and 1.2%), the fiber core and cladding do not rupture (after a large unloading due to the slippage), and data-taking can be continued. Based on a linear fit of the BFS-strain curve (between 0-0.65%), the strain sensitivity of this D-0.25mm bare fiber is about 47.40Mhz/0.1%. The relaxation potential of this fiber is very small and hence its effects can be neglected.

According to the test results, the maximum working strain of this D-0.25mm bare fiber is about 0.65%, while the limit strain is about 0.7% at which strain coating breakage occurs (and although the signal transmission is continued, the exposed core and cladding are too fragile and can break quite easily). Note this bare fiber is very fragile and would rarely be used for field strain sensing applications, unless reliable protection is provided.
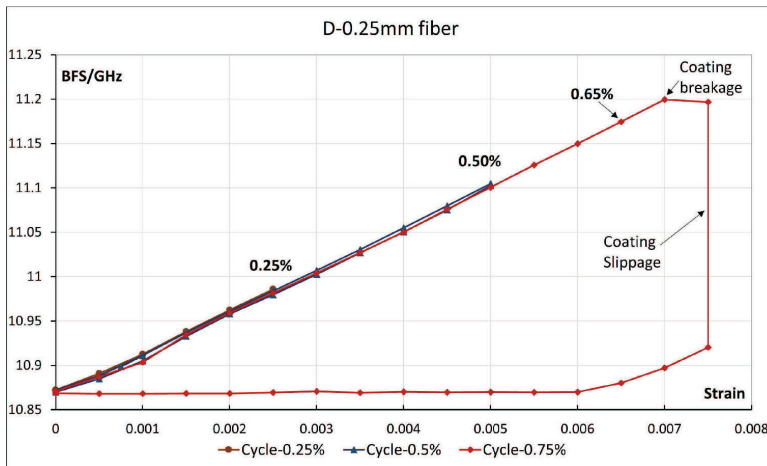
Figure 3.8: Cyclic loading of D-0.25mm bare fiber

Fig.3.10 shows the BFS-strain curve of the D-0.9mm-Y fiber (yellow-jacket, as shown in Fig.3.6) under cyclic loading. At each cycle, the load is imposed rapidly until it reaches the

(a) D-0.25mm bare fiber (b) D-0.90mm-Y fiber
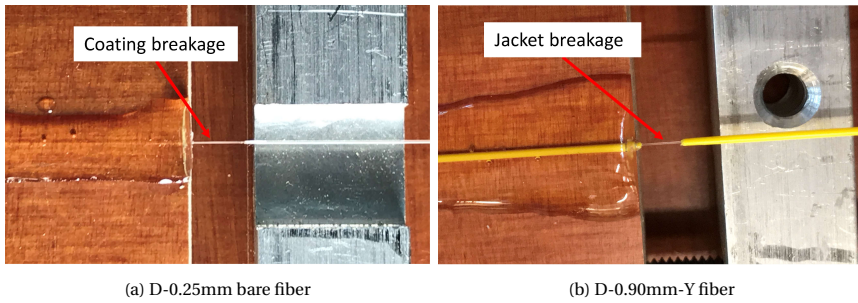
Figure 3.9: Fiber breakage at limit strain

maximum strain (2 mins. per load step) and the fiber strain is sustained until the rate of BFS decrease (caused by relaxation) is below 0.4MHz per hour. Then the fiber is unloaded to zero strain rapidly. Therefore, it is assumed the relaxation within a cycle occurs at the maximum load (the highest imposed strain). From Fig.3.10 it can be seen the load-unload process results in a hysteresis loop in the BFS-strain curve, which indicates relaxation occurs when tensioned even at a low strain level of 0.25%. Unlike the D-0.25mm fiber which exhibits a small amount of relaxation, this fiber shows quite significant relaxation behavior, which may affect the measurement results. The BFS reduction caused by relaxation are:(1) 6.4MHz at 0.25% after 16hrs;(2) 25.4MHz at 0.50% after 66hrs;(3) 48.8MHz at 0.75% after 42hrs; and (4) 47.1MHz at 1.0% after 61hrs.

Also, it can be observed in Fig.3.10 that the loading and unloading curves for each cycle are highly parallel (with a very similar gradient), which indicates that every load cycle generates additional residual plastic strain in the fiber. The relaxation of this D-0.9mm-Y fiber is mainly due to inter-layer slippage and creep of the jacket. In the subsequent load stages, the fiber jacket breaks at 1.1% strain and large inter-layer slippage occurs, which result in a sharp reduction of the measured BFS, see Fig.3.9b and Fig.3.10. The limit strain of this fiber is obtained as 1.1%, while at normal working strain level significant relaxation occurs. The measurement error caused by this relaxation will be discussed in the next section.

The D-0.9mm-W fiber (white-jacket, as shown in Fig.3.6) shows similar relaxation behavior under tension as the D-0.9mm-Y fiber does. Fig.3.11 shows the BFS-strain curve of the D-0.9mm-W fiber under cycle-0.75% and 1.0%, and as can be seen the BFS decrease is quite significant. The result of five load cycles is shown here and discussed in detail in Section 4. It can be seen that relaxation behavior of the D-0.9mm-W fiber is actually different to that of the D-0.9mm-Y fiber, as there exists a significant gap between the unloading curve of cycle-0.75% and the loading curve of cycle-1.0%. This gap indicates partial recovery of the residual strain after unloading.

To better illustrate the relaxation behavior, recoverable or elastic strain is defined here as that portion of the strain that is recovered or reversed over time after unloading (to zero strain), whereas the plastic strain, once it has occurred, will not be recovered. This is distinct from the instant portion of strain reversal that occurs directly after unloading, as the elastic strain reversal occurs over a similar time period as the initial strain.

That recoverable elastic strain occurs is also verified in Fig.3.11, where a BFS increase
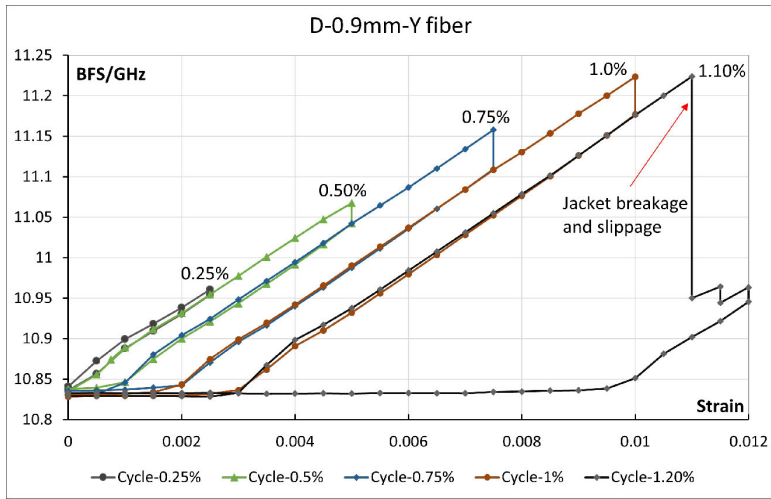
Figure 3.10: Behavior of D-0.9mm-Y fiber under cyclic loading

is detected during the unloading process of cycle-1.0%. This increase of measured BFS is due to the elastic relief over a 98hrs period at a fixed strain of 0.35%. The dotted line indicates the most likely unloading curve under a fast unloading scenario (when no time lapse is set for elastic creep relief). The behavior of this fiber type is probably related to creep of the sheath material or inter-layer debonding. In the subsequent loading to 1.2%, sheath breakage was not found, and hence the limit strain is verified to be no smaller than 1.2%.
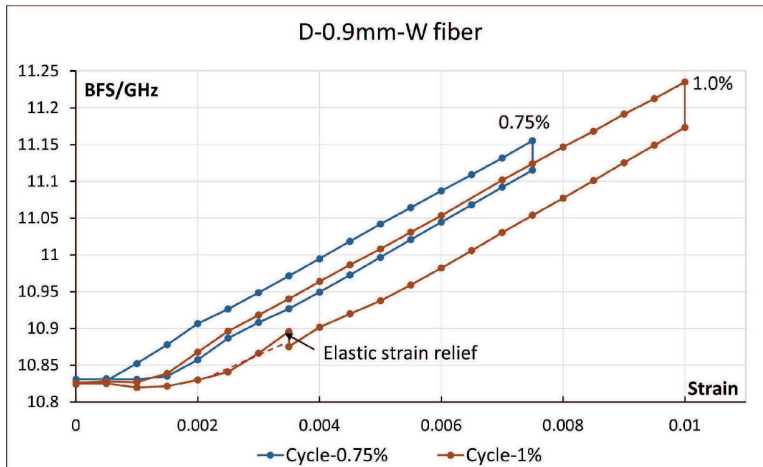
Figure 3.11: Behavior of D-0.9mm-W fiber (Cycle-0.75% and 1.0%)

Fig.3.12 shows the BFS-strain curves of the D-2mm fiber under five successive load

cycles. From the results, it can be seen the fiber keeps a highly linear response even under an imposed tension of 1.2% (the actual fiber strain is found to be about 1.25% due to a primary tension at baseline status), and shows very little creep behavior (a BFS reduction of less than 1 MHz is observed in each load cycle, except at cycle-0.5%, where a BFS increase of 3MHz in 66hrs at 0.50%, which is most probably due to a system error in signal interpretation). Based on a linear fit of the BFS-strain curve (between 0-1.2%), the strain sensitivity of this D-2mm fiber is about 48.40Mhz/0.1%. The maximum working strain is verified to be above 1.20% and, among the four types of fiber tested in this test, this D-2mm fiber is the most qualified type for strain sensing applications outside of lab conditions.

3
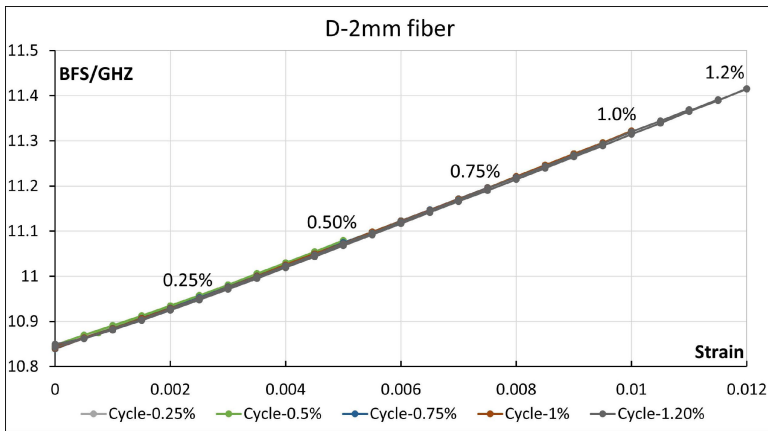
Figure 3.12: Behavior of D-2mm fiber under cyclic loading

According to the calibration tension test, the D-2mm fiber is the most suitable type for point displacement measuring, considering it has the lowest relaxation effects and the highest maximum working strain (MWS) among the four tested types of fiber. The D-0.25mm bare fiber also has potential in measuring point displacement applications but at a reduced MWS of 0.65% (or even lower to obtain some safety margin) and under delicate protection. Both of the D-0.9mm fiber types show significant relaxation that introduces measurement errors if they are used directly without any beforehand processing. These results show it is possible to select a potential sensing fiber which shows little relaxation or creep and calibrate the parameters using the proposed manual tension test. However, considering the possible sources resulting in relaxation, such as randomness in fiber manufacturing quality control or improper handling during the fiber transportation and field installation, even some specially made sensing fibers still show creep behavior, see Iten *et al.* (2011). Therefore, it is still reasonable and necessary to quantitatively analyze the relaxation behavior of optical fibers to be able to verify the validity of field measurements.

3.4. RELAXATION ANALYSIS OF SENSING FIBER

3.4.1. INTRODUCTION OF FIBER RELAXATION

According to the calibration tests shown in Fig.3.10 and Fig.3.11, tight-buffered optical fiber (cable) may show significant relaxation behavior in a tensioned state. When a fiber gauge length is pre-strained at installation, relaxation will result in a reduction of the measured BFS, and hence a smaller measured strain than the actual imposed strain (by the host structure). Therefore, relaxation affects the measurement accuracy of DOFS and should be studied carefully.

For a strained fiber length that is fixed well at both ends, the relaxation mainly comes from (1) the inter-layer slippage due to inadequate interface bonding and (2) creep of the external jacket material. Inter-layer bonding is the key for strain transfer and sensing, but when the bonding is not strong enough, inter-layer slippage may occur, which results in a permanent decrease of measured strain. Slippage may occur at the coating-cladding interface, or jacket-coating interface, see Fig.3.2. For ordinary telecommunication fibers, the interface bonding may not be strong enough and slippage may occur even at very low strain levels, which is also shown by (Ding *et al.*, 2004; Song *et al.*, 2010). Creep of the external jacket is highly related to the material properties. According to the tension test results in this study, the relaxation due to jacket creep consists of plastic and elastic components, where the plastic strain is unrecoverable whilst the elastic strain can recover over time after the strain is unloaded. Therefore, the total fiber strain decrease ε_t (by relaxation) can be expressed as Eq.3.1:

$$\varepsilon_t = \varepsilon_s + \varepsilon_j = \varepsilon_p + \varepsilon_e \tag{3.1}$$

where ε_s is the strain decrease by inter-layer slippage; ε_j is the strain decrease by creep of the jacket material; ε_p is the total plastic strain, which consists of ε_s and the plastic component of ε_j; ε_e refers to the elastic component of ε_j.

For both ordinary telecommunication fibers and special-made sensing fibers, relaxation is always possible and should be well checked in the calibration test before using for monitoring tasks. Optical fibers which show relaxation may still have potential for strain sensing use, but the key issues are: (1) the amount of relaxation; (2) how to estimate the measurement error due to relaxation; and (3) what measures can be taken to reduce such measurement error? As mentioned in Section 3, fiber relaxation behavior can be verified by a cyclic tension test, since it will result in a hysteresis loop in the loading-unloading curve as shown in Fig.3.11.

3.4.2. DESCRIPTION OF RELAXATION PROPERTIES BASED ON TENSION TEST RESULTS

To illustrate the typical relaxation behavior of an optical fiber, the cyclic tension test results of the D-0.9mm-W fiber are firstly presented here in Fig.3.13. In the tension test, five loading cycles are conducted, with the maximum strain imposed successively being 0.25%, 0.5%, 0.75%, 1.0% and 1.2%. The BFS-strain history curve shows that:(1) relaxation occurs, though not very significantly, during the first loading cycle to 0.25% strain; (2) significant relaxation occurs in the second loading cycle to 0.5% strain, and a highly identified hysteresis loop is present; (3) the total plastic strain due to relaxation

accumulates and becomes larger in the subsequent load cycles with increased strain imposed (from 0.5% to 1.2%); (4) for a given loading cycle (for example the cycle-1%), the corresponding relaxation could be fully triggered (with a time delay) when the fiber is pre-tensioned (to 1%), and can be removed as a contributing factor in subsequent load cycles, which indicates that pre-tensioning of the fiber can potentially reduce the measurement errors introduced by relaxation.

What's more, it should be mentioned that the elastic strain component is recovered gradually during the unloading process, as can be seen in the Fig.3.11 and Fig.3.13, where the subsequent new loading curve does not overlap completely with the unloading curve of the previous cycle. For example, the loading curve of cycle-1.0% is above the unloading curve of cycle-0.75%, and this small difference indicates a (recoverable) elastic strain component makes up part of the imposed strain of 0.75%.
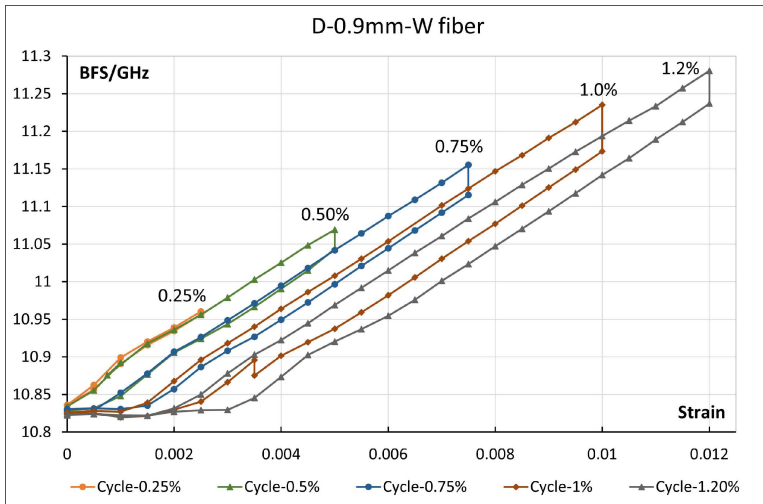
Figure 3.13: Cyclic loading history of D-0.9mm-W fiber

Another important aspect of fiber relaxation is the extent of it. It should be noted that theoretically relaxation will continue for quite a long time (as it is closely related to the theoretically long lasting creep behavior), but generally is proportional to log(t) and after a limited time period most of the relaxation has already occurred. Fig.3.14 shows the measured BFS decrease (due to relaxation) as a function of $ln(t)$ at an imposed strain of 1.0%. This BFS change is highly linear, and the predicted time-history curve of BFS decrease within a one-year period is shown in Fig.3.15. It can be seen that within that period, for the D-2mm-W fiber 50.5% of the total relaxation occurs on the first day, while 59.7% occurs within the first 3 days; and for the D-2mm-Y fiber the corresponding percentages are 44.3% and 54.6%, respectively. Besides, the measurement results also show that for an imposed strain below 1.0% the magnitude of observed relaxation is smaller. For example, the BFS decrease of the D-0.9mm-W fiber at 0.25% strain is about 6.5MHz after 12 hours and tends to be stable afterwards. Therefore, the results in this study show that in order to experimentally establish relaxation of at least 50% of the total

that would occur over a year long period at high strain levels of 1.0%, a sustained tension test of about 2 days is needed.
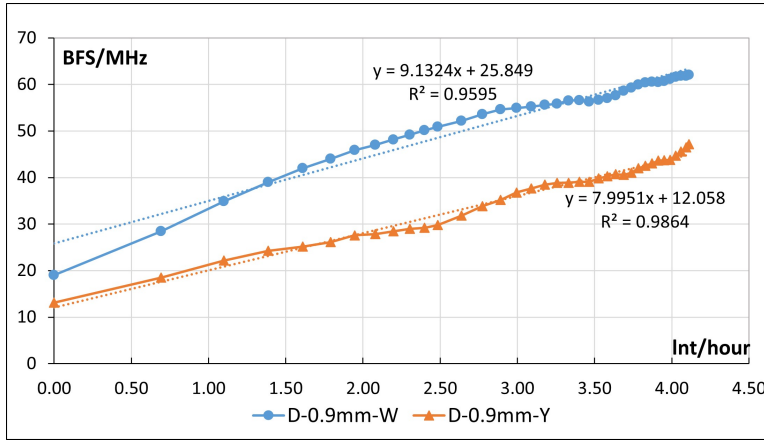
Figure 3.14: BFS decrease due to relaxation (strain of 1.0%)
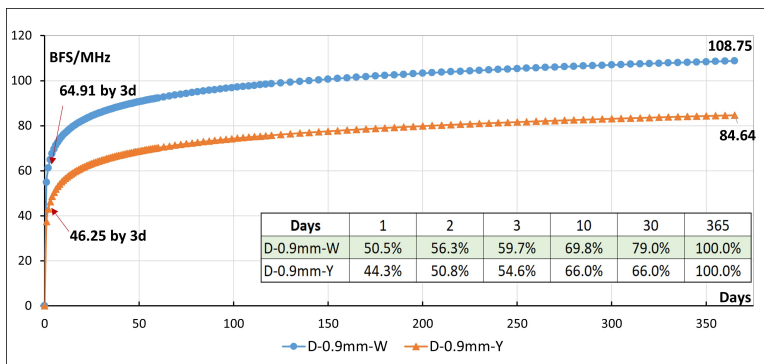
Figure 3.15: Time-history of BFS decrease due to relaxation (strain of 1.0%)

3.4.3. A RELAXATION MODEL FOR SENSING FIBER

According to the tension test results, it is reasonable to assume the plastic component corresponding to a certain imposed strain can be fully triggered and becomes a permanent residual strain when the fiber is fully unloaded to zero strain. Therefore, a fiber pre-tensioning to the anticipated maximum strain before fiber sensor installation will help to remove the error due to residual plastic strain in subsequent measurements. However, as elastic strain is dependent on the imposed fiber strain and elapsed time, it is important to properly model the elastic component and estimate the potential measurement error this may introduce.

Here a simplified model is proposed based on the tension test results in this study.

Fig.3.16 shows a typical hysteresis loop of a BFS-strain (f-ε) curve during a loading-unloading cycle. The fiber is first loaded (from zero strain) to a designated strain ε_m (shown in the loading curve $O - P$), and relaxation occurs over time, which results in a reduction of measured BFS, as shown by curve $P - Q$ and Δf in Fig.3.16. Finally, the measured BFS reaches a stable value (at point Q) which indicate the relaxation (corresponding to ε_m) process has finished. After that the fiber is unloaded to zero strain (see curve $Q - R - O$), and a residual strain is found which consist of a plastic ε_p and elastic component ε_e. If the fiber is loaded again from zero strain (from point O), the new loading will follow curve $O - S - T$, and it should be noted that new loading curve $S - T$ is above the previous unloading curve $Q - R$, and the gap between them indicates the recoverable elastic component ε_e. According to the tension test results, it is reasonable to assume that afterwards the loading-unloading process (to a maximum strain of ε_m) will follow the narrow loop bounded by curve S-T-Q-R-S, and the geometry of this loop is determined by the fiber type (under the imposed strain ε_m). Therefore, this loop can be referred to as the "characteristic loop" of the optical fiber. It should be noted that after the loading-unloading cycle of ε_m, the strain sensing range of the fiber is reduced to (ε_m-ε_p).
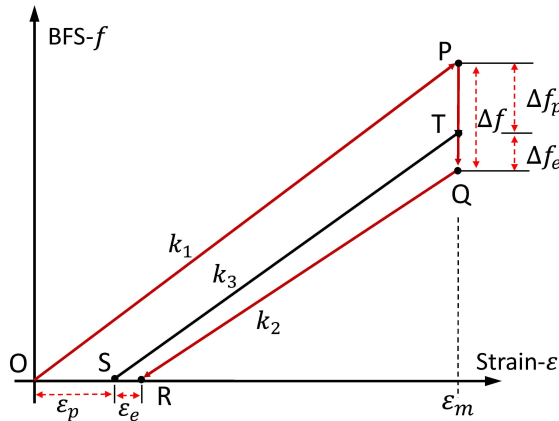
Figure 3.16: Loop BFS-strain curve of optical fiber under cyclic loading

To better analyze the elastic strain behavior of optical fiber, the characteristic loop is moved to the origin (point S overlaps at point O), as shown in Fig.3.17. For simplicity, the relation between elastic strain ε_e and the corresponding imposed strain ε is assumed to be linear, and hence the dotted line $O - Q$ defines the ultimate BFS-strain curve when relaxation has finished, and this ultimate BFS-strain curve is used for strain interpretation of the fiber sensor. Accordingly, after rapid loading to point $M(\varepsilon_1, f_1)$ with an imposed strain ε_1, the relaxation will finally result in a BFS decrease from f_1 to f_2 where a stable value is reached, see $M - N$ in Fig.3.17. In order to estimate the error, consider a rapidly imposed loading and unloading step at $N(\varepsilon_1, f_2)$.

For this loading scenario, the maximum error occurs right after the loading stage when relaxation has not started to manifest yet, see Fig.3.17. The maximum relative error is calculated below from the actual imposed strain $\Delta\varepsilon_1$ shown in Eq.3.2,

Figure 3.17: Measurement error analysis based on characteristic loop

$$\Delta\varepsilon_1 = \frac{\Delta f}{k_1} \tag{3.2}$$

The measured strain $\Delta\varepsilon_2$ as observed by the fiber sensor is expressed in Eq.3.3,

$$\Delta\varepsilon_2 = \frac{\Delta f}{k_3} \tag{3.3}$$

where k_1 and k_3 are the gradient of rapid loading curve $O - T$ (the upper boundary curve of the characteristic loop) and ultimate $BFS - \varepsilon$ curve $O - Q$, respectively, see Fig.3.17.

The maximum relative error (MRE) of measurement under loading conditions is deduced as Eq.3.4:

$$MRE(load) = \frac{\Delta\varepsilon_2 - \Delta\varepsilon_1}{\Delta\varepsilon_1} = \frac{k_1 - k_3}{k_3} \tag{3.4}$$

From the above equation, the maximum relative error (MRE) of the optical fiber is decided by the gradients k_1 and k_3, which are related to the chacteristic loop, and hence determined by the fiber properties. Note that the measued Δf decreases with time due to relaxation, and the measured $\Delta\varepsilon_2$ will reduce gradually until to $\Delta\varepsilon_1$, which means over time the measurement error will decrease.

For the unloading scenario, the maximum error occurs right after the unloading when elastic bounce-back has not started yet. The maximum relative error in unloading MRE(unload) of measurement can be similarly deduced as in Eq.3.5:

$$MRE(unload) = \frac{k_2 - k_3}{k_3} \tag{3.5}$$

where k_2 is the gradient of unloading curve $R - Q$ (the lower boundary curve of the characteristic loop), see Fig.3.17. It should be noted that for a fiber which exhibits relaxation,

according to the fiber tension test in this study, there is a difference between k_1 and k_2 because the elastic component tends to bounce back slowly with reduced strain in the unloading process, and therefore k_1 is somewhat larger than k_2, while the difference is determined by the fiber type.

According to the proposed relaxation model and the characteristic loop, the maximum relative error (due to relaxation or creep) of the D-0.9mm-W fiber and D-0.9mm-Y fiber are calculated. The fiber is assumed to be first tensioned to 1% and hence plastic strain is triggered. After that the fiber is unloaded to zero strain, and reloaded to 1% again. By this pre-tensioning cycle the characteristic loop is obtained, but it should be noted that the maximum sensing strain of the fiber is reduced by removing the plastic strain. The results are shown in Tab.3.2.

Table 3.2: Maximum relative error of D-0.9mm fiber

Fiber Type	D-0.9mm-W	D-0.9mm-Y
k_1 (MHz/0.1%)	45.87	46.68
k_2 (MHz/0.1%)	44.00	48.04
k_3 (MHz/0.1%)	42.72	48.98
MRE(load)	7.37%	-4.72%
MRE(unload)	3.0%	-1.93%

For the two D-0.9mm fiber types, the MRE(load) of D-0.9mm-W and D-0.9mm-Y are 7.37% and −4.72%, respectively, while the MRE(unload) are much smaller at 3.0% and -1.93%, respectively. It can be concluded that after pre-tensioning, the error due to relaxation is limited for both fiber types. Besides, the positive MRE(load) and MRE(unload) for D-0.9mm-W means most probably that the measured strain by DOFS is larger than the actual strain, while for D-0.9mm-Y the negative values indicate the opposite. The results also show that the elastic strain component of D-0.9mm-Y is very small as to be negligible, as for each loading cycle the accumulated strain is mostly the plastic component. As stated above, the proposed relaxation model predicts that the measurement error due to relaxation decreases over time, and the error values indicated here are therefore considered an upper bound estimate of the measurement error. Finally, it is highly suggested that pre-tensioning can effectively reduce the error due to relaxation (and creep) and therefore is a good way to process the sensing fiber before field installation.

3.5. CONCLUSION

A proper fiber selection for using distributed optical fiber sensor (DOFS) as a means to obtain point displacement measurements, depends on understanding the general physical behavior of the optical fiber and selecting a fiber type with proper metrics for optimal sensing. Two fiber calibration tests, a combined tension test and a manual tension test, are proposed here to obtain the fiber properties. Based on the manual tension test results in this study, the influence of fiber relaxation is investigated, and a quantitative model is proposed that describes relaxation behavior and can be used to assess measurement errors.

The main conclusions are summarized as follows:

(1) For the selection of sensing fibers in DOFS point-displacement measurements, the important metrics are: the physical structure of optical fiber, the maximum working strain (MWS), the limit strain, the relaxation behavior, the strain coefficient and the temperature coefficient. In addition, the axial stiffness is also an important metric when manual pre-tensioning is needed during sensor installation. An axial stiffness of no more than 3kN is suggested for manual pre-tensioning above 0.5% strain when used for point-displacement measurements.

(2) The mechanical properties of the optical fiber can be verified by a combined calibration test, preferably on a tension machine. The BFS-strain curve and axial stiffness can be obtained simultaneously in that way. In addition, a manual tension test also works for determining the properties of optical fibers with low axial stiffness, as shown in this study.

(3) The relaxation of optical fibers causes measurement errors and shall be checked prior to field installation. According to the experimental test results, relaxation of typical tight-buffered optical fibers (at a given primary imposed strain) generally consists of an (unrecoverable) plastic component and (recoverable) elastic component. The plastic component can be fully triggered and removed by beforehand pre-tensioning, and hence a pre-tensioning of the sensing fiber before installation can help reduce measurement errors caused by relaxation.

(4) The relaxation behavior can be described by the characteristic loop of the sensing fiber, and the maximum relative error of the measurement can be assessed accordingly. The proposed relaxation model can describe an upper bound estimate of measurement error quantitatively. The maximum (absolute) measurement errors of the D-0.9mm-W and D-0.9mm-Y fiber are 7.37% and 4.72% respectively.

DOFS is expected to gain increasing attention in field monitoring and will be more widely used in the future, but a proper fiber selection is key to successful and reliable measurements. This study provides insight into parameter verification of optical fibers.

REFERENCES

Antunes, P., Domingues, F., Granada, M. & André, P. (2012). *Mechanical properties of optical fibers*. INTECH Open Access Publisher.

Corning (2021). Information sheets-corning® smf-28® ultra fiber. https://www.corning.com/optical-communications/worldwide/en/home/products/fiber/optical-fiber-products/smf-28-ultra.html, accessed: July-2022.

Ding, Y., Shi, B., Bao, X. & Gao, J. (2004). A study on the jacket effect of fiber optic sensors. In *Photonics North 2004: Photonic Applications in Telecommunications, Sensors, Software, and Lasers*, vol. 5579, SPIE, pp. 43–50.

fibrisTerre (2021). *User manual for fibristerre ftb series-fiber-optic sensing system for distributed strain and temperature monitoring (rev4.1)*. fibrisTerre Systems GmbH, Berlin, Germany.

Glaesemann, G. S. (2017). Review of research at corning's optical fiber strength laboratory white paper. *Technical report*.

Gue, C. Y., Wilcock, M., Alhaddad, M., Elshafie, M., Soga, K. & Mair, R. J. (2015). The monitoring of an existing cast iron tunnel with distributed fibre optic sensing (dfos). *Journal of Civil Structural Health Monitoring* **5**, No. 5, 573–586.

Horiguchi, T., Shimizu, K., Kurashima, T., Tateda, M. & Koyamada, Y. (1995). Development of a distributed sensing technique using brillouin scattering. *Journal of lightwave technology* **13**, No. 7, 1296–1302.

Iten, M., Hauswirth, D. & Puzrin, A. M. (2011). Distributed fiber optic sensor development, testing, and evaluation for geotechnical monitoring applications. In *Smart Sensor Phenomena, Technology, Networks, and Systems 2011*, vol. 7982, SPIE, pp. 67–81.

Lienhart, W., Moser, F., Schuller, H. & Schachinger, T. (2014). Reinforced earth structures at semmering base tunnel—construction and monitoring using fiber optic strain measurements. In *10th International Conference on Geosynthetics (10ICG)*, ., pp. 8p–CD.

Motil, A., Bergman, A. & Tur, M. (2016). State of the art of brillouin fiber-optic distributed sensing. *Optics & Laser Technology* **78**, 81–103.

Ohno, H., Naruse, H., Kihara, M. & Shimada, A. (2001). Industrial applications of the botdr optical fiber strain sensor. *Optical fiber technology* **7**, No. 1, 45–64.

Pelecanos, L., Soga, K., Elshafie, M., de Battista, N., Kechavarzi, C., Ye Gue, C., Ouyang, Y. & Seo, H.-J. (2018). Distributed fiber optic sensing of axially loaded bored piles. American Society of Civil Engineers.

Schwamb, T., Soga, K., Mair, R. J., Elshafie, M. Z., Sutherden, R., Boquet, C. & Greenwood, J. (2014). Fibre optic monitoring of a deep circular excavation. *Proceedings of the Institution of Civil Engineers-Geotechnical Engineering* **167**, No. 2, 144–154.

Song, S., Yang, C., Wu, Z., Zhang, Y. & Shen, S. (2010). Study on the creep properties of distributed optical fiber sensors. In *Sensors and Smart Structures Technologies for Civil, Mechanical, and Aerospace Systems 2010*, vol. 7647, SPIE, pp. 794–802.

Wang, X., Shi, B., Wei, G., Chen, S.-E., Zhu, H. & Wang, T. (2018). Monitoring the behavior of segment joints in a shield tunnel using distributed fiber optic sensors. *Structural Control and Health Monitoring* **25**, No. 1, e2056.

Xu, Z. & Ansari, F. (2009). Measurement of creep of optical fiber by a low coherent white light double interferometer system. *Science in China Series E: Technological Sciences* **52**, No. 3, 647–650.

Zhang, X. & Broere, W. (2022). Sensing fiber selection for point displacement measuring with distributed optic fiber sensor. *Measurement* **197**, 111275.

4

DESIGN OF A DISTRIBUTED OPTICAL FIBER SENSOR (DOFS) SYSTEM FOR MEASURING IMMERSED TUNNEL JOINT DEFORMATIONS

Monitoring the deformations of immersed tunnels is important during the entire tunnel service life to assess the structural integrity of the tunnel. In this chapter a new joint monitoring system using distributed optical fiber sensors (DOFS) is developed. A special sensor layout is designed that allows simultaneous measurements of three-direction joint deformation (horizontal joint opening, vertical uneven settlement and transverse drift) for both immersion and dilation joints. For this sensor scheme the transfer relation from fiber strain to joint deformation is derived and verified by in-lab experiments. The sensor system proves able to detect sub-millimeter joint deformations, indicating a more than sufficient accuracy for structural monitoring of immersed tunnel joints. Subsequently, the First Heinenoordtunnel in the Netherlands is instrumented using this distributed optical fiber sensor(DOFS) system, in order to obtain additional data for both long-term and short-term assessment of its structural condition.

4.1. INTRODUCTION

For a general segmented immersed tunnel, displacement of adjoining segments in three directions (namely vertical settlement, longitudinal expansion and transverse drift) will theoretically result in joint deformation along three directions: (1) joint openings; (2) uneven settlements(of the two joint sides) and (3) transverse shear displacement. Monitoring joint deformation is a more explicit and practical way to study the behavior of immersed tunnel, than monitoring the whole segment body. Joint deformation is closely related to both structural safety and watertightness (Wang *et al.*, 2020; Bai & Lu, 2016; Gavin *et al.*, 2019; Leeuw, 2008), and such problems observed (listed in Tab.2.2 in Chapter 1) has reminded us that a qualified deformation monitoring is more important than we have anticipated to immersed tunnel safety.

The distributed optical fiber sensor (DOFS) feature long-distance sensing, which means the sensing part of the optic fiber can be attached on the targeted structure while the fiber itself is extended to a remote-control data-taking system some distance away from the observed structure itself. Therefore, it is especially useful for cases where the monitoring location is mostly inaccessible (like an in-service tunnel).

This chapter aims to design a DOFS system for immersed tunnel joint monitoring and assess the monitoring system performance experimentally. For the first time, DOFS is used in setting up a joint deformation monitoring system which fulfills high-frequency and remote-control data-taking requirements, and it targets to instrument all the immersion and dilations joints. In the rest of this chapter, the targeted joint deformation modes and the general DOFS system information will be firstly introduced; secondly, the sensor layout design that allows for joint deformation monitoring along three axes of movement is described, as well as the joint displacement-fiber strain transform relations; thirdly, this sensor layout with in-lab experiments and determine the accuracy and reliability of the method; finally, the DOFS monitoring system is further successfully applied for field installation in the First Heinenoordtunnel.

4.2. DEFORMATION PATTERNS OF IMMERSED TUNNEL JOINTS

4.2.1. DILATION JOINTS

Dilation joints (or segment joints) are located between adjoining segments within an immersed tunnel element. For watertightness, a special steel-rubber gasket water-stop is embedded in the segment body during casting and crosses the dilation joint gap, see Fig. 4.1a. The concrete collar at segment ends provides interlocking and allows for shear force transfer between adjoining segments, see Fig. 4.1b.

Cyclic opening and closure of the dilation joints may deteriorate the integrity of the rubber gasket and induce leakages in the tunnel, while uneven settlements between segments may trigger a significant shear force in the collar which may damage the gasket and the concrete body directly, see Fig. 4.1b. Commonly observed problems at dilation joints are leakages and local concrete cracking due to high stress concentrations (van Montfort, 2018; Gavin *et al.*, 2019). The lateral drift at dilation joints is rarely monitored and hence it remains unclear if this contributes significantly to collar damage. For monitoring structural safety, the joint opening and uneven vertical settlements should form the minimum aspects to be measured during the service life of the tunnel.

(a) Schematic of a typical dilation joint

(b) Deformed dilation joint
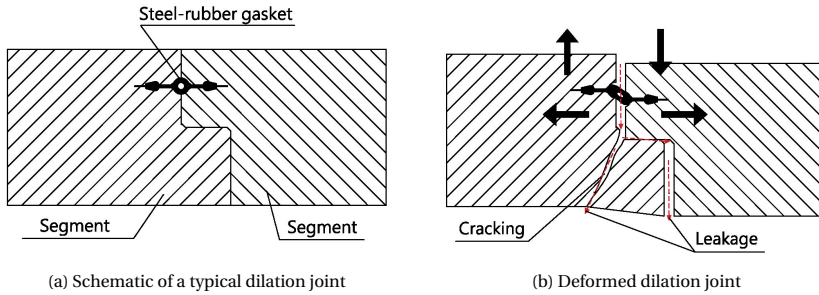
Figure 4.1: Dilation joint deformation at tunnel roof

4.2.2. IMMERSION JOINT

A typical immersion joint has a different profile than a dilation joint, as shown in Fig. 4.2a. Immersion joints will compress and relax somewhat due to the tunnel element thermal shrinkage with temperature change (Rahadian *et al.*, 2018). Also, tilting of segment (by uneven settlement) in vertical plane will cause local joint opening or closure at tunnel roof or floor. Excessive joint opening or closure may deteriorate watertightness or over-compression damage of the GINA (Bai & Lu, 2016), see Fig. 4.2a. In addition, significant uneven settlement may occur if the vertical shear keys don't function properly. In summary, available monitoring has shown at least a two-directional deformation mode can occur at the immersion joints, consisting of vertical uneven settlement (of two sides of the joint) and a horizontal joint opening, see Fig. 4.2b. A competent joint monitoring system should be able to detect both these deformation modes, and if possible, the transverse drift on foundation plane is also preferred.

(a) Schematic of a typical immersion joint

(b) Deformed immersion joint
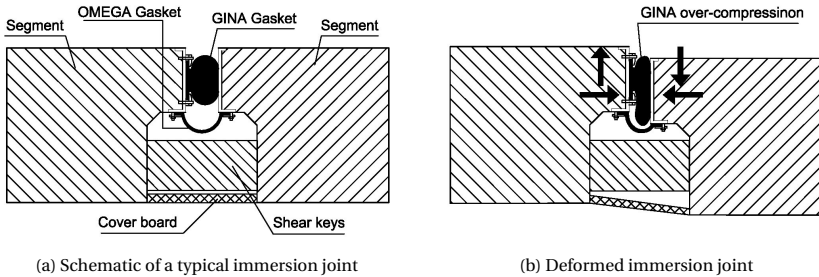
Figure 4.2: Immersion joint deformation at tunnel roof

4.3. DESIGN OF A DISTRIBUTED OPTICAL FIBER SENSOR SYSTEM FOR MEASURING JOINT DEFORMATIONS

4.3.1. MONITORING REQUIREMENT DESCRIPTION

A complete DOFS system consists of a continuous optical fiber (as a sensing fiber) plus a signal interrogator (with measurement management software), see Fig. 4.3. As Heinen-

oordtunnel (a segmented immersed tunnel in Netherlands) is selected for field monitoring validation, the installed DOFS monitoring system should impose no interference to tunnel traffic. Moreover, there is no utility tube in this tunnel which indicate the interrogator system has to be set outside the tunnel.

Therefore, a suitable field monitoring configuration should be that: a long optical fiber extends along the tunnel axis longitudinally, and it is specially installed at individual joint for deformation sensing, while the fiber ends extend further outside the tunnel to the interrogator, as shown in Fig. 4.4.

(a) Optical fiber cables   (b) Interrogator with operation computer
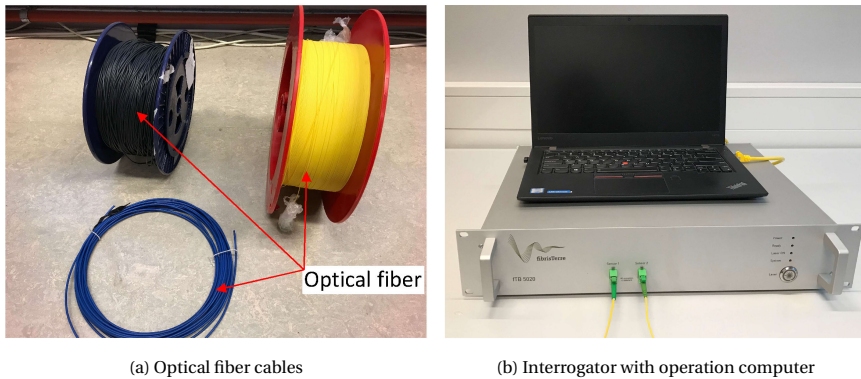
Figure 4.3: Components of the DOFS system
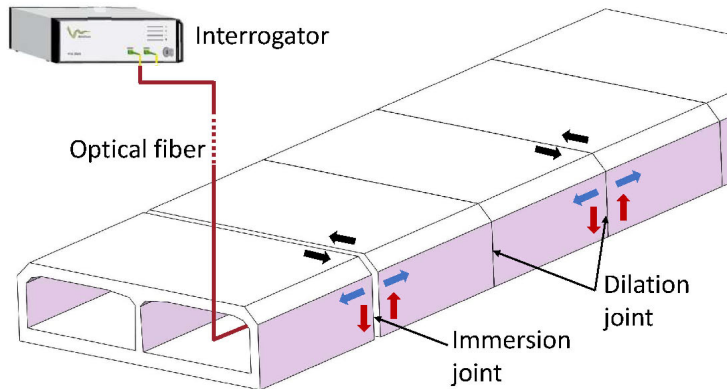
Figure 4.4: Field monitoring network configuration

4.3.2. Sensor layout at joint

In DOFS monitoring, note that DOFS only directly measure the axial strain (after decoupling the temperature effect) along fiber axis. This distributed axial strain is the desired observable, for instance when the sensing fiber is embedded into the structure or continuously bonded on structure surface. For example, optical fibers can be embedded

into concrete piles or secant walls for vertical strain measuring (Pelecanos *et al.*, 2018; Schwamb *et al.*, 2014), or bonded continuously on structure surfaces for strain monitoring (Gue *et al.*, 2015).

However, for immersed tunnel joint deformation monitoring in this study, we are interested more in the relative displacement (of two sides) at a joint, rather than the distributed strain along the segment bodies. Therefore, the sensing fiber should be installed as an extensometer which can effectively detect the opening and uneven settlement (of two sides) of joint. In this case, the observable displacement is indirectly derived from the local fiber strain, and an effective sensing layout design should take into account: (1) the potential displacement range; (2) a distinct and unique fiber strain to displacement transfer relation; and (3) ease of sensor installation.

For single-direction joint deformation monitoring, a simple sensing layout for displacement measurements can consist of a short length (gauge length) of fiber cable fixed at two points, and the relative displacement between these points can thus be monitored and calculated, see Wang *et al.* (2018); Mohamad *et al.* (2010).

In order to detect three-directional joint displacement (joint opening, vertical uneven settlement and transverse drift), more gauge lengths are needed and aligned in a way which can transfer displacement to fiber strain effectively. Also, in order to detect both extension and contraction, pre-tensioning of the fiber is usually needed during optical fiber installation. As an additional requirement, the sensing fiber layout should be designed in such a way as to reduce the field installation difficulty as much as possible, which means a uniform layout for all monitored joints is preferred. These requirements have resulted in a sensor layout design as shown in Fig.4.5, and the transfer relation between fiber strain and joint displacement for this layout is derived below.

(a) Sensor layout at joint   (b) Sensor block configuration
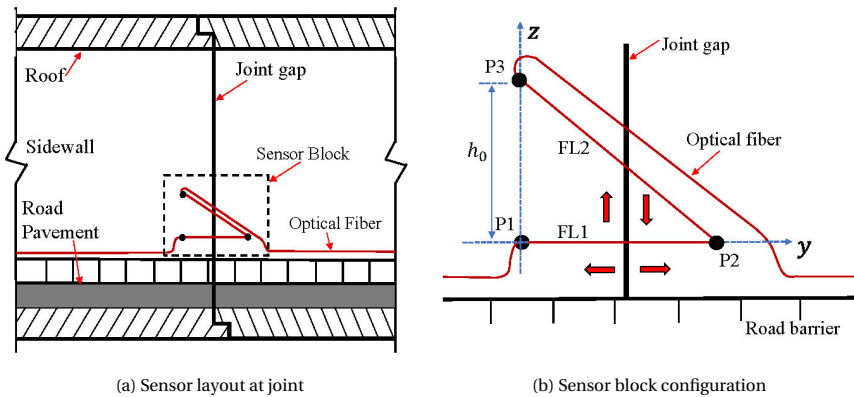
Figure 4.5: Sensor layout for two-directional joint displacement measurement

At each joint, two short sections of the optical fiber lines (FLs) are fixed at 3 points, see fixation points FP1 to FP3 in Fig.4.5. The two sensing fiber lines (FL1 and FL2) plus 3 fixation points form a sensor triangle (or sensor block) which detects two-directional joint displacements (joint opening along Y-axis and vertical uneven settlement along Z-axis). During installation, FL1 is oriented horizontally and FP1 and FP3 are aligned on a vertical

line (along the Z-axis in Fig.4.5).

The deformation of the horizontal fiber line FL1 can be described using Eq.4.1 to Eq.4.6 below, assuming that FL1 only detects horizontal deformations, while simplification is valid as the impact of any vertical deformations on the strain in FL1 is negligible. At time interval i, the relation between fiber strain and deformation for FL1 can be established as:

$$\varepsilon_{1,i} = \frac{f_{1,i}}{C_\varepsilon} \tag{4.1}$$

$$l_{1,i} = l_1(1 + \varepsilon_{1,i}) \tag{4.2}$$

$$\Delta Y_i = l_1 \varepsilon_{1,i} \tag{4.3}$$

For FL2, it follows that:

$$\varepsilon_{2,i} = \frac{f_{2,i}}{C_\varepsilon} \tag{4.4}$$

$$l_{2,i} = l_2(1 + \varepsilon_{2,i}) \tag{4.5}$$

and the height difference between FP1 and FP3 is given by:

$$h_i = \sqrt[2]{l_{2,i}^2 - l_{1,i}^2} \tag{4.6}$$

where l_1/l_2 are the gauge lengths of FL1/FL2; $l_{1,i}/l_{2,i}$ are the lengths of FL1/FL2 at interval i; $f_{1,i}/f_{2,i}$ are the measured Brillouin frequency shifts of FL1/FL2 at interval i (decoupling temperature component); C_ε is the strain sensitivity of fiber; $\varepsilon_{1,i}/\varepsilon_{2,i}$ are the measured strains of FL1/FL2 at interval i; ΔY_i is the extension of FL1 at interval i; and h_i is the height difference between FP1 and FP3.

For a measurement at the same location at a subsequent time interval j, the displacement-strain relations will be equal to Eq.4.1 to Eq.4.6, and the joint deformation relative to interval i can be derived from an observed change in Brillouin frequency shifts as :

$$\Delta Y = \Delta Y_j - \Delta Y_i \tag{4.7}$$

$$\Delta Z = h_j - h_i \tag{4.8}$$

It is noted that potential transverse displacements ΔX also cause strains in the sensor fibers. However, as for most optical fibers the maximum allowable strain is below 1.2%, under normal working conditions the effects of a transverse displacement ΔX on the measured fiber strain only results in negligible second order effects and an ignorable error well below 0.1%. Hence the derived relation between actual displacements and measured strain is a reasonable basis to obtain joint displacements.

The analysis above shows that a sensor block, consisting of two fiber lines fixed at three discrete points at a joint, works effectively to detect two-directional joint displacements. For field applications, theoretically two sensor blocks installed at both the tunnel wall and roof of the same joint could measure all three directions of joint displacement $(\Delta X, \Delta Y, \Delta Z)$ simultaneously, see Fig. 4.6. However, sensor installation on the tunnel

roof is often difficult or even impossible due to limited access and the extended traffic closures that would be required for installation, but nonetheless it is possible for instance in utility or escape tubes, as shown in Fig. 4.6. For a simplified monitoring scheme, only the sidewall of the tunnel is instrumented which can still effectively measure the two main joint deformation modes (opening and uneven settlement).
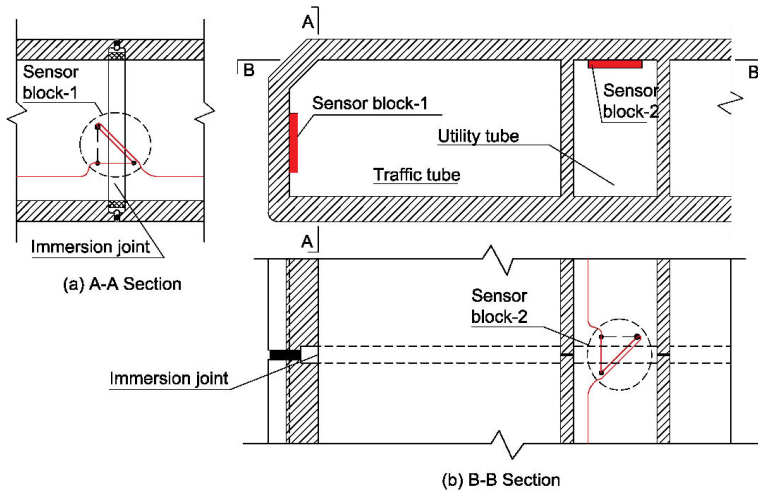
Figure 4.6: Fiber layout for three directional joint deformation monitoring

4.4. VERIFICATION OF THE SENSOR PRINCIPLE

4.4.1. EXPERIMENT SETUP DESCRIPTION

In order to verify the reliability of the designed sensor setup we performed a number of in-lab experiments first. In these experiments, we checked (1) whether the anticipated displacement range can be measured reliably; (2) what the maximum allowable strain of the optical fiber is before errors become too large, and before the fiber is destroyed; and (3) what the axial stiffness of the optical fiber is, which is especially important when pre-tensioning is required during fiber installation. A low axial stiffness usually indicates that the optical fiber is fragile and tends to break easily even under normal operation conditions, whereas a high stiffness makes the sensing fiber difficult to be pre-tensioned and fixed during installation.

In the lab experiment, two types of optical fiber were selected: a polyurethane sheath fiber type NZS-DSS-C07 with a diameter of 2mm (D-2mm), and a tight-buffered sensing fiber type NZS-DSS-C09 with a diameter of 0.9mm (D-0.9mm). Both are manufactured by Nanzee Sensing Company from Suzhou, China. The strain sensitivity coefficients of the D-2mm and D-0.9mm fiber are tested as 48.55 MHz/0.1% and 49MHz/0.1% respectively. A BOFDA interrogator, type fTB5020 (shown in Fig. 4.3b) and manufactured by fibrisTerre Systems GmbH, is used to measure the Brillouin frequency shift of the sensing fibers at each displacement step. This BOFDA device has a stated spatial resolution of 0.2m (up to

2km) and 0.5m (up to 25km), a spatial accuracy of 0.05m, and fiber strain accuracy of 2 micro-strain (0.0002%), according to fibrisTerre (2021).

Fig. 4.7 and Fig. 4.8 show the joint model test setup. Important parts of the setup are: (1) a movable platform, which consists of two wood plates, marked as bottom plate (BP) which controls the horizontal movement, and a vertical plate (VP) which allows for vertical movement. The BP and VP are assembled perpendicularly with adjustable clamps (AC), and can be fixed in place with tension screws, while they still can be moved independently by adjusting the AC.

(2) a fixed platform and fixed frame. The sensor fiber is attached to the fixed frame at two fixture points (FP1 and FP3 in Fig. 4.7 and Fig. 4.8), while fixture point 2 (FP2) is at the edge of VP. Note that the fixed platform also serves as the reference plane on which the BP slides.

(3) a sensor fiber. The selected sensor fiber is fixed at 3 points (FP1/FP2/FP3) with epoxy glue, while the fiber lines between (fiber line 1 and 2, see FL1/FL2 in Fig. 4.8) span the joint gap and function as deformation sensors. The two fiber lines (FL1/FL2) plus 3 fixture points (FP1/FP2/FP3) form a sensor block at the joint, and both fiber ends are extended to the BOFDA interrogator. In the lab experiment both the D-0.9mm and D-2mm optical fiber are attached to the fixed frame at the two sides of VP, front and back, to form two parallel sensor triangles, see Fig. 4.8.

(4) a number of displacement gauges. The measuring gauges include two dial gauges at the VP to measure vertical displacement ΔZ (indicated as VG1/VG2 in Fig. 4.7), and two dial gauges at the fixed platform (just in front of the BP) to measure horizontal displacement ΔY (indicated as HG1/HG2 in Fig. 4.8). All gauges have an accuracy of 0.01mm. The use of two parallel gauges can help to reduce tilting at each displacement step in each direction.
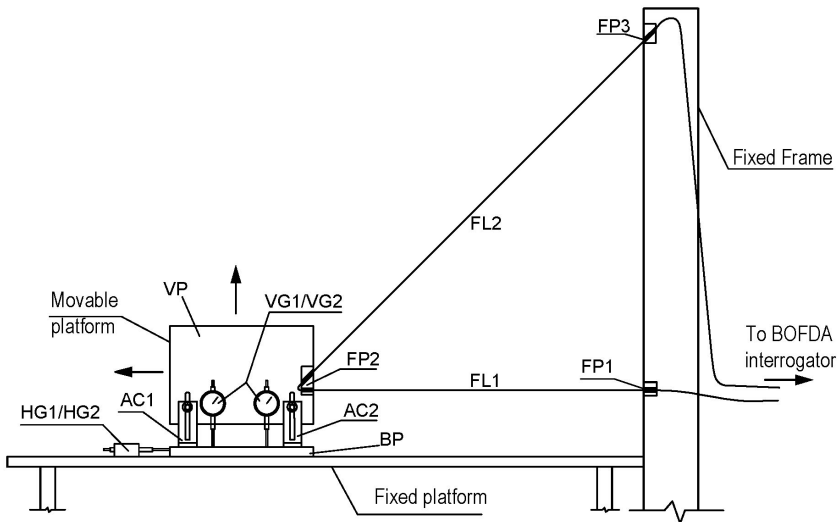
Figure 4.7: Joint model displacement test set-up
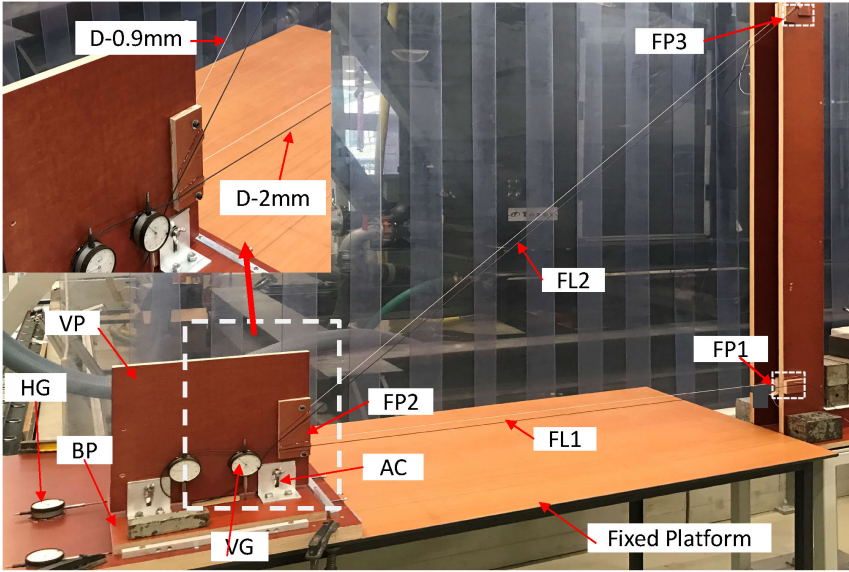
Figure 4.8: Lab verification experiment set-up

As this verification experiment is designed to verify future application of the designed sensor setup in the First Heinenoordtunnel, the parameter selection is kept consistent with the actual tunnel joint dimensions, where the immersion joint gap is between 1m to 1.4m wide. The parameters of the sensor block are listed in Tab.4.1.

Table 4.1: Parameters of joint model setup

Parameters	Value
Gauge length FL1	1200mm
Gauge length FL2	1693mm
Height difference h_0 at installation	1200mm
Anticipated joint displacement range	ΔY(-6mm,+6mm) ΔZ(-5,+5mm)

The movable platform is first set at a pre-strain displacement of 7mm to provide the initial installation status, and then moved forward or backward to simulate various deformation modes. Different combinations of joint opening and closure and differential settlement can be thus modelled. The imposed ΔY can be directly read on the two HGs. The vertical plate height can be adjusted to model joint differential settlements, and at each displacement step, the vertical displacement is read directly from the two VGs. Eq.4.1 to Eq.4.8 are used to transfer the measured Brillouin frequency shift to displacements. At each displacement step, the VP is first adjusted to impose a certain vertical displacement

(0mm,±1mm,±3mm,±5mm) and secondly a horizontal displacement is imposed to the BP with increments of 1mm.

4.4.2. Experimental results

The measured displacements from the optical fiber sensors are compared with the imposed displacements as obtained from the dial gauges, and potential errors are analyzed. First we analyze the results for strain combinations with an imposed downward vertical displacement of ΔZ = 0, 1, 3 or 5mm, where positive vertical displacement ΔZ indicates that FP2 moves downwards. The results of each loading step are shown in Fig. 4.9 to Fig. 4.14. ΔY_{ref} indicates the imposed (reference) displacement read from dial gauges, and negative ΔY values indicate a joint closure whereas positive values indicate joint opening or additional strain imposed on the fiber.

Fig. 4.9 shows the experimental results of the thin D-0.9mm optical fiber when ΔZ=5mm, and it can be seen that the measured ΔZ is smaller than the imposed 5mm, while the maximum gap is about 0.23mm (when ΔZ=4.77mm). For the joint opening and closure, a maximum relative error of 9% is detected when ΔY=1.09mm (ΔY_{ref} =1mm), and most displacement steps show a maximum relative error of below 3%, which indicates the measuring accuracy is acceptable for field monitoring. However, the D-0.9mm fiber is found very fragile and will not be adopted in the actual field test. Therefore, only the experimental results of the D-2mm optical fiber are further analyzed in detail here, as this type of fiber will also be used in subsequent field monitoring.
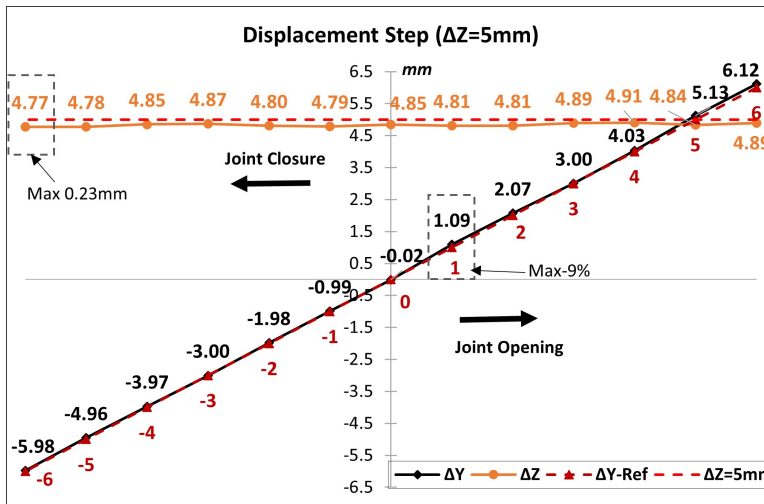
Figure 4.9: Measurement result comparison of D-0.9mm fiber (ΔZ=5mm)

The results for the D-2mm optical fiber are:

The reference test with ΔZ=0mm, where no vertical settlement is imposed, ΔY shows a maximum relative error of 4%, as shown in Fig. 4.10, when a measured ΔY=1.04mm is compared with the imposed displacement ΔY_{ref} of 1mm. This Figure also shows that when the bottom plate (BP in Fig. 4.8) is moved horizontally, the measured vertical

settlement varies a little, which indicates that second order effects neglected in the fiber strain derivation do play a role or that limitations exist that prevent from in keeping the lab setup completely horizontally aligned. A maximum error of 0.63mm is observed when ΔY_{ref} =6mm. However, it should be noted that, as this is the baseline, uneven settlement relative to this baseline measured in subsequent displacement tests is a more important indication of accuracy.
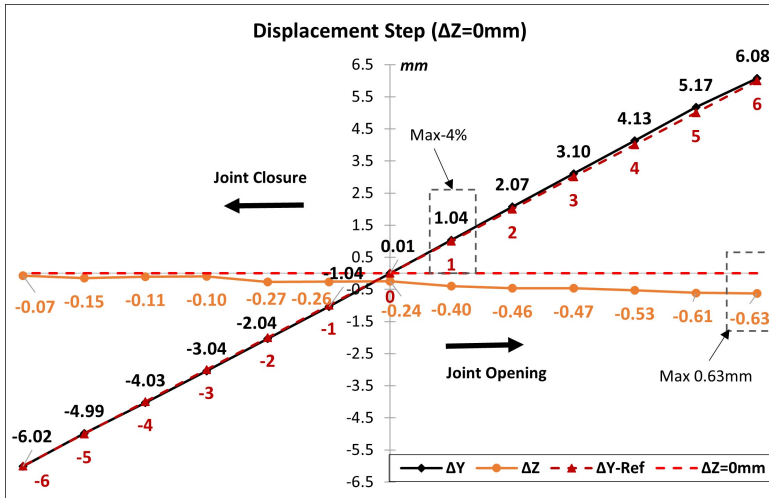
Figure 4.10: Measurement result comparison (ΔZ=0mm)

For ΔY=1mm, as shown in Fig. 4.11, a maximum relative error of 2.5% occurs, where an imposed displacement of 6mm compares to a measured 6.15mm. For ΔZ a maximum error of 0.18mm (relative error of 18%) is found when ΔY_{ref} =1mm, although for most values of ΔY, the absolute error in ΔY is within 0.1mm.

For ΔZ=3mm, as shown in Fig. 4.12, a maximum relative error of 2.8% is found, when an imposed displacement of -6mm is compared to a measured -5.83mm. For ΔZ a maximum error of 0.27mm (a relative error of 9%) occurs when ΔY_{ref} =-6mm, although for most ΔY the error in ΔZ is within 0.1mm.

For ΔZ=5mm, as shown in Fig. 4.13, a maximum relative error of 2.2% is found, when an imposed displacement of 5mm is compared to a measured 5.11mm. For ΔZ a maximum error of 0.25mm (5%) occurs when ΔY_{ref}=-6mm, while for most ΔY the error in ΔZ is within 0.20mm.

Secondly, we look at the impact of imposed upward vertical displacement of ΔZ = -1, -3 and -5 mm. Negative ΔZ indicates that FP2 moves upwards and a relaxation of the optical fiber FL2 with respect to the (downwards) pretensioned state results. The results of each displacement step are shown in Fig. 4.14 to Fig. 4.16.

For ΔZ=-1mm, as shown in Fig. 4.14, a maximum relative error of 3% for ΔY is found, when an imposed displacement of -2mm is compared to a measured -2.06mm. For ΔZ a maximum error of 0.17mm (17%) occurs when ΔY_{ref}=-1mm, while for most ΔY the absolute error in ΔZ remains within 0.15mm.
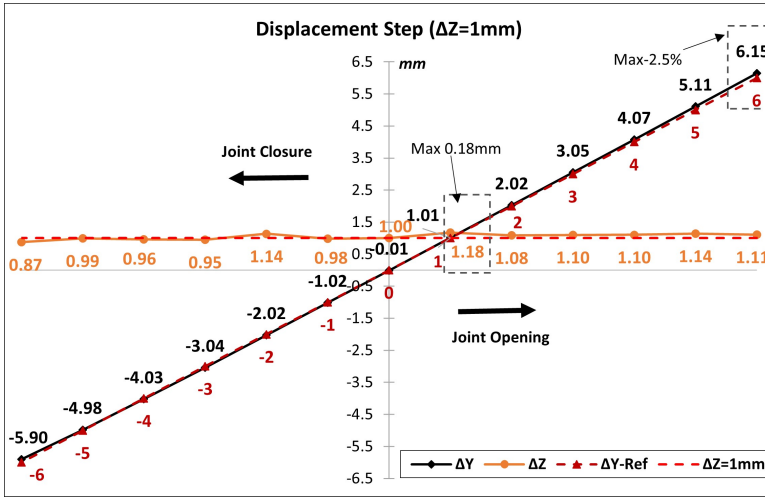
Figure 4.11: Measurement result comparison (ΔZ=1mm)
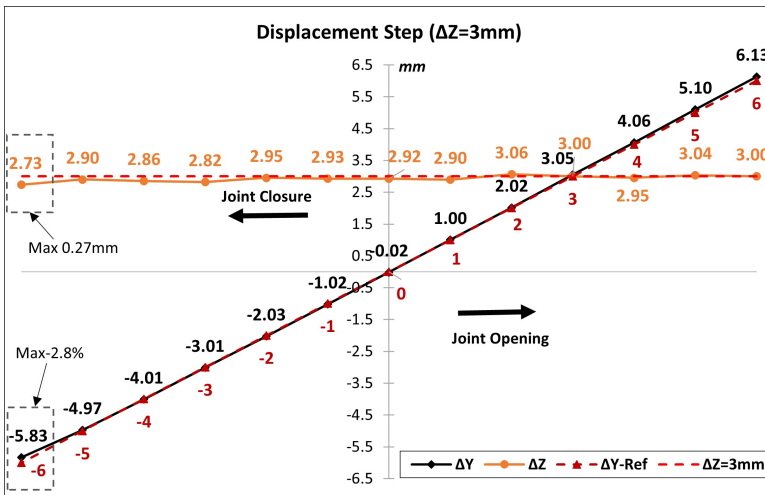
Figure 4.12: Measurement result comparison (ΔZ=3mm)

For ΔZ=-3mm, as shown in Fig. 4.15, a maximum relative error of 6% is found for ΔY, at an imposed displacement of -1mm compared to a measured -1.06mm. For ΔZ a maximum error of 0.18mm (6%) occurs when ΔY_{ref} =2mm, while for most ΔY the absolute error in ΔZ remains within 0.15mm.

For ΔZ=-5mm, as shown in Fig. 4.16, a maximum relative error of 2.4% occurs for ΔY at an imposed displacement of 5mm compared to a measured 5.12mm. For ΔZ a maximum error of 0.47mm (9.5%) occurs when ΔY_{ref} =-5mm, while for most ΔY the absolute error of ΔZ is within 0.3mm.
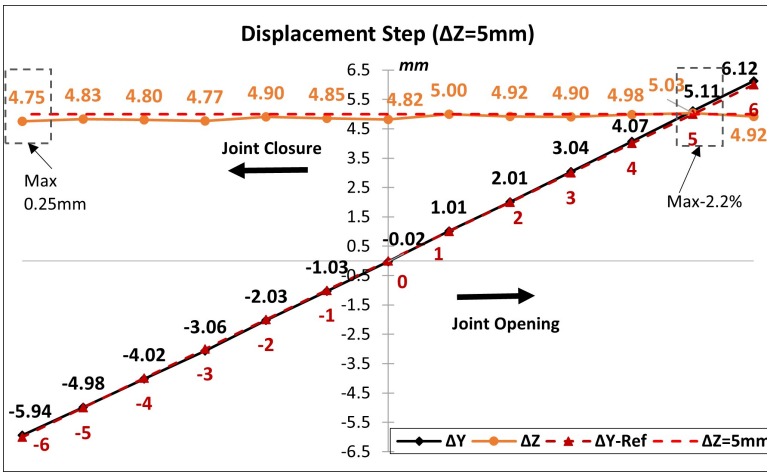
Figure 4.13: Measurement result comparison (ΔZ=5mm)
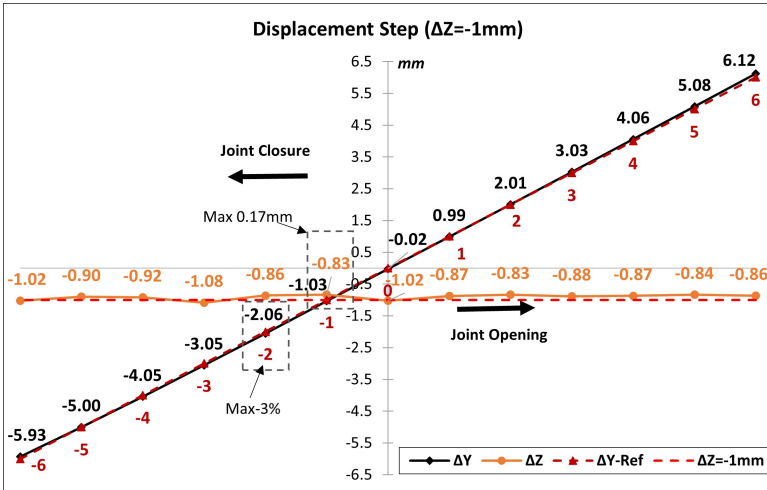
Figure 4.14: Measurement result comparison (ΔZ=-1mm)

4.4.3. GENERAL ACCURACY ASSESSMENT OF THE DESIGNED DOFS SYSTEM

From the lab experiment results we conclude the DOFS system can accurately detect two-directional joint displacements. But like any other type of sensor, measurement errors do occur. The results indicate a highly acceptable accuracy for measuring horizontal joint opening, as a maximum relative error of only 6% is found (for an imposed ΔZ=-3mm, ΔY=-1.06mm when ΔY_{ref} =-1mm). For most displacement steps, the relative error of ΔY remains below 2.5%. Under normal operational conditions where ΔY are expected to remain between -4mm and 4mm, the absolute error is smaller than 0.1mm, which means the DOFS can register relative joint openings as accurately as 0.1mm. Also, for
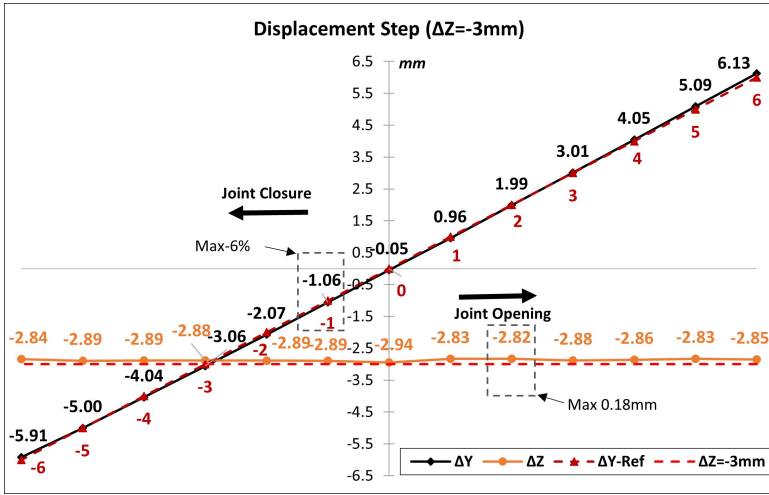
Figure 4.15: Measurement result comparison (ΔZ=-3mm)
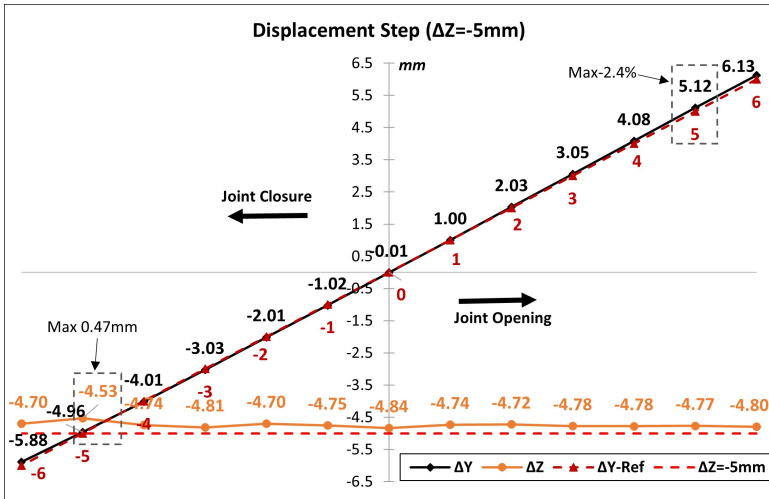
Figure 4.16: Measurement result comparison (ΔZ=-5mm)

extreme deformation conditions where ΔY is within the range of (-6mm, -4mm) and (4mm, 6mm), the observed maximum absolute error is 0.15mm (a relative error of only 2.5% when ΔZ=1mm, ΔY_{ref} of 6mm compared to a measured 6.15mm).

For vertical differential settlements, the results show a more significant error. Especially for a scenario with limited uneven settlements, where ΔZ=±1mm, the maximum relative error observed is 18% (when ΔZ=1mm while measured ΔZ=1.18mm). The maximum absolute error is found 0.47mm (a relative error of 9.5%), which only occurs when ΔZ=-5mm while the measured ΔZ=-4.53mm. However, for most imposed displacements,

the measured displacement has a relative error below 10%, and absolute error below 0.3mm, which is better than the reported accuracy of ±1mm for manual levelling measurements. Despite a careful check and the experimental setup being assembled as accurately as possible, errors in the setup still exist. These error sources include: (1) a possible difference between the actual length of sensing fiber and the designed length, especially for the inclined fiber line FL2; (2) a small inclination of the fixed platform, which means the BP may not move in an absolutely horizontal plane in the test; (3) a small tilting of the vertical frame (where FP1 and FP3 are bonded) or vertical plate (VP in Fig.4.7) under tension forces of FL2; (4) the stated accuracy of the BOFDA interrogator when collecting data. It should be noted that especially some limited tilting of VP and the vertical frame when imposing different displacement steps (which has been observed in the test) contributes most significantly to these errors, as the strain of FL2 is quite sensitive to even very small vertical movements caused by tilting. However, this error source is less likely to be present in the field tests, as the tensioned fiber will, of course, not be able to tilt the entire tunnel segment to which the fixture points are bonded.

In summary, the DOFS system is verified to have a more than acceptable accuracy and a good performance for subsequent field testing.

Of the two fiber types tested in the experiment, the D-2mm optical fiber physically proves to have a moderate axial stiffness of about 3kN, which can be pre-tensioned easily while still adequately resistant to external impacts or damage due to handling during installation, compared with the thin D-0.9mm fiber. Therefore, the D-2mm optical fiber is chosen for a subsequent field installation test in the First Heinenoordtunnel.

4.5. Sensor Installation at the First Heinenoordtunnel

4.5.1. Introduction of the first Heinenoordtunnel

The distributed optical fiber sensor (DOFS) system is installed in the First Heinenoordtunnel in Netherlands to show the applicability and robustness in field conditions. The First Heinenoordtunnel is a typical Dutch immersed tunnel and opened to service in 1979, see Fig. 4.17. It consists of five concrete elements each about 115m long, which in turn consist of six segments each about 19m long. The total length of the closed section is about 754m, with the immersed section 574m. The Heinenoordtunnel has 31 joints in total, including 25 dilation joints and 6 immersion joints, see Fig. 4.18.

Heinenoordtunnel features a typical Dutch segmented immersed tunnel in that : (1) it is a rectangular cross-section concrete tunnel; (2) each element is concreted segment by segment, with an embedded metal-rubber strip (typed W9Ui) as water barrier at dilation joint; (3) GINA gasket and OMEGA gasket are used as water-stop at immersion joint; (4) sand-flow method was used to form the foundation; (5) a closure joint (immersion joint) is formed by on-site concreting from inside tunnel.

Previous monitoring by manual levelling has shown that significant uneven settlement has occurred along the tunnel (NEBEST, 2016). Compared to the reference measurement in year 1978, the maximum settlement equals about 67mm at the middle of 1st element, and the minimum settlement is about 24 mm, which indicates a maximum settlement difference of about 43mm longitudinally according to the measurement results for 2018.

Figure 4.17: The Heinenoordtunnel under Oude Maas River (Rijkswaterstaat, 2022)
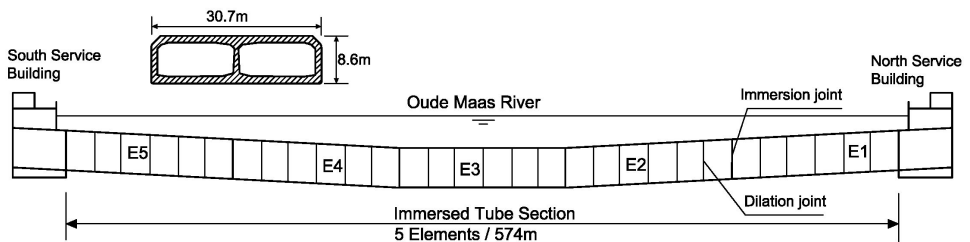
Figure 4.18: Side view of the Heinenoordtunnel

Only vertical settlement is monitored at a limited number of locations (next to each immersion joint and the center points of the elements) by conventional manual leveling with a minimum interval of 1 year.

After a service period of more than 50 years, structural integrity of the tunnel structure has become an issue and for several joints the watertightness is a point of concern, as at a two dilation joints leakage had been observed and were subsequently repaired by major maintenance (NEBEST, 2016). However, the dilation joints have not been monitored due to limitation of manual monitoring practice. Observations from similar immersed tunnels and room lab experiments show that seasonal temperature loading may negatively impact the structural safety, but no definitive measurements confirming or denying this behavior are available for the Heinenoordtunnel and a yearly or multi-year monitoring interval will not show such seasonal influences (Rahadian *et al.*, 2018). What's more, there is no central tube for utility and human evacuation in Heinenoordtunnel, which makes it not conveniently accessible for regular monitoring.

Therefore, the DOFS system is designed to instrument all the joints of First Heinen-oordtunnel and form a remote-controlled monitoring system which allows for high-frequency measurement while imposing no disturbance to tunnel service.

4.5.2. Field sensor installation

Field installation work

As there is no utility tube in Heinenoordtunnel, placing a sensor block at roof for three direction monitoring is not practicable (however, an escape tube is being constructed in the ongoing retrofitting work, which provides possibility for sensor block installation in future monitoring). What's more, according to previous field checks, joint opening and uneven settlement were observed while there is no sign of significant transverse drift displacement. Here only the sidewall was selected for sensor installation. Fig. 4.19 gives an impression of the sidewall of the west tube (North to South, from Rotterdam to Barendecht) which is to be instrumented with the DOFS system.

When determining the practical dimensions (gauge lengths) of the sensor layout in field application, the following issues have to be considered: the maximum working strain of the fiber, the anticipated joint deformation range to be sensed, the physical dimensions of the joints to be instrumented (for instance, the joint gap width that a fiber has to span). The immersion joints and dilation joints have different dimensions and hence two different types of sensing layouts are designed.
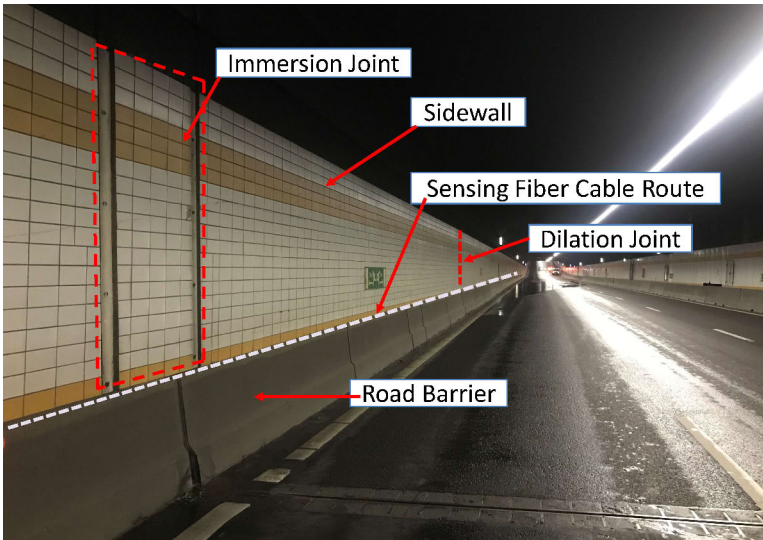
Figure 4.19: Sidewall of west tube to be instrumented by DOFS

A polyurethane sheath fiber type NZS-DSS-C07 with a diameter of 2mm was adopted as sensing optical fiber. This type of fiber has been experimentally verified (in Chapter3) with no sign of relaxation, and has a strain sensitivity of 48.55 MHz/0.1% and a maximum working strain of above 1.2%.

To form a sensor block, the optical fiber shall be fixed at three points on the wall, such that two pre-strained fiber lines (FL1 and FL2 in Fig. 4.5) cross the joint gap. However, it is difficult or even impossible to directly bond the small optical fiber onto the tunnel wall surface sufficiently accurate and leave a predetermined length of sensor fiber unbonded in between. The key problem is how to fix the fiber lines (FL1/FL2) as accurately as

possible, while imposing a designated pre-strain at the same time, see Fig. 4.20. In addition, considering that the time for field installation is limited by the short tunnel maintenance windows, which occur at night only to limit traffic hindrance, work flow efficiency is highly important so as to reduce field installation duration.

   To solve this dilemma, the optical fiber is pre-bonded to small pads at designated points, and thus assembled to form a sensor block, see Figure Fig. 4.20. The subsequent field installation will focus on fixing these pads at precise locations on the tunnel joints. In order to protect the bare sensor blocks and fibers on the wall, special cover boards have been made by cold-bending thin steel plate. These are installed over the sensors to fully isolate the sensor block from potential external impacts, see Fig. 4.20. It should be noted the fiber line 3 (FL3) in Fig. 4.20 is untensioned and aligned parallel to FL2 for sake of easy installation and protection. In each sensor block only FL1 and FL2 are pre-strained and function as joint displacement sensors. The field sensor parameters (gauge length and dimensions) are shown in Fig.4.5 and detailed in Tab.4.2.
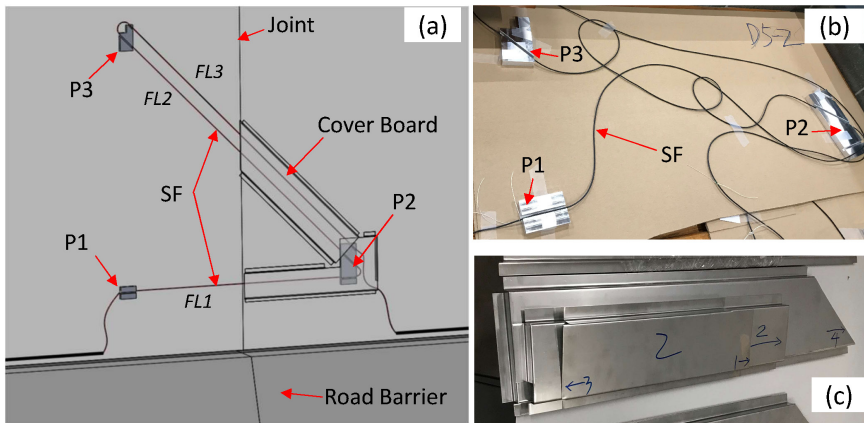
Figure 4.20: Field sensor installation plan: (a) field sensor block installation plan; (b) indoor optical fiber-pad assembly; (c) cover boards for fiber sensor protection (Note: SF as sensing fiber)

Table 4.2: Sensor parameters as used in field installation

Parameters	Immersion joint	Dilaiton joint
Gauge length FL1	1350mm	800mm
Gauge length FL2	1902mm	1127mm
Height difference h_0	1350mm	800mm

   The field installation in the First Heinenoordtunnel was limited to night tunnel closures with an effective working time of 3.5 hours to install a continuous fiber loop with 31 sensor blocks. The unstressed optical fiber cable between each joint is buried into a long PVC duct which is fixed on top of the roadway barrier, see Fig. 4.21. The two fiber cable ends are extended outside the tunnel at the North portal and plugged into the BOFDA

interrogator inside the service building. As the whole system can be remotely controlled, the installed DOFS system can obtain measurements at sub-hour or better intervals while imposing no disturbance to road traffic in the tunnel.

The installation procedure is robust enough to be handled even during the peak of the covid pandemic, although this has caused some delays and has put restrictions on the amount of personnel that could be used simultaneously to install the sensors. The first 13 joints (including 3 immersion joints and 10 dilation joints between) from north end were successfully instrumented in the first stage field work, and one starting data-taking (as a reference measurement) was conducted on December 11, 2020. The rest 17 joints are instrumented by June 11, 2021, and since then a complete optical fiber sensing loop covering the whole tunnel joints was formed. It should be noted the second dilation joint (from north) of the 5th element was not instrumented due to working space limitation.
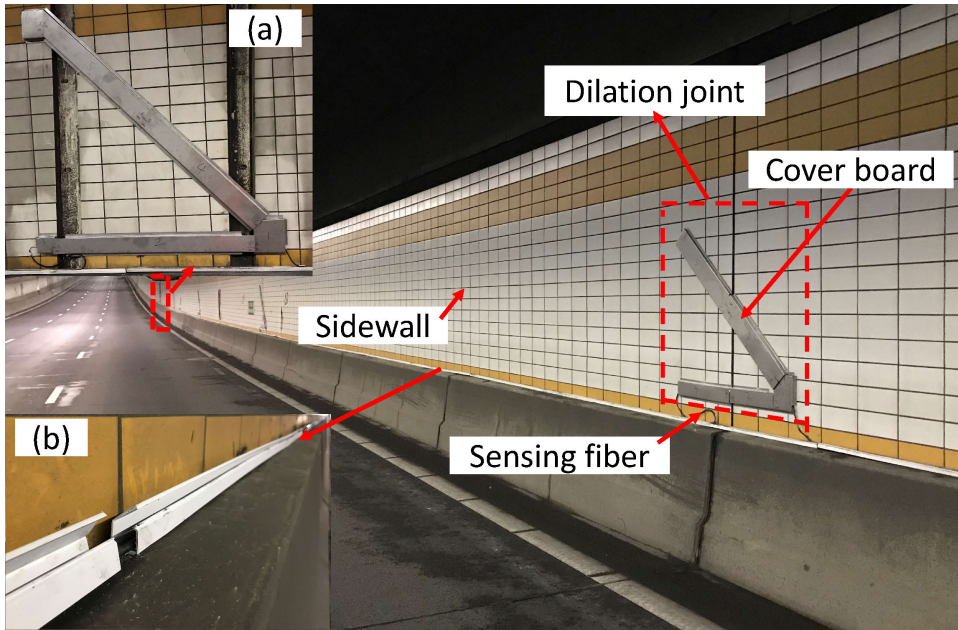
Figure 4.21: Finished fiber sensor installation in the First Heinenoordtunnel:(a) Sensor at immersion joint;(b) Loose fiber in PVC duct.

Field measurement

A BOFDA interrogator type fTB2505, is used to measure the Brillouin frequency shift. This BOFDA type has the same parameters as type fTB5020 as provided by fibrisTerre (2021). The BOFDA interrogator is connected to a computer with measurement management software installed, and in this way signal-processing and results analysis can be performed efficiently.

Fig. 4.22 shows an initial Brillouin frequency shift (BFS) measurement result of the installed DOFS monitoring system on December 11, 2020, which shows the designed system succeeds to generate data. The Fig. 4.22 represents a BFS sampling result of 13

joints (the first to the third immersion joint and 10 dilation joints between, from north portal). The local BFS peaks indicate the strained fiber lengths of each sensor block at the joint, while the interval loose fiber section (about 19m) stands for the zero-strain fiber length between each joint.

It should be noted that at a few joints the inclined fiber line 3 (as FL3 in Fig. 4.20) is imposed some tension due to some error in fiber-pad assembly work (see the BFS result of the second immersion joint in Fig. 4.23), although this does not affect the performance of the two sensing fiber lines (FL1 and FL2 in Fig. 4.20).

Fig. 4.24 shows a BFS sampling result of 30 joints (with 6 immersion joints and 24 dilation joints instrumented) on June 11, 2021, the starting of the second monitoring stage. A complete sensing network for the Heinenoordtunnel has been set up ever since. This installed DOFS system proves effective in monitoring joint deformation at sub-hour frequency, which further provides highly supportive information for subsequent tunnel behavior analysis.
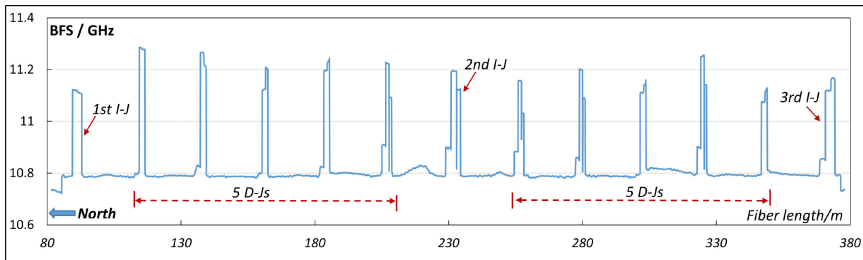
Figure 4.22: First BFS measurement result by DOFS in Heinenoordtunnel (I-J as immersion joint, D-J as dilation joint)
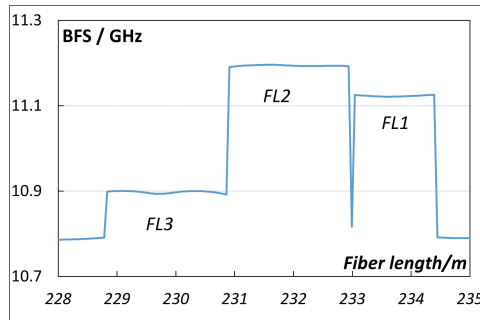
Figure 4.23: BFS result curve of sensor block at the second immersion joint

4.6. CONCLUSIONS

DOFS is able to measure continuously distributed strain and temperature along an optical fiber axis, and has a high potential in structural monitoring systems. A distributed optical fiber sensor has been designed to acts as a joint displacement monitoring system for an
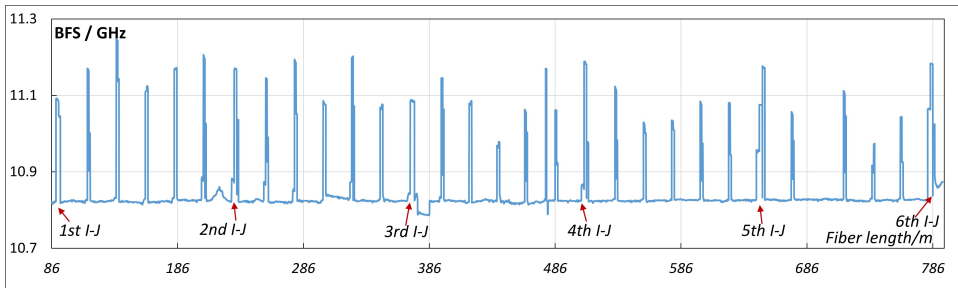
Figure 4.24: BFS measurement result of all instrumented joints by DOFS (I-J means immersion joint)

immersed tunnel.

The exact optical fiber sensor layout is designed based on the relation between measured fiber strains and the actual joint displacements. For the specific layout we designed, the accuracy has been verified by a lab experiment first. Results show it can effectively monitor two-directional joint deformations with more than acceptable accuracy. Sub-millimeter deformations of the tunnel can be well captured by the DOFS, and for monitoring of horizontal joint opening or closure, a maximum relative error of 6% (absolute error of 0.09mm) is found while in most cases the error remains below 2.5%. For vertical uneven settlement, in cases with small settlement deformations of ±1mm, the maximum absolute error observed in the lab experiments is 0.18mm, while for most cases the measured displacement has a relative error below 10% and an absolute error below 0.5mm. This study shows the DOFS system has an acceptable accuracy for joint displacement monitoring in field conditions.

Subsequently, the DOFS has been successfully installed to instrument both immersion joints and dilation joints at the First Heinenoordtunnel in the Netherlands, and data collection has started. Monitoring results for a full seasonal cycle showing the impact of temperature change on the tunnel construction will be available in the near future, but initial results show the system is capable of delivering daily (and even hourly) deformation readings for the instrumented joints. This shows a major improvement in the capabilities to monitor actual tunnel deformations in real-time.

REFERENCES

Bai, Y. & Lu, H. (2016). Damage analysis and rpair technology of omega gasket in immersed tube tunnel. *Journal of Railway Engineering Society* **33**, No. 9, 87–92.

fibrisTerre (2021). *User manual for fibristerre ftb series-fiber-optic sensing system for distributed strain and temperature monitoring (rev4.1)*. fibrisTerre Systems GmbH, Berlin, Germany.

Gavin, K., Broere, W., Kovačević, M. & de Haas, K. (2019). Investigation of the remaining life of an immersed tube tunnel in the netherlands. In *Tunnels and Underground Cities: Engineering and Innovation meet Archaeology, Architecture and Art*, CRC Press, pp. 4831–4838.

Gue, C. Y., Wilcock, M., Alhaddad, M., Elshafie, M., Soga, K. & Mair, R. J. (2015). The monitoring of an existing cast iron tunnel with distributed fibre optic sensing (dfos). *Journal of Civil Structural Health Monitoring* **5**, No. 5, 573–586.

Leeuw, L. (2008). Lekkage in tunnels-dilatatievoegen en beton. *Technical report*, RWS Bouwdienst.

Mohamad, H., Bennett, P., Soga, K., Mair, R. & Bowers, K. (2010). Behaviour of an old masonry tunnel due to tunnelling-induced ground settlement. *Géotechnique* **60**, No. 12, 927–938.

NEBEST (2016). Report-deformatiemeting-37h-312-01 heinenoordtunnel onder de oude maas.

Pelecanos, L., Soga, K., Elshafie, M., de Battista, N., Kechavarzi, C., Ye Gue, C., Ouyang, Y. & Seo, H.-J. (2018). Distributed fiber optic sensing of axially loaded bored piles. American Society of Civil Engineers.

Rahadian, R., van der Woude, S., Wilschut, D., Blom, C. & Broere, W. (2018). A new test setup for studying sand behaviour inside an immersed tunnel joint gap. In *Physical Modelling in Geotechnics*, CRC Press, pp. 443–448.

Rijkswaterstaat (2022). Photography of heinenoordtunnel at rijkswaterstaat website, netherlands. https://www.rijkswaterstaat.nl, accessed: June-2022.

Schwamb, T., Soga, K., Mair, R. J., Elshafie, M. Z., Sutherden, R., Boquet, C. & Greenwood, J. (2014). Fibre optic monitoring of a deep circular excavation. *Proceedings of the Institution of Civil Engineers-Geotechnical Engineering* **167**, No. 2, 144–154.

van Montfort, R. (2018). *Insufficiency of immersion joints in existing immersed tunnels: Case study on functioning of gina-seal and omega-seal in the kil tunnel.* Master's thesis, Delft University of Technology.

Wang, S., Zhang, X. & Bai, Y. (2020). Comparative study on foundation treatment methods of immersed tunnels in china. *Frontiers of Structural and Civil Engineering* **14**, No. 1, 82–93.

Wang, X., Shi, B., Wei, G., Chen, S.-E., Zhu, H. & Wang, T. (2018). Monitoring the behavior of segment joints in a shield tunnel using distributed fiber optic sensors. *Structural Control and Health Monitoring* **25**, No. 1, e2056.

Zhang, X. & Broere, W. (2022). Design of a distributed optic fiber sensor system for measuring immersed tunnel joint deformations. *Tunnelling and Underground Space Technology, Under review* .

5

BEHAVIOR OF IMMERSED TUNNEL UNDER DAILY TIDE AND TEMPERATURE VARIATION

The installed distributed optical fiber sensor (DOFS) system in Heinenoordtunnel can measure joint opening and uneven settlement simultaneously at high frequency of sub-hour interval. This chapter focuses on the interpretation of short-term (daily) joint deformation monitoring results. Measurements show the impact of tidal variations and temperature changes on the joint opening and the relative settlement differences between tunnel elements at sub-hour intervals. Analysis shows that the variation in joint opening is strongly correlated with temperature change, and the joint gap has a tendency to open at low temperature and to close at increasing temperatures. Simultaneously, the entire immersed section behaves more like a rigid body and moves upwards and downwards periodically due to tidal fluctuations in the river, with an observed vertical movement of slightly less than one millimeter. The tide also causes local tilting of tunnel segments, and this tilting behavior differs between winter and summer, which implies the (seasonal) temperature induced joint deformations affect the robustness of the tunnel to tidal loads. A numerical soil-tunnel structure interaction analysis reveals that the cyclic vertical movement of the tunnel is driven by retardation of the tidal wave in the deeper soil layers, which can be captured by a coupled flow model. This study provides new insights into short-term deformation behavior of immersed tunnels.

Parts of this chapter appear in Zhang & Broere (2022).

5.1. Introduction

With more and more concerns shown in tunnel safety, the short-term daily deformation behavior of immersed tunnel has become another important aspect in structure health monitoring. For example, thermal expansion of the segment due to daily or seasonal temperature change has been observed which may cause variation of joint opening and negatively impact the structural safety (Rahadian *et al.*, 2018; van Amsterdam, 2019), but monitoring with yearly interval fails to capture such deformation accurately. What's more, in some immersed tunnels it was estimated daily tide fluctuation (with a period of about 12 hours) causes cyclic vertical response of tunnel (Grantz, 2001a,b), but it is pitiful that tidal effects on immersed tunnel is rarely investigated due to low-frequency limitation of the present monitoring techniques.

The installed distributed optical fiber sensor (DOFS) system in the First Heinenoord-tunnel proves capable of measuring immersion and dilation joint deformation (joint opening and uneven settlement) at high frequency (with half-hour interval). Therefore, the field monitoring data by DOFS system makes it possible to look into the daily behavior of immersed tunnel under short-period impacts such as tide and daily temperature fluctuation.

This chapter focuses on the interpretation of daily deformation behavior of the Heinenoordtunnel based on field monitoring using DOFS system. In the rest of this chapter, the field data-taking will be firstly introduced briefly; secondly, the daily joint deformation behavior is studied based on measurement results, and tide impacts on tunnel structure longitudinally is specifically analyzed based on monitoring results; finally, the behavior of tunnel-soil domain under tidal impacts is investigated based on a 2-D numerical modelling. The results and conclusions in this study provide critical insights into daily behavior of immersed tunnel structure.

5.2. Field Data-taking at the First Heinenoordtunnel

5.2.1. Field Data-taking

The DOFS was used to instrument both the immersion and dilation joints at west tube sidewall, and this monitoring system is remote-control which imposes no disturbance to traffic in tunnel.

For clarity, here the joints are numbered firstly: Ij indicate the jth immersion joint from north to south end (see Fig. 5.1); while Dik represents the kth dilation joint (from north end) within the ith element (see Fig. 5.2). For example, I1 refers to the first immersion joint, while D12 indicates the second dilation joint (from north) within the first element.
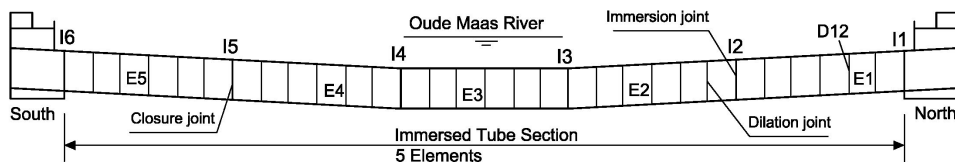
Figure 5.1: Joint numbering in the Heinenoordtunnel
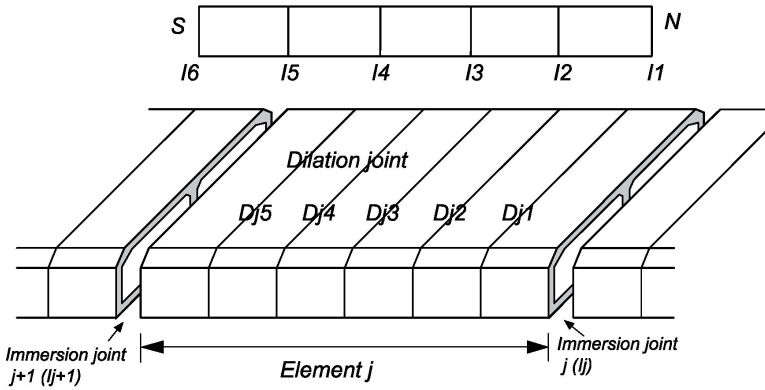
Figure 5.2: Joint numbering in the Heinenoordtunnel

With the installed DOFS system in the tunnel, two-directional joint deformation and temperature can be measured simultaneously at designated sampling intervals. For the first monitoring period, continuous data-taking with hourly periods started from the late afternoon of December 16, 2020, with 13 joints(I1 to I3, see Fig.5.1) being monitored; the second monitoring period started from June 11, 2021, with also the remaining 17 joints(D31 to I6, from tunnel center to south end, excluding D52) instrumented and incorporated. The data-taking frequency is set to be once per half hour, and hence 48 measurements are obtained daily per direction for each joint.

The BOFDA interrogator directly measures the BFS and interprets the fiber strain, while the fiber strain within a sensor block is subsequently transferred to joint deformation using Eq.4.1 to Eq.4.8 in Chapter 4. For an unstrained (zero-strain) fiber length, the measured BFS is theoretically only related to temperature effects. Therefore, at each joint, the BFS of a short unstrained fiber section (about 40cm long) directly adjoining the strained fiber lines (in a sensor block) is measured for temperature compensation, and in this way the temperature effects could be deducted from the total BFS of the tensioned FL1 and FL2 in Fig.4.20.

5.3. MONITORING RESULT ANALYSIS

As an initial verification of the accuracy of temperature measurements by the DOFS, the measured temperature of joint I1 (the north portal of Heinenoordtunnel) is compared with the outside temperature (daily mean, from Meteoblue (2022)) as observed by a nearby meteorological station in the Heinenoord area. The BFS of the unstrained fiber at reference temperature (T_0= 22.8°C) was measured before field installation, and the temperature measured at each joint in Heinenoordtunnel can be derived from Eq.5.1:

$$T = T_0 + \frac{(f_{t,i} - f_{t,0})}{C_T} \tag{5.1}$$

where C_T is the temperature sensitivity coefficient of the optical fiber (1.89 MHz/°C), $f_{t,0}$ indicates the BFS at reference temperature T_0; $f_{t,i}$ is the measured BFS at time interval i.

As shown in Fig. 5.3, the measured temperature results of the first 10 days in January 2021 follow the weather temperature, and the difference between the outside temperature and the temperature observed at joint I1 within the closed section of the tunnel near the tunnel portal stays within 1 °C, which indicates the temperature accuracy of DOFS system is acceptable.
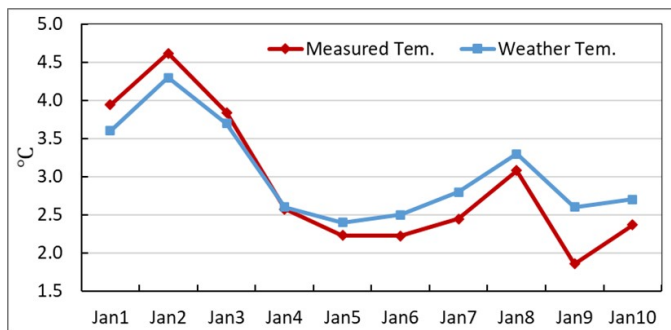
Figure 5.3: Measured temperature and weather temperature at joint I1

Monitoring results of two periods of three successive days each are analyzed below. The first period runs from December 17 to 19, 2020, which represents the first three days since monitoring of the northernmost 13 joints (from I1 to I3) started; the second period runs from June 12 to 14, 2021, which were the first three days since monitoring of all 30 joints (from I1 to I6) started. These two selected periods cover both a winter and summer season, which will help to indicate distinctions in daily tunnel behavior between different seasons.

5.3.1. Monitoring result in winter period

Temperature result in winter period

The observed temperatures at 13 joints from December 17 to 19, 2020, are shown in Fig. 5.4 to Fig. 5.6. In this period the data-collection frequency is set to once per hour. For each joint, the daily temperature fluctuation is captured, and there are differences in the observed temperatures between joints, but these differences lie within a range of 2 °C. The temperature at joint I3, the immersion joint furthest into the tunnel of the three immersion joints in this set is, most of the time, higher than the other two immersion joints. As shown in Fig. 5.4, the maximum temperature difference between joints at a given time amounts to 2 °C. The observed temperature at joint D13 is about 0.5 °C lower than that of the other 4 dilation joints in the first element, see Fig. 5.5; the temperature of D24 is 1.5 °C higher than that of the rest 4 dilation joints in the second element, see Fig. 5.6.

In addition, it can be seen from Fig. 5.4 that the temperature fluctuations within a daily period at different joints also show differences. For instance, at three immersion joints, the temperature fluctuation on December 18 is the most significant at I1 (the north portal), with a variation of approximately 5.8 °C during the entire day, while that of I2 ranks second for a total of change of 5.2 °C, and the temperature at I3 shows the smallest

fluctuation of 4.1 °C. As could be expected, the temperature further inside the tunnel tends to fluctuate less than that at the portal.
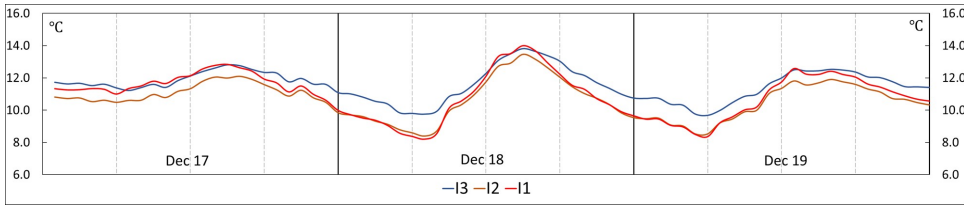
Figure 5.4: Measured temperature of three immersion joints (I1 to I3)
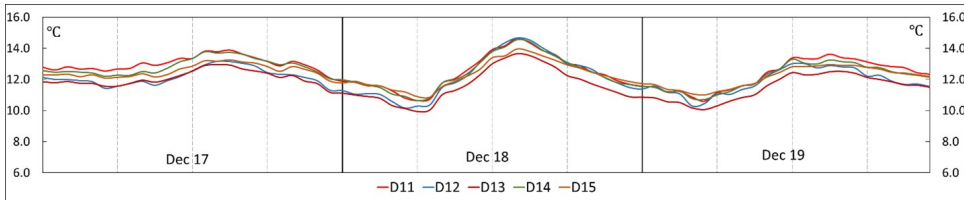
Figure 5.5: Measured temperature of five dilation joints within the 1st element
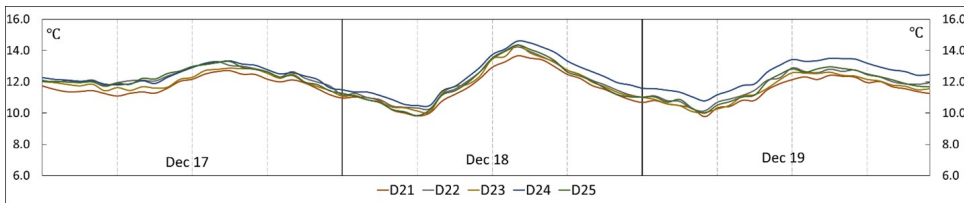
Figure 5.6: Measured temperature of five dilation joints within the 2nd element

JOINT OPENING IN WINTER PERIOD

As shown in Fig. 5.7, for joint opening if the fiber gets shorter, the strain change is negative and the joint closes compared to the baseline status (the first measurement on December11,2020), while a positive value shows joint opening. For joint uneven settlement, if the north side (of the joint) is assumed static, a positive settlement value indicates the an upward movement of south side, while a negative value indicates a downward settlement.

Fig. 5.8 to Fig. 5.10 show the joint opening between December 17 to 19, 2020. The negative sign indicates all the 13 joints close compared to the baseline status. Within a daily period, the joint opening show fluctuation, especially at joints I1, I3 and D11. As shown in Fig. 5.8, the joint opening of the 3 immersion joints is within a range of -0.6 to -0.3mm, with I3 showing a larger movement than I1 and I2. In Fig. 5.9 and Fig. 5.10, it can be seen joint D11 shows the largest opening (over a range of -0.8 to -1.3 mm) of all 13 monitored joints, while the opening of the other 9 dilation joints falls within a range of -0.25 to -0.5mm.
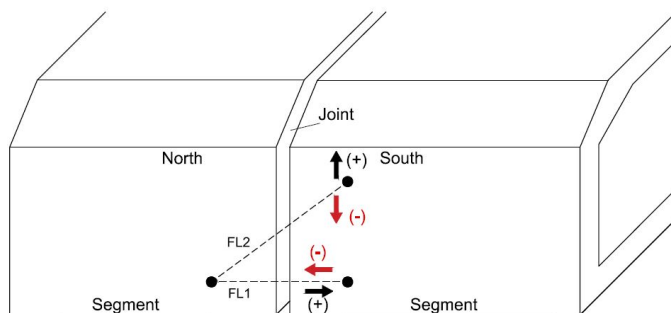
Figure 5.7: Joint deformation mode analysis (not to scale, viewed from outside tunnel)

Another significantly distinguishable aspect observed in the daily behavior at joint I1, I3 and D11, as shown in Fig. 5.8 and Fig. 5.9, are the two regular opening and closing cycles during a 24-hour period, which are attributed to the tunnel responding to tidal effects in the river. This aspect will be discussed in more detail in section 4.3.
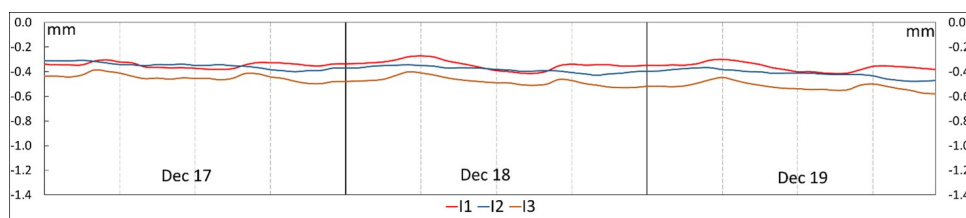
Figure 5.8: Measured opening of the three immersion joints
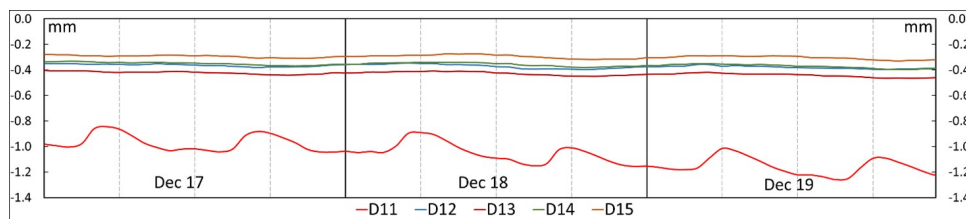
Figure 5.9: Measured opening of five dilation joints within the 1st element

JOINT UNEVEN SETTLEMENTS IN WINTER PERIOD

Fig. 5.11 to Fig. 5.13 show the measured uneven settlements over the joints between December 17 to 19, 2020. The results show that, except for joint D11 and D25, eight of the dilation joints show a negative uneven settlement (within a range of 0 to -0.12 mm) compared to the baseline status. This indicates that for most dilation joints the south side settles relative to the north side, which implies (if the tunnel segments are assumed to
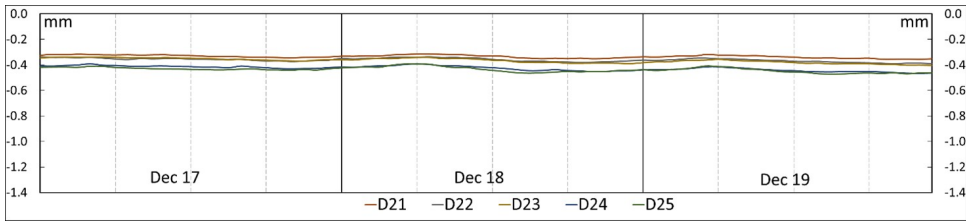
Figure 5.10: Measured opening of five dilation joints within the 2nd element

only displace vertically without tilting) there is a gradual increase of settlements from the north portal to the tunnel center.

Joint D11 shows a positive relative settlement of around 0.1mm, which could imply a relative upward movement at the south side, or tilt of the element at the north side which is relatively restricted at its other end by the northern tunnel abutment. Lacking detailed tilt measurement at this location, the distinction between these two possible deformation modes cannot be made based on these joint measurements alone. At joint D25, there is a similar deformation behavior, but with a smaller magnitude than at D11, limited to a range of -0.01 to 0.03mm.

Comparing the behavior of the three immersion joints, I1 exhibits quite distinct behavior as the settlement curve within a daily period shows two recurring peaks and troughs, with an amplitude of about 0.25mm; Joint I3 shows similar behavior, but at a reduced amplitude of about 0.05mm. For example, on December 17 the amplitude of the twice-daily movement of I1 is about 0.32mm, and for I3 is about 0.05mm.

Note that I1 forms the transition between the northern tunnel service building and the immersed section. As the northern tunnel entrance ramp and service building are founded on piles and have shown insignificant settlements over time (NEBEST, 2016), the measured troughs in Fig. 5.11 indicate that the immersed tunnel moves up and down periodically. This daily cyclic behavior is explained as the tunnel response to tidal effects and to be discussed in detail below.

When comparing the magnitude of the uneven settlements with the joint opening, it can be concluded that magnitude of joint opening is generally larger than that of the uneven settlements. For example, at joint D11 the joint opening varies within between -1.26 to -0.85mm, while the uneven settlement lies between 0.08 to 0.16mm. For all 12 joints except I1, the magnitude of the joint opening magnitude is larger than that of the uneven settlements, whereas at joint I1 the two deformation modes have a very similar magnitude during this monitoring period.

5.3.2. MONITORING RESULT DURING SUMMER PERIOD

Starting the early morning of June 11, 2021, also the second set of joints, numbered D31 to I6 (with the exception of D52) from the tunnel center to the south abutment, has been instrumented and monitored. Measurement of joint opening and uneven settlement for a total of 30 joints are available from that time onward. The result of the period between June 12 to June 14 are presented in Fig. 5.14 to Fig. 5.16. For clarity the measurements of all 30 joints are explicitly given in Append.A, but are plotted here as
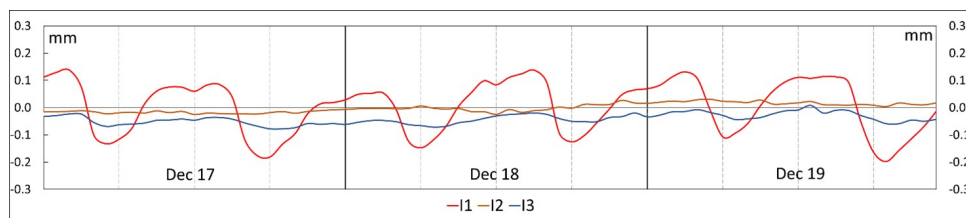
Figure 5.11: Uneven settlement of the three immersion joints
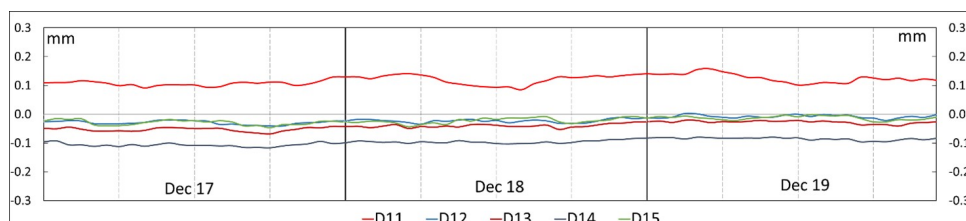
Figure 5.12: Uneven settlement of five dilation joints within the 1st element
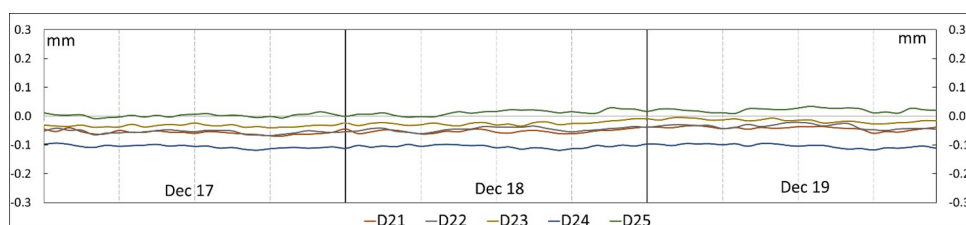
Figure 5.13: Uneven settlement of five dilation joints within the 2nd element

a complex of superimposed curves without individual labels. Fig. 5.14 to Fig. 5.16 still explicitly indicate what the general tendency of joint deformation behavior within a daily period is, as well as highlight the highly distinctive behaviors of certain joints.

The temperature results in Fig. 5.14 show there is a high consistency in the temperature fluctuation occurring at all joints, while a more detailed look into the data will reveal that further inside tunnel the temperature is slightly lower than the two ends during this summer period. Again, this is expected as the center of the tunnel is less exposed directly to sunlight and the tunnel structure will remain buffered from surface temperature fluctuations more the deeper the tunnel is located. The joint openings, during this period, lie within a range of -0.20 to 0.22mm. Between the 30 joints, joints I1, I2 and D11 show a more significant fluctuation than the other 27 joints. Comparing Fig. 5.14 and Fig. 5.15, it can be seen that the joint opening exhibits a correlation with temperature change, and a decrease in temperature generally corresponds to an increase of joint opening.

From the uneven settlement results, the most distinctive behavior is that two troughs of joints I1 and I6, which has also been shown in Fig. 5.11. Fig. 5.16 reveals that the troughs of I1 and I6 match quite well and repeat with a period of about 12 hours, while the settlement results of the other 28 joints do not show such cyclic behavior as signifi-

cantly (the measured uneven settlement at I6 is positive, but for a more straightforward comparison with the other joints its y-values are inverted in Fig. 5.16). Note that I1 and I6 are the immersion joints at the north and south end of the immersed section and form the transitions to the piled tunnel abutments. Considering the specific sensor installation at these two immersion joints, the regular troughs indicate the entire immersed tunnel section moves up and down cyclically, almost as a rigid body, with reference to the service buildings. This phenomenon is attributed to tidal effects in the river and will be discussed in section 4.3. Except for joint I1 and I6, the uneven settlement of the other 28 joints lies within a small range of -0.13mm to 0.1mm.
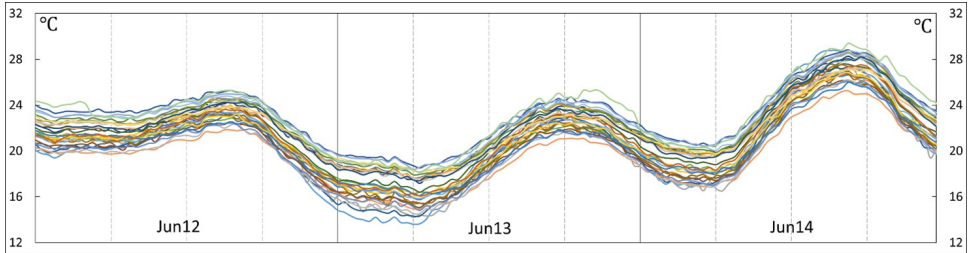
Figure 5.14: Measured joint temperature
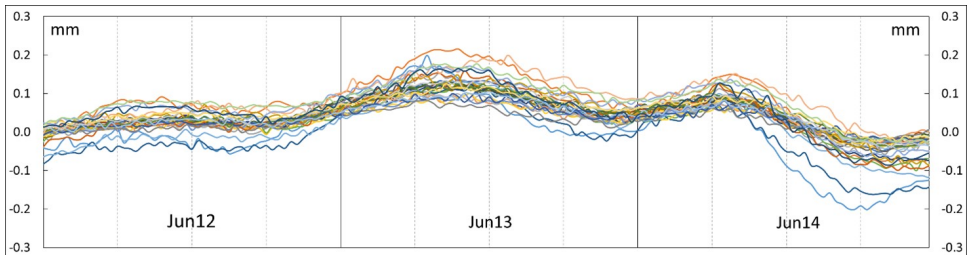
Figure 5.15: Joint opening result
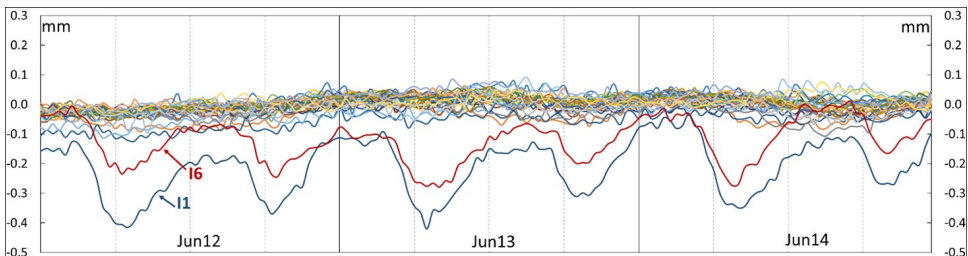
Figure 5.16: Joint uneven settlement result(y-values for I6 plotted inverted)

5.3.3. Correlation of joint deformation with temperature

The Pearson correlation coefficients between joint uneven settlements and joint openings on one hand and temperature (at joint) on the other hand have been calculated, and for joints I1 to I3 the results are shown in Tab.5.1 and Tab.5.2. The results for the other joints are listed in Apendix A.

As shown in Tab.5.1 (and Tab.A.1 in Appendix A), the opening of all joints shows a negative correlation with temperature. At several joints the correlation is distinctively significant, such as joints I1, D12, D21, D25, and D32. This indicates that the joint gap has a tendency to open at low temperature (like in a winter period), whilst it closes at high temperature (like in a summer period). The expectation that seasonal joint opening and closure occurs, driven by temperature change, is validated by the observations in the Heinenoordtunnel. It should be noted that during the first day (December 17) of the studied period, the correlation coefficients are significantly lower than for the two subsequent days. This is due to the fact that during this first monitoring day most joints still have low to negligibly low relative deformations, which magnifies the impact of any system errors (such as the influence of temperature effects on the observed fiber strain).

Table 5.1: Correlation coefficients of joint opening with joint temperature (I1 to I3)

Joint	I1	D11	D12	D13	D14	D15	I2	D21	D22	D23	D24	D25	I3
Dec17	-0.62	-0.20	-0.63	-0.32	-0.41	-0.30	-0.08	-0.59	-0.29	-0.48	-0.38	-0.56	-0.06
Dec18	-0.94	-0.75	-0.80	-0.52	-0.47	-0.32	-0.57	-0.70	-0.67	-0.64	-0.73	-0.88	-0.65
Dec19	-0.86	-0.56	-0.76	-0.68	-0.69	-0.57	-0.61	-0.77	-0.78	-0.74	-0.79	-0.90	-0.68
Jun12	-0.82	-0.23	-0.76	-0.48	-0.48	-0.22	-0.60	-0.58	-0.64	-0.46	-0.30	-0.71	-0.24
June13	-0.86	-0.56	-0.78	-0.59	-0.58	-0.54	-0.70	-0.67	-0.73	-0.62	-0.61	-0.72	-0.40
June14	-0.84	-0.69	-0.80	-0.72	-0.74	-0.70	-0.75	-0.81	-0.80	-0.75	-0.72	-0.82	-0.70

The correlation of joint uneven settlements with temperature (at joint) is listed in Tab.5.2 (and Tab.A.2 in Appendix A). It is clear that the correlation coefficients determined for each joint vary significantly. Of all 30 joints, 19 joints (for example D11, D14, D21) show a negative correlation during the entire representative periods, whereas for 2 joints (I3 and I5) the correlation remains positive, and for the other 9 joints it varies (and can be both negative and positive). Looking at each individual joint, it can be seen the correlation varies quite significantly with time, which means that the impact of the temperature on uneven settlements at the joints is not that significant, and clearly less significant than for the joint opening behavior. It should also be noted that the uneven settlement of most joints (except I1, I6 and D11) in the studied periods is quite small, within a range of -0.1mm to 0.1mm, and the accuracy of the correlation with temperature at several joints may be influenced by correction errors for temperature effects on the fiber strain.

5.3.4. Tunnel behavior under tidal Impacts

The daily cyclic behavior of the measured deformation at several joints, characterized by two regular peaks and troughs in the observed opening (see Fig. 5.8 and Fig. 5.9) and uneven settlement (see Fig. 5.11 and Fig. 5.16), has a roughly 12-hour period which is consistent with the tidal fluctuations observed in the River Oude Maas at the location of Heinenoord.

Table 5.2: Correlation coefficients of joint uneven settlement with joint temperature (I1 to I3)

Joint	I1	D11	D12	D13	D14	D15	I2	D21	D22	D23	D24	D25	I3
Dec17	0.21	-0.42	-0.36	-0.15	-0.42	-0.17	-0.68	-0.41	-0.11	-0.11	-0.58	0.01	0.10
Dec18	0.57	-0.71	-0.10	0.04	-0.40	0.69	-0.43	-0.03	0.67	-0.06	-0.66	0.68	0.81
Dec19	0.01	-0.90	0.03	-0.34	-0.58	0.15	-0.75	-0.35	0.08	-0.65	-0.70	0.48	0.07
Jun12	-0.13	-0.78	-0.73	-0.68	-0.46	-0.28	-0.39	-0.57	0.10	-0.44	-0.37	-0.32	0.00
Jun13	0.09	-0.76	-0.73	-0.69	-0.60	0.22	-0.13	-0.35	0.22	-0.50	-0.26	-0.36	0.75
Jun14	-0.07	-0.74	-0.89	-0.91	-0.74	-0.03	-0.62	-0.68	-0.31	-0.81	-0.66	-0.41	0.50

The Heinenoordtunnel lies inland within the estuary of the River Maas where the river is still influenced by the tidal fluctuation from the North Sea. The closest tidal measuring station is located at Goidschalxoord, approximately 4 km downriver, and shows a tidal variation between 1.1 to 1.4 m with the expected period of 12 hours and 25 minutes (Rijkswaterstaat, 2022); for instance, the measured tide on December 17 to 18 is demonstrated in Fig. 5.17. Tidal heights are given here with respect to the national reference level N.A.P. (in Dutch, Normaal Amsterdams Peil), which corresponds roughly to mean sea level.
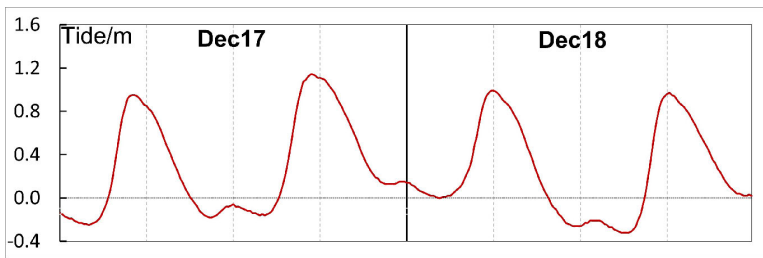
Figure 5.17: Tidal curve of Heinenoordtunel site (from Goidschalxoord station)

According to the measurement results shown in Fig. 5.8, Fig. 5.9, Fig. 5.11 and Fig. 5.16, both the joint opening and uneven settlements of some joints (mainly the immersion joints and D11) show a consistent twice-daily cyclic behavior which is closely linked to the tidal cycle. Fig. 5.11 and Fig. 5.16 reveal the significance of the tidal effects on the whole immersed section in vertical direction, while cyclic joint opening at D11 and I1 (in Fig. 5.8 and Fig. 5.9) indicates that the tidal impact probably also leads to tilting of some segments (such as the first segment bounded by I1 and D11). More specifically, the joint opening behavior of I1 and D11 implies that, at high tide one possible tilting mode is the tunnel segment rotates slightly in a clockwise direction, with the center of rotation at the bottom of D11, as shown in Fig. 5.18.

However, the measurements also show the tidal impact on the segment behavior differs between the different seasons. Fig. 5.19 details the joint opening behavior of D11 in summer and winter seasons compared to tidal levels (tidal data of December 17-18, 2020, and June 12-13, 2021 is highly similar and only the tidal data for December 2020 has been plotted). It can be seen that during the winter season (both in December 2020 and December 2021) the cyclic behavior of joint opening is much more pronounced
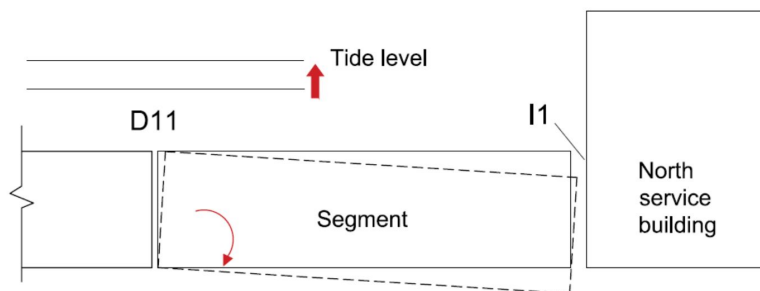
Figure 5.18: Possible tilting mode of segment under tide impact

than during the summer season in June 2020. As the measured joint opening indicates, joint D11 closes in summer and opens again in winter. This implies the seasonal joint deformation affects the robustness of the tunnel to tidal impacts. In addition, the Pearson correlation coefficients of joint opening and uneven settlement with tidal levels (based on a best-fit tide curve, further explained below) are listed in Tab.5.3 and Tab.5.4 (and Tab.A.3 and Tab.A.4 in Append.A). These coefficients show that during the winter period for most joints the joint deformations are more strongly correlated with tidal levels than that during the summer period. This also indicates that the tidal impact on the tunnel joint deformation varies between seasons.
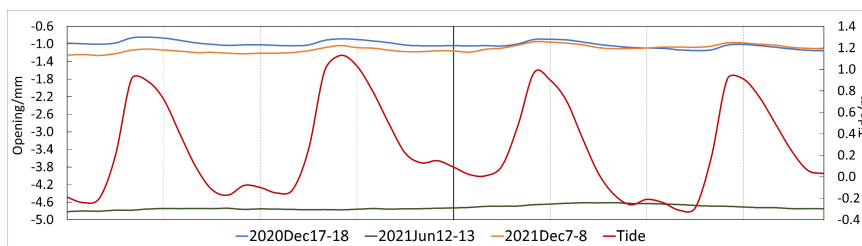
Figure 5.19: Joint opening of D11 with tide at different seasons

Table 5.3: Correlation coefficients of joint opening with tidal levels

Joint	I1	D11	D12	D13	D14	D15	I2	D21	D22	D23	D24	D25	I3
Dec17	0.75	0.86	-0.54	-0.58	-0.47	-0.66	-0.39	-0.37	-0.41	-0.31	-0.04	0.02	0.48
Dec18	0.71	0.72	0.07	-0.13	-0.14	-0.28	0.04	0.09	0.01	0.06	0.15	0.33	0.56
Dec19	0.52	0.77	-0.24	-0.42	-0.38	-0.46	-0.35	-0.13	-0.23	-0.11	0.01	0.08	0.42
Jun12	0.29	0.56	0.19	-0.07	0.03	0.08	0.03	-0.05	0.00	0.03	0.08	0.12	0.27
Jun13	0.24	0.21	0.17	0.03	0.03	0.02	0.03	0.02	0.05	0.08	0.14	0.13	0.16
Jun14	-0.09	-0.09	-0.11	-0.18	-0.20	-0.23	-0.20	-0.15	-0.16	-0.16	-0.18	-0.15	-0.13

Compared with local segment behavior, the response of the entire immersed section in vertical direction due to tidal variations is more consistent between both winter and summer seasons. As shown in Fig. 5.11 and Fig. 5.16 and discussed above, the monitoring

Table 5.4: Correlation coefficients of joint uneven settlement with tidal levels

Joint	I1	D11	D12	D13	D14	D15	I2	D21	D22	D23	D24	D25	I3
Dec17	-0.98	0.19	-0.83	-0.85	-0.64	-0.91	-0.30	-0.68	-0.91	-0.67	-0.63	-0.62	-0.81
Dec18	-0.98	0.67	-0.58	-0.44	0.02	-0.75	0.44	-0.52	-0.83	-0.15	0.00	-0.53	-0.64
Dec19	-0.98	0.30	-0.65	-0.70	-0.47	-0.93	-0.17	-0.77	-0.82	-0.48	-0.36	-0.69	-0.79
Jun12	-0.93	-0.19	0.21	0.12	0.08	-0.41	-0.22	-0.10	-0.28	-0.09	-0.01	-0.02	-0.30
Jun13	-0.96	-0.08	0.45	-0.01	-0.08	-0.26	-0.52	-0.30	-0.32	-0.14	-0.12	-0.18	-0.16
Jun14	-0.92	-0.24	0.12	0.01	-0.15	-0.14	-0.19	-0.28	-0.39	-0.10	-0.06	0.00	-0.15

results indicate that the whole immersed section behaves more like a rigid body and moves upwards and downwards periodically with the tidal variations.

Correlating the observed tunnel deformations to the tidal variations poses some additional issues. First, although the acquisition time of joint deformations obtained by the DOFS system is specified exactly, in reality this represents a series of measurements that has been integrated and averaged over a half-hour period. Secondly, the exact arrival time of the tidal wave at Heinenoordtunnel is not available, as the closest tidal station is located 4km downstream, and an estimated 13 minute time delay exists between high tide in the Oude Maas River at Heinenoord and at the tidal station, but a further time shift might exist between the moment of high tide and the maximum impact on the tunnel. For this analysis, a best-fit tidal curve is obtained by shifting the tidal curve in time with respect to the settlement measurements and maximizing the Pearson correlation coefficient between uneven settlement of I1 and tidal level.

To illustrate this, here the measurements from June 12 to 13 are analyzed and plotted in Fig. 5.20. On June 12, the first measurement of the settlements is registered at 00:09, while five different tidal curves with starting times from 22:00 June 12 to 0:00 June 13 are also plotted. The best-fit tidal curve is determined to be the one with starting time at 22:30, which represents a 99-minute delay with respect to the tidal station measurement at Goidschalxoord.
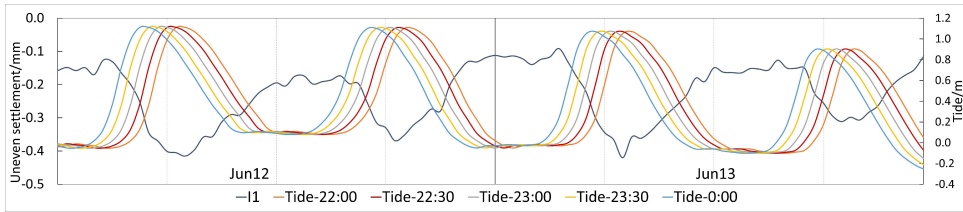
Figure 5.20: Determination of best-fitting tide curve

The joint uneven settlement results (of I1 and I6, from June 12 to 14) and the corresponding tidal curve are plotted in Fig. 5.21. The Pearson correlation coefficients of the settlements with tide are also shown in Tab.5.4 (and Tab.A.4 in Append.A), where it can be seen that joint I1 and I6 have a consistently high correlation (with an average of around -0.95 and -0.85, respectively) between observed uneven settlements and tidal fluctuations, which shows the significance of the tide on the tunnel response.

It is interesting to note that the immersed tunnel settles downwards with increasing

tidal level and returns upwards with decreasing tide, as shown in Fig. 5.22. And the amplitudes of the daily cyclic deformation (the maximum difference of uneven settlement within a daily period) of I1 and I6 are slightly different. For example, on June 12 the amplitude of this cyclic movement is about 0.30mm at joint I1 and about 0.24mm at joint I6. This implies the two ends of the immersed section show a slightly different response to tidal impacts.
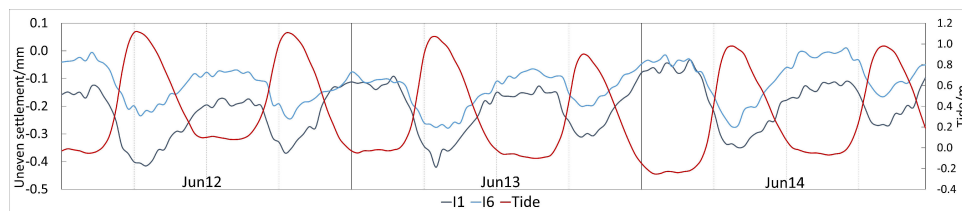
Figure 5.21: Uneven settlement of joint I1and I6 (y-values inverted) with tide (June 12 to 14)
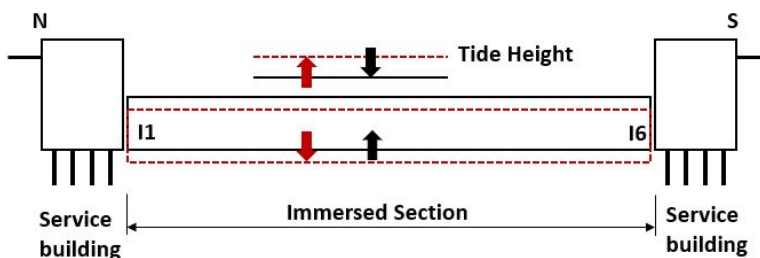
Figure 5.22: Schematic of cyclic movement of Heinenoordtunnel under tidal impact

In order to quantitatively assess the impacts of the tide on the tunnel, the sensitivity index η is defined as in Eq.5.2:

$$\eta = \frac{\Delta s}{\Delta h} \tag{5.2}$$

where Δs is the amplitude of uneven settlement within a period, which is equal to the (absolute) difference between the maximum and minimum joint uneven settlement; while Δh indicates the tidal amplitude which equals the (absolute) height difference between the highest and lowest tidal level.

The sensitivity index η indicates the sensitivity for uneven settlement changes (or the measured tunnel vertical deformation) when subjected to a tidal height change. The sensitivity indices corresponding to periods of December 17 to 20, 2020 and June 12 to 15, 2021 are shown in Tab.5.5. It can be seen that, for the period of June 12 to 15, the sensitivity index of I1 (with a four-day average of 0.265) is slightly larger than that of I6 (with a four-day average of 0.225), which means the tide has a higher impact on the north side of immersed section. Also, for joint I1 the tidal sensitivity exhibits a very small variation between seasons, as in the winter period η has a four-day average of 0.232

compared to 0.265 in the summer period. This also implies the tunnel response due to tidal impacts varies with seasons.

Table 5.5: Sensitivity of tunnel vertical deformation to tidal variation

Parameter		Dec 17	Dec 18	Dec 19	Dec 20	Jun 12	Jun 13	Jun 14	Jun 15
Δh (m)		1.37	1.25	1.31	1.24	1.16	1.17	1.23	1.23
Δs (mm)	I1	0.32	0.28	0.33	0.27	0.30	0.33	0.32	0.32
	I6					0.24	0.23	0.30	0.30
η	I1	0.23	0.23	0.25	0.22	0.26	0.28	0.26	0.26
	I6					0.21	0.19	0.25	0.25

A periodic vertical movement of a tunnel due to tidal effects has also been monitored and reported by Schotte *et al.* (2016) for the Liefkenshoek rail tunnel. Although this is a bored tunnel under the River Scheldt in Belgium, the tunnel shows a similar cyclic movement under tidal variations, which are more pronounced at Liefkenshoek than at Heinenoord. However, they provide no theoretical analysis or numerical simulation study for this phenomenon of a fully submerged body responding to variations of the water level.

NUMERICAL SIMULATION

In order to simulate the observed vertical response of the tunnel due to tidal level variation, a 2D finite element model is built in PLAXIS 2D (Bentley, 2022). This model can simulate the groundwater flow and consolidation behavior of the soil during the relatively short-term construction period, the long-term operation phase and during a tidal cycle. For the behavior of the soil under transient tidal impacts, both coupled flow and consolidation process will be simulated. Here the Biot's 2D consolidation theory is used to model the coupled flow and consolidation process. Biot (1941) established the governing equations describing the coupled flow and consolidation of soil, as in Eq.5.3 to Eq.5.5:

$$\frac{k}{\gamma}\nabla^2 p = \frac{n}{K'}\frac{\partial p}{\partial t} + \frac{\partial \varepsilon_v}{\partial t} \tag{5.3}$$

$$\frac{\partial p}{\partial x} = G\left[\nabla^2 u + \frac{1}{1-2v}\frac{\partial \varepsilon_v}{\partial x}\right] \tag{5.4}$$

$$\frac{\partial p}{\partial z} = G\left[\nabla^2 w + \frac{1}{1-2v}\frac{\partial \varepsilon_v}{\partial z}\right] \tag{5.5}$$

where k is the permeability of soil, n is the porosity; K' is the bulk modulus of water; γ is the saturated unit weight of water; p is the pore pressure of soil; G is the shear modulus of soil; v is Poisson's ratio; and ε_v is the volumetric strain of porous medium, which is expressed in the below Eq.5.6.

$$\varepsilon_v = \frac{\partial u}{\partial x} + \frac{\partial w}{\partial z} \tag{5.6}$$

where u and w are the horizontal and vertical displacement of soil respectively.

In PLAXIS 2D software, Biot's 2D transient equation under pre-defined boundaries and for varying soil layers can be solved, and the time-history of pore water pressure development and soil deformation can be obtained (Bentley, 2022).

In this numerical simulation, the soil domain has a dimension of 300m wide and 50m high, while the tunnel cross-section itself is 30.7m wide and 8.60m high, as shown in Fig. 5.23 (the different colors indicate different soil layers as listed in Tab.5.6). Of course the exact depth of the tunnel cross-section varies along the longitudinal gradient. For this case the tunnel bottom level of the transverse section at the middle of the first element (from the north) is chosen, which lies at about -13m NAP. A 1m-thick sand layer below tunnel floor slab is used to simulate the sand flow foundation, and the backfill covering the tunnel top and two sides is modelled as a sand layer.
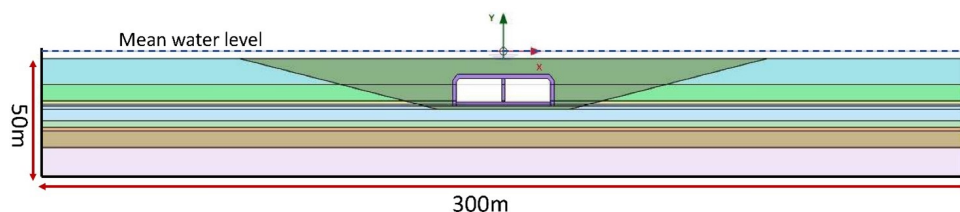
Figure 5.23: The modelled tunnel-soil domain

The soil parameters for each soil stratum are obtained from a site investigation report of the Second Heinenoordtunnel (TCH, 1995). This bored tunnel was constructed in 1996 directly parallel to the immersed First Heinenoordtunnel, at a distance of about 80m, and far more detailed site investigation data is available from this project compared to the original immersed tunnel design reports from 1964 (NEBEST, 2016). From this site investigation, the approximate soil profile for the first immersed tunnel element is listed in Tab.5.6. The soil strata beneath the other elements are generally quite similarly to those in Tab.5.6, although slight variations occur longitudinally along the tunnel.

Table 5.6: Site soil parameter information

Depth (NAP)	Geological Unit	Unit weight (kN/m^3)	Friction angle (°)	Cohesion (KPa)	$E_{50.ref}$ (MPa)	$E_{ode.ref}$ (MPa)	$E_{ur.ref}$ (MPa)	Permeability (ms^{-1})
-2.25 – -10m	Sand mixed with single layer of clay	20	37.8	0	28	28	140	2.47×10^{-5}
-10 m – -15m	Moderate Dense Clean Sand	21	41.1	0	22.3	22.3	111.9	5.85×10^{-4}
-15m – -16 m	Clay	21	28.3	17.51	10.6	5.3	53	9.03×10^{-10}
-16m – -21 m	Moderate Dense Clean Sand	21	40.5	0	50	50	250	5.18×10^{-4}
-21m – -23m	Moderate Dense Clay	21	26.8	13.39	8.2	4.1	40.8	6.48×10^{-10}
-23m – -24m	Clay	21	25.9	10	13.9	6.9	69.7	3.08×10^{-10}
-24m – -29m	Silty Clay (Over-consolidated)	21	31.1	30	42.3	21.16	211.7	1.00×10^{-9}
-29m – -38m	Moderately Dense Sand (With few embedded clay layer)	21	38.4	0	30	30	152	7.69×10^{-5}

The bottom of the soil domain is set as an impermeable boundary (as the geological

investigation reveals an over-consolidated clay layer below); the top boundary (riverbed) is set as permeable with a head equal to the designated tidal level; at the two side boundaries, both dynamic head (equal to the dynamic hydrostatic water pressure, for the upper sand layers, between -0.25 to -21m) and seepage boundary conditions (for the lower clayey layers, between -21m to -38m) are specified. The tidal variation is simulated by setting a user-defined time-history series of tidal levels as the piezometric head of the free water table at the top of the model. For this case study, the measured tidal levels of June 14, 2021 are used (see Fig. 5.23). The concrete tunnel structure is modeled as a non-porous medium, with unit weigh of 25kN/m^3, a void ratio of 0.03, Poison's ratio of 0.2 and an elastic modulus of 30GPa.

In initial construction stage, dredging the trench removed the upper 9-10m thick soil layers, which caused a significant unloading to the underlying soil layer. In the subsequent construction stages, the soil was reloaded but to a lower stress level than initial. Here the Hardening Soil (HS) model (Schanz *et al.*, 2019) is used, as it captures the unloading-reloading behavior of the soil from the initial construction to the long-term operational period. In the tide impact simulation, the top boundary water head is set to follow the tie tide level, see Fig.5.24.
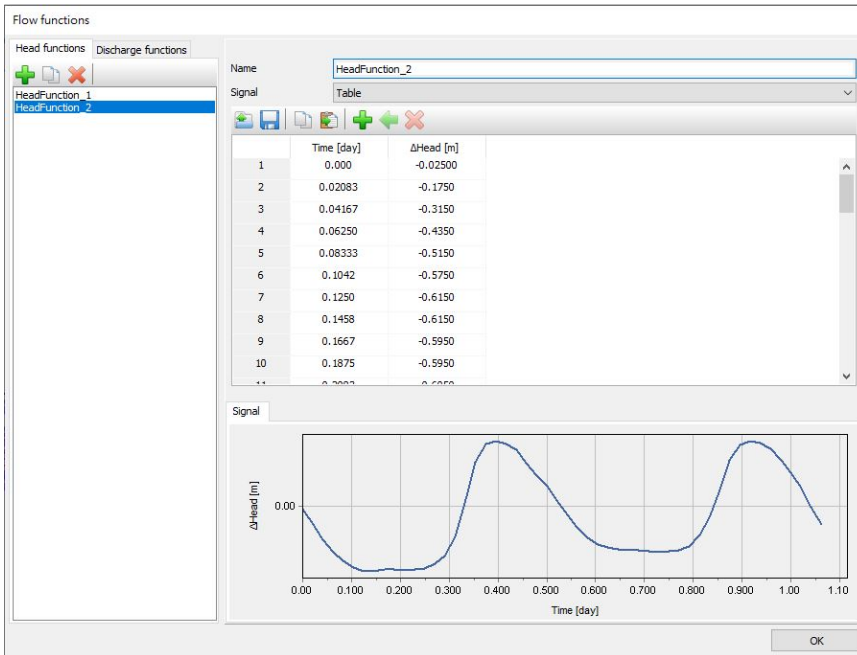
Figure 5.24: The input tidal level in simulation

The simulation results are shown and discussed specifically subsequently. Fig. 5.25 shows the deformation of the tunnel-soil domain at low tide level (with tide height of -0.595m below mean water level), and the settlement at tunnel bottom about +0.24mm. Fig. 5.26 shown the deformation of tunnel-soil domain at the first tide peak (with tide
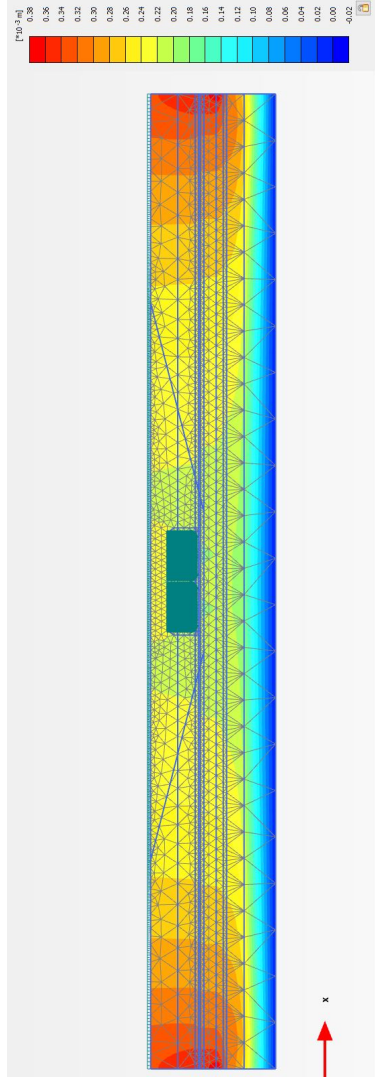
Figure 5.25: The vertical deformation of tunnel-soil domain at low tide level
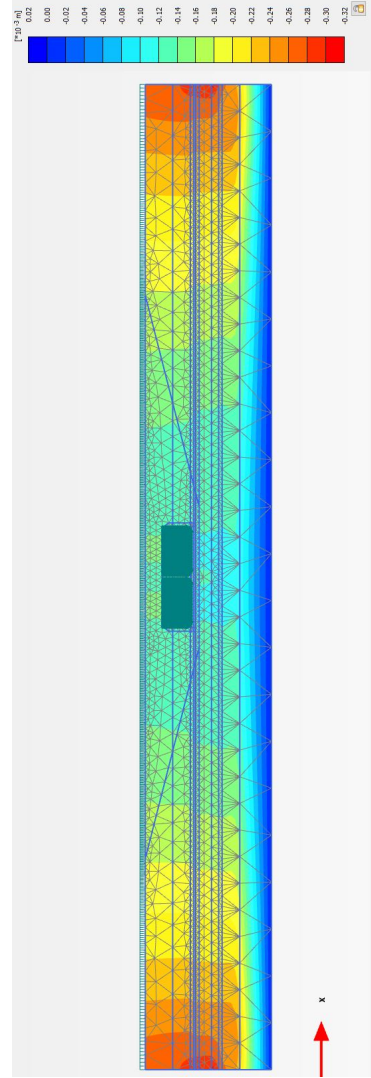
Figure 5.26: The vertical deformation of tunnel-soil domain at high tide level

height of +0.595m above mean water level), and the settlement at tunnel bottom is about -0.12mm. Due to boundary effects of the prescribed variable head at the sides, the soil shows a slightly larger deformation than in the center close to tunnel, which is the area of interest for this study. Close to the tunnel (about 90m left and right of the tunnel walls), the settlement results are stable.

The simulation results are compared to the measured uneven settlement of I1 in Fig. 5.27. For comparison, the measured and simulated settlement results are presented relative to the first measurement point (on June 14). It can be seen that the phenomenon of cyclic vertical movement of the tunnel under tidal impacts is captured well in the numerical simulation, and the two curves show a highly consistent behavior, although the calculated vertical response of tunnel (with amplitude of about 0.41mm) is larger than the measured result from the DOFS sensor (with amplitude of about 0.33mm), which may be attributed to the uncertainties in soil parameter determination.
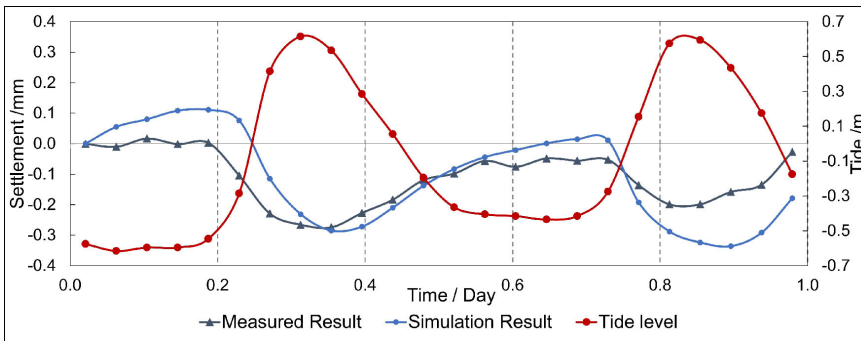
Figure 5.27: Comparison of simulated and measured tunnel response under tidal impacts

As shown in Fig. 5.27 there is a phase lag between the simulated settlement curve and the input tidal curve, with a time delay of about one hour. In order to investigate the possible delayed response of the tunnel and soil at the actual site, the tidal curve at Heinenoordtunnel should be determined and compared with the measurements. In Fig. 5.28 the water levels (on June 5, 2022) at Goidschalxoord (4km downstream) and Dordrecht (12km upstream) stations are plotted, and the tidal wave travel time can be estimated as approximately one hour. As the Heinenoordtunnel is located between Goidschalxoord and Dordrecht, it is reasonable to conclude that the delay of the tidal curve between Heinenoord and Goidschalxoord is less than one hour. The measured daily settlement curve (peaking at 00:09, June 14) fits most closely with the tidal curve that shows high tide at 22:30 June 13 at Goidschalxoord. Therefore, the arrival of high tide at Heinenoordtunnel falls between 22:30 and 23:30, and the delay of the tunnel response is estimated to fall between 39 and 99 minutes. This is consistent with the simulation result, which predict a delay of about 60 mins.

The excess pore water pressure within the soil domain at low and high tide levels are respectively shown in Fig. 5.30 and Fig. 5.31. It can be seen that in the upper soil layers (-2.25m to -24m, mainly sand layers) excess pore water pressure generated by tide fluctuation is insignificant. However, within the thick clay layer (-24 to -29m) and the
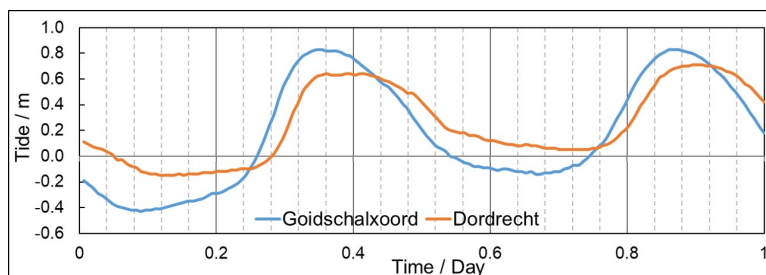
Figure 5.28: Tidal curve comparison between Goidschalxoord and Dordrecht stations

bottom sand layer (-29 to -38m), the resultant excess pore water pressure is significant. At low tide Fig. 5.32 shows a maximum excess pore pressure of about 2.8kPa within the clay layer and about 2.1kPa in the bottom sand layer. Fig. 5.30 indicates a maximum of about -5.6kPa within the clay layer and about -4.8kPa within the sand layer at high tide. At low tide, the lower soil layers (clay and bottom sand) bounce back, and water flows into these layers which results in a positive excessive pore water pressure, while at high tide, the soil layers are compressed and water is squeezed out which leads to a negative excessive pore water pressure. In Fig. 5.31, the excess pore water pressure results within the clay (the layer middle point, below tunnel at -26.49m NAP) and sand layer (the layer middle point, below tunnel at -32.27m NAP) are also plotted, and it can be seen the excess pore water pressure shows a cyclic variation with tidal fluctuation.
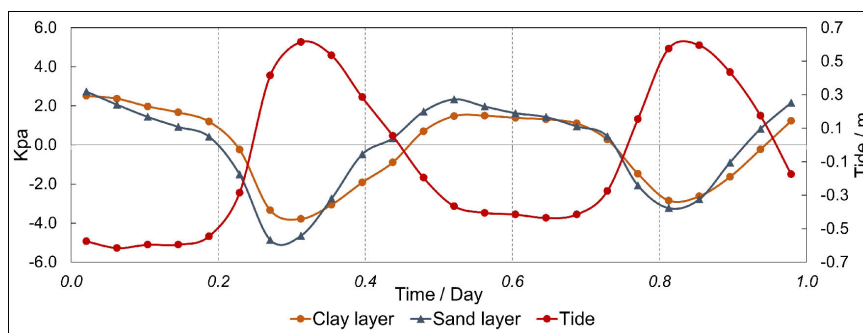
Figure 5.29: Excess pore water pressure fluctuation with tide fluctuation

In addition, the simulation results demonstrate the majority of soil deformation under tidal loads occurs in the thick clay layer (-24 to -29m) and the bottom sand layer (-29 to -38m). Fig. 5.32 displays the vertical distribution of compression and the excess pore water pressure within the soil profile at the high tide. The most significant compression occurs in the bottom sand layer and the thick clay layer, while for the upper sand layers both deformation and excess pore water pressure development are insignificant. Fig. 5.33 displays the compression deformation curve of these two layers under tidal fluctuation, and it can be concluded these two layers are more tide-sensitive than the shallow sand
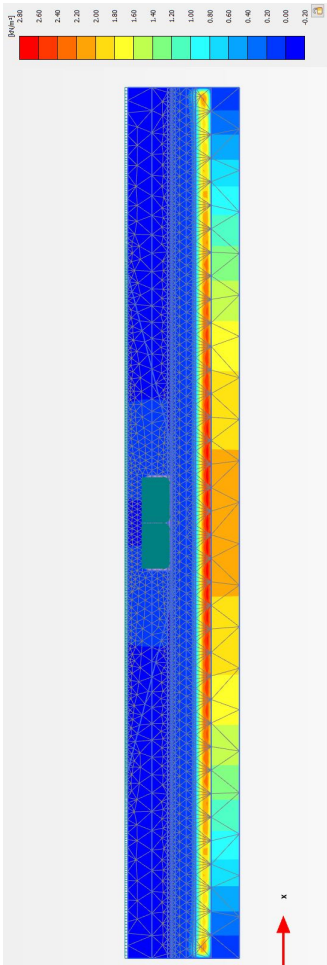
Figure 5.30: Excess pore water pressure within soil domain at low tide level
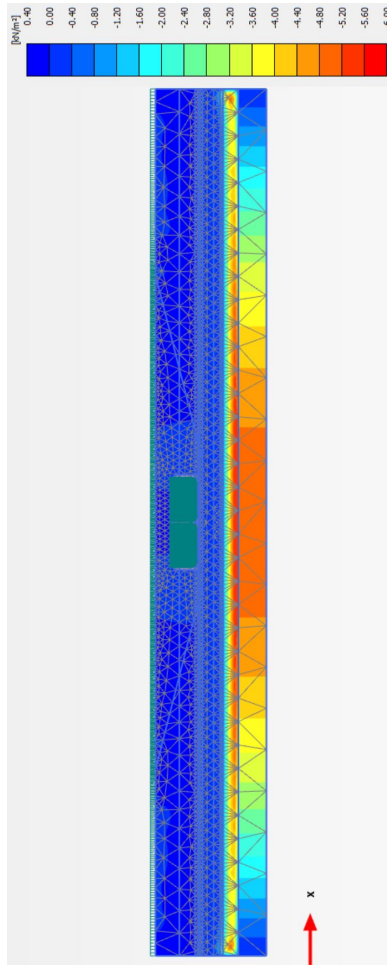
Figure 5.31: Excess pore water pressure within soil domain at high tide level
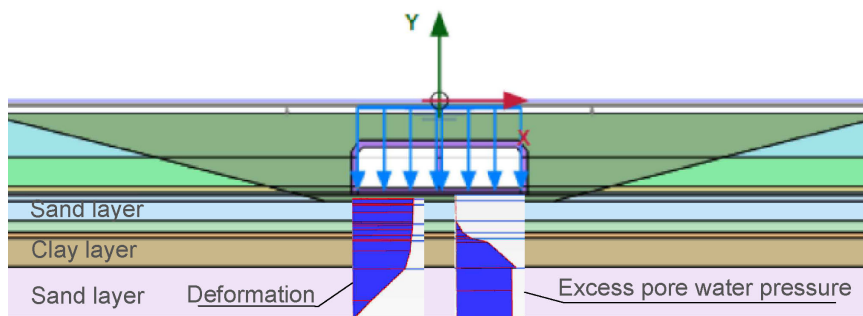
Figure 5.32: Compression and excess water pressure gradient within soil profile
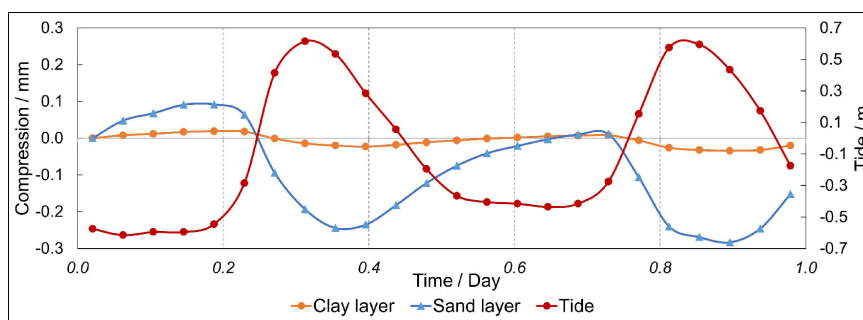
Figure 5.33: Soil layer compression with tide fluctuation

layers and they contribute dominantly to the the cyclic response of soil domain under tidal fluctuation.

Similar simulations have been made for the transverse cross-sections of all five tunnel elements (E1 to E5) taking into account the local variation in soil layers and the depth of the tunnel, and the tunnel settlement results are shown in Fig. 5.34. It can be seen that the periodical vertical movement of all five elements under tidal impacts are quite consistent, with only minor differences (the uneven settlement) between two adjoining elements compared to their individual absolute settlement. This is consistent with the monitored tunnel response, which shows that the uneven settlements at joints other than I1 and I6 are small (as not to be detected with any significance by the DOFS), and hence the whole immersed tube section behaves more like a rigid body and moves upwards and downwards cyclically with tidal fluctuation.

5.4. CONCLUSIONS

Short-term (daily or monthly) deformation behavior is an interesting but mostly overlooked aspect in structural health monitoring of existing immersed tunnels. In this study, a distributed optical fiber sensor (DOFS) is used to monitor relative joint movements in the Heinenoordtunnel, and short-term (daily) deformation behavior based on field monitoring is investigated in detail.
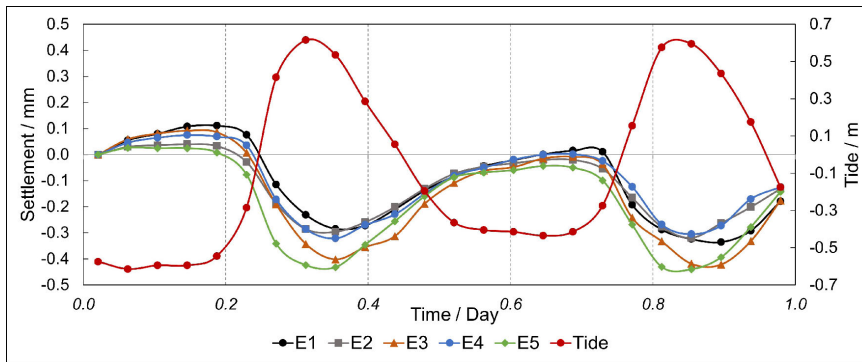
Figure 5.34: Simulated tunnel response under tide impacts

The main conclusions are firstly that the distributed optical fiber sensor (DOFS) is an effective method to construct a monitoring system for immersed tunnel joint deformations that is robust enough for field conditions, and is proven capable of conducting high frequency monitoring (where high frequency means half-hour intervals compared to year or multi-year intervals for traditional techniques), which highlight its applicability in immersed tunnel monitoring.

Secondly, monitoring results of two characteristic periods in this study show that joint opening is negatively correlated with temperature variations, which indicates that the joint gap has a tendency to open at low average temperature and to close at high temperatures. Therefore, the hypothesis that (seasonal) cyclic joint opening and closure driven by temperature variations occurs in the Heinenoordtunnel is validated.

Thirdly, tidal variations in the river above the tunnel generate a vertical response of the immersed tunnel. Monitoring results show the whole immersed section behaves more or less like a rigid body and moves upwards and downwards periodically with tidal variations, with a sub-millimeter movement amplitude. The cyclic movement can be explained by a coupled flow and consolidation model of underlying soil layers under tidal variations, and the response of the soil domain exhibits a time lag compared to the imposed tidal fluctuation.

Finally, monitoring results also indicate that the tidal variations give rise to tilting of some segments in the tunnel, but the extent of this tilting behavior varies between winter and summer seasons. The reduced tilt response in summer, when the tunnel structure is expanded and the joint openings are reduced (i.e. the rubber GINA gaskets are compressed more), implies the seasonal joint deformation affects the response of the tunnel to tidal and other load variations.

REFERENCES

Bentley (2022). *Plaxis 2d-reference manual for connect edition v22.01*. Bentley, Exton, United States.

Biot, M. A. (1941). General theory of three-dimensional consolidation. *Journal of applied physics* **12**, No. 2, 155–164.

Grantz, W. C. (2001a). Immersed tunnel settlements. part 1: nature of settlements. *Tunnelling and Underground Space Technology* **16**, No. 3, 195–201.

Grantz, W. C. (2001b). Immersed tunnel settlements: Part 2: case histories. *Tunnelling and Underground Space Technology* **16**, No. 3, 203–210.

Meteoblue (2022). Meteoblue weather report information. https://www.meteoblue.com, accessed: March-2022.

NEBEST (2016). Report-deformatiemeting-37h-312-01 heinenoordtunnel onder de oude maas.

Rahadian, R., van der Woude, S., Wilschut, D., Blom, C. & Broere, W. (2018). A new test setup for studying sand behaviour inside an immersed tunnel joint gap. In *Physical Modelling in Geotechnics*, CRC Press, pp. 443–448.

Rijkswaterstaat (2022). Tide level information. https://waterinfo.rws.nl/, accessed: April-2022.

Schanz, T., Vermeer, P. & Bonnier, P. G. (2019). The hardening soil model: formulation and verification. In *Beyond 2000 in computational geotechnics*, Routledge, pp. 281–296.

Schotte, K., Nuttens, T., De Wulf, A., Van Bogaert, P. & De Backer, H. (2016). Monitoring the structural response of the liefkenshoek rail tunnel to tidal level fluctuations. *Journal of Performance of Constructed Facilities* **30**, No. 5, 04016007.

TCH (1995). Definitief ontwerp tweede heinenoordtunnel. *Technical report*, tunnel combinatie heinenoord.

van Amsterdam, B. (2019). *Probabilistic analysis of immersed tunnel settlement using cpt and masw*. Master's thesis, Delft University of Technology, the Netherlands.

Zhang, X. & Broere, W. (2022). Monitoring tide and temperature induced joint deformation of immersed tunnel. *Tunnelling and Underground Space Technology, Under review* .

6

BEHAVIOR OF IMMERSED TUNNEL UNDER SEASONAL TEMPERATURE VARIATION

In this chapter, the monitoring results of joint opening and uneven settlement over one year are analyzed, and the seasonal behavior of an immersed tunnel is investigated. Field monitoring results reveal that: joint opening shows a seasonal cyclic effect, and the total expansion of the closed immersed tunnel in longitudinal direction is about 41.5mm over the observed period; the joint opening shows a strong correlation with environmental temperature, i.e., the joint gap opens in winter (as a result of segment shrinkage) and closes in summer (due to segment expansion); the joint uneven settlement indicates segment tilting exists along the tunnel axis, and the amount of tilting also shows a seasonal variation. Also, the effects of longitudinal segment expansion on the tunnel structural behavior are investigated with a beam on elastic foundation model, and the results show: segment expansion causes a redistribution of deformation on both joints and tunnel segment; it mitigates the shear deformation at partial joints at the cost of increasing the shear deformation on the rest joints; the redistribution of deformation is more significant within the two end elements; the simulation results generally agree with measurement in deformation development tendency.

6.1. INTRODUCTION

The behavior of segmented immersed tunnel under seasonal temperature variation is of interest to tunnel structure managers, as there are signs that seasonal behavior of the tunnel body affects the structure safety and watertightness. For example, in the Limfjord tunnel (an immersed tunnel in Denmark), the seasonal expansion and shrinkage of the tunnel body changes the cracking width and leads to a variable leakage rate(ATKINS *et al.*, 2019). In some immersed tunnels, the longitudinal segment expansion can potentially cause seasonal joint opening and closure, which in turn affects the watertightness of immersion joint(Rahadian *et al.*, 2018; van Montfort, 2018; Bai & Lu, 2016).

Previous studies on the seasonal behavior of immersed tunnels are mainly based on assumed deformation modes. For example, van Montfort (2018)analyzed the effects of longitudinal element expansion and vertical uneven settlement on the gasket's water-proofing performance, but the deformation range is derived from a rough estimate that requires field monitoring validation. Moreover, although more new types of sensors are gradually applied at immersion joints(Xu *et al.*, 2019; Liu *et al.*, 2008), allowing for richer deformation data to be obtained, the dilation joint is mostly ignored in previous monitoring campaigns (for instance in most immersed tunnels in Netherlands). Considering the fact that significant deformation and potential problems occur at dilation joints as commonly as at immersion joints, a comprehensive study on the seasonal behavior of immersed tunnels should start from monitoring both immersion and dilation joints.

The distributed optical fiber sensor (DOFS) system installed in Heinenoordtunnel proves capable of monitoring both immersion and dilation joints, and joint deformation in dual-direction (longitudinal joint opening and vertical uneven settlement) is measured simultaneously.

This chapter interprets the monitoring data of Heinenoordtunnel collected by the DOFS system. These results come from the monitoring data of thirteen joints (from tunnel north portal) lasting for a one-year period, and that of the remaining seventeen joints (from tunnel middle to south portal) lasting for a half-year period. Based on the data analysis, the seasonal behavior of the segmented immersed tunnel is investigated specifically. Moreover, a numerical simulation is also conducted to study the effects of seasonal segment expansion on the tunnel structure's behavior.

6.2. FIELD MONITORING WITH DOFS SYSTEM

As introduced in section 5.2 of Chapter 5, the DOFS is used to instrument both dilation joints and immersion joints of Heinenoordtunnel, with a BOFDA interrogator for data acquisition, see Fig.6.1.

Here the instrumented tunnel joints are numbered to be easily distinguished: Ij denotes the jth immersion joint from the north end (see Fig.6.1), while Dik refers to the kth dilation joint (from north) in the ith element. For instance, I1 refers to the first immersion joint, while D21 means the first dilation joint (from the north) in the second element. The monitoring periods of the individual joint are:

(1) The first set of thirteen joints (I1 to I3, see Fig. 6.1) with a full-year monitoring duration. The data acquisition started on December 16, 2020, until to December 11, 2021;

(2) The second set of seventeen joints (D31 to I6, from tunnel middle to the south end,
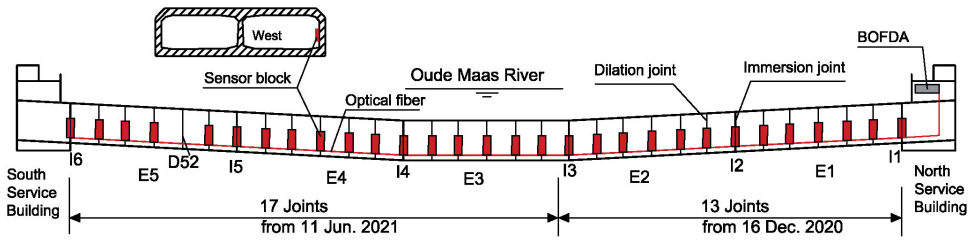
Figure 6.1: Sensor installation and monitoring at Heinenoordtunnel

excluding D52) with a half-year monitoring duration. The data acquisition started on June 11, 2020, until to December 11, 2021.

In summary, the field monitoring covers a long period from summer to winter, and the monitoring results can help to interpret the seasonal behavior of Heinenoordtunnel.

6.2.1. ACCURACY OF THE DOFS SYSTEM IN FIELD CONDITIONS

The measurement accuracy of the DOFS system for a one-year period in field conditions shall be assessed firstly. Here the measurement accuracy is evaluated with regard to three aspects: (1)a comparison of temperature measurements with ambient weather temperature; (2)the possibility of fiber relaxation and its effects; and (3)the effects of sensor installation errors.

The measured temperature at the first immersion joint (as I1 at the north portal) is compared with the ambient weather temperature in the Heinenoord area (daily mean temperature, from Meteoblue (2022)). As shown in Fig.6.2, the measured temperature closely follows the ambient weather temperature throughout the monitoring period. Considering the weather station in Heinenoord is located approximately 3km from the north tunnel portal, a slight temperature difference between them is reasonable. In summary, the temperature measurement results from the DOFS sensor in field conditions are reliable.

The creep of a strained optical fiber will result in a gradually decreased fiber strain with time, which causes measurement errors. Although the optical fiber utilized (typed NZS-DSS-C07, see section 3.3 of Chapter 3) has been experimentally validated to exhibit negligible creep, it is still necessary to evaluate any eventual creep in field conditions. Here the strain of horizontal fiber line (FL1) at joint D11 (the first dilation joint of the 1st element) is investigated, as it demonstrates the highest working strain level (which is correlated with a higher occurrence of creep when present) among all the tensioned gauge lengths in field. The strain level of FL1 at D11 displayed a seasonal cycle: it decreased from about 1.02% (December 28, 2020, with a temperature of about 7°C) to about 0.4% (June 18, 2020, with a temperature of about 27°C), and afterward it increased again to about 0.92% (December 8, 2021, with a temperature of about 7°C). Since the fiber strain at the starting and end of the monitoring period remains almost the same level (under the same temperature conditions), the predicted fiber creep in the field is negligible.

In addition, a 0.8m-long reference fiber length was fixed at the tunnel sidewall (not spanning a joint) with an initial strain of around 0.5%. During the half-year period from

June 12 to December 10, 2021, the strain fluctuation range of this fiber length is less than 0.01%. Theoretically, this reference fiber length only measures the thermal deformation of the sidewall concrete over the 0.8m length, and this thermal deformation is estimated to be about 0.11mm, given an expansion coefficient of 6.0×10^{-6} per $^{\circ}C$ and a temperature difference of $24\,^{\circ}$C. The deformation measured by the reference fiber length falls in a range of 0.09mm over the observed period, which agrees with the theoretical value (0.11mm) on the scale. This implies the strained fiber length with an initial strain of 0.5% exhibited no creep and was capable of conducting accurate deformation measurements.

Moreover, the effects of sensor installation deviation on sensor performance should be checked. In the field, when placing the individual fixing pads on the wall (see P1 to P3 in Fig.4.20), deviation from the optimal position may occur, which may affect the measurement accuracy. The effects of field installation errors are analyzed in detail in Appendix B. As determined by the error analysis results provided there, the measurement error of joint deformation remains below 0.1mm, under an extreme placement deviation situation.

A further factor that influences the measurement reliability is the signal attenuation in the optical fiber. The signal attenuation of the optical fiber loop is generally related to the fiber length, the quality of connector and splice, and local fiber bending. Typical values should be around 0.3 dB/km with additional 0.5 dB for a connector and 0.1 to 1dB for a splice. If the total attenuation exceeds 3 dB per km, the loop might have suffered strong bending, or the connectors are not clean. Depending on the local distribution of the attenuation sources, a total attenuation of 12-15dB might still lead to reasonable results. However, attenuation values below 6 dB are desirable in order to get reliable and reproducible results (fibrisTerre, 2021). The BOFDA interrogator can detect signal loss and adjust the output power automatically to get optimal results. Before field installation, the 1.4km optical fiber loop has a signal attenuation of below 1.5dB, and in the field working conditions the measured signal attenuation is about 3dB, which indicates a limited attenuation level and the measurement results are reliable.

In summary, it is reasonable to conclude the installed DOFS monitoring system has an acceptable accuracy of 0.1mm in field conditions.

6.3. Seasonal Monitoring Result Analysis

6.3.1. Temperature result interpretation

Here for brevity, only the measured temperature(daily mean) of the immersion joints is presented, which helps to show the temperature variation along the tunnel axis longitudinally. Fig.6.3 shows the temperature of joints I1 to I3 within one year. The DOFS system accurately measures the seasonal temperature variation, as shown in the temperature curves. It can be noticed that the temperatures of the three immersion joints are very close with a maximum difference of about $3\,^{\circ}$C. According to the measurements, the seasonal temperature fluctuation (absolute value) inside Heinenoordtunnel over the monitoring period is about $30\,^{\circ}$C.

Fig.6.4 shows the temperature results of joints I4 to I6 within a half-year period. As seen in the temperature curves, the temperatures of these three immersion joints are very close, with the highest difference of around $4.5\,^{\circ}$C. From June 11 to December 10, the

amplitude of temperature fluctuation is about 23 °C. As shown by the temperature curves on the overlapping period (June 11 to December 10) in Fig.6.3 and Fig.6.4, the measured temperatures at six immersion joints are very close and share a highly similar tendency, while the difference between them is very small (below 4.5 °C), which indicates that the environment temperature varies little along the tunnel axis longitudinally.

6.3.2. JOINT DEFORMATION RESULTS

JOINT OPENING

Positive joint opening denotes a joint gap opening compared to the reference status, whereas a negative opening indicates a joint gap closure. Fig.6.5 depicts the joint opening of the first thirteen joints (from I1 to I3) during the entire year period. Results show that generally the three immersion joints have a more significant joint opening range than most dilation joints, with the exception of D11 which exhibits the most significant deformation (-5.18 to -0.26 mm, see Table 6.1). Compared with three immersion joints and dilation joint D11, the deformation range of the other nine dilation joints is significantly lower (between -2.0mm to +1.0mm);

It should be pointed out that the local peak opening of joint I2 and I3 on February 18 was recorded after a two-week monitoring pause. As seen in Fig.6.2, the coldest period of the year occurs over these two weeks. This cold episode lasted from around February 7 to 16, with the lowest mean temperature reaching −9 °C in the Heinenoord region on February 16 (Meteoblue, 2022). Although on February 18 the temperature rose to a positive value (about 7 °C), the peak deformations at I2 and I3 in Fig.6.5 indicate that the opening deformation curve exhibits a delay in comparison to the ambient temperature change. This deformation delay occurs in the result curves and will be analyzed in further detail in the section below. As the temperature recovered to a positive level after February 18, the openings at I2 and I3 decreased rapidly during the following days, see Fig.6.5.

Observing the whole year of monitoring, it is evident that the measured joint opening exhibits cyclic behavior. Specifically, the joint opening decreases (a joint gap closure) from spring to summer seasons, while in summer (June to September) the joint demonstrates the maximum negative opening (namely the maximum joint gap closure); after September, the joint opening gradually increases in the cold period from October to December (an indication of joint gap opening). Note that this cyclic seasonal opening deformation is present at all instrumented joints, as shown in Fig.6.5.

6
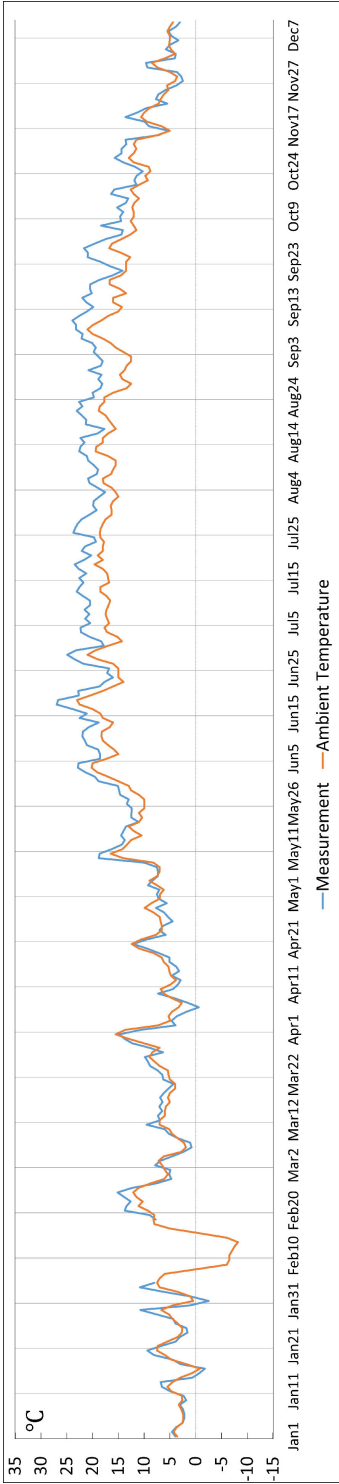
Figure 6.2: Temperature result comparison with ambient air temperature
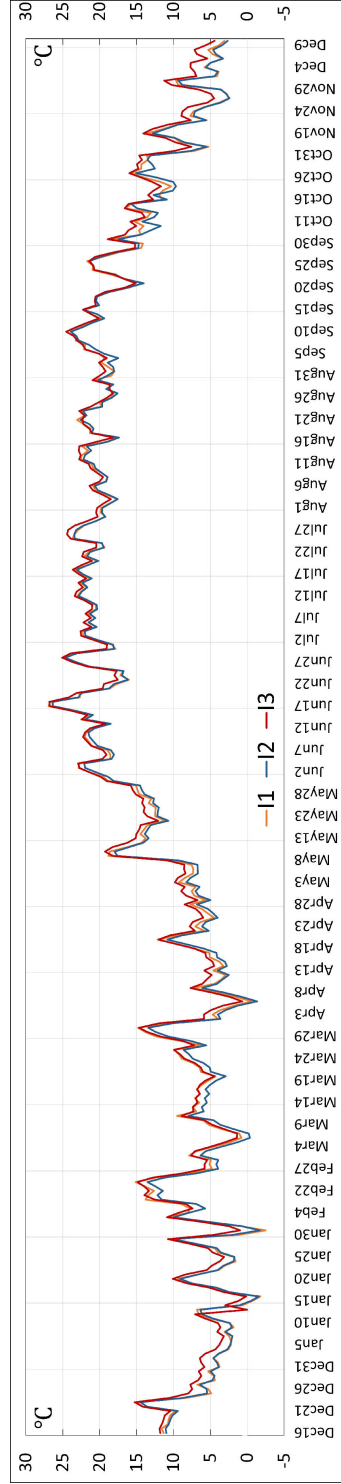
Figure 6.3: Temperature of immersion joint (I1 to I3, full-year period)
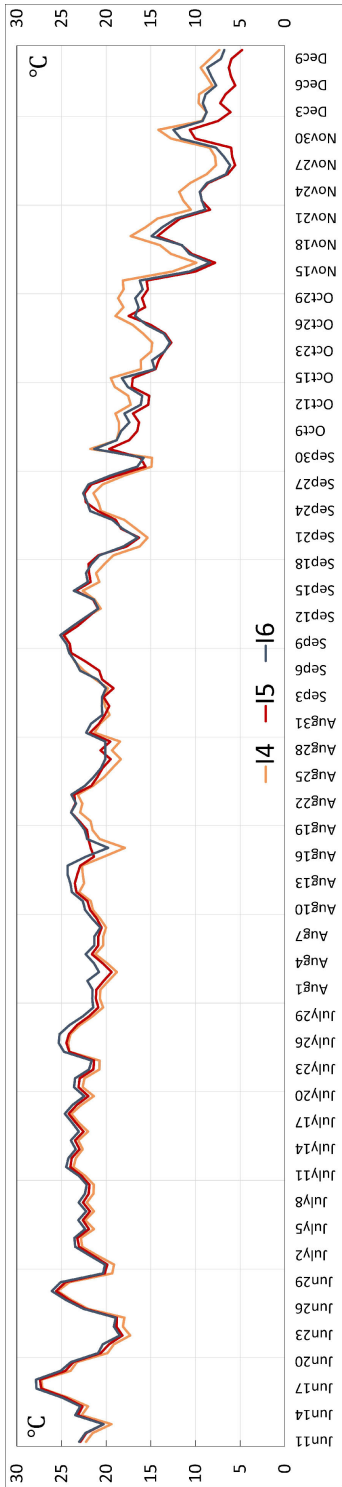
Figure 6.4: Temperature of immersion joint (I4 to I6, half-year period)

Figure 6.5: Opening ΔY_i of first-set 13 joints(full-year period)

6
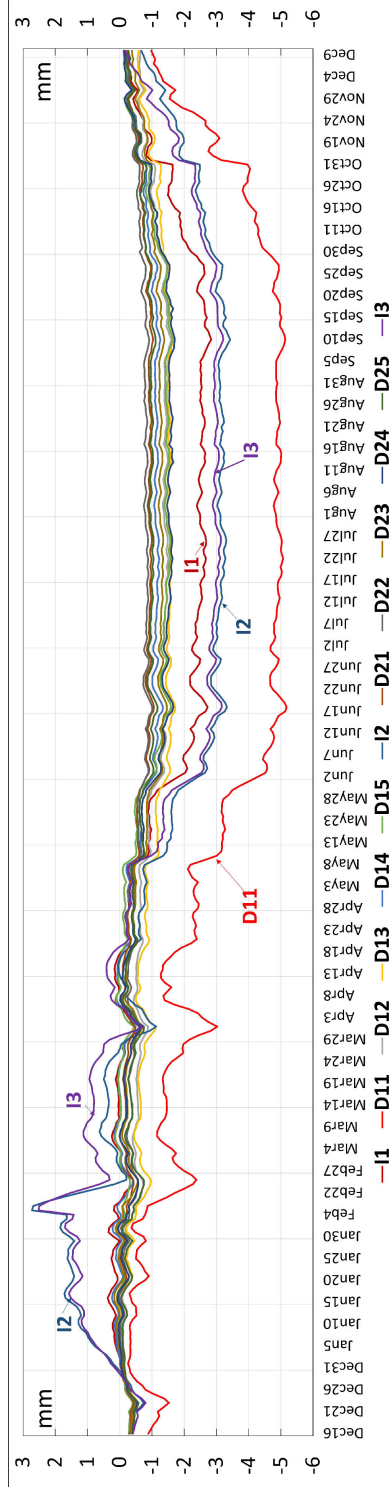
Moreover, the degree of joint opening also varies with joint location. Among the three immersion joints, the opening range (a difference between the highest and the lowest value) of I2 and I3 is higher than that of I1 (see Fig.6.5), as I2, I3 and I1 have opening ranges of 6.15mm, 5.73mm and 3.21mm, respectively. In addition, among the thirteen joints, D11 had the highest joint closure at -5.18mm (on June 18, also with the highest reported temperature). It should be noted that during previous maintenance work, a significant leakage was observed at joint D11 (Leeuw, 2008). This may indicate that D11 has higher deformation flexibility than the other nine dilation joints, which is consistent with the large joint opening measured by the DOFS system.

The monitoring result of joint I1 is analyzed in depth to investigate the potential correlation of seasonal temperature with joint deformation. Fig.6.6 presents the measured temperature and joint deformation within one year period. Monitoring results show: the joint gap closes in warm seasons (summer period, with the maximum closure of around 2.84mm), and opens in cold seasons (winter period, with the maximum opening of about 0.33mm), and this cyclic opening deformation is related to the thermal expansion of tunnel segment body; within one year, the scale of joint uneven settlement (between -1.28mm to 0.7mm) is smaller than that of opening (between -2.84mm to 0.33m), and uneven settlement is measured to show seasonal variation as well; joint deformation shows a correlation with temperature, which will be discussed more in Section 6.3; there exists a delay between joint opening deformation and temperature, indicating the joint opening is delayed after the temperature change. At joint I1 (also most of the joints), this delay is measured to be about 1 to 2 days; this delay phenomenon is more significant especially when strong temperature fluctuation occurs, as seen in Fig.6.6 from March 29 to April 3.

Fig.6.7 shows the measured opening of the second set seventeen joints (from D31 to I6) over a half-year period (June 11 to December 10, 2021). During the summer period (June to September), joint opening remains relatively steady within the range of -0.5mm to 0.5mm. Nonetheless, when the weather temperature gradually falls from October, tunnel segment shrinkage results in a gradually increasing joint opening. D55 and I4 exhibit the most significant deformation of the seventeen joints, with the maximum opening of 2.80mm and 2.69mm, respectively, by December 10, 2021; while at other joints the maximum joint opening is below 2.0mm. The measurement results validate that cyclic seasonal joint opening also occurs on the second set of instrumented joints.

The range of joint opening throughout the monitoring period is listed in Tab.6.1 and Tab.B.1 in Appendix B. From the results listed, it can be seen that generally the opening deformation amplitude of immersion joints is larger than that of dilation joint. However, at a few dilation joints (D11, D54 and D55), a larger joint opening occurs compared with the nearby immersion joint, and D11 exhibits the most significant opening deformation, with a maximum about -5.18mm. In summary, the monitoring results by DOFS system have properly revealed the magnitude of seasonal joint opening deformation, which can help analyze seasonal tunnel behaviors.
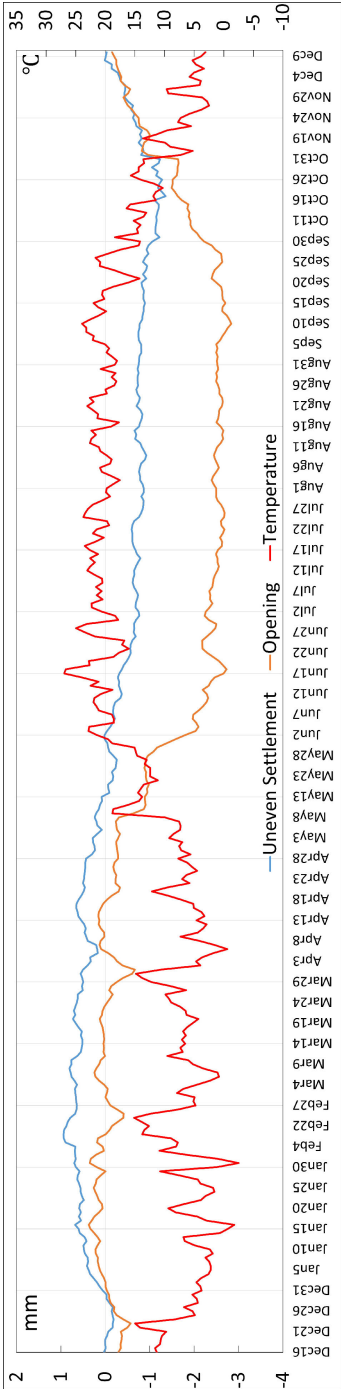
Figure 6.6: Joint deformation and temperature of immersion joint I1
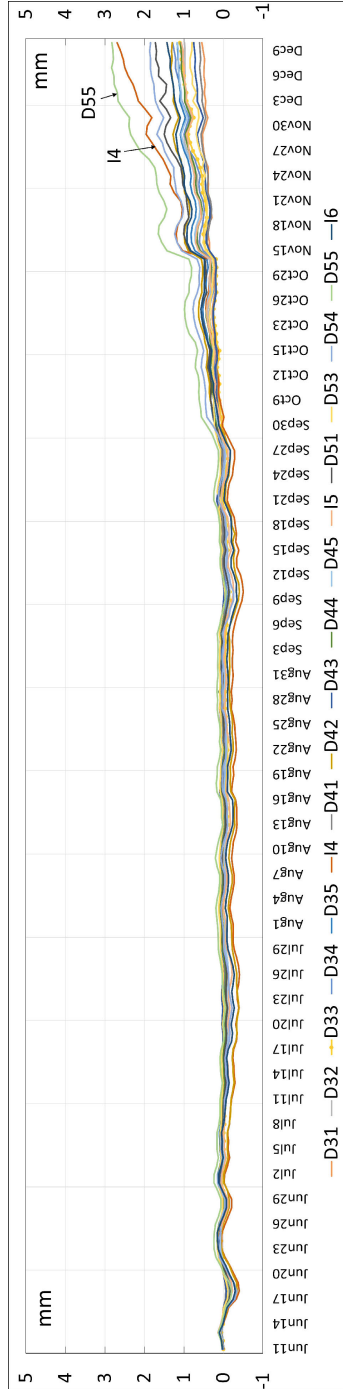
Figure 6.7: Opening ΔY_i of second-set I7 joints (half-year period)

6

Table 6.1: Joint opening deformation range

Joint	I1	D11	D12	D13	D14	D15	I2	D21	D22	D23	D24	D25	I3
Min	-2.84	-5.18	-1.60	-1.72	-1.34	-1.65	-3.42	-1.06	-1.01	-1.47	-1.71	-1.18	-3.22
Max	0.37	-0.26	-0.08	0.05	0.24	0.14	2.72	0.08	0.02	0.18	0.07	-0.04	2.51
Amplitude	3.21	4.92	1.53	1.77	1.59	1.79	6.15	1.14	1.03	1.65	1.78	1.14	5.73

Given the thermal behavior of concrete, the seasonal joint opening is closely related to the thermal expansion of the segment body longitudinally. For instance, the maximum joint closure occurs in summer period, when the segment expansion causes a narrowed joint gap. Specifically, in summer the segment expansion narrows the joint gap (resulting in a joint closure), and in winter the segment shrinkage widens the joint gap (with a resultant joint opening). The joint opening measurement results help to quantitatively assess the scale of longitudinal thermal expansion of the full immersed section. Here the total joint opening of all the measured joints is summed up as in Eq.6.1:

$$\Delta L = \sum_{i=1}^{30} \Delta Y_i \tag{6.1}$$

Where ΔL is the longitudinal thermal deformation of the full immersed section (about 574m), and ΔY_i indicates the measured joint opening at joint i.

Considering a total of thirty joints over a half-year period (baseline on June 11, 2021), the total opening is calculated as 0.12m on June 11 and 41.67mm on December 10, 2021. This indicates throughout the half-year course (from summer to winter), the overall thermal shrinkage deformation of the 574m immersed section is approximately 41.5mm. Moreover, the theoretical thermal expansion of this entire immersed section is tentatively calculated to be around 62mm within this half-year period (with an expansion coefficient of 6.0×10^{-6} per °C) and a temperature change of 18°C, which is on the same scale as the measured result. Therefore, based on measurement results, the entire immersed tube section exhibits cyclic thermal expansion and contraction with an amplitude of around 41.5mm over the one-year monitoring period (see Fig.6.8), and this longitudinal thermal deformation is primarily compensated by joint opening variation(especially at immersion joints).
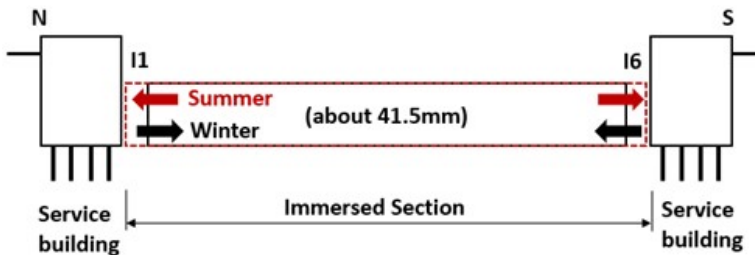
Figure 6.8: Longitudinal expansion and contraction deformation of Heinenoordtunnel

Joint uneven settlement

Fig.6.9 to Fig.6.10 show the joint uneven settlement results of the first set of thirteen joints (full-year period, from December 16, 2020, to December 10, 2021) and the second set of seventeen joints (half-year period, from June 11, 2021, to December 10, 2021).

In the majority of the thirteen joints in a full-year period, the joint uneven settlement is small (with an absolute value of below 1.5mm). Except for joints I1, D11 and D24, the uneven settlement of all other joints falls within a range of -1.0m to 1.0mm (more specifically, the majority of joints only have a deformation range of -0.3mm to 0.5mm); however, D11 exhibits a maximum uneven settlement of about 1.3mm, while I1 has a maximum (negative) deformation of around -1.4mm.

Joint uneven settlement over a full-year period shows seasonal variation as well. As shown in Fig.6.9, for instance the uneven settlement of joint I1 increases from December 2020 to March 2021, then it decreases gradually from April until November 2021, and afterward it recovers to about 0.0mm by December 2021, demonstrating a cyclic behavior. Nonetheless, the seasonal variation of the uneven settlement is not as significant as that of joint opening, and this will be explored in further detail in Section 6.3. At joint I2, the deformation curve reaches a peak value in February (on February 18). This local peak is the result of unusually low temperatures during a two-week period, as also shown in the opening result curve in Fig.6.5. Afterward, this deformation curve gradually decreases with time.

When comparing uneven settlement with opening, it can be seen the magnitude of joint opening is generally much larger than that of uneven settlement, as shown in Tab.6.1 and Tab.6.2. At joint D11, for example, the joint opening ranges from -5.18 to -0.26mm, while the range of uneven settlement is only from 0.03 to 1.18mm.

Fig.6.10 shows the measured uneven settlement of the second set of seventeen joints over a half-year period. It can be seen that most joints exhibit a fairly minor deformation range (-0.3 mm to +0.4mm) within this monitoring period, but joint D55 exhibits a larger deformation (about -0.6mm by December 10) in the winter period; during the summer months (June to September, with reasonably steady temperatures), the uneven settlement is very stable and within a limited range of -0.2mm to 0.2mm for the majority of joints (excluding I6). However, from November when the temperature fluctuates more significantly, the uneven settlement starts to show significant fluctuation also. For example, as demonstrated in Fig.6.10, at I4 and D55 the fluctuation is more significant than at the other fifteen joints.

6
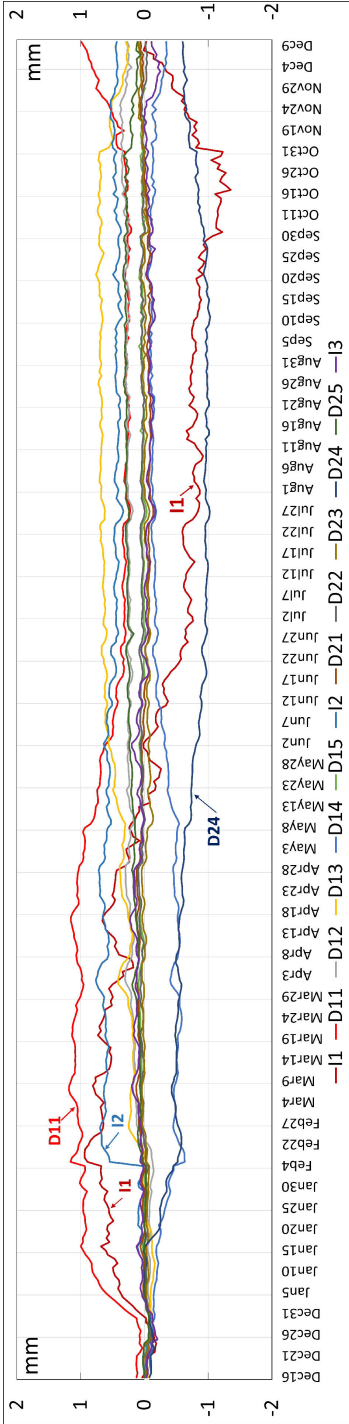
Figure 6.9: Uneven settlement ΔZ_i of first-set 13 joints (full-year period)
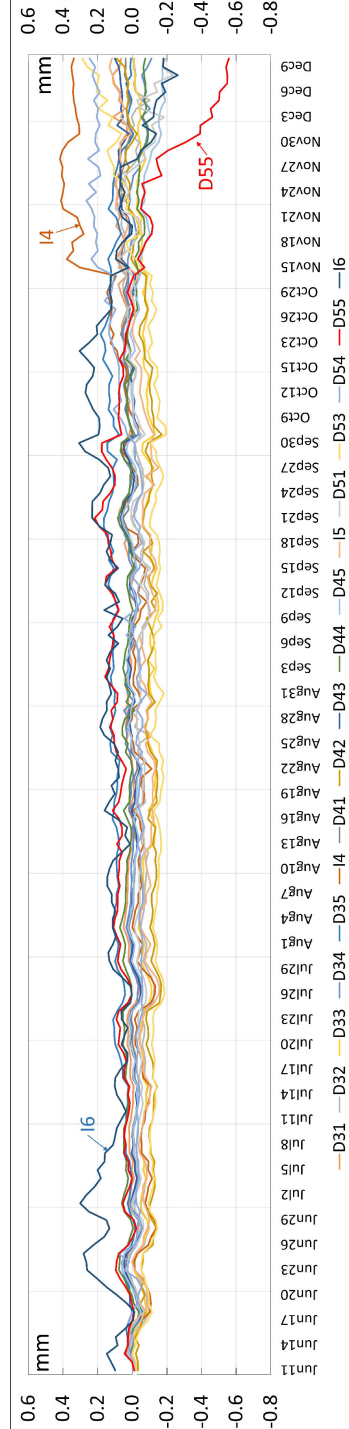
Figure 6.10: Uneven settlement ΔZ_i of second-set 17 joints

The amplitudes of joint uneven settlement are reported in Tab.6.2 and Tab.B.2 in Appendix B. Generally, the scale of uneven settlement is significantly smaller than that of opening. For the first set of thirteen joints over an entire year, the deformation amplitude of most joints is below 1.0mm, while I1 and D11 show a significantly larger deformation range, especially at joint I1. The measurement results shows the uneven settlement of some joints also exhibit cyclic seasonal behavior, and the correlation to temperature will be discussed in section 6.3.5.

Table 6.2: Joint uneven settlement range

Joint	I1	D11	D12	D13	D14	D15	I2	D21	D22	D23	D24	D25	I3
Min	-1.36	0.03	-0.15	-0.16	-0.63	-0.12	-0.11	-0.14	-0.11	-0.14	-1.03	-0.07	-0.25
Max	0.94	1.18	0.38	0.76	-0.05	0.10	0.76	0.13	0.10	0.10	0.01	0.33	0.23
Amplitude	2.30	1.15	0.53	0.92	0.58	0.22	0.88	0.27	0.21	0.24	1.05	0.41	0.48

Joint uneven settlement helps to illustrate the vertical plane deformation of an immersed tunnel. Here, the cumulated joint uneven settlement along the longitudinal axis of the tunnel is calculated using Eq.6.2:

$$\Delta S_k = \sum_i^k \Delta Z_i \tag{6.2}$$

where ΔS_k is the cumulated joint uneven settlement at the kth joint (from the north), and ΔZ_i indicates the uneven settlement at individual joint i(between the first and the kth joint).

Fig. 6.11 plots the cumulated joint uneven settlement on some selected days. Here the settlement is set as relative to the north portal, and it can be seen the calculated settlement of the south portal is not equal to zero.

Considering the southern tunnel entrance ramp and service building have exhibited negligible settlements over time (NEBEST, 2016) and can be considered a fixed point, the measured uneven settlement implies segment tilting exists in the vertical plane. Furthermore, because the cumulative settlement curves show seasonal fluctuation, this may suggest that segment tilting also exhibits seasonal variation. For a specific tilting behavior analysis, additional information, such as the tilting angle of each segment, should be monitored in addition to the joint uneven settlement data provided by the DOFS system.

DISCUSSION

The joint deformation monitoring by DOFS covers one year, and it is of significance to investigate the tunnel behavior from the perspective of the occurred long-term settlement state. The Heinenoordtunnel was opened to traffic in 1969, but the continuous settlement measuring started in 1978. The settlement of several selected locations relative to a reference point (on the approach section) is measured by manual leveling at a minimum interval of one year. The settlement curves by year 2018 are displayed in Fig.6.12. Note that for the entire 40-year monitoring period, only the settlement next to the immersion joints and in the middle of each the element have been recorded.
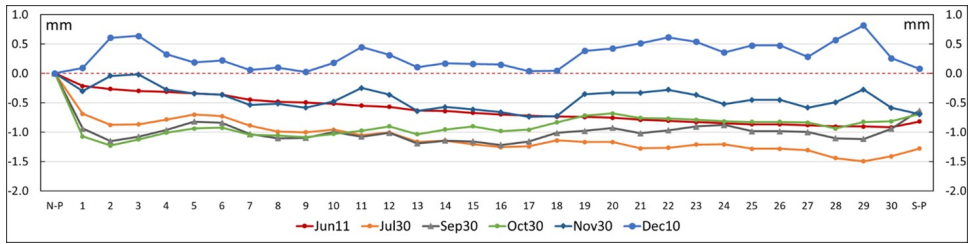
Figure 6.11: Cumulated uneven settlement ΔS_k along the longitudinal tunnel axis (N-P and S-P mean north and south portals)

As shown in Fig.6.12, the maximum settlement of the west tube is about 67mm at the middle of the first element; while the middle of the fifth element also exhibits a significant settlement of about 57mm. Significant differential settlement occurs longitudinally, and high gradients on the curve show along the two end sections (joint I1 to Element-1 middle, Element-5 middle to joint I6) adjacent to the approach structures.
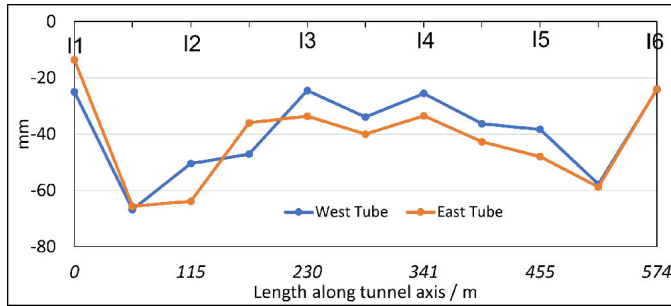
Figure 6.12: Long-term settlement curve of the Heinenoordtunnel (between 1978 and 2018)

According to Kwok (2022), the long-term settlement observed at the Heinenoordtunnel is most likely caused by the presence of uncompacted voids in the sand foundation and secondary creep of foundation soil brought on by a continuous increase in traffic loading (as the traffic volume nearly doubled over the course of the 50 years' service life). Pockets of softer soil, particularly the soil beneath element 1, is likely the cause of the unusually high settlement concentrated in the middle of the first and fifth elements. The shear wave velocity (Vs) profile produced by the MASW (Multichannel Analysis Shear Wave) method, which will be covered in Section 6.4, further verified the existence of a local weak soil layer underneath the first tunnel element.

The differential settlement will generally result in segment tilting, which may further trigger excessive joint opening at the upper or lower cross-section. This excessive joint opening creates more freedom of deformation at the joint compared to when the joint keeps complete contact. Note that along the first element joint D11 exhibits a significantly higher-level seasonal opening (with an amplitude of 4.92mm) as well as a higher sensitivity to tidal variation than other dilation joints. Joints D55 and D54 also exhibit a higher seasonal opening (with an amplitude of 3.04mm and 2.20mm, respectively) than the

other three dilation joints within the 5th element. It is highly possible that an excessive opening has occurred earlier at these three dilation joints, and the joint interface contact has been lost fully or partially.

In addition, larger openings were reported at immersion joints I2 (with an amplitude of 6.15mm) and I3 (with an amplitude of 5.73mm) than at other immersion joints. Considering the settlement curve gradient near the joint locations, it can be inferred that a counterclockwise rotation (along the bottom of Joint I2) may have occurred on the section between the middle of the 2nd element and joint I3. These segment rotation behaviors may trigger further joint opening (and decompression of the GINA gasket) at the upper cross-section of immersion joints I2 and I3. Therefore, evaluation of the deformation status based on the long-term settlement curve and seasonal monitoring data by DOFS suggests to pay more attention and perform safety checks on these joints that exhibit a higher degree of deformation freedom.

6.3.3. CORRELATION OF JOINT DEFORMATION WITH TEMPERATURE

In this section, the joint deformation and temperature data are explicitly compared, in order to investigate the potential correlation. The Pearson correlation coefficient between joint opening and uneven settlement on one hand, and temperature on the other hand, are obtained. The correlation coefficients of the first set of thirteen joints (I1 to I3, full-year period) are shown in Tab.6.3, while those of the remaining seventeen joints (half-year period) are provided in Tab.B.2 in Appendix B. Note here $C_{o,t}$ and $C_{s,t}$ mean opening-temperature correlation and uneven settlement-temperature correlation.

Table 6.3: Correlation of joint deformation with temperature(I1 to I3)

Joint	I1	D11	D12	D13	D14	D15	I2	D21	D22	D23	D24	D25	I3
$C_{o,t}$	-0.93	-0.89	-0.92	-0.92	-0.95	-0.94	-0.85	-0.96	-0.97	-0.93	-0.93	-0.97	-0.89
$C_{s,t}$	-0.67	-0.70	0.38	0.79	0.55	-0.05	0.12	-0.75	0.32	-0.35	-0.79	0.80	-0.44

As demonstrated in Tab.6.3 and Tab.B.2, the opening at all joints has a strong negative correlation to temperature, with all values above -0.85 (most are above -0.90). The significant negative correlation strongly implies the joint gap tends to widen with decreasing temperature (winter period) and close with increasing temperature (summer period). As described in section 6.3.3, the joint opening variation during seasonal temperature change is strongly connected to the longitudinal thermal expansion of tunnel segments (see Fig.6.13).

Compared with joint opening, the correlation between uneven settlement and temperature varies significantly between joints. This implies the relationship between uneven settlement and temperature is generally much weaker than that between opening and temperature. In addition, it should be mentioned the temperature effects on the sensing fiber may amplify system error, since most joints present a very low uneven settlement amplitude of far below 1mm over the one-year or half-year period. Observing the deformation range of joint opening and uneven settlement, it is reasonable to conclude that for a long segmented immersed tunnel, the seasonal temperature change will cause a much more significant deformation reaction longitudinally than in the vertical direction.
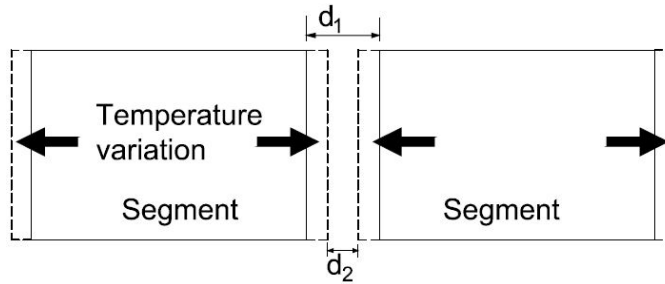
Figure 6.13: Longitudinal segment expansion and resultant joint opening variation

6.4. ASSESSING THE EFFECTS OF SEGMENT EXPANSION ON TUNNEL STRUCTURES

According to the field monitoring results by the DOFS system, seasonal joint uneven settlement in the Heinenoordtunnel generally has a very small submillimeter scale, and such low or even negligible uneven settlement generally has a limited impact on the tunnel structure safety. However, the seasonal joint opening range is much more significant (with a scale of several millimeters) and its potential impacts on the tunnel should be assessed.

The seasonal joint opening indicates the occurrence of longitudinal segment thermal expansion under temperature change. It should be noted that potential effects of seasonal segment expansion on immersed tunnel behavior have been discussed only qualitatively in literature, such as in the case of Limfjord tunnel in Denmark, the seasonal segment thermal expansion leads to a variation of the leakage rate on tunnel wall (ATKINS *et al.*, 2019). In the Kil tunnel in Netherlands, the seasonal joint opening is supposed to cause a decompression of GINA gasket and a subsequent leakage risk, while its effects are further analyzed with an assumed deformation range (van Montfort, 2018). In the Shanghai Outer-ring Expressway Tunnel, it is inferred that the seasonal segment expansion causes a cyclic joint opening and closure which may be related to the observed damage of the GINA gasket (Bai & Lu, 2016).

However, due to a lack of field monitoring studies to quantify the accurate scale of longitudinal tunnel expansion, the previous studies are mostly qualitative and concentrated on evaluation of these effects on joint watertightness. From perspectives of structural behavior, the seasonal segment expansion imposes pretensioning effects on the tunnel axis longitudinally, and also alters the joint mechanical properties (i.e. flexural, axial and shear behaviors). It would be preferred to execute an investigation that takes into account the full tunnel structure model rather than only the individual joints. The following section quantitatively investigates the consequences of segment expansion based on a full-length longitudinal structural model.

6.4.1. LONGITUDINAL STRUCTURE MODEL

Longitudinally a segmented immersed tunnel can be modeled as a discontinuous beam on an elastic foundation, while immersion joints and dilation joints should be explicitly

considered in this model. In this section, a simplified 2D beam-spring model (as shown in Fig. 6.14) is built to assess the effects of segment expansion on the overall tunnel structural behavior.
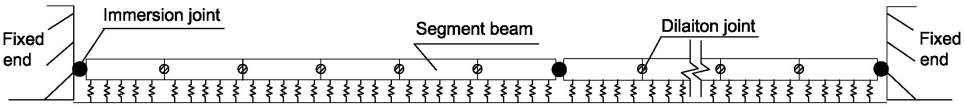
Figure 6.14: Longitudinal beam on elastic foundation model of immersed tunnel

The 2D model is simulated in ABAQUS CAE software, a commercial FEA software for linear and nonlinear structure problems (Abaqus, 2022). In the simulation, the beam is modelled as a Timoshenko (shear flexible) beam using a B21 beam element (a 2-node linear beam in a plane). The ground support is modeled as distributed springs, whilst the joint is modeled using a connector element (Cartesian and rotation type, see Abaqus (2022)), which can simulate the joint flexural, axial and shear behaviors with predefined parameters.

In the 2D modeling shown in Fig.6.15, the following parameters are to be obtained firstly: the cross-section properties of the tunnel segment; the joint mechanical parameters which properly characterize the axial, shear and flexural deformation behavior; the external loading on the beam in the vertical direction; and the foundation stiffness.

Figure 6.15: Longitudinal beam model in Abaqus

To study the consequences of thermal expansion, the following two separated models are built and solved: the first model, representing a normal scenario, does not take the segment expansion into account; and the second model represents an expansion scenario that accounts for the segment expansion effects. In both models, only the joint mechanical parameters are different, whereas all other model parameters (segment cross-section parameter, the external loading and foundation stiffness) remain the same. The effects of segment expansion are analyzed by comparing the joint and tunnel deformation results of the two models.

CROSS-SECTION PROPERTIES OF TUNNEL SEGMENT
The tunnel consists of five elements and each with six 19m-long segments. Each segment is modeled as a beam, with cross-section parameters as indicated in Fig.6.16a and specified in Tab.6.4. The elastic modulus of concrete material is set as 30GPa, while the shear modulus is 11.2GPa.

JOINT MECHANICAL PROPERTY
The joint between segments is modeled using springs (see Fig.6.16b) according to their individual layout. As shown in Fig.6.17a, at immersion joints the compressed GINA works

Table 6.4: Cross-section parameters of the tunnel

Parameter	Section Area (m^2)	Cross section inertia(I_x, m^4)	Section centroid (h_c, m)	Self-weigh (kN/m)
Value	93.66	1085.18	4.3	2111

(a) Tunnel cross-section

(b) Joint mechanical model
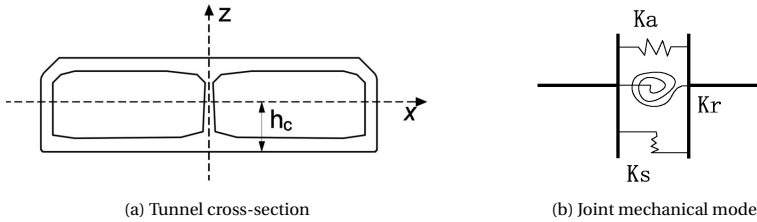
Figure 6.16: Tunnel segment cross-section and joint model

as an elastic buffering layer which decides the joint behavior (axial and bending) in normal working conditions, while the initial compression status of GINA should be first determined for behavior analysis; the shear key provides shear resistance at these joints. At dilation joints, a direct concrete-concrete interface exists as shown in Fig.6.17b.

The mechanical behavior of joint is modeled using a flexural spring (as k_r), an axial spring (as k_a), plus a shear spring (as k_s), see Fig.6.16b. These springs are either linear or nonlinear, and the spring parameters corresponding to normal and expansion scenarios are derived specifically in Appendix B, while the detailed parameters are listed in Tab.B.5 and Tab.B.6 in Appendix B.

(a) Immersion joint

(b) Dilation joint
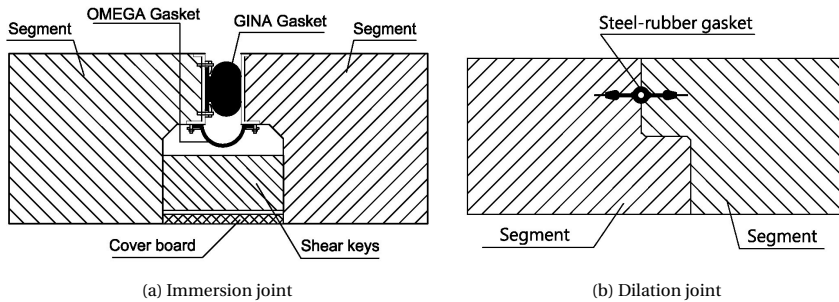
Figure 6.17: Tunnel joint formation

EXTERNAL LOADING AND FOUNDATION STIFFNESS

The following load aspects (along vertical direction) imposed on the immersed tunnel are considered: (a) the self-weight of the tunnel; (b) the ballast concrete and pavement (1m thickness); (c) the buoyancy; (d) the top backfilling soil (3m thickness). These factors result in a distributed load of 1161 kN/m longitudinally.

The subgrade reaction coefficient (as K_s) is an important parameter to characterize

the foundation soil behavior. In engineering practice, this coefficient is mostly obtained by field testing (mostly by a plate loading test or standard penetration test) or empirical estimate. As at the Heinenoordtunnel there are no field test results available for determining the subgrade reaction coefficient, an estimate is necessary. Here the shear wave velocity of the soil beneath the tunnel obtained by MASW (Multichannel Analysis Shear Wave) method is used to calculate K_s. Determination of K_s values is specified in Appendix B.

The subgrade reaction coefficients corresponding to each individual tunnel element are: 21MPa at E1; 31MPa at E2 and E5; 34MPa at E3 and E4.

6.4.2. Simulation result analysis

The beam on elastic model is solved in Abaqus, while tunnel segment and joint deformation corresponding to normal and expansion scenarios are explicitly compared.

The vertical shear displacement (absolute value) and shear forces at individual joints and tunnel structure are plotted in Fig.6.18 and Fig.6.19, with the exact values listed in Tab.B.8 and Tab.B.9 of Appendix B. It can be concluded from the results that: (1) generally, in both normal and expansion scenarios, the maximum shear displacement occurs at the two end immersion joints (I1 and I6), which are the transition points between the approach structure and the immersed tunnel section; (2) joints on the two end elements (E1 and E5) have a more significant shear displacement than the joints on other three middle elements (E2, E3 and E4), indicating that the two end elements serve as the shear deformation transition section with a higher deformation gradient along tunnel axis, whereas along the three middle elements the shear deformation on dilation joints is insignificant; (3) the tunnel shear displacement plotted in Fig.6.20 also validates a high shear deformation gradient within the two ends elements, especially on the most northern (in E1) and most southern segments (in E5). This implies that for an immersed tunnel, vertical shear deformation tends to concentrate on the two end elements, and more attention should be paid to the joints on these two elements during maintenance work. In the Heinenoordtunnel, the monitoring result indicates a significant cyclic opening (with an amplitude of about 5mm over one year period) on joint D11, which is much larger than other dilation joints; and previously leakage has been observed at joint D11 (at E1) and joint D54 (at E5). These phenomena imply a higher deformation flexibility within these two end elements, which agrees with the simulation results.

Comparing the tunnel vertical deformation results with long-term settlement curves in Fig.6.21, it can be demonstrated that both simulation results and actual settlement curve reveal a concentrated settlement at the first and last immersion joints; the concentrated shear deformation in the simulation result agrees with the actual settlement curve, in that a higher deformation gradient occurs on the two end sections (between the first immersion joint and first element middle, and between fifth element middle and final immersion joint); in addition, the simulation result shows that along the three middle elements the settlement is around 1.8mm with insignificant differential settlements, which is consistent with the initial settlement curve in 1979 (baseline 1978), where the actual settlements fall within the range of 3.2mm to 7.8mm in the three middle elements and the differential settlement is insignificant (compared with the settlement curve in 2018). However, the continuously ongoing settlement tendency from 1978 to 2018, as well as

the local peak settlement (as high as 67mm) occurring in the middle of the first and fifth elements, is not adequately revealed in the simulation.

The continuous development of the long-term settlement at the Heinenoordtunnel may be due to factors such as weak geological soil conditions, the continuously increasing traffic loads the additional load from riverbed deposition, and/or creep of the foundation soil. The significant differential settlement at several locations may originate from the existence of weak soil layers distributed locally below the element, or the presence of voids in the sand bed foundation. Lacking precise geological and structure information, the 2D beam on the elastic foundation model possesses limitations in accurately simulating the long-term settlement behavior of the Heinenoordtunnel.

Comparing the shear deformation results of normal and expansion scenarios, it can be seen the segment expansion alters the shear displacement distribution along joints longitudinally. Observing the exact values in Tab.B.8 and Tab.B.9 of Appendix B, the shear displacement at all immersion joints is increased in the segment expansion scenario; however, the shear displacement at dilation joints is significantly smaller than those in the normal scenario, particularly among dilation joints on the two end elements. Therefore, the simulation result implies that seasonal segment expansion tends to reduce the shear deformation at dilation joints at the cost of increasing the shear deformation at immersion joints, hence enhancing the element's structural integrity.
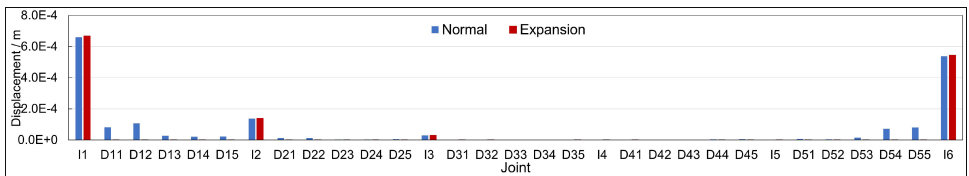
Figure 6.18: Comparison of joint shear deformation(unit:m)
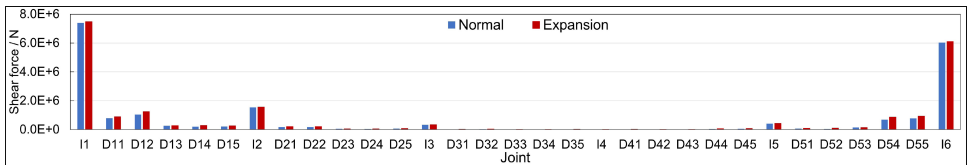
Figure 6.19: Comparison of joint shear force(unit:N)
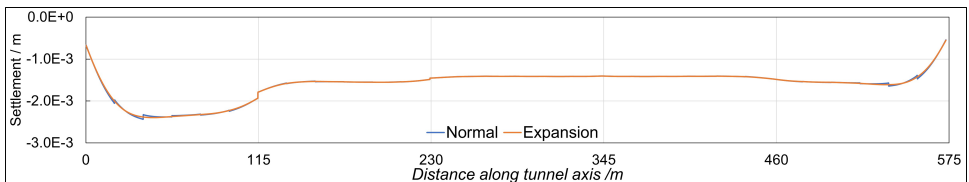
Figure 6.20: Comparison of tunnel shear deformation(unit:m)
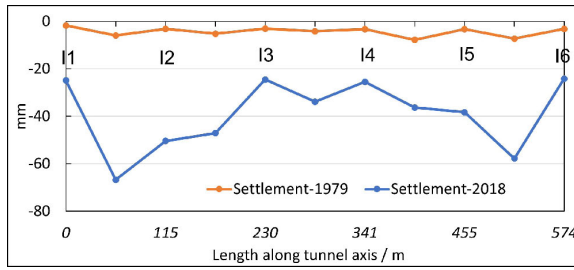
Figure 6.21: Long-term settlement curve of the Heinenoordtunnel (west tube)

Furthermore, the simulation results are compared with field measurements from the DOFS system. Firstly the average joint uneven settlement (absolute value) of the period December 1 to 10 (representing a normal scenario in winter) and that of the period June 20 to 30 (representing a segment expansion scenario in summer) are obtained, and the difference between the average joint uneven settlement for these two periods is calculated; similarly, the difference in joint shear displacement between normal and expansion situations is derived from simulation results. The comparison of six immersion joints and four dilation joints (of the two end sections) is summarized in Tab.6.5, with more detailed information presented in Tab.B.10 of Appendix B. The negative values indicate a decreasing tendency of joint shear deformation relative to a normal scenario, while a positive value means an increasing tendency.

Results in Tab.6.5 indicate that: both simulation and field measurements reveal segment expansion results in an increase in shear deformation at immersion joints I1 and I6, and the same trend holds true for dilation joints D11, D54, D55, and immersion joint I4; Observing the precise values of each joint, the measurement results indicate a reduced shear deformation at the majority of dilation joints in segment expansion scenario, and this decreasing shear deformation tendency is also demonstrated in the simulation. For immersion joints I3 and I4, however, simulation results are inconsistent with the measurements. Furthermore, despite consistency in the general trend of shear deformation development, there is a discrepancy in the magnitude of deformation values, which is primarily due to the uncertainties in model parameter determination.

Table 6.5: Shear deformation comparison (unit: mm)

Joint	I1	D11	D12	I2	I3	I4	I5	D54	D55	I6
Simulation	8.2×10^{-6}	-8.1×10^{-5}	-1.1×10^{-4}	1.8×10^{-6}	3.7×10^{-7}	1.7×10^{-8}	1.5×10^{-8}	-7.1×10^{-5}	-8.0×10^{-5}	7.8×10^{-6}
Measurement	3.8×10^{-1}	-2.3×10^{-1}	2.9×10^{-3}	-3.0×10^{-2}	-1.7×10^{-1}	-2.5×10^{-1}	-1.7×10^{-1}	-2.0×10^{-1}	-4.5×10^{-1}	3.0×10^{-2}

The cross-section rotation at individual joints is depicted in Fig.6.22 to Fig.6.23, with the exact values listed in Tab.B.11 and Tab.B.12 in Appendix B. It can be seen that: generally, in both normal and expansion scenarios, the maximum rotation occurs at the first and final immersion joints (I1 and I6); and rotation at immersion joints is much more significant than that at dilation joints. As immersion joints generally possess a substantially lower flexural stiffness than the dilation joints, it helps to mitigate the peak value of tunnel moment longitudinally compared with a tunnel beam without a joint.

Nonetheless, the moment at the immersion joint is significantly lower than that at dilation joints (see Fig.6.23), as the latter has a far higher flexural stiffness. For example, Fig.6.23 demonstrates that joint moment at D11 and D55 are significantly larger than those at other joints. This implies that at dilation joints large flexural moments exist, and if the flexural stress is not uniformly distributed at the joint interface, the local stress concentration may be highly likely to cause concrete cracking at the dilation joint, as observed in several immersed tunnels in the Netherlands, see Fig.1.5 and Tab.1.1 in Chapter 1.

Moreover, the rotation at the five immersion joints is mitigated in the expansion scenario compared to the normal scenario. However, among dilation joints, this change in joint rotation differs by joint position, according to the result listed in Tab.B.11 and Tab.B.12 of Appendix B.
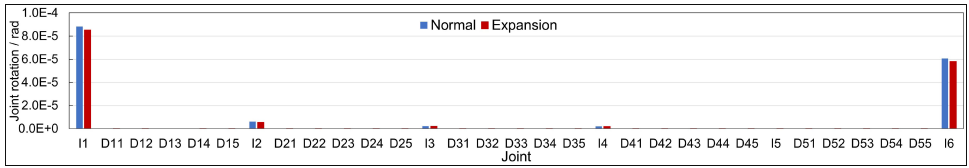
Figure 6.22: Comparison of joint rotation deformation(unit:rad)
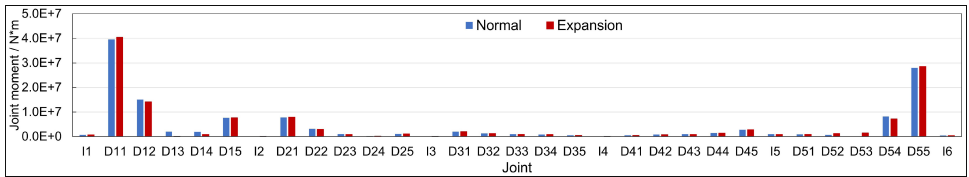
Figure 6.23: Comparison of joint moment(unit:N*m)

Additionally, cross-section rotation of the tunnel segments is presented in Fig.6.24. Observing the rotation deformation curve, a large gradient occurs within the two end elements (E1 and E5), which indicates a significant deformation concentration; while the curve is reasonably flat and has a low deformation gradient over the middle three elements (E2, E3, and E4). Note that the tunnel shear displacement curve in Fig.6.20 also show similar behavior. On the curve in Fig.6.24, three local discontinuous points occur, corresponding to three immersion joint locations (I2, I3 and I4).
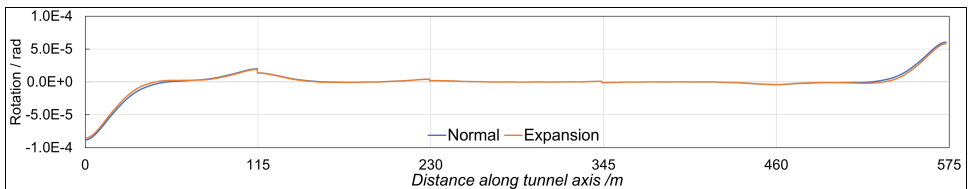
Figure 6.24: Comparison of tunnel section rotation

Moreover, segment expansion causes an alteration in the tunnel structural defor-

mation, which is most pronounced in the first and last elements (E1 and E5) along the tunnel's longitudinal axis, although the difference in deformation between the intermediate elements (E2 to E4) is insignificant. The curve in Fig.6.24 reveals that the segment expansion significantly reduces the cross-section rotation along tunnel elements E1 and E5. For instance, within the first segment of E1 (between 0 and 19m along the tunnel axis), the expansion reduces the rotation by a maximum of 8% compared with that in a normal scenario. Simulation results suggest that for tunnel maintenance, more attention should be paid to the joints within the first and last elements, as a significantly greater rotation may result in an excessive joint opening at the higher and lower cross-sections, therefore increasing the risk of leakage. In the Heinenoordtunnel, the leakage detected in the prior field check at joint D11 (at E1) and joint D54 (at E5) supports the suppositions drawn from the simulation results.

6.4.3. DISCUSSION

In this section, the effects of segment expansion on the tunnel structure are investigated using a simplified 2D beam on an elastic foundation model. The joint mechanical parameters are derived properly to take into account the segment expansion effects. The results demonstrate that the general tunnel settlement behavior from the simulation is consistent with the actual settlement curve in the initial monitoring of service period. Compared with normal conditions, segment expansion alters the distribution of shear and rotation deformation along the tunnel longitudinally, and this alteration is much more pronounced within the first and last elements, which serve as transition zones between immersed section and approach structure.

Due to a lack of precise model information, it should be noted that this 2D model possesses limitations in simulating the actual behavior of immersed tunnels precisely. In particular, a gap exists between simulation results and actual monitoring results regarding aspects of continuous development of long-term settlement, and differential settlement locally and potential excess joint opening.

Generally, the simulation precision is mainly determined by an accurate characterization of joint mechanical properties (structure parameters) and soil properties (a reasonable estimation of foundation soil parameters). For further study, more advanced modeling could be achieved by, on the one hand, improving the characterization of the tunnel structure considering the current joint status through more complete joint opening measurements, since the joint mechanical behavior is related to the current opening status; and on the other hand, obtaining more precise geological information and considering the possible soil spatial variation along tunnel axis longitudinally by conducting more field geological investigations. In addition, upgrading the 2D model to a 3D model could more appropriately simulate the complicated joint contact status and soil spatial variation in 3D space.

6.5. CONCLUSIONS

In this chapter, the field monitoring data collected over a one-year period by the distributed optical fiber sensor (DOFS) system is analyzed, and the seasonal deformation behavior of the Heinenoordtunnel is investigated in greater depth. The main conclusions

are as follows:

About seasonal behavior of the Heinenoordtunnel

The mechanism of seasonal cyclic joint opening at tunnel joints is strongly confirmed by the DOFS measurement, and these joint openings are negatively correlated with temperature, i.e. the joint gap tends to close during the summer and open during the winter.

The amplitudes of seasonal joint opening at immersion joints (joint I1 to I6 except I5) fall within a range of 1.77 to 6.15mm and are larger than those of most dilation joints (which fall within a range of 0.6mm to 2.0mm); however, at a few dilation joints (D11, D54 and D55), the amplitude of the joint opening shows a range of 2.2mm to 4.9mm and is comparable to that of immersion joints, indicating that for segmented immersed tunnel monitoring, dilation joint should be given the same extent of consideration as immersion joints. The monitoring results suggest that in particular the joints near the approach structure, namely I1 to D11 on the north end and D54 to I6 on the south end, exhibit substantial opening deformation, indicating a greater deformation flexibility along these two transition sections.

There exists a lag between joint opening deformation and temperature, suggesting that joint opening variation is delayed with respect to temperature change. At joint I1 (as well as the majority of joints), this delay is observed to be around 1 or 2 days. The stronger the temperature fluctuations are, the clearer this effect can be observed.

At most joints, the amplitude of uneven settlement is less than 1 mm; however, at joints I1 and D11, the amplitude reaches 2.35 mm and 1.15 mm, respectively; at individual joints, the scale of uneven settlement is significantly less than that of joint opening. The measured joint uneven settlement also shows seasonal variation, but at each joint the correlation (of uneven settlement) to temperature can be both negative and positive. Longitudinally tunnel segment tilting exists, and the degree of tilting also shows seasonal variation.

About the performance of DOFS monitoring system

The measured temperature strongly follows the ambient weather temperature throughout the monitoring period, indicating the temperature measurements by the DOFS sensors in field conditions are reliable. By selecting the optimal sensing fiber, the impacts of creep on measurement accuracy can be eliminated, and a measurement accuracy of 0.1mm can be maintained even with the anticipated maximum sensor installation deviations (with a horizontal deviation of 1 cm) in this field installation.

In the field installation, signal attenuation of the optical fiber loop mainly results from strong local optical fiber bending (beyond the specified bending limit), in addition to other factors such as connection quality. A total signal attenuation below 6 dB is preferable for a reliable measurement.

In summary, it is reasonable to conclude the installed DOFS monitoring system has an acceptable accuracy of 0.1mm in field conditions.

About structural behavior of the Heinenoordtunnel

The general, simulated tunnel settlement behavior is consistent with the actual settlement curve during the initial monitoring period; the seasonal segment expansion enhances the

REFERENCES123

integrity of the tunnel element longitudinally, and it tends to reduce the shear deformation at dilation joints while increasing it at immersion joints, which generally agrees with the deformation tendency revealed by the measurements.

The seasonal segment expansion modifies the joint rotation behaviour, with varying effects (increase or reduction in rotation) depending on the specific joint. Immersion joints have a greater amount of rotation than dilation joints, but dilation joints have a greater moment due to their greater flexural stiffness.

Seasonal segment expansion alters the tunnel segment shear and rotation deformation, and the change is more pronounced in the first and last elements. For tunnel maintenance, simulation and measurement results indicate that more attention should be paid to the first and last tunnel elements, namely the transition sections close to the north and south approach structures, because along these two sections a higher deformation flexibility was observed than along the middle tunnel elements.

REFERENCES

Abaqus (2022). *Abaqus analysis's guide 6.14*. Dassault Systèmes, RI, USA.

ATKINS, COWI, TEC, ChristiansenEssenbak, DeltaMarineConsultants, nmGeo & RAMBOLL (2019). Limfjord tunnel assessment and retrofitting-technical summary report, v 1.0. *Technical report*.

Bai, Y. & Lu, H. (2016). Damage analysis and rpair technology of omega gasket in immersed tube tunnel. *Journal of Railway Engineering Society* **33**, No. 9, 87–92.

fibrisTerre (2021). *User manual for fibristerre ftb series-fiber-optic sensing system for distributed strain and temperature monitoring (rev4.1)*. fibrisTerre Systems GmbH, Berlin, Germany.

Kwok, K. (2022). *Settlement behaviour of heinenoordtunnel-a numerical study*. Master's thesis, Delft University of Technology.

Leeuw, L. (2008). Lekkage in tunnels-dilatatievoegen en beton. *Technical report*, RWS Bouwdienst.

Liu, Z., Huang, H., Zhao, Y. *et al.* (2008). Immersed tube tunnel real-time health monitoring system. *Chinese Journal of Underground Space and Engineering* **4**, No. 6, 1110–1115.

Meteoblue (2022). Meteoblue weather report information. `https://www.meteoblue.com`, accessed: March-2022.

NEBEST (2016). Report-deformatiemeting-37h-312-01 heinenoordtunnel onder de oude maas.

Rahadian, R., van der Woude, S., Wilschut, D., Blom, C. & Broere, W. (2018). A new test setup for studying sand behaviour inside an immersed tunnel joint gap. In *Physical Modelling in Geotechnics*, CRC Press, pp. 443–448.

van Montfort, R. (2018). *Insufficiency of immersion joints in existing immersed tunnels: Case study on functioning of gina-seal and omega-seal in the kil tunnel.* Master's thesis, Delft University of Technology.

Xu, X., Tong, L., Liu, S. & Li, H. (2019). Evaluation model for immersed tunnel health state: A case study of honggu tunnel, jiangxi province, china. *Tunnelling and Underground Space Technology* **90**, 239–248.

Zhang, X. & Broere, W. (2022). Monitoring seasonal deformation behavior of an immersed tunnel with distributed optical fiber sensors. *Measurement, Under review* .

6

7

CONCLUSIONS AND RECOMMENDATIONS

7.1. CONCLUDING REMARKS

This thesis reported on a monitoring study on the behavior of immersed tunnels. It started by designing a qualified monitoring system using distributed optical fiber sensor (DOFS) and its subsequent field application in the Heinenoordtunnel, an immersed tunnel in the Netherlands. Based on the field monitoring results over one year period, the daily and seasonal behaviors of the immersed tunnel are explicitly investigated.

7.1.1. APPLICABILITY OF DOFS MONITORING SYSTEM

DESIGN DOFS FOR GENERAL EXTENSOMETER USE

For deformation monitoring, distributed optical fiber sensor(DOFS) offers advantages such as distributed sensing and long-distance sensing. In this thesis, DOFS is designed to function as extensometers for tunnel joint deformation monitoring, and it proves to work with a sub-millimeter accuracy in field conditions.

When designing DOFS for general extensometer use :

(1) The accuracy of the extensometer is generally decided by the optical fiber property, fiber fixation quality and interrogator performance. For a qualified optical fiber exhibiting negligible creep, the accuracy of a properly installed extensometer can be determined by multiplying the gauge length by the strain accuracy of the interrogator.

(2) In setting up an extensometer, the optical fiber can be generally fixed at two points by adhesive or physical clamping, The gauge length of the extensometer is preferably no less than the interrogator's spatial resolution, in order to minimize the systematic error caused by spatial resolution. The final determination of gauge length must take into account the anticipated displacement range, the maximum allowable strain of optical fiber, and the convenience of field installation.

(3) The temperature effects on deformation measurement must be appropriately compensated for, and a commonly adopted method is to set up a parallel zero-strain fiber length for dedicated temperature effect measuring.

(4) Tight-buffered fiber is preferred in extensometer use. The critical metrics for optimal fiber selection include the physical structure of optical fiber, the maximum working strain (MWS), the limit strain, the relaxation behavior, the strain coefficient, and the temperature coefficient. In addition, axial stiffness is also an important metric when manual pre-tensioning is required during sensor installation.

(5) For fiber property calibration, a combined tension test or a manual tension test can work effectively to obtain the fiber properties. The mechanical properties of the optical fiber can be verified by a combined tension test, preferably on a tension machine; the BFS-strain curve and axial stiffness can be obtained simultaneously in that way. In addition, a manual tension test also works for determining the properties of optical fibers with low axial stiffness, as demonstrated in this thesis.

(6) The relaxation of optical fibers causes measurement errors and shall be checked prior to field installation. According to the experimental results, relaxation of typical tight-buffered optical fibers (at a given initial imposed strain) generally consists of a (unrecoverable) plastic component and an (recoverable) elastic component. The plastic component can be fully triggered and removed by beforehand pre-tensioning, and hence a pre-tensioning of the sensing fiber before installation can help reduce measurement errors caused by relaxation.

(7) The relaxation behavior can be described by the characteristic loop of the sensing fiber, and the maximum relative error of the measurement can be assessed accordingly. The proposed relaxation model can quantify the upper bound estimate of measurement error.

APPLICABILITY OF DOFS SYSTEM FOR IMMERSED TUNNEL MONITORING

DOFS has been applied to monitor the behavior of an immersed tunnel in this thesis. The entire monitoring system comprises an interrogator and a long optical fiber that extends inside the tunnel longitudinally. At the joint position, the optical fiber was installed as an independent sensor block, which consists of two extensometers mounted by the three-point fixation method.

The designed sensor block was experimentally validated as capable of measuring joint deformation along three directions, including longitudinal joint opening, vertical uneven settlement(of the two sides) and lateral drift, with acceptable submillimeter measure accuracy. Experiment validates the sensor block can register joint openings as accurately as 0.1mm; For joint uneven settlements, the experiment shows a relative error below 10%, and an absolute error below 0.3mm for general use, which is superior to the reported accuracy of 1mm for the current manual levelling measurements in immersed tunnel.

The DOFS system was successfully implemented in the Heinenoordtunnel, where it monitors joint opening and uneven settlements of both immersion and dilation joints, with an accuracy of 0.1mm and data-collection frequencies in the order of once per 30 minutes. Moreover, this monitoring system is remote-controlled and imposes no disturbance to tunnel operation.

In field conditions, the measured temperature closely follows the ambient weather temperature throughout the monitoring period, confirming the measurement reliability of the DOFS system. By selecting the optimal sensing fiber, the impacts of creep on measurement can be eliminated; the measurement accuracy of 0.1mm can be maintained even with the anticipated maximum sensor installation deviation (with a horizontal deviation of 1 cm) in this study.

Signal attenuation of optical fiber loop in field monitoring mainly results from severe local optical fiber bending (beyond the prescribed bending limit), in addition to other factors such as connection quality. In this study, a total signal attenuation of below 2 dB (much lower than the threshed value of 6dB indicated by the interrogator manufacturer) is achieved on the 1.4 km-long sensing fiber loop in normal working conditions. Furthermore, a deformed cover board due to traffic impacts was observed which caused a local bending on the optical fiber, but it only temporarily influences the system as the signal deterioration was recovered after a cover board maintenance.

When building a DOFS monitoring system for joint deformation measuring as in this thesis, the following aspects shall be taken into account: the anticipated joint deformation range, ease of sensor installation, sensor and fiber protection, and remote availability of monitoring data.

The DOFS based monitoring can be combined with regular settlement measuring by manual levelling for a more comprehensive tunnel status monitoring. Settlement monitoring by manual leveling at yearly (or multiple years) interval is still the most common deformation monitoring practice in the current immersed tunnel monitoring,

7

but it only reveals the general longitudinal settlement behavior (macroscopic deformation behavior) of the entire tunnel body; DOFS features long-distance sensing (as long as one hundred kilometers) and all target points (or locations of interest) in a mega tunnel can be instrumented using a single optical fiber, which reveals the deformations behavior of local points or areas (microscopic deformation behavior) along the long immersed tunnel, such as joint opening at different positions of cross sections longitudinally.

In conclusion, DOFS has been validated with high applicability in behavior monitoring of immersed tunnels. The frequency of field monitoring (at sub-hour intervals) and the quality of the data obtained allow an investigation into both the daily and seasonal behavior of immersed tunnel.

7.1.2. BEHAVIOR OF THE IMMERSED TUNNEL

The DOFS system was successfully applied in the Heinenoordtunnel (a concrete segmented immersed tunnel in the Netherlands, with a rectangular cross-section) and measures joint opening and uneven settlements of both dilation and immersion joints, over a one-year period. The daily and seasonal behavior of the Heinenoordtunnel is investigated specifically.

DAILY BEHAVIOR OF THE IMMERSED TUNNEL

Field monitoring shows that joint opening is negatively correlated with temperature variations, indicating that the joint gap tends to open at low temperatures and to close at high temperatures. Therefore, the hypothesis that cyclic joint opening and closure driven by temperature variations occurs in the Heinenoordtunnel is validated.

Tidal variations (exhibiting an amplitude of around 1.2m with a half-day period) in the river above the tunnel generate a vertical response of the immersed tunnel. Monitoring results indicate the whole immersed section (five elements with a total length of 575m) behaves more or less like a rigid body and moves upwards(at low tide) and downwards(at high tide) periodically with tidal variations, with a sub-millimeter movement amplitude (about 0.3mm).

This cyclic movement of the tunnel can be explained by a coupled flow and consolidation model of underlying soil layers subject to tidal variations, and the response of the soil domain exhibits a time lag compared to the imposed tidal fluctuation. The numerical simulation reveals the tidal wave retards in the bottom sand layer below the clay; the soil domain response shows a lag of about 60 mins to tidal variation, which fits within the time lag range of 39 and 99 minutes as estimated by field conditions.

Moreover, tidal impact also causes tilting of some local segments in the Heinenoordtunnel (especially the most northern segment adjacent to the approach structure), but the extent of this tilting behavior varies between winter and summer seasons. The reduced tilt response in summer, when the tunnel structure is expanded and the joint openings are reduced (i.e. the rubber GINA gaskets are compressed more), implies the seasonal joint deformation affects the response of the tunnel to tidal and other load variations.

SEASONAL BEHAVIOR OF THE IMMERSED TUNNEL

The seasonal periodic opening at tunnel joints exhibits a negative correlation with temperature, indicating that the joint gap tends to close during the summer and open during the

winter. If longitudinal thermal segment expansion is fully compensated by joint opening, the immersed tube section (575m long) experiences a total seasonal expansion of about 41.5mm.

The amplitudes of seasonal joint opening at immersion joints (within a range of 1.77 to 6.15mm) are larger than those of most dilation joints (within a range of 0.6mm to 2.0mm); however, at a few dilation joints, the amplitude (within range of 2.2mm to 4.9mm) of the joint opening is comparable to that of immersion joints, indicating that for segmented immersed tunnel monitoring, dilation joint should be given the same extent of consideration as immersion joints.

The monitoring results reveal that the joints in close proximity to the approach structure display significant opening deformation, indicating increased deformation flexibility along the end segments close to the approach structure.

There exists a lag between joint opening deformation and temperature, suggesting that joint opening variation precedes temperature change. At the majority of joints, this delay is observed to be around 1 or 2 days; however, this effect is amplified when strong temperature fluctuations occur.

At most joints, the amplitude of uneven settlement is less than 1 mm; at individual joints, the scale of uneven settlement is significantly smaller than that of joint opening; the measured joint uneven settlement also exhibits seasonal variation, but at each joint the correlation (of uneven settlement) to temperature can be both negative and positive. Longitudinally tunnel segment tilting exists, and the tilting degree also shows seasonal variation.

Simulation results illustrate that the seasonal segment expansion enhances the integrity of the tunnel element longitudinally, and it tends to reduce the shear deformation at all dilation joints while increasing it at immersion joints, which generally agrees with the deformation tendency revealed by the measurement results. In addition, seasonal segment expansion also modifies the joint rotation, with varying effects (increase or reduction in rotation) depending on the joint.

Simulation results further show that seasonal segment expansion alters tunnel segment shear and rotation deformation, and the degree of change is more pronounced in the first and last elements. For tunnel maintenance, simulation and measurement results indicate that more attention should be paid to the first and last tunnel elements, namely the transition sections close to the north and south approach structures, because along these two sections a higher deformation flexibility was observed than along the middle tunnel elements.

As the joint rotation behavior of the model is influenced by the initial compression of the rubber seals and joint gaps, additional study is needed to detail the joint behavior in the actual tunnel. These studies require firstly measuring current joint width and estimating the original and current prestressing of the GINA at immersion joints, and evaluating the reliability of the embedded metal-rubber gasket at dilation joints, which is both time dependent and strongly joint-width dependent.

7.2. RECOMMENDATIONS

7.2.1. ABOUT APPLICABILITY OF DISTRIBUTED OPTICAL FIBER SENSOR (DOFS)

In this thesis, the DOFS are designed as extensometers to measure the joint deformation of the immersed tunnel. This DOFS monitoring system proves advantageous to conventional manual leveling in that the former can measure joint deformation along two directions at a significantly higher frequency, hence facilitating the investigation into daily and seasonal tunnel deformation behavior.

However, like any type of sensor, DOFS was found to expose some defects in this project which requires the attention of both sensor users and manufacturers. The first is a conflict between a high-sensitivity fiber and a well-buffered robust fiber. Specifically, an optical fiber with a thin buffering layer or sheath externally is preferred for high sensitivity. However, for the non-sensing section, the fiber cable is preferred to be well protected with a reinforcement sheath. The above criteria will result in a sensing optical fiber that is more applicable in harsh environments. It is recommended that future research should focus on developing ideal sensing fibers with acceptable deformation sensitivity (at the sensing end) and resilience in handling (at the non-sensing end).

Moreover, no technical standard exists for the property validation of optical fiber in deformation sensing. With more research projects using the DOFS system, such a standard will be of great significance for both the DOFS industry and academia. Note that this will require extensive collaboration between sensor users and manufacturers.

When implementing DOFS for large structure monitoring as demonstrated in this thesis, field instrumentation work can be performed section by section, where the sensing fiber loop can be extended along the monitoring area, since a qualified welding connection (fusing-splice) on fiber cable generally results in a low to negligible signal loss. Note that by dividing the instrumentation work section by section, the field workload per each entrance and the handled optical fiber length can be both reduced (which usually indicates a lower risk of fiber damage and a higher assurance of instrumentation quality), particularly when instrumenting an in-service tunnel that is not easily accessible, as in the case of this study.

In this thesis, the BOFDA interrogator (typed fTb2505 manufactured by fibrisTerra) performances generally meet the extensometer requirements (for joint deformation monitoring) in terms of strain accuracy, data-taking frequency and spatial resolution. The data collection interval is set at every 30 minutes, but can be lowered to a minimum of 8 minutes for the 1.4-kilometer-long fiber loop. This frequency performance completely satisfies the criteria for behavior monitoring during tidal fluctuation (with a period of about 12 hours) and daily temperature variation. However, this form of DOFS interrogator gives a spatial precision of 0.2 m, which has limits if a portion fiber length is desired to instrument the tunnel body (through continuous bonding) for distributed strain sensing. In that case, an interrogator type (for example the advanced PPP-BOTDA interrogator) with more precise centimeter-order spatial resolution will be preferable.

Another important aspect of DOFS application is temperature effects compensation in deformation sensing. In this thesis, a short zero-strain fiber length very close to the tensioned fiber length (gauge length) is used to indicate temperature effects, which is

a commonly used measure for temperature effects compensation in most monitoring studies. However, there remain errors in this temperature effects compensation, since a strained fiber may exhibit a different sensitivity to temperature change compared with a zero-strain fiber. This system error is basically caused by the interrogator's signal processing technique (the BFS-strain-temperature relation is expressed into a simplified linear relation by omitting the second-order component). A more precise temperature effects compensation can be achieved by using a multi-mode interrogator that operates on both Brillouin and Raman scattering modes, as the latter is only temperature dependent.

Finally, a reasonable monitoring scheme design may have to consider system cost in addition to the technical requirement. Note that for a complete DOFS system, the optical fiber cable was generally not costly, but an advanced interrogator is usually expensive. In the optical fiber sensing industry, an interrogator with more precise spatial resolution and multi-mode operation (Brillouin scattering, Raman scattering and Rayleigh scattering) generally entails a much higher cost. An acceptable monitoring scheme design will have to strike a balance between monitoring requirements and budgetary constraints.

7.2.2. ABOUT IMMERSED TUNNEL BEHAVIOR MONITORING

Although the designed DOFS monitoring system proves capable of measuring joint deformation along three directions in the laboratory experiment, in field monitoring the DOFS instruments only the joints on one sidewall due to space and accessibility limitations. For more comprehensive monitoring of immersed tunnels, the following recommendations are suggested:

(1) Monitoring transverse shear deformation at the joint should be preferred, and hence joint deformation along three directions can be obtained simultaneously.

(2) More measurement points (or locations) should be set to get more information about tunnel behavior. The deformation and the corresponding measurement points recommended include: (a) joint opening at both lower and upper cross-sections, which can indicate the segment tilting behavior; (b) sidewalls of both tubes should be instrumented, and the measured uneven settlement difference (on the two sides) help reveal the segment tilting/torsion in the transverse section; and (c) strain of selected points on tunnel segment, which helps to interpret the flexural and axial deformation of segment body.

(3) Besides joint deformation monitoring with DOFS in this thesis, other sensor types such as tilt sensors, are recommended to obtain additional deformation data. For instance, the relative settlement of the tunnel (to the approach structure) longitudinally can be obtained by combining the segment tilting information (from tilt sensors) with joint uneven settlement data (by DOFS).

(4) In addition to tunnel structure monitoring, interpreting the ground geological conditions as precisely as possible by methods such as geophysical investigations, also helps to analyze the tunnel settlement behavior in the service period.

As a recommendation for future immersed tunnel behavior monitoring, the proposed deformation measurements, potential sensor types, and monitoring locations are briefly listed in Tab.7.1.

Table 7.1: Recommendations for immersed tunnel behavior monitoring

Measurand	Sensor type	Monitoring location	Motivation
Joint opening	DOFS	Upper and lower positions at the joint cross-section	To measure the potential segment tilting longitudinally
Joint uneven settlement	DOFS	Sidewalls of both tubes	To measure the potential segment tilting/torsion transversely
Strain of segment body	DOFS or strain gauges	Sidewall, roof	To measure the expansion strain and flexural strain on segment body
Foundation soil property	Geophysical methods (wave-based method. et al.)	Tunnel foundation	To evaluate the foundation soil parameters

7.2.3. About immersed tunnel behavior simulation

In this thesis, the effects of segment expansion on tunnel structure are explored using a simplified 2D beam on an elastic foundation model. Due to a lack of precise model information, this 2D model possesses limitations in accurately simulating the actual deformation behavior of immersed tunnels. Specifically, there is a discrepancy between the simulation result and actual monitoring results in terms of the continuous development of long-term settlement, differential settlement locally, and the potential excess joint opening locally. The continuous growth of long-term settlement at the Heinenoordtunnel may be due to such factors as weak geological soil conditions, the continuously increasing traffic loading, the additional loading from riverbed deposition and secondary creep of the foundation soil. The significant differential settlement at several locations may originate from the existence of weak soil strata distributed locally beneath the tunnel element, or the presence of voids in the sand bed foundation.

Generally, the simulation precision is mainly determined by an accurate characterization of joint mechanical properties (structure parameters) and geological soil property (a reasonable estimation of foundation soil parameters). For further study, a more advanced modelling could be achieved by, on the one hand, improving the characterization of the tunnel structure considering the current joint status through a careful field joint measurement campaign, since the joint mechanical parameters are related to the current opening status; and on the other hand, acquiring more precise geological information and taking into account the possible soil spatial variation along tunnel axis longitudinally by conducting more field geological investigations on the tunnel foundation. In addition, upgrading the 2D model to a 3D one could simulate more precisely the complicated joint contact status and soil spatial variation in 3D space.

7

A

APPENDIX A

This appendix provides supplemental data to Chapter 5, specifically correlation factors of joint deformation with temperature and tide.

A

A.1. Joint Deformation Correlation with Temperature and Tide

This part includes the joint deformation correlation to temperature and tide level.

Table A.1: Correlation of joint opening with temperature (joint D31 to I6)

Joint	D31	D32	D33	D34	D35	I4	D41	D42	D43	D44	D45	I5	D51	D53	D54	D55	I6
Jun12	-0.59	-0.64	-0.33	-0.55	-0.43	-0.30	-0.64	0.07	-0.50	-0.37	-0.32	-0.05	-0.35	-0.39	-0.56	-0.09	-0.13
Jun13	-0.77	-0.72	-0.56	-0.61	-0.50	-0.53	-0.81	-0.40	-0.61	-0.55	-0.46	-0.23	-0.54	-0.64	-0.68	-0.43	-0.67
Jun14	-0.84	-0.81	-0.71	-0.72	-0.75	-0.74	-0.87	-0.62	-0.68	-0.72	-0.67	-0.61	-0.74	-0.77	-0.80	-0.68	-0.78

Table A.2: Correlation of joint uneven settlement with temperature (joint D31 to I6)

Joint	D31	D32	D33	D34	D35	I4	D41	D42	D43	D44	D45	I5	D51	D53	D54	D55	I6
Jun12	-0.33	-0.89	-0.36	-0.53	-0.31	-0.53	-0.40	-0.77	-0.49	-0.81	-0.28	0.11	-0.42	-0.57	0.54	-0.46	-0.27
Jun13	-0.17	-0.82	-0.14	-0.46	-0.22	0.24	-0.62	-0.84	-0.34	-0.74	-0.42	0.69	-0.51	-0.30	0.48	-0.24	-0.48
Jun14	-0.42	-0.92	-0.67	-0.79	0.15	-0.20	-0.82	-0.82	-0.85	-0.91	-0.91	0.67	-0.82	-0.89	0.73	-0.88	-0.44

Table A.3: Correlation of joint opening with tide (D31 to I6)

Joint	D31	D32	D33	D34	D35	I4	D41	D42	D43	D44	D45	I5	D51	D53	D54	D55	I6
Jun12	0.00	0.26	0.12	0.05	0.13	0.38	0.03	0.21	0.14	0.04	0.00	0.05	0.05	0.04	0.33	0.42	0.17
Jun13	0.10	0.07	0.10	0.10	0.05	0.16	0.19	0.19	0.04	0.10	-0.02	-0.04	0.08	0.06	0.20	0.30	0.18
Jun14	-0.21	-0.11	-0.16	-0.18	-0.14	-0.15	-0.13	-0.17	-0.17	-0.23	-0.24	-0.20	-0.21	-0.24	-0.15	-0.10	-0.08

Table A.4: Correlation of joint uneven settlement with tide (D31 to I6)

Joint	D31	D32	D33	D34	D35	I4	D41	D42	D43	D44	D45	I5	D51	D53	D54	D55	I6
Jun12	0.01	0.04	0.11	-0.04	-0.13	0.00	0.05	0.07	-0.14	0.03	-0.01	-0.45	0.40	-0.05	-0.17	0.06	0.94
Jun13	-0.15	-0.03	-0.14	-0.31	-0.15	-0.26	-0.22	-0.03	-0.33	-0.06	-0.09	-0.42	0.15	-0.35	-0.25	0.03	0.89
Jun14	-0.05	0.05	0.07	-0.07	-0.11	-0.28	-0.11	0.08	0.00	0.01	0.00	-0.10	0.12	-0.07	-0.14	0.04	0.81

A.2. Joint Deformation Data

The joint deformations corresponding to June 12 to June 14 are available by contacting the thesis author.

B

APPENDIX B

This appendix provides supplemental data to Chapter 6, specifically estimates of measurement errors due to installation effects, the determination of joint mechanical parameters for the longitudinal beam model and joint deformation results calculated from the numerical model.

B.1. Measurement Error Estimation Due to Installation Error

As shown in Fig. B.1, locating and fixing point P3 precisely is relatively more difficult than P2 according to field installation experience, as the tensioned fiber FL2 tends to pull the pad 3 and causes deviation. For horizontal joint opening measurement, the deviation of P2 in the vertical direction (within a range of 5mm) only results in second-order effects that create insignificant errors; the installation deviation of P3 will impact the precision of uneven settlement measurement.

Note the deviation of P3 in the vertical direction alone will not affect the strain-displacement mathematical relations (derived from the right-angled triangle M-P2-P3) mentioned in Eq.4.2 to Eq.4.8 in Chapter 4, and hence it has no influence on measurement accuracy. However, the deviation in the horizontal direction will alter the strain-displacement mathematical relations and should be considered, as seen in Fig.B.1b.

(a) Normal installation   (b) Installation with potential horizontal deviation
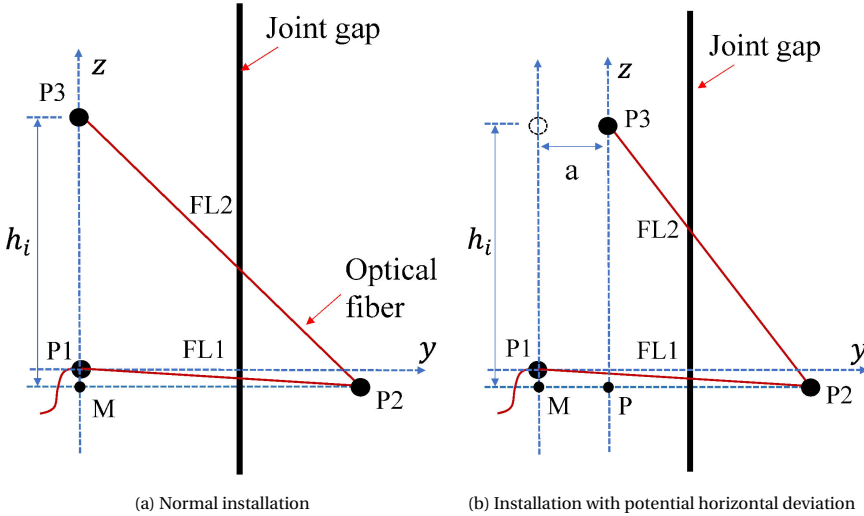
Figure B.1: Sensor installation error analysis

If a horizontal deviation (see a in Fig.B.1b), with an estimated maximum of 10mm occurs at initial sensor installation, from the right-angled triangle P-P2-P3, the height difference between P2 and P3 can be calculated as:

$$h_i = \sqrt[2]{l_{2,i}^2 - (l_{1,i} - a)^2} \tag{B.1}$$

While in normal working conditions,

$$h_i = \sqrt[2]{l_{2,i}^2 - l_{1,i}^2} \tag{B.2}$$

Where $l_{1,i}/l_{2,i}$ are the lengths of FL1/FL2 at interval i which were calculated by Eqs.4.1 to 4.6 in Chapter 4.

Tab.B.1 listed the calculated uneven settlement of 7 joints (I1 to I2) from the optical fiber sensor system considering different horizontal deviation levels. The results corresponding to a=0 indicate a proper installation scenario with no errors. It can be demonstrated the measurement error under extreme deviation condition (a=10mm) is smaller than 0.1mm in both winter and summer seasons, with mostly below 0.04mm on June5, 2021. Therefore, field installation errors have limited effects on the measurement accuracy of DOFS.

Table B.1: Uneven settlement measurement error estimation

	December 17, 2020					June 5, 2021				
a	10mm	5mm	0	-5mm	-10mm	10mm	5mm	0	-5mm	-10mm
I1	-0.01	-0.01	-0.01	-0.01	-0.01	-0.18	-0.18	-0.17	-0.16	-0.15
D11	0.09	0.10	0.11	0.11	0.12	0.44	0.47	0.50	0.53	0.56
D12	-0.03	-0.03	-0.03	-0.03	-0.03	0.24	0.25	0.26	0.27	0.28
D13	-0.06	-0.06	-0.05	-0.05	-0.05	0.56	0.57	0.58	0.60	0.61
D14	-0.11	-0.11	-0.11	-0.11	-0.10	-0.31	-0.31	-0.30	-0.30	-0.29
D15	-0.03	-0.03	-0.03	-0.03	-0.03	0.03	0.04	0.04	0.05	0.06
I2	-0.02	-0.02	-0.02	-0.02	-0.01	0.54	0.55	0.57	0.58	0.59

B.2. Joint Mechanical Parameters Determination

This part focuses on the joint mechanical parameter determination for the 2D model solution. In the first model representing the normal scenario, the joint parameters are obtained from the initial status following construction; in the second model representing the segment expansion scenario, the joint parameters are revised appropriately.

The seasonal longitudinal segment expansion will impose a pretension effectön the immersed tunnel structure and affects the joint mechanical properties. At each joint, the joint closure (by segment expansion) is assumed as below: (a) at immersion joints a compression of 4mm is assumed, based on field measurement; (b) for majority of dilation joints, the seasonal expansion varies between 0.4 to 1.5mm, and here a compression of 1mm is assumed at all the dilation joints; (c) the closure joint compression is set as 1mm according to measurement.

B.2.1. Immersion joint

At immersion joints, GINA gasket seal is placed and further compressed in tunnel element immersion process. The force-compression property of it affects joint stiffness and should be first studied. In the Heinenoordtunnel, two types of GINA gasket are used, namely G-190-148-50 and G-190-109-60. Type G-190-109-60 gasket has a lower compression limit and was used in the first and final immersion joints (see Fig.B.2a), while Type G-190-148-50 (see Fig.B.2b) has a larger dimension and was placed at the other three immersion joints (the 2nd, 3rd and the 4th joint from north). Note that the 5th immersion joint was constructed by on-site concreting and has different behaviors than a standard immersion joint with a GINA gasket.

Fig.B.3 illustrates the compression curve (force-compression) for the two types of GINA gaskets. For simplicity, the compression curve is modeled as a polyline with two
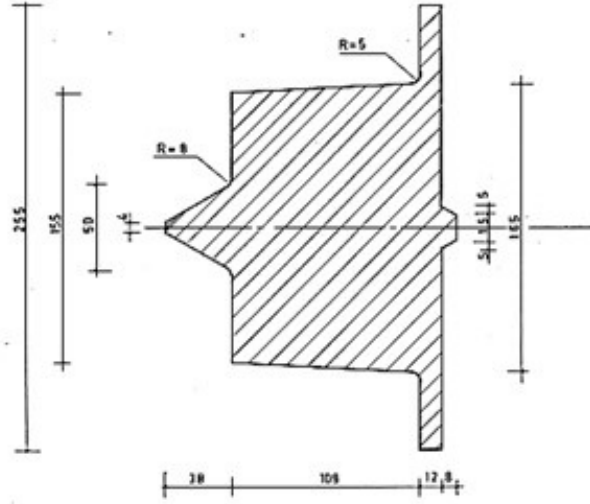
(a) G-190-109-60 GINA gasket
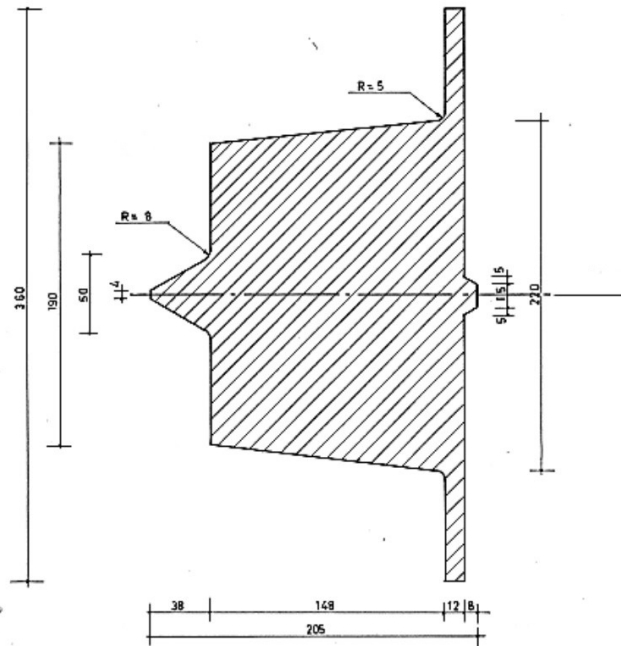
(b) G-190-148-50 GINA gasket

Figure B.2: GINA gasket profile

linear curves, as seen in Fig.B.4, and the relevant parameters are shown in Tab.B.2.

B
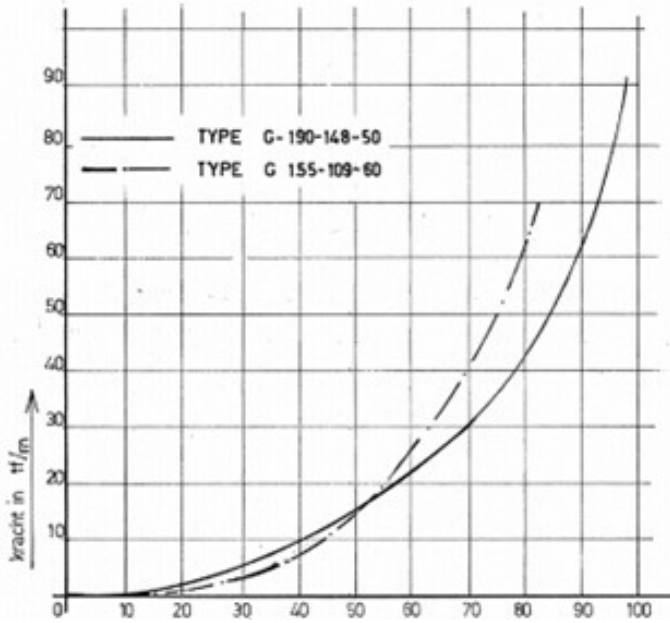
Figure B.3: Compression curve of GINA gasket
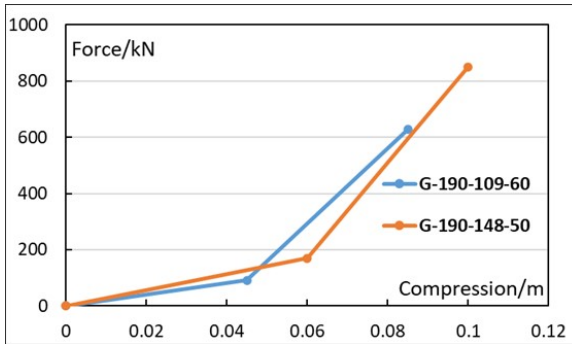
Figure B.4: Modelled Compression curve of GINA gasket (per meter)

AXIAL DEFORMATION

The GINA gasket at immersion joints will be compressed or decompressed under longitudinal axial forces. Here the joint axial force-compression curve is also a polyline, but note that the GINA gasket has an initial compression in the construction process. The joint axial deformation curve is shown in Fig.B.5. Setting the tension force as the right direction, the base point is moved to the initial compression point. The normal force at the immersion joint is shown in Eq.B.3:

$$F_N = f(d) * L \tag{B.3}$$

Table B.2: Compression curve parameters of GINA gasket

Type	Compression stiffness (kN/m)
G-190-109-60	2027 (compression <0.045m); 13412 (compression >0.045m)
G-190-148-50	2833 (compression <0.06m); 17000 (compression >0.06m)

Where F_N is normal axial force, while $f(d)$ is the compression force of GINA (per meter) and L indicates the total length of GINA at joint (77m). According to the tunnel alignment, the initial hydrostatic water pressure at element immersion is about 32MN (for joint I1, I4, I5 and I6) and 44MN (for joint I2 and I3), and the initial GINA compression at each joint are: 70mm at joint I1 and I6, 87mm at joint I2 and I3, 79mm at joint 4. Some the key parameters are listed in Tab.B.6.

In the expansion scenario, GINA gasket is set to be further compressed by 4mm due to joint closure. This does not alter the axial stiffness of the immersion joint but changes the division points $d_{N,1}$ on the $F_N - d_N$ curve. The altered joint parameters are listed in Tab.B.6.

(a) Axial behavior   (b) Flexural behavior   (c) Shear behavior

Figure B.5: Mechanical behavior of immersion joint

FLEXURAL DEFORMATION

Under normal working circumstances, the GINA gasket will not be compressed to its maximum value (109mm for Type G-190-109-60 and 148mm for Type G-190-148-50) or decompressed to the point where a joint leakage occurs. Flexural deformation of the immersion joint is also determined by the GINA gasket behavior, as shown in Fig.B.6.

If the flat section bending assumption is adopted, the GINA compression along the cross-section vertically is described in Eq.B.4:

$$x = x_0 + \theta z \tag{B.4}$$

Where x_0 indicates the GINA compression at section centroid; θ is the rotation angle (rad) and z is the distance to the centroid.

The internal force equilibrium equations at joint are described in Eq.B.5 and Eq.B.6:
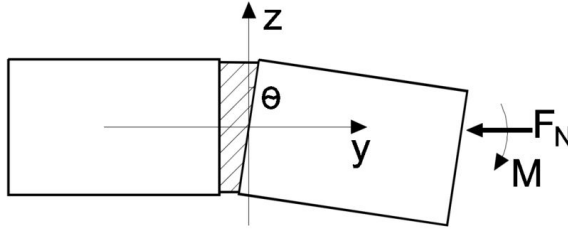
Figure B.6: Flexural deformation of immersion joint

$$M = L_t * f(x_0 + \theta z_t) z_t + L_b * f(x_0 + \theta z_b) z_b + 2\int_{z_b}^{z_t} f(x_0 + \theta z) z dz \qquad (B.5)$$

$$F_N = L_t * f(x_0 + \theta z_t) + L_b * f(x_0 + \theta z_b) + 2\int_{z_b}^{z_t} f(x_0 + \theta z) dz \qquad (B.6)$$

Where L_t and L_b mean the GINA gasket length at top and bottom side (here as 30.1m); z_t and z_b indicate the distance of GINA gasket at top and bottom side to the centroid (here as 4.1m); it should be noted to decide the moment-rotation angle relation, the initial compression forces F_N of GINA at each joint should be firstly determined (I1 to I6 excluding I5, as 70mm, 87mm, 87mm, 79mm, and 70mm). The key parameters of moment-rotation angle curve at each immersion joint are listed in Tab.B.6, and here the maximum rotation angle refers to the status where the GINA at the top or bottom reaches the maximum compression value.

Note that in the expansion scenario, a further compression (due to joint closure) of 4mm is added to x_0 in Eq.B.4. This does not alter the bending stiffness of the immersion joint but changes the division points of the $M - \theta$ curve. The altered joint parameters are displayed in Tab.B.6.

SHEAR DEFORMATION

At each immersion joint of Heinenoordtunnel, a shear key is constructed on the central wall by on-site concreting after the tunnel element is connected. The joint shear deformation is characterized as in Eq.B.7:

$$F_S = GA_s \frac{d_s}{L_s} \qquad (B.7)$$

Where d_s is the vertical shear displacement; G indicates the shear modulus of concrete (11.2GPa); A_s indicates the cross-section area of shear key (0.8m^2); L_s is the shear key length (0.9m). The parameters of shear keys at each immersion joint are listed in Tab.B.6. The joint closure generally does not affect the shear key behavior at immersion joints, and the parameters remain the same for both models.

B.2.2. DILATION JOINT

The dilation joint has a different layout compared to the immersion joints, and hence different mechanical properties.

AXIAL DEFORMATION

At dilation joints the concrete interface transfers axial forces. The relation of normal axial forces with deformation is described in Eq.B.8:

$$F_N = \frac{AE * x}{l_0} \tag{B.8}$$

where x is the axial deformation at the dilation joint; F_N is the normal axial force at the dilation joint; A is the contact area (93.66 m^2); E indicates the elastic modulus of concrete (30 GPa); l_0 means the characteristic length of dilation joint (0.02m).

Note that at each dilation joint an initial compression force (as N_0, equals to the hydrostatic pressure) is imposed during the element immersion. Here the tension force is set as the right direction, and the joint axial deformation curve is illustrated in Fig.B.7a. It should be noted that at the dilation joint, when the axial force (tension, or decompression) exceeds N_0, the initial compression, $d_{N,0}$ is fully compensated by external forces, and a full joint opening occurs which indicates an unsafe or failure status of the dilation joint. This unsafe status is not considered in the modeling since it suggests an abnormal operational state. Some key model parameters are listed in Tab.B.7.

In the expansion scenario, a further compression (due to joint closure) of 1mm is added to l_0 in Eq.B.4. This does not alter the axial stiffness of dilation joints but changes the division points of N_0 and $d_{N,0}$ is the $F_N - d_N$ curve. The altered joint parameters are presented in Tab.B.7.

(a) Axial behavior   (b) Flexural behavior   (c) Shear behavior
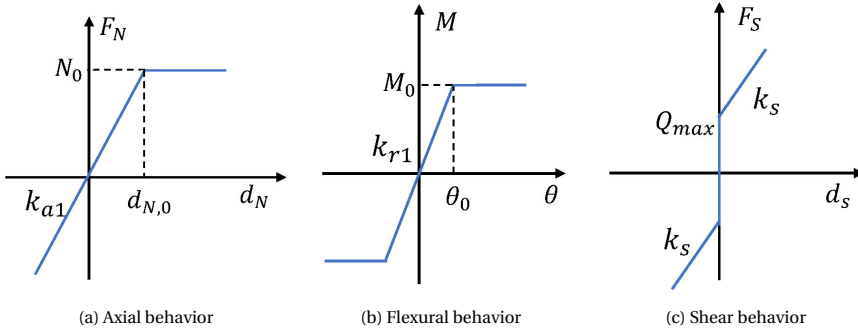
Figure B.7: Mechanical behavior of dilation joint

FLEXURAL DEFORMATION

As initial compression pressures are exerted on a typical dilation joint during the tunnel immersion process, the bending moment will firstly compensate for these stresses. As the bending moment increases, the compression stress will be entirely compensated at the most external border of the cross-section (say the farthest upper boundary in Fig.B.8), indicating the critical status. After then the joint opening occurs partially to completely at the joint cross-section with an increasing bending moment, which indicate an unsafe or failure status of dilation joint as damage of the gasket seal and joint leakage may occur.

The flexural deformation of a dilation joint under normal working conditions is described in Eq.B.9:
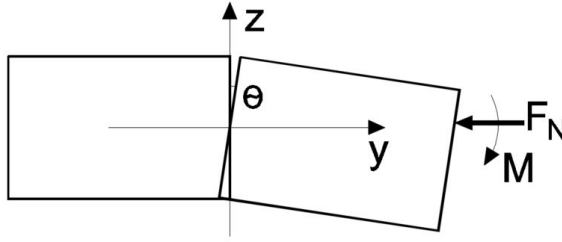
Figure B.8: Flexural deformation of dilation joint

$$M = \frac{\theta}{l_0} EI \tag{B.9}$$

Where θ is the rotation angle (rad); I means the cross-section inertia ($1085.18\,\text{m}^4$); E indicates the elastic modulus of concrete (30 GPa); l_0 means the characteristic length of dilation joint (0.02m).

For a dilation joint under normal working conditions, the critical status will generally not be reached. Here the maximum allowed bending moment M_0 at dilation joint is defined as the moment at which compression stress at the most external edge of the cross-section is fully compensated, and M_0 is determined as in Eq.B.10:

$$M_0 = \frac{N_0}{A} W \tag{B.10}$$

Where N_0 means the initial normal compression force at dilation joint(the hydrostatic pressure); A is the section area ($93.66\,\text{m}^2$) ; W indicates the section modulus. The key parameters of flexural property at dilation joints are listed in Tab.B.7.

Note in the expansion scenario, a further compression (due to joint closure) of 1mm is added to $d_{N,0}$ in Eq.B.4. This does not alter the bending stiffness of dilation joints but changes the division points θ_0 of the $M - \theta$ curve. The altered joint parameters are listed in Tab.B.7.
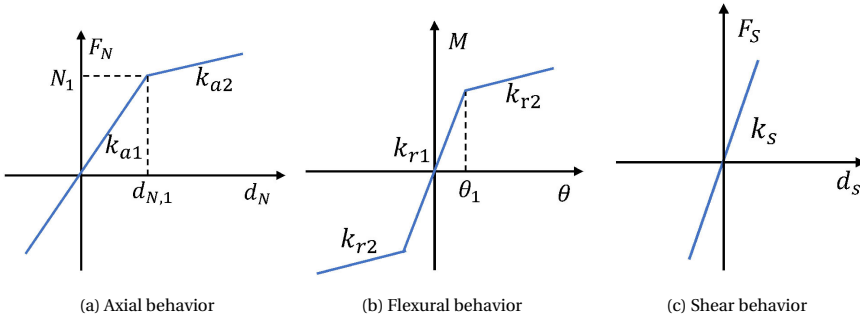
SHEAR DEFORMATION

At each dilation joint the shear deformation is characterized as in Eq.B.11:

$$F_S = GA \frac{d_s}{l_0} \tag{B.11}$$

Where d_s is the vertical shear displacement; G indicates the shear modulus of concrete (11.2 GPa); A_s indicate the cross-section area of dilation joint ($93.66\,\text{m}^2$); l_0 means the characteristic length of dilation joint (0.02m).

As the contact area of the dilation joint cross-section is relatively large, and there exists static friction at the interface, which is described as in Eq.B.12:

$$Q_{max} = \mu * N_0 \tag{B.12}$$

Where Q_{max} is the estimated maximum static friction force; μ is the friction coefficient at concrete interface (0.6); N_0 means the initial normal compression force at dilation joint.

As an infinite shear stiffness will cause unstable results in FEM analysis, here a limited shear displacement of 2mm is assumed at Q_{max}.

Note in the expansion scenario, a further compression (due to joint closure) of 1mm is exerted along the joint characteristic length l_0, and this cause an additional compression force of 0.05E at joints (E indicates the elastic modulus of concrete). This additional force does not alter the shear stiffness of dilation joints but changes the maximum static friction force of the $F_S - d_s$ curve. The key parameters of shear deformation at dilation joints are listed in Tab.B.7.

The cast-in-situ closure joint (the 5th immersion joint) has a similar formation as dilation joints, and hence a similar mechanical property but with a characteristic length of 1m. The key parameters are listed in Tab.B.7.

In Abaqus CAE, the connector element is used to simulate the joint, while the spring mechanical curve (force-displacement or moment-rotation angle curves) can be defined with input values, see Fig.B.9.

B.3. SUBGRADE REACTION COEFFICIENT Ks

In the beam on foundation model, the subgrade reaction coefficient (as Ks) should be firstly determined. There is no field plate loading test conducted to determine the Ks in Heinenoordtunnel, and here the shear wave data obtained by MASW (Multichannel Analysis Shear Wave) method in Heinenordtunnel is used to estimate the K_s.

The shear wave profile measured from MASW method is presented in Fig.B.10, here the x-axis started from the north tunnel portal. The locations of tunnel elements are illustrated in Fig.B.10, and at each element the V_s profile at the middle are used.

According to Robertson and Cable (2015), the estimation of K_s from ground soil shear wave velocity (V_s) are as below:

$$K_s = \frac{E}{B(1-v^2)} \tag{B.13}$$

$$E = 2(1+v)G_{eq} \tag{B.14}$$

$$G_{eq} = \Psi G_0 \tag{B.15}$$

Where E is Young's modulus of the subgrade soil; B is the foundation width, as 19m for a single segment in Heinenoordtunnel; v is the poison's ratio of soil, ranging between 0.2 to 0.3; G_{eq} is the shear modulus of the soil, G_0 is the small-strain shear modulus of soil; Ψ is the conversion factor which is related to the stress history (normal-consolidated or over-consolidated) and stress level (q/q_{ult}) of the subgrade soil, namely the bearing pressure q and estimated ultimate resistance q_{ult}.

The small-strain shear modulus G_0 can be directly estimated from V_s, as

$$G_0 = \gamma * (V_s)^2 = a * (V_s)^b * (V_s)^2 \tag{B.16}$$

where γ is the density of subgrade soil in kN/m^3; V_s is the shear velocity in m/s (averaged along the influence depth of foundation); a, b are relation factors determined as 4.12 and 0.262 respectively.

An individual tunnel segment (with a length of 30.7m and width of 19m) can be seen as a rectangular shallow foundation. The zone of influence is the zone of soil that
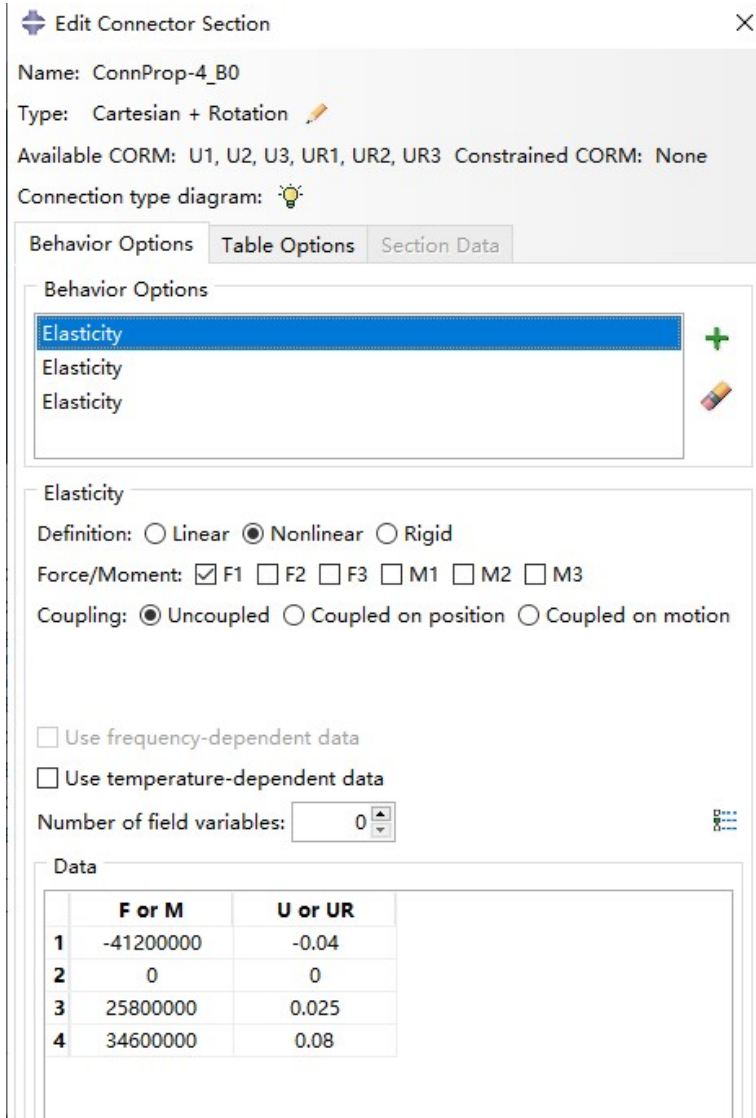
Figure B.9: Joint mechanical parameter input in Abaqus model

is influenced by stress caused by the shallow foundation causing it to settle. Here the influence depth under the tunnel is assumed to be the depth to which the increase in stress due to the load is larger than 20% of the previous in-situ effective stress (hence the 20% rule). The stress increase calculation beneath the centroid point of the rectangular foundation has been detailed in Poulos and Davis (1974). With a load of $37.7 kN/m^2$ distributed along the foundation area, the influence depth is determined as 12m.

To determine the conversion factor Ψ in Eq.3 as specified in Robertson and Cable
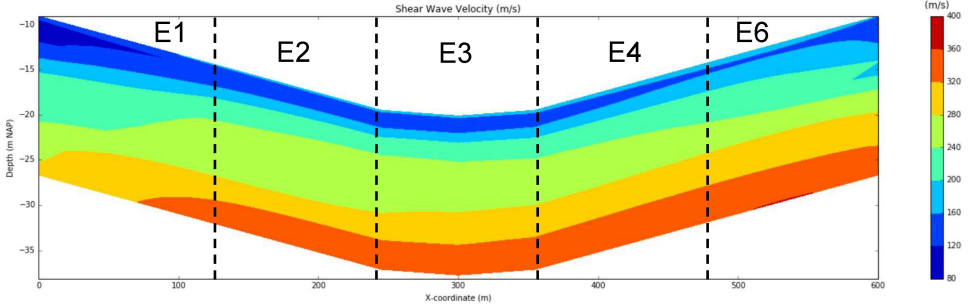
Figure B.10: Shear wave velocity profile beneath tunnel elements

(2015), the stress level (q/q_{ult}) of the subgrade soil should be initially estimated. The q_{ult} is estimated as in Eq.4 according to Keçeli (2012):

$$q_{ult} = 0.1 * \gamma * V_s * \beta \tag{B.17}$$

Where β is a correction factor of q_{ult} based on foundation size, which is expressed as (0.83-0.01B). According to Xia et al.(2002), the shear wave velocities obtained from MASW differ from that obtained from direct borehole measurements, with a difference of approximately 15% or less. Here the V_s from MASW is reduced by 15% when used to calculate the K_s. The results are listed as in Table B.3.

Table B.3: Determination of subgrade reaction coefficient

Element No.	V_s (m/s)	G_0 (MPa)	q_{ult} (kPa)	Ψ	K_s (MPa)
E1	164	422	164	0.38	21
E2	190	589	198	0.4	31
E3	198	650	209	0.4	34
E4	198	650	209	0.4	34
E5	191	600	200	0.4	31

REFERENCES

(1) Poulos, H.G and Davis, E.H.(1974). Elastic solutions for soil and rock mechanics.John Wiley, New York.

(2) Robertson, P. K. and Cabal, K.L.(2015). Guide to cone penetration testing, 6th Edition. Gregg Drilling.

(3) van Amsterdam, B. (2019). Probabilistic analysis of immersed tunnel settlement using cpt and masw. Master's thesis, Delft University of Technology, the Netherland.

(4) Keçeli, A. (2012). SOIL PARAMETERS WHICH CAN BE DETERMINED WITH SEISMIC VELOCITIES. Jeofizik 16: 17-29.

(5) Xia J., Miller R. D., Park C. B., et al. (2002). Comparing shear-wave velocity profiles inverted from multichannel surface wave with borehole measurements.Soil Dynamics and Earthquake Engineering, 22(3):181–190.

B.4. PARAMETERS COLLECTION

Table B.4: Measured joint deformation range (D31 to I6)

Deformation		D31	D32	D33	D34	D35	I4	D41	D42	D43	D44	D45	I5	D51	D53	D54	D55	I6
Opening	Min	-0.07	-0.17	-0.16	-0.15	-0.20	-0.50	-0.06	-0.40	-0.08	-0.18	-0.19	-0.26	-0.18	-0.11	-0.34	-0.21	-0.35
	Max	0.55	1.01	1.10	1.29	1.17	2.69	0.61	1.33	0.75	1.09	1.17	1.06	1.72	0.85	1.87	2.83	1.43
	Amplitude	0.62	1.18	1.26	1.44	1.37	3.19	0.67	1.73	0.83	1.27	1.36	1.32	1.91	0.96	2.20	3.04	1.77
Settlement	Min	-0.05	-0.13	-0.15	-0.11	-0.02	-0.14	-0.06	-0.17	-0.06	-0.09	-0.19	-0.16	-0.24	-0.19	-0.08	-0.56	-0.26
	Max	0.11	0.08	0.00	0.07	0.18	0.42	0.07	0.09	0.10	0.08	0.06	0.13	0.10	0.29	0.26	0.22	0.31
	Amplitude	0.16	0.21	0.16	0.18	0.20	0.55	0.12	0.26	0.16	0.18	0.25	0.29	0.33	0.48	0.35	0.78	0.57

Table B.5: Correlation of joint deformation with temperature (joint D31 to I6)

Joint	D31	D32	D33	D34	D35	I4	D41	D42	D43	D44	D45	I5	D51	D53	D54	D55	I6
$C_{o,t}$	-0.99	-0.96	-0.92	-0.94	-0.96	-0.90	-0.97	-0.96	-0.96	-0.96	-0.97	-0.94	-0.96	-0.96	-0.94	-0.87	-0.95
$C_{s,t}$	-0.86	-0.72	-0.46	0.15	-0.12	-0.92	-0.83	-0.82	-0.84	0.59	0.61	-0.82	-0.06	-0.82	-0.88	0.55	0.32

Table B.6: Joint parameter in longitudinal tunnel structure modeling (immersion joint)

Parameter		Unit	I1		I2		I3		I4		I6	
			Normal	Expansion	Normal	Expansion	Normal	Expansion	Normal	Expansion	Normal	Expansion
Flexural	K_{r1}	kN*m	8.06×10^6	8.06×10^6	1.02×10^7	1.02×10^7	1.02×10^7	1.02×10^7	1.02×10^7	1.02×10^7	8.06×10^6	8.06×10^6
	θ_1	rad	6.10×10^{-3}	7.00×10^{-3}	6.00×10^{-3}	6.60×10^{-3}	6.00×10^{-3}	6.60×10^{-3}	5.00×10^{-3}	5.80×10^{-3}	6.10×10^{-3}	7.00×10^{-3}
	M_0	kN*m	4.92×10^4	5.64×10^4	6.12×10^4	6.73×10^4	6.12×10^4	6.73×10^4	5.10×10^4	5.92×10^4	4.92×10^4	5.64×10^4
	K_{r2}	kN*m	8.06×10^5	8.06×10^5	9.44×10^5	9.44×10^5	9.44×10^5	9.44×10^5	1.02×10^6	1.02×10^6	8.06×10^5	8.06×10^5
Shear	K_s	kN/m	1.12×10^7	1.12×10^7	1.12×10^7	1.12×10^7	1.12×10^7	1.12×10^7	1.12×10^7	1.12×10^7	1.12×10^7	1.12×10^7
Axial	K_{a1}	kN/m	1.03×10^6	1.03×10^6	1.31×10^6	1.31×10^6	1.31×10^6	1.31×10^6	1.31×10^6	1.31×10^6	1.03×10^6	1.03×10^6
	K_{a2}	kN/m	1.60×10^5	1.60×10^5	2.20×10^5	2.20×10^5	2.20×10^5	2.20×10^5	2.20×10^5	2.20×10^5	1.60×10^5	1.60×10^5
	$K_{N,1}$	m	2.50×10^{-2}	2.90×10^{-2}	2.40×10^{-2}	2.80×10^{-2}	2.40×10^{-2}	2.80×10^{-2}	2.50×10^{-2}	2.90×10^{-2}	2.50×10^{-2}	2.90×10^{-2}
	K_l	kN	2.58×10^4	2.99×10^4	3.14×10^4	3.67×10^4	3.14×10^4	3.67×10^4	3.28×10^4	3.80×10^4	2.58×10^4	2.99×10^4

B

B

Table B.7: Joint parameter in longitudinal tunnel structure modelling (dilation joint)

Parameter		Unit	D11-D15, D41-D45, D51-D55		D21-D25, D31-D35		I5	
			Normal	Expansion	Normal	Expansion	Normal	Expansion
Flexural	K_{r1}	kN*m	1.63×10^{12}	1.63×10^{12}	1.63×10^{12}	1.63×10^{12}	2.00×10^{10}	2.00×10^{10}
	θ_0	rad	5.30×10^{-8}	2.24×10^{-4}	7.30×10^{-8}	2.24×10^{-4}	5.30×10^{-8}	2.30×10^{-4}
	M_0	kN*m	8.66×10^{4}	3.70×10^{8}	1.18×10^{5}	3.70×10^{8}	8.66×10^{4}	5.11×10^{6}
Shear	Q_{max}	kN	1.93×10^{4}	8.40×10^{7}	2.64×10^{4}	8.40×10^{7}	7.50×10^{8}	7.50×10^{8}
	k_s	kN/m	5.62×10^{10}	5.62×10^{10}	5.62×10^{10}	5.62×10^{10}	Na	Na
Axial	d_{N0}	m	2.30×10^{-7}	1.00×10^{-3}	3.13×10^{-7}	1.00×10^{-3}	1.72×10^{-5}	1.00×10^{-3}
	N_0	kN	3.22×10^{4}	1.40×10^{8}	4.40×10^{4}	1.40×10^{8}	3.22×10^{4}	1.90×10^{6}
	K_{a1}	kN/m	1.40×10^{11}	1.40×10^{11}	1.40×10^{11}	1.40×10^{11}	1.87×10^{9}	1.87×10^{9}

Table B.8: Joint shear displacement-1 (unit:m)

Joint	I1	D11	D12	D13	D14	D15	I2	D21	D22	D23	D24	D25	I3	D31	D32
Normal	6.60×10^{-4}	8.11×10^{-5}	1.07×10^{-4}	2.72×10^{-5}	2.05×10^{-5}	2.21×10^{-5}	1.37×10^{-4}	1.32×10^{-5}	1.32×10^{-5}	3.76×10^{-6}	3.47×10^{-6}	4.90×10^{-6}	2.96×10^{-5}	1.45×10^{-6}	2.23×10^{-6}
Expansion	6.68×10^{-4}	2.11×10^{-8}	2.95×10^{-8}	6.66×10^{-9}	6.90×10^{-9}	6.34×10^{-9}	1.39×10^{-4}	4.75×10^{-9}	4.86×10^{-9}	1.10×10^{-9}	1.08×10^{-9}	1.75×10^{-9}	3.00×10^{-5}	5.21×10^{-10}	8.45×10^{-10}

Table B.9: Joint shear displacement-2 (unit:m)

Joint	D33	D34	D35	I4	D41	D42	D43	D44	D45	I5	D51	D52	D53	D54	D55	I6
Normal	5.75×10^{-7}	5.39×10^{-7}	1.83×10^{-6}	4.34×10^{-9}	2.34×10^{-6}	7.10×10^{-7}	1.06×10^{-6}	4.64×10^{-6}	5.77×10^{-6}	5.54×10^{-7}	6.43×10^{-6}	4.76×10^{-6}	1.56×10^{-5}	7.13×10^{-5}	8.01×10^{-5}	5.38×10^{-4}
Expansion	1.60×10^{-10}	1.48×10^{-10}	6.76×10^{-10}	2.15×10^{-10}	6.67×10^{-10}	1.13×10^{-10}	1.86×10^{-10}	1.32×10^{-9}	1.59×10^{-9}	5.68×10^{-7}	2.09×10^{-9}	2.37×10^{-9}	3.30×10^{-9}	2.04×10^{-8}	2.23×10^{-8}	5.46×10^{-4}

Table B.10: Joint shear displacement comparison(unit:mm)

Joint	D13	D14	D15	D21	D22	D23	D24	D25	D31	D32	D33	D34	D35	D41	D42	D43	D44	D45	D51	D52	D53
Simulation	-2.7×10^{-5}	-2.0×10^{-5}	-2.2×10^{-5}	-1.3×10^{-5}	-1.3×10^{-5}	-3.8×10^{-9}	-3.5×10^{-6}	-4.9×10^{-6}	-1.4×10^{-6}	-2.2×10^{-6}	-5.7×10^{-7}	-5.4×10^{-7}	-1.8×10^{-6}	-2.3×10^{-6}	-7.1×10^{-7}	-1.1×10^{-6}	-4.6×10^{-6}	-5.8×10^{-6}	-6.4×10^{-6}	-4.8×10^{-6}	-1.6×10^{-5}
Measurement	-2.8×10^{-1}	-9.0×10^{-2}	2.7×10^{-2}	5.0×10^{-2}	-7.7×10^{-2}	-1.2×10^{-1}	-1.7×10^{-1}	-1.3×10^{-1}	-6.7×10^{-2}	3.9×10^{-2}	2.3×10^{-2}	-6.5×10^{-2}	5.6×10^{-3}	-2.4×10^{-2}	5.8×10^{-2}	-6.8×10^{-2}	-4.1×10^{-2}	-1.7×10^{-1}	-1.2×10^{-1}	Na	-8.7×10^{-2}

Table B.11: Joint rotation result-1 (unit:rad)

Joint	I1	D11	D12	D13	D14	D15	I2	D21	D22	D23	D24	D25	I3	D31	D32
Normal	8.82×10^{-5}	2.42×10^{-8}	9.18×10^{-9}	1.22×10^{-9}	1.21×10^{-9}	4.69×10^{-9}	6.04×10^{-6}	4.82×10^{-9}	1.93×10^{-9}	6.27×10^{-10}	1.37×10^{-10}	6.91×10^{-10}	2.27×10^{-6}	1.25×10^{-9}	7.97×10^{-10}
Expansion	8.53×10^{-5}	2.48×10^{-8}	8.70×10^{-9}	2.39×10^{-11}	5.17×10^{-10}	4.69×10^{-9}	5.54×10^{-6}	4.86×10^{-9}	1.84×10^{-9}	5.17×10^{-10}	1.16×10^{-10}	7.02×10^{-10}	2.17×10^{-6}	1.26×10^{-9}	7.84×10^{-10}

Table B.12: Joint rotation result-2 (unit:rad)

Joint	D33	D34	D35	I4	D41	D42	D43	D44	D45	I5	D51	D52	D53	D54	D55	I6
Normal	5.77×10^{-10}	5.09×10^{-10}	3.16×10^{-10}	2.10×10^{-6}	3.11×10^{-10}	4.94×10^{-10}	5.74×10^{-10}	9.00×10^{-10}	1.73×10^{-9}	5.92×10^{-10}	5.31×10^{-10}	4.21×10^{-10}	2.91×10^{-11}	5.03×10^{-9}	1.71×10^{-8}	6.06×10^{-5}
Expansion	5.57×10^{-10}	5.13×10^{-10}	3.18×10^{-10}	1.96×10^{-6}	3.17×10^{-10}	4.99×10^{-10}	5.33×10^{-10}	8.62×10^{-10}	1.75×10^{-9}	4.46×10^{-8}	5.62×10^{-10}	7.77×10^{-10}	9.00×10^{-10}	4.46×10^{-9}	1.75×10^{-8}	5.81×10^{-5}

NOTATION

ACRONYMS

AC	Adjustable clamps (in the model joint test set-up)
BFS	Brillouin frequency shift
BOFDA	Brillouin Optical Frequency Domain Analyzer
BOFDR	Brillouin Optical Frequency Domain Reflectometry
BOTDA	Brillouin Optical Time Domain Analyzer
BOTDR	Brillouin Optical Time Domain Reflectometry
BP	Bottom plate (in the model joint test set-up)
DOFS	Distributed optical fiber sensor
FBG	Fiber Bragg Grating
FEA	Finite element analysis
FEM	Finite Element Method
FL	Fiber line in a sensor block at joint
FP	Fixation point
GINA	GINA gasket at immersion joint
HG	Horizontal gauge (in the model joint test set-up)
MRE	Maximum relative error
MWS	Maximum working strain
NAP	Normaal Amsterdams Peil
OMEGA	OMEGA gasket at immersion joint
VG	Vertical gauge (in the model joint test set-up)
VP	Vertical plate (in the model joint test set-up)
2D	Two dimension
3D	Three dimension

B

GREEK SYMBOLS

β	Correction factor of ultimate foundation resistance
γ	The saturated unit weight of water / density of subgrade soil
Δf	The decrease of measured Brillouin frequency shift in the fiber loading curve
Δf_e	The decrease of measured Brillouin frequency shift due to elastic creep in the fiber loading curve
Δf_p	The decrease of measured Brillouin frequency shift due to plastic creep in the fiber loading curve
Δh	The tide amplitude
$\Delta \varepsilon_1$	The actual imposed strain in a loading scenario of the fiber loading curve
$\Delta \varepsilon_2$	The measured strain by the fiber sensor in the fiber loading curve
ΔL	The longitudinal thermal deformation of the full immersed sections
Δs	The amplitude of uneven settlement within a tide period
ΔS_k	The cumulated joint uneven settlement at the kth joint (from the north)
ΔX	The joint lateral drift deformation
ΔY	The joint opening measured by DOFS
ΔY_{ref}	The imposed joint opening displacement in model test
ΔZ	The joint uneven settlement measured by DOFS
η	Sensitivity index of uneven settlement to tide variation /
ε	Strain
ε_v	The volumetric strain of porous medium
ε_e	The elastic component of strain decrease by jacket material creep
ε_j	The strain decrease by creep of the jacket material
ε_m	The initial imposed maximum strain in the optical fiber loading curve
ε_p	The total plastic strain of optical fiber
ε_s	The strain decrease by inter-layer slippage in optical fiber
$\varepsilon_{1,i}$	The measured strains of horizontal fiber lines in a sensor block at sampling point i
$\varepsilon_{2,i}$	The measured strains of inclined fiber lines in a sensor block at sampling point i
θ	The rotation angle (rad) of joint cross-section

B

θ_0	The allowable rotation angle at dilation joint
θ_1	The first turning point at joint flexural curve
μ	The friction coefficient at concrete interface
ν	Poisson's ratio
Ψ	Conversion factor for shear modulus of soil

LATIN SYMBOLS

a	Horizontal deviation (of the top point) at sensor installation / Conversion factor from shear wave velocity to soil density
b	Conversion factor from shear wave velocity to soil density
B	Foundation width
A	Area of cross-section
A_s	The cross-section area of shear key
C_ε	Strain sensitivity of fiber
C_T	Temperature sensitivity of fiber
$C_{o,t}$	Opening-temperature Pearson correlation coefficient
$C_{s,t}$	Uneven settlement-temperature Pearson correlation coefficient
d_N	The normal compression at joint
$d_{N,0}$	The initial compression of dilation joint
$d_{N,1}$	The joint compression at the division points of axial behavior curve
d_s	The shear displacement at joint
Dik	The kth dilation joint (from north end) within the ith element (Heinenoordtunnel)
E	Young's modulus
E_{oed}	Odometer stiffness of soil
E_{100}	Stiffness of soil corresponding to an effective vertical stress of 100 KPa
f	Brillouin frequency shift
f_0	The reference Brillouin frequency shift
$f_{t,0}$	The BFS at reference temperature T_0
$f_{t,i}$	The measured BFS corresponding to T_i
$f(d)$	The compression force of GINA (per meter)
F	Force
$f_{1,i}$	The measured Brillouin frequency shifts of horizontal fiber lines in a sensor block at sampling point i

$f_{2,i}$	The measured Brillouin frequency shifts of inclined fiber lines in a sensor block at sampling point i
F_N	Normal force at joint
F_S	Shear force at joint
G	The shear modulus
G_0	The small-strain shear modulus of soil
G_{eq}	The shear modulus of soil
h_c	Cross section centroid height
Ij	The jth immersion joint from north end (Heinenoordtunnel)
I	The cross-section inertia
I_x	Cross section inertia of tunnel along X-axis
k	The permeability of soil
k_{a1}	The (first) compression stiffness of joint
k_{a2}	The (second) compression stiffness of joint
k_{r1}	The (first) bending stiffness of joint
k_{r2}	The (second) bending stiffness of joint
k_s	The shear stiffness of joint
k_1	The gradient of upper boundary curve in the characteristic loop
k_2	The gradient of unloading curve in the fiber the characteristic loop
k_3	The gradient of ultimate curve in the fiber characteristic loop
K'	The bulk modulus of water
K_s	Subgrade reaction coefficient
l_0	The characteristic length of dilation joint
l_1	The gauge lengths of horizontal fiber lines in a sensor block
l_2	The gauge lengths of inclined fiber line in a sensor block
$l_{1,i}$	The lengths of horizontal fiber line in a sensor block at sampling point i
$l_{2,i}$	The lengths of inclined fiber lines in a sensor block at sampling point i
L	The total length of GINA at joint
L_b	The GINA gasket length at bottom side
L_s	The shear key length
M	Cross-section moment at joint
M_0	The allowable bending moment at dilation joint

B

n	The porosity of soil
N_0	The initial compression force at dilation joint
q	The bearing pressure under foundation
q_{ult}	The ultimate resistance of foundation soil
Q_{max}	The maximum static friction at dilation joint
T	Temperature
T_0	Reference(baseline) temperature
V_s	The shear wave velocity
w	The vertical displacement
x_0	The GINA compression at section centroid
z_t	The distance of GINA gasket at top side to the centroid
z_b	The distance of GINA gasket at bottom side to the centroid

ACKNOWLEDGEMENTS

During a period of around five years (Oct. 2017– Nov. 2022) as a PhD researcher at the Department of Geoscience and Engineering in TU Delft, I explored the possibility of distributed optical fiber sensor(DOFS) in immersed tunnel behavior monitoring. I hope my research work has provided some improved insights in this area. This PhD period has become a really unforgettable journey in my life, it is my great honor to have so many friends, colleagues and not the least, supervisors to help and guide me. Without their support, it would have been impossible for me to finish this challenging journey. I have obtained not only precious research experience but also invaluable friendships which I will carry with my lifetime. I would like to apologize firstly for not being able to list all whom I am grateful for. This doctoral dissertation is dedicated to them. And the following is not necessarily in the sequence of significance.

I would like to thank my promotor, Prof. Ken Gavin, for the support and supervision he provided in my PhD research. His critical thinking in the supervision broadened my vision. I really appreciate the valuable inspiration and deep insight he gave me during the meetings. His passion and optimism towards research as well as life impressed me a lot.

I must express my gratitude to my daily supervisor, Dr. Wout Broere, who has offered strong support throughout this journey. He not only inspired me when I felt depressed in my research by asking insightful questions and offering invaluable advice but also encouraged me during the tough times. He joined my every time of field experiments personally and we worked together to overcome the negative effects of the COVID-19 lockdown. I have been extremely lucky to have a daily supervisor who is also a sincere friend.

Special thank-yous to my technician friends in Geo-laboratory, as their excellent supports contributed a lot to this research. I would like to particularly thank Michiel Slob, Jens van den Berg, Marc Friebel, Roland Klasen, Han de Visser, and others in our laboratory. Without their wise counsel and support in my laboratory and field experiments, the research work would not have been possible.

I would like to acknowledge all my committee members who devoted time and effort to reviewing my thesis and giving precious comments, which helps me improve the quality of my thesis.

Thanks to all my PhD colleagues and staff members of the GeoEngineering section and colleagues from other sections, in particular: Xiangcou, Aoxi, Liang, Weiyuan, Haoyuan, Qiang, Yuen, Zheng, Zhaojiang, Lexin, Fengwen, Huang, Wen, Na, Tianyang, Matthew, Kevin, Ivaylo, Anne-Catherine, Dominique, Phil, Stefano, Arash, Juan, Varenya, Cristhian. Their sincerity and humor make me feel warm. I am grateful to spend this time with them. Deep thanks to Yifang, Jiantuan, Jiaxi, Kan, Mei, Lijuan for offering help in my field experiment work. Special thanks to my friend Na Li and Xiangcou's family, who offered sincere help in my PhD journey.

B

CURRICULUM VITÆ

Xuehui ZHANG

27–11–1990   Born in Ji'an, Jiangxi, China.

EDUCATION

2017–2022   Ph.D Candidate in Geotechnical Engineering
              Delft University of Technology, the Netherlands

2014–2017   Master of Engineering in Architectural and Civil Engineering
              Tongji University, Shanghai, China

2010–2014   Undergraduate in Civil Engineering
              Chang'an University, Xi'an, China

LIST OF PUBLICATIONS

Journal Publications

- **Zhang, X.** & Broere, W. (2022). Sensing fiber selection for point displacement measuring with distributed optic fiber sensor. *Measurement* **197**, 111275.

- **Zhang, X.** & Broere, W. (2023). Design of a Distributed Optic Fiber Sensor System for Measuring Immersed Tunnel Joint Deformations. *Tunnelling and Underground Space Technology* **131**, 104770.

- **Zhang, X.** & Broere, W. (2022). Monitoring Tide and Temperature Induced Joint Deformation of Immersed Tunnel. *Tunnelling and Underground Space Technology*. (Under review)

- **Zhang, X.** & Broere, W. (2022). Monitoring Seasonal Deformation Behavior of An Immersed Tunnel with Distributed Optical Fiber Sensors. *Measurement*. (Under review)

- **Zhang, X.** & Broere, W. (2022). Design of Optical Fiber Extensometers for Structural Monitoring of a Tunnel Case Study. *Journal of Civil Structural Health Monitoring*. (Under review)

Conference Publications

- **Zhang, X.** & Broere, W. (2022). Applying distributed optic fiber sensor for tunnel monitoring. *ITA-AITES World Tunnel Congress, WTC2022 and 47th General Assembly Bella Center, Copenhagen 22-28 April 2022.*

- **Zhang, X.**, Wu X. & Broere, W. (2022). Impact of subsoil spatial variability on deformations of immersed tunnel.. *In 10th International Symposium on Geotechnical Aspects of Underground Construction in Soft Ground, IS-CAMBRIDGE 2022*, 738-745.